RCA Review

March 1975 Volume 36 No. 1

RCARCI 36(1) 1-210 (1975)

RCA Review, published quarterly in March, June, September and December by RCA Research and Engineering, RCA Corporation, Princeton, New Jersey 08540. Entered as second class matter July 3, 1950 under the Act of March 3, 1879. Second-class postage paid at Princeton, New Jersey, and at additional mailing offices. Effective Jan. 1, 1971, subscription rates as follows: United States and Canada: one year $6.00, two years $10.50, three years $13.50; in other countries, one year $6.40, two years $11.30, three years $14.70. Single copies (except for special issues) up to five years old $3.00.

RCA Review

A technical journal published quarterly by RCA Research and Engineering in cooperation with the subsidiaries and divisions of RCA

Contents

Optical Properties of Materials

March 1975 Volume 36 Number 1

RCA Corporation

Robert W. Sarnoff Chairman of the Board and Chief Executive Officer
A. L. Conrad President and Chief Operating Officer

Editorial Advisory Board

Chairman, J. A. Rajchman RCA Laboratories

A. A. Ahmed Solid State Division
E. D. Becken RCA Global Communications
G. D. Cody RCA Laboratories
D. M. Cottler Government and Commercial Systems
N. L. Gordon RCA Laboratories
G. B. Herzog RCA Laboratories
J. Hillier RCA Research and Engineering
E. O. Johnson International Licensing
J. Kurshan RCA Laboratories
C. H. Lane Electronic Components
D. S. McCoy Consumer Electronics
K. H. Powers RCA Laboratories
R. E. Quinn RCA Laboratories
P. Rappaport RCA Laboratories
J. H. Scott, Jr. RCA Laboratories
L. A. Shotliff International Licensing
T. O. Stanley RCA Laboratories
F. Sterzer RCA Laboratories
J. J. Tietjen RCA Laboratories
W. M. Webster RCA Laboratories

Secretary, Charles C. Foster RCA Laboratories

Editor

Ralph F. Ciafone

Associate Editors

W. A. Chisholm RCA Limited (Canada)
M. G. Gander RCA Service Company
W. O. Hadlock RCA Research and Engineering
D. R. Higgs Missile and Surface Radar Division
W. A. Howard National Broadcasting Company
C. Hoyt Consumer Electronics
E. McElwee Solid-State Division
C. A. Meyer Electronic Components
M. G. Pietz Government and Commercial Systems
C. W. Sall RCA Laboratories
I. M. Seideman Astro-Electronics Division
R. N. Hurst Communications Systems Division

© RCA Corporation 1975 All Rights Reserved Printed in USA

Optical Properties of Materials—Introduction

Many advances in electronics depend on phenomena involving light. While this dependence is not new, it has assumed a far greater importance in recent years and much of today's frontier of electronics is connected with the generation, transmission, control, and sensing of light. Well known applications such as imaging, displays, communication, information storage and processing, probing into the nature of matter and others have been at once both spectacular and limited. Spectacular, because of the novel functions they have been able to provide by exploiting options opened by the laser and coherent light optics, by solid state light sources and sensors, and by a host of electronically changeable optical properties of materials. Limited, because they fall short of their inherent quantitative potentialities and because many more have and can be conceived that have not yet even been crudely demonstrated. No better climate can exist for stimulating search toward deeper understanding, greater mastery over materials, and imaginative inventions.

Over the years the RCA Laboratories in its Princeton, Zurich, and Tokyo locations have been engaged in precisely such searches. The ten papers in this issue of RCA Review give a perspective of the work as of this time. The papers, in the nature of tutorial reviews, containing the newest results, cover a variety of subjects related to optical properties of materials and address a broad readership not limited to narrow specialists.

Optical properties of materials provide a powerful, convenient and nondestructive insight into a broad range of characteristics that distinguish various substances. Wherever a phase transformation occurs it can be monitored optically. Subtle features in the band structure of crystals leave a decipherable signature in the optical spectra. Indeed most of the papers are concerned with understanding physical properties of matter from optical measurements.

The first five deal mostly with optical studies of nearly ideal structures. D. Baeriswyl and W. Czaja are concerned with a new effect of a high density exciton gas observed at low temperatures by photoluminescence. This new phenomenon is the quantum effect of a degenerate Bose gas, known as Bose-Einstein condensation. Experimental data on excitons in AgBr are compared with a well-known Bose system, liquid helium. The next paper, by G. Harbeke and E. Tosatti, is concerned with the optical properties of layer structure compounds and discusses optical spectra of such materials in terms of electronic band structure. R. K. Wehner and E. F. Steigmeier explain how fluctuations in the dielectric susceptibility give rise to light scattering, particularly for the case of two interacting modes. This problem is important in analyzing experimental light-scattering spectra. The fourth paper, by J. R. Sandercock, describes an interferometer of extremely high contrast and gives an example of its use in measurements of Brillouin scattering in some materials. The paper by H. Fujita et al on polystyrene suspension in water concerns the remarkable quasi-crystal-like suspension of microscopic spheres in a liquid and their optical properties.

The next five papers concern investigation of actual materials. R. Casanova Alig's paper on rare earth impurities in alkaline earth halide hosts discusses the nephelauxetic effect (the reduction of the electrostatic interaction between the impurity and the host crystal) found in recent measurements of the optical spectra of these materials. Peter Wojtowicz presents a theoretical model that predicts two-dimensional phase transitions involving the distribution of mobile positive ions at SiO_2-Si interfaces and estimates the magnitudes of the critical temperatures and accompanying thermal anomalies. The next two papers discuss the optical properties of $SrTiO_3$ and $LiNbO_3$ (H. A. Weakliem et al) and of GaN (J. I. Pankove et al), materials that have a range of properties of potential practical application. The last paper, by B. W. Faughnan et al, considers electrochromism in WO_3 films, a phenomenon of interest for display applications.

In closing, I would like to acknowledge the contribution of Drs. Jacques I. Pankove, Richard Williams, and Gunter Harbeke, who served as Guest Editors for this special issue. Anyone who has ever been involved in such a task fully appreciates the depth of knowledge and dedication necessary to perform it successfully.

J. A. Rajchman
Chairman, Editorial Advisory Board, *RCA Review*

Bose–Einstein Condensation in Exciton Systems and Liquid Helium

D. Baeriswyl and W. Czaja

Laboratories RCA Ltd., Zurich, Switzerland

Abstract—Excitons (bound electron–hole–pairs) form a Bose gas provided their average distance is large compared to the exciton Bohr radius. Triplet-excitons, generated in AgBr crystals by optical means, have a temperature close to the bath temperature. The properties of the exciton luminescence indicates Bose–Einstein condensation of these triplet excitons below 3 K. The experimental data are interpreted based on the model of weakly interacting bosons.

1. Introduction

More than twelve years ago, Moskalenko, Blatt and coworkers and Casella[1] discussed, independently, the possibility of Bose–Einstein condensation of excitons. Seven years later, the first experimental paper appeared in which a particular emission line of CdSe was attributed to the radiative recombination of Bose–Einstein condensed excitons. Since then, this subject has attracted various groups and, quite recently, the evidence for Bose–Einstein condensation of excitons has become more and more convincing.

The first application of the theory of Bose–Einstein condensation was to superfluid helium. Even today, however, no stringent experimental proof exists for Bose–Einstein condensation in liquid helium, mainly because the ground state of liquid helium is stable and, therefore, not directly accessible experimentally.

On the other hand, the ground state of excitons is directly observable by optical means, because excitons can radiatively decay to the ground state of the host crystal. Therefore, both the optical properties of the crystal and the cooperative aspect of the many-exciton system will be essential for the phenomena discussed in this paper. Nevertheless, the main arguments concerning the Bose–Einstein condensation are similar for both systems. Thus, we shall discuss both superfluid helium and excitons on an equal footing in the light of different aspects of the theory of Bose–Einstein condensation.

2. The Ideal Bose Gas

Nowadays quantum statistics usually starts with the concept of the undiscernability of identical particles expressed by the symmetry of the wave functions under the permutation of particle coordinates. Thus it is surprising that one of the most peculiar effects of quantum statistics—the Bose–Einstein condensation—was predicted before the formalism of quantum mechanics was fully developed. In 1924 the Indian physicist S. N. Bose, virtually unknown to the scientific community at that time, published a paper[2] in which he derived Planck's formula for black-body radiation using a new method that contained the essential points of "Bose-Statistics".* Einstein realized the importance of Bose's work and applied the method to the case of an ideal gas of particles.[3] In contrast to photons, particles have a mass. Therefore, the total number of particles cannot be changed, say, by isothermal compression. Instead, they redistribute among the energy levels. Einstein found that an increasing number of particles goes into the state of zero kinetic energy under compression at sufficiently low temperatures, similarly to the condensation of saturated vapor in a real gas.†

After a long period, during which the applicability and even the correctness of Einstein's theory was questioned, London revived interest in the Bose–Einstein condensation by rederiving it on the basis of quantum mechanics and applying it to the λ-transition of superfluid helium.[5]

Before reproducing the details of London's derivation, let us give an estimate of the temperature region where quantum effects become important. We consider N ideal (i.e., noninteracting) particles of

---

* It seems that Bose sent his manuscript to Einstein who, impressed by its originality,[4] immediately translated it into German and had it published in *Zeitschrift für Physik* with some very favorable and kind comments by the translator.

† Therefore, the discoverer of this condensation phenomenon is Einstein, and it would be appropriate to call it "Einstein condensation." Correspondingly, particles obeying Bose's statistics are actually called "bosons."

mass M in a cubic box of volume V. The average distance between the particles is $(V/N)^{1/3}$. On the other hand, the thermal de Broglie wavelength λ at a temperature T is[6]

$$\lambda = \left(\frac{2\pi\hbar^2}{Mk_BT}\right)^{1/2} \qquad [2.1]$$

(corresponding to a mean kinetic energy of the order of k_BT). Interference effects are important if λ is of the order of, or larger than, the interparticle spacing, i.e., for temperatures

$$T \lessapprox \frac{2\pi\hbar^2}{Mk_B}\left(\frac{N}{V}\right)^{2/3} \qquad [2.2]$$

This argument gives an estimate of the "degeneracy temperature" that is valid for both fermions and bosons. Quantum effects become important below the degeneracy temperature.

Let us now return to the case of bosons and London's treatment. The mean number n_p of particles with momentum p at a temperature T is given by

$$n_p = \frac{1}{\exp\left\{\beta\left(\frac{p^2}{2M} - \mu\right)\right\} - 1}, \qquad [2.3]$$

where $\beta = 1/k_BT$ and μ is the chemical potential determined by the requirement

$$N = \sum_p n_p. \qquad [2.4]$$

μ must be negative to ensure that n_p is always a positive number. It is tempting to replace the sum by an integral in the usual way

$$\sum_p \longrightarrow \frac{V}{(2\pi)^3}\int d^3p. \qquad [2.5]$$

Note that a statistical weight zero is attributed to the zero momentum term under the integral. This will not be serious unless this omitted term is of the same order as the whole expression or, more precisely, unless, in the thermodynamic limit ($N \to \infty$, $V \to \infty$, $N/V =$ constant) a finite fraction N_0 of particles has momentum zero. From Eq. [2.3] it follows that this can only occur if the chemical potential is of the order $1/N$, for then

$$N_0 \approx -\frac{1}{\beta\mu} = O(N). \qquad [2.6]$$

On the other hand, the kinetic energy of the excited states is at least of order $N^{-2/3}$ (as is easily seen by applying periodic boundary conditions on the plane wave states) and therefore, μ can be neglected in n_p ($p \neq 0$). Therefore, by replacing the sum in Eq. [2.4] by an integral, but taking into account the zero momentum term Eq. [2.6], we get

$$N = N_0 + \frac{V}{(2\pi)^3}\int d^3p \frac{1}{\exp\left\{\frac{\beta p^2}{2M}\right\} - 1} \qquad [2.7]$$

The integration can be performed[7] and one obtains

$$N = N_0 + \zeta\left(\frac{3}{2}\right)\left(\frac{Mk_BT}{2\pi\hbar^2}\right)^{3/2} V. \qquad [2.8]$$

where

$$\zeta\left(\frac{3}{2}\right) = 2.612\ldots$$

N_0 must be positive and thus, for given values of N and V, the temperature must be smaller than the "critical temperature"

$$T_C = 1 - \frac{1}{\left(\zeta\left(\frac{3}{2}\right)\right)^{2/3}} \frac{2\pi\hbar^2}{Mk_B}\left(\frac{N}{V}\right)^{2/3}. \qquad [2.9]$$

Note that this value is of the same order as the previously estimated degeneracy temperature Eq. [2.2]. From Eqs. [2.8] and [2.9] we get

$$\frac{N_0}{N} = 1 - \left(\frac{T}{T_C}\right)^{3/2} \quad \text{for} \quad T < T_C \qquad [2.10]$$

We conclude that below T_c a finite fraction of particles is "condensed" in the lowest state. The chemical potential is zero (in the thermodynamic limit) which means that all particles added go into the condensate. In a similar way one shows that for temperatures above T_c, the chemical potential is of the order of unity, and therefore no condensation occurs.

Clearly the derivation given here is mathematically not fully satisfactory. A rigorous treatment,[8] however, leads to the same results, Eqs. [2.9] and [2.10].

3. Interacting Bose Systems

3.1 Theory

London's idea of applying the picture of ideal bosons to superfluid helium, as attractive it may be, is certainly not adequate, because liquid helium is a strongly interacting system (as he himself realized[5]). The extension of the theory to this case turns out to be extremely difficult, and thus far no microscopic theory of superfluid helium comparable to the BCS theory of superconductivity exists. In the weak coupling limit, of course, the problem has been solved by Bogoliubov,[9] but for strong coupling, the properties of the ground-state cannot be evaluated without extensive numerical work. The main problem we are concerned with here is the Bose–Einstein condensation or, more generally, the momentum distribution function n_p for an interacting Bose system. The Hamiltonian is assumed to be of the following form

$$\mathcal{H} = \sum_{\mathbf{k}} \epsilon_k b_{\mathbf{k}}^+ b_{\mathbf{k}} + \frac{1}{2V} \sum_{\mathbf{k}\mathbf{k}'\mathbf{q}} v(q) b_{\mathbf{k}}^+ b_{\mathbf{k}'}^+ b_{\mathbf{k}'+\mathbf{q}} b_{\mathbf{k}-\mathbf{q}} \qquad [3.1]$$

where $\epsilon_k = \hbar^2 k^2/(2M)$ and $v(q)$ is the Fourier transform of the interatomic potential. The creation and annihilation operators $b_{\mathbf{k}}^+$, $b_{\mathbf{k}}$ satisfy the commutation relations

$$\begin{aligned} [b_{\mathbf{k}}, b_{\mathbf{k}'}^+] &= \delta_{\mathbf{k},\mathbf{k}'} \\ [b_{\mathbf{k}}, b_{\mathbf{k}'}] = [b_{\mathbf{k}}^+, b_{\mathbf{k}'}^+] &= 0 \end{aligned} \qquad [3.2]$$

3.1.1 The Weakly Interacting Bose Gas[9]

In the weak coupling limit, a macroscopic number N_0 of particles is expected to have momentum zero (at low T). Therefore the operators b_0^+, b_0 can be treated as numbers

$$b_0 \approx b_0^+ \approx (N_0)^{1/2}. \qquad [3.3]$$

The most important contributions to the interaction energy are those where most of the operators $b_{\mathbf{k}}^+$, $b_{\mathbf{k}}$ have momentum zero. With the above substitution, the leading terms will be quadratic and linear in

N_0. Keeping only these terms and using the identity

$$N_0 \equiv N - \sum_{k\neq 0} b_k^+ b_k, \tag*{[3.4]}$$

the Hamiltonian is reduced to a quadratic form

$$\begin{aligned} \mathcal{H} &= N\frac{\rho}{2}v(0) + \sum_k \epsilon_k b_k^+ b_k \\ &+ \frac{\rho}{2}\sum_{k\neq 0} v(k)(2b_k^+ b_k + b_k^+ b_{-k}^+ + b_k b_{-k}), \end{aligned} \tag*{[3.5]}$$

where $\rho = N/V$, and easily diagonalized by the canonical transformation

$$b_k = \frac{1}{(1 - u_k^2)^{1/2}}(B_k + u_k B_{-k}^+), \tag*{[3.6]}$$

where B_k, B_k^+ are Bose operators describing excitations of the system. The coefficients u_k are determined by te requirement that the Hamiltonian is diagonal in terms of B_k, B_k^+, and are found to be

$$u_k + 1 = \frac{\epsilon_k}{\rho v(k)}\left[\left(\frac{2\rho v(k)}{\epsilon_k} + 1\right)^{1/2} - 1\right]. \tag*{[3.7]}$$

The transformed Hamiltonian is

$$\mathcal{H} = E_0 + \sum_{k\neq 0} E_k B_k^+ B_k, \tag*{[3.8]}$$

where

$$E_0 = N\frac{\rho}{2}v(0) + \ldots \tag*{[3.9]}$$

is the energy of the ground state.

The excitation spectrum E_k has the form

$$E_k = [\epsilon_k^2 + 2\epsilon_k \rho v(k)]^{1/2}, \tag*{[3.10]}$$

with limiting behavior

$$E_k \sim \begin{cases} s\hbar k & k \longrightarrow 0 \\ \epsilon_k & k \longrightarrow \infty \end{cases} \tag*{[3.11]}$$

Here $s = (\rho v(0)/M)^{1/2}$ is the sound velocity at $T = 0$. This can easily be seen from Eq. [3.9] by using the thermodynamic definition of the sound velocity.

The system is stable if s is real, i.e., if

$$v(0) = \int d^3r v(r) > 0. \qquad [3.12]$$

The mean number n_k of particles with momentum $\hbar k \neq 0$ is obtained from Eq. [3.6]

$$n_k \equiv \langle b_{\mathbf{k}}^+ b_{\mathbf{k}} \rangle = \frac{\epsilon_k + \rho v(k) - E_k}{2E_k} + \frac{\epsilon_k + \rho v(k)}{E_k} \frac{1}{\exp\{\beta E_k\} - 1}. \qquad [3.13]$$

whereas the mean occupation number of the zero momentum state follows from Eq. [3.4]

$$N_0 = N - \sum_{\mathbf{k} \neq 0} n_k. \qquad [3.14]$$

Note that, by inserting Eq. [3.13] into [3.14], one obtains a "depletion" of the condensate even at zero temperature (due to the zero-point motion). The second term in Eq. [3.13] gives rise to a temperature-dependent decrease of N_0 due to the thermal motion, quite similar to the case of the ideal gas. The temperature dependence of N_0 is shown for three different densities in Fig. 1. At zero temperature the depletion grows with density as a consequence of the interaction.

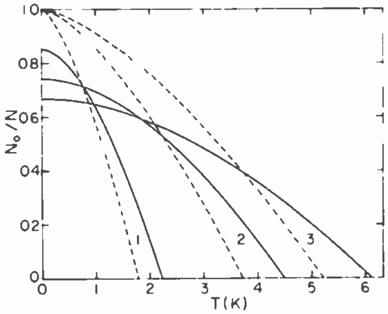

Fig. 1—Temperature dependence of the condensate fraction for an ideal Bose gas (dashed lines) and a weakly interacting Bose gas (solid lines) for 3 different densities. Parameter values: mass $M = 1.1 \times 10^{-27}$ g, scattering length (see Eq. [4.9]) $a \approx 80$ Å, densities (1) 6×10^{16} cm^{-3}, (2) 8×10^{16} cm^{-3}, (3) 1×10^{17} cm^{-3}.

The transition temperature increases with density similar to an ideal gas.

3.1.2 Strongly Interacting Bose Systems, Ground State

As already mentioned, a satisfactory microscopic theory for a strongly interacting system of bosons does not exist. Even for approximate calculations of the properties of the ground state, extensive numerical computation is needed. Let us therefore limit our consideration to the following two problems:

(1) How to determine the wave function of the ground state,

(2) Given this wave function, how to calculate the fraction of particles that are in the condensate (at zero temperature). This question will lead us to the concept of "off-diagonal long-range order" (ODLRO).

Wave Function

The following general properties of the ground-state wave function of the N boson system are known[10]: it is symmetric, it is nondegenerate and it can be chosen positive semidefinite. In the variational approach[11] Φ_0 usually is represented as a product of pair-functions $f(r)$

$$\Phi_0(\mathbf{r}_1, \ldots, \mathbf{r}_N) = \prod_{i \neq j} f(|\mathbf{r}_i - \mathbf{r}_j|), \qquad [3.15]$$

where $f(r)$ contains some adjustable parameters, is positive semidefinite, and must behave properly in the limits $r \to 0$ and $r \to \infty$. Zero-point fluctuations may be explicitly built in.[12]

The parameters in $f(r)$ must be chosen in such a way as to minimize the expectation value of the energy which, due to Eq. [3.15], can be related to the correlation function $p(r)$ defined as

$$p(|\mathbf{r}_1 - \mathbf{r}_2|) = N(N-1)\int d^3r_3 \ldots d^3r_N \Phi_0^2(\mathbf{r}_1, \ldots, \mathbf{r}_N). \qquad [3.16]$$

The probability amplitude Φ_0^2 plays the same role here as the Gibbs' distribution in classical statistical mechanics and, therefore, the numerical methods applied successfully there, such as the Monte-Carlo technique[13] or molecular dynamics,[14] have been used to evaluate the above integral.

Very recently Kalos, Levesque, and Verlet[15] found a "numerically exact" solution of the Schrödinger equation for a Bose system with hard-sphere forces. The modifications that are necessary to account for the difference between a hard-sphere model and a realistic potential are subsequently evaluated by a perturbation treatment. The "realistic potential" is represented by a Lennard–Jones potential with parameters determined[16] in the gas phase of He^4.

Off-Diagonal Long-Range Order

Let us, for convenience, introduce the field operators $\psi^+(\mathbf{x})$ and $\psi(\mathbf{x})$, which create and annihilate, respectively, a particle at the point $\mathbf{x}$ and are related to the operators in Eq. [3.2] by

$$\psi(\mathbf{x}) = V^{-1/2}\sum_k \exp\{i\mathbf{kx}\}b_\mathbf{k}; \qquad [3.17]$$

$\psi^+(\mathbf{x})$ is given by a similar relation. Let us also define the reduced density matrices[17]

$$\begin{aligned} \rho_1(\mathbf{x},\mathbf{x}') &= \langle\psi^+(\mathbf{x}')\psi(\mathbf{x})\rangle \\ \rho_2(\mathbf{x},\mathbf{y};\mathbf{x}',\mathbf{y}') &= \langle\psi^+(\mathbf{y}')\psi^+(\mathbf{x}')\psi(\mathbf{x})\psi(\mathbf{y})\rangle, \end{aligned} \qquad [3.18]$$

where the bracket denotes an average over either the ground state or a statistical ensemble. As a special case, one obtains, by using Eq. [3.16]

$$\rho_2(\mathbf{x},\mathbf{y};\mathbf{x}',\mathbf{y}') = p(\mathbf{x},\mathbf{y}). \qquad [3.19]$$

Thus the pair correlation function is equal to the *diagonal* part of the second reduced density matrix. This is the reason why the long-range order expressed by the nonvanishing of the pair correlation function at large distances (and occurring for instance in a crystal lattice) is called diagonal long-range order. As we shall now show, in a Bose–Einstein condensed system, it is the *off-diagonal* part of the first reduced density matrix that does not vanish at infinity, and therefore Bose–Einstein condensation is an example of "off-diagonal long-range order" (ODLRO).*

Condensate Fraction for Liquid He^4 at $T = 0$

Consider a homogenous system in which a finite fraction of all particles is in the zero-momentum state. From Eq. [3.17] and [3.18] we get

---

* This concept was invented by Penrose[18] but the name was first used by Yang.[19] He showed that ODLRO also occurs in Fermi systems (superconductivity is an example). But then the density matrix of lowest order that shows ODLRO must contain an even number of fermion operators.[20]

$$\rho_1(\mathbf{x},\mathbf{x}') = \rho_1(\mathbf{x} - \mathbf{x}') = \frac{N_0}{V} + \sum_{\mathbf{k}\neq 0} \exp\{i\mathbf{k}(\mathbf{x} - \mathbf{x}')\langle b_{\mathbf{k}}{}^{+}b_{\mathbf{k}}\rangle; \qquad [3.20]$$

thus $\rho_1(\mathbf{x},\mathbf{x}') \rightarrow N_o/V$ for $|\mathbf{x} - \mathbf{x}'| \rightarrow \infty$. At zero temperature the one-particle density matrix, in terms of the N-body wave-function Φ_0, is

$$\rho_1(\mathbf{x},\mathbf{x}') = N\int d^3r_2 \ldots d^3r_N \Phi_0(\mathbf{x},\mathbf{r}_2,\ldots\mathbf{r}_N)\Phi_0(\mathbf{x}',\mathbf{r}_2,\ldots\mathbf{r}_N). \qquad [3.21]$$

Therefore, once the ground-state wave function is known, one must calculate the integral Eq. [3.21] and, especially, look for its asymptotic behavior for $|\mathbf{x} - \mathbf{x}'| \rightarrow \infty$. For an interatomic potential appropriate to He^4 the numerical calculations[10-15] indicate that Bose–Einstein condensation exists at zero temperature and the fraction of condensed particles is about 10%.

3.2 Experiments in Superfluid He^4

It has been proposed by Miller, Pines, and Nozières,[21] and later in more detail by Hohenberg and Platzman,[22] to use neutron scattering at large momentum transfer for measuring the condensate fraction in liquid He^4. The differential cross section is proportional to the dynamic structure factor $S(k,\omega)$, where $\hbar k$ and $\hbar\omega$ are the momentum and energy transfer to the liquid, respectively. If k and $\hbar\omega$ are much larger than typical wave vectors and energies associated with the collective behavior of the liquid, the scattering can be thought of as taking place on individual atoms ("impulse approximation"). If an atom of initial momentum p is struck by a neutron and left with momentum $\mathbf{p} + \hbar\mathbf{k}$, it will gain an energy

$$\hbar\omega = \epsilon_{\mathbf{p}+\hbar\mathbf{k}} - \epsilon_p = \epsilon_k + \hbar\frac{\mathbf{k}\cdot\mathbf{p}}{M}. \qquad [3.22]$$

To obtain the scattered intensity one has to average over the initial momentum distribution n_p in the liquid. Thus, in the impulse approximation,

$$S(k,\omega) \sim \frac{1}{N}\sum_p n_p\delta\left(\omega - \frac{\epsilon_k}{\hbar} - \frac{\mathbf{k}\cdot\mathbf{p}}{M}\right). \qquad [3.23]$$

This formula is exact[23] in the limit $k,\omega \rightarrow \infty$. Separating the condensed part from the rest, we get

$$S(k,\omega) \sim \frac{N_0}{N}\delta\left(\omega - \frac{1}{\hbar}\epsilon_k\right) + \frac{1}{N}\sum_{\mathbf{p}\neq 0} n_p\delta\left(\omega - \frac{1}{\hbar}\epsilon_k - \frac{\mathbf{k}\cdot\mathbf{p}}{M}\right). \qquad [3.24]$$

A very sharp line with an intensity proportional to the condensate fraction should be seen sitting on top of a wide Doppler-broadened second peak, centered at the free particle energy ϵ_k.

Before discussing the actual experiments, we should be aware of the following difficulties:

(1) n_p represents the momentum distribution of the interacting liquid and is not well represented by a simple Gaussian.[24] This follows from Eq. [3.13] in the case of weak interaction. For superfluid He^4, n_p must be taken from numerical calculations.[13]

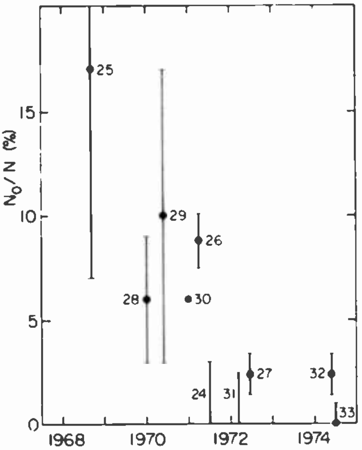

Fig. 2—Values of the condensate fraction in superfluid He^4, estimated from neutron scattering data, as a function of publication date. The numbers (24)–(33) indicate the references.

(2) The experiments must be carried out at finite k and ω, and the question as to what extent Eq. [3.23] is valid in that case is not easy to answer. Certainly a broadening of the condensate line occurs due to final-state interactions.[22]

(3) The experiments must be performed at finite temperatures (actually all three experiments reported were carried out between 1.1° and 1.3°K). An additional broadening should therefore be taken into account and, furthermore, a consistent discussion

should be based on the momentum distribution at finite temperature (for which, to our knowledge, no reliable calculation exists).

The experiments[25-27] (with momentum transfer up to 20.3 $Å^{-1}$) showed clearly the Doppler-broadened peak centered at the free particle energy, but not the expected sharp condensate line. Information about N_0 had therefore to be extracted from an analysis of the line shape. Fig. 2 shows the different results. The estimated value for N_0 seems to be a monotonically decreasing function of the publication date. This is partly due to increasing experimental accuracy, and partly to the growing sophistication of the interpretation.

Comparing the most recent values obtained in this way ($T = 1.2°K$) with those calculated numerically from first principles ($T = 0$, see previous section), one is faced with a clear discrepancy, at least if one assumes that the difference in temperature is not important. If one believes that the *condensate* density is proportional to the *superfluid* density, the difference should in fact be negligibl, because at 1.2°K the superfluid density still represents 97% of the total density.[34]

To answer the question of whether Bose–Einstein condensation actually occurs in superfluid He^4, further experiments at still lower temperature are needed.

4. Excitons

4.1 Theory

4.1.1. The Wannier Exciton

Effective Mass Equation

An exciton can be defined as the lowest excited electronic state of a pure insulating crystal. As compared to a single particle excitation (electron–hole pair) the energy of the exciton is lowered by the coulomb binding energy between conduction-band electron and valence-band hole. If the electron–hole interaction changes slowly in space over a lattice period (i.e., the exciton extends over many unit cells) excitons can be described in the effective mass approximation. This treatment was first introduced by Wannier.[35] In its simplest form, one derives the following two-particle Schrödinger equation (neglecting spin)

$$\left(-\frac{\hbar^2\nabla_e^2}{2m_e} - \frac{\hbar^2\nabla_h^2}{2m_h} - \frac{e^2}{\kappa_0 r}\right)\psi = E\psi. \qquad [4.1]$$

Here, $r = |\mathbf{r}_e - \mathbf{r}_h|$, and $(\hbar/i)\nabla_e$ and $(\hbar/i)\nabla_h$ are the momentum operators corresponding to the electron and hole coordinates, respectively. The bands are characterised by their effective masses m_e and m_h and the coulomb interaction between electrons and holes is screened by the static dielectric constant κ_0. In this form, the wave equation describes excitons in a covalent insulator with isotropic, parabolic, and nondegenerate bands, where the extrema of the bands are at the center of the Brillouin zone. Eq. [4.1] is equivalent to the Schrödinger equation for the hydrogen atom. By transforming to the relative coordinate r and the center of mass coordinate

$$\mathbf{R} = \frac{m_e\mathbf{r}_e + m_h\mathbf{r}_h}{m_e + m_h},$$

the wave function can be expressed as

$$\psi = \exp\{i\mathbf{K}\cdot\mathbf{R}\}\varphi(r), \qquad [4.2]$$

where $\hbar\mathbf{K}$ is the center-of-mass momentum and $\varphi(r)$ are Hermite polynomials. The corresponding eigenvalues $E_n(K)$ are

$$E_n(K) = E_g - \frac{1}{n^2}\frac{me^4}{2\hbar^2\kappa_0^2} + \frac{\hbar^2K^2}{2M}. \qquad [4.3]$$

Here we have introduced the reduced effective mass m and the total effective mass M of the exciton

$$\frac{1}{m} = \frac{1}{m_e} + \frac{1}{m_h}, \qquad M = m_e + m_h.$$

E_g is the width of the energy gap, which means that energies are measured relative to the top of the valence band. In this simple model the exciton ground state defined by $K = 0$, $n = 1$ has a binding energy

$$E_b = \frac{me^4}{2\hbar^2\kappa_0^2} = \frac{e^2}{2\kappa_0 a_0}, \qquad [4.4]$$

where a_0 is the effective exciton Bohr radius.

Generalizations

For applications to real crystals one must generalize the formalism. The case of a *degenerate valence band* has been treated by Baldereschi and Lipari.[36]

Dresselhaus and, later, Hopfield and Thomas[37] considered *anisotropic bands.* We quote the effective mass equation including the center-of-mass motion of the exciton for an isotropic conduction band and a valence band of uniaxial symmetry (appropriate to AgBr). By choosing the axis of high symmetry parallel to the z-axis and the wavetion of the form of Eq. [4.2], we obtain the following Schrödinger equation for the relative motion

$$\left[-\frac{\hbar^2}{2\bar{m}}\nabla^2 - \frac{\hbar^2}{2\bar{m}}\gamma\left(\frac{1}{2}\frac{\partial^2}{\partial x^2} + \frac{1}{2}\frac{\partial^2}{\partial y^2} - \frac{\partial^2}{\partial z^2}\right) - \frac{e^2}{\kappa_0 r}\right]\varphi(r)$$
$$= \left[E_g - E_b + \frac{\hbar^2}{2}\left(\frac{K_x^2}{M_\perp} + \frac{K_y^2}{M_\perp} + \frac{K_z^2}{M_\parallel}\right)\right]\varphi(r). \qquad [4.5]$$

where

$$M_i = m_e + m_{hi}, \qquad i = \perp, \parallel$$
$$\frac{1}{\bar{m}} = \frac{1}{m_e} + \frac{1}{3}\left(\frac{2}{m_{h\perp}} + \frac{1}{m_{h\parallel}}\right),$$
$$\gamma = \frac{2}{3}\bar{m}\left(\frac{1}{m_{h\perp}} - \frac{1}{m_{h\parallel}}\right).$$

x,y,z are the Cartesian components of the relative coordinate r and $(\hbar/i)\nabla$ the corresponding momentum operator. For small values of γ ($\gamma \approx 0.1$ for AgBr), the influence of the anisotropy on the binding energy E_b is treated as a perturbation.

For an exciton in a *polarizable crystal* the interaction between electron and hole can no longer be described by a coulomb potential with a constant screening parameter, the Haken potential (see, e.g., Knox[35]) is generally used instead

$$V(r) = -\frac{e^2}{\kappa(r) r}$$
$$\times \frac{1}{\kappa(r)} = \frac{1}{\kappa_\infty} - \left(\frac{1}{\kappa_\infty} - \frac{1}{\kappa_0}\right)\left(1 - \frac{\exp\{-u_e r\} + \exp\{-u_h r\}}{2}\right), \qquad [4.6]$$

where the reciprocal polaron radii u_i are defined as

$$\hbar u_i = (2m_i \hbar\omega_{LO})^{1/2}, \qquad i = e,h$$

$\hbar\omega_{\mathrm{LO}}$ is the LO-phonon energy and κ_∞ is the high-frequency dielectric constant. A measure for the strength of the polar coupling is the Fröhlich parameter

$$\alpha_i = \frac{1}{2}\left(\frac{1}{\kappa_\infty} - \frac{1}{\kappa_0}\right)\frac{e^2 u_i}{\hbar\omega_{\mathrm{LO}}}, \qquad i = e,h. \qquad [4.7]$$

Numerical values of the α_i for AgBr are given in Appendix 1. With this potential the exciton binding energy is no longer accurately described by the hydrogen formula.[38]

Finally one must consider a crystal with an *indirect bandgap.* In AgBr (Appendix 1), for instance, the minimum of the conduction band is at the zone center and the maximum of the valence band at the zone boundary (L-point), characterized by $k_h{}^0$. Following Dresselhaus[37] (see also Knox[35]) the following modifications arise for an indirect-bandgap semiconductor: The wave vector K corresponding to the center-of-mass momentum of the exciton is measured relative to $k_h{}^0$. Then the energy spectrum Eq. [4.3] remains unchanged whereas the wave function Eq. [4.2] is multiplied by a factor $\exp\{i\mathbf{k}_h{}^0\mathbf{r}_h\}$. This factor requires a radiative recombination to be accompanied by a momentum-conserving phonon. In most cases effective mass anisotropies are intimately related to the occurrence of an indirect bandgap. Although the general reasoning will not change in this case, an exact solution is impossible to obtain.[35,37]

4.1.2 Many-Exciton Systems

Early Theories

Wannier excitons, as hydrogenic bound states of an electron and a hole, are expected to behave like bosons, as long as the mean distance between them is large compared to the exciton Bohr radius a_0, i.e.,

$$\rho a_0{}^3 \ll 1. \qquad [4.8]$$

In fact, the first theories suggesting the possibility of Bose–Einstein condensation of excitons[1] considered them as structureless particles obeying Bose statistics. Blatt and coworkers, and also Casella, used the simple ideal gas model of London, whereas Moskalenko discussed the problem with the theory of the hard-sphere Bose gas developed by Lee, Huang, and Yang.[39] This latter theory seems to be appropriate since it represents an expansion in powers of $(\rho a^3)^{1/2}$, where a is the diameter of the spheres and, for excitons, must be of the order of a_0. The leading terms of this expansion are easily obtained from the

Bogoliubov theory of the weakly interacting Bose gas by replacing the Fourier transform of the potential $v(0)$ by the corresponding particle-particle scattering amplitude f_0 (in Born approximation)

$$f_0 = a = \frac{M}{4\pi\hbar^2}v(0). \qquad [4.9]$$

Inserting this relation into the expressions for the ground-state energy Eq. [3.9] and the excitation spectrum Eq. [3.8], one obtains for the $n = 1$ excitons,

$$\frac{E_0}{N} = E_g - E_b + \frac{2\pi\hbar^2}{M}\rho a[1 + O((\rho a^3)^{1/2})], \qquad [4.10]$$

$$E_k = \frac{\hbar^2 k}{2M}(k^2 + 16\pi\rho a)^{1/2}. \qquad [4.11]$$

Recent Developments

The first theory starting from the basic model of electrons and holes coupled by the coulomb interaction was developed by Keldysh and Kozlov.[40] Applying first the Bogoliubov transformation (as in Eq. [3.6]) to the fermion operators and using the formalism of Green's functions, they were able to calculate the ground state energy and the excitation spectrum in lowest order of $\rho a_0{}^3$. It turns out that the Eqs. [4.10] and [4.11] remain valid provided that the scattering length a is replaced by the full exciton–exciton scattering amplitude f including effects from the internal structure of the excitons. The Pauli exclusion principle adds a positive quantity to f, in addition to the purely dynamical term. The stability criterion corresponding to Eq. [3.12] is now

$$f > 0. \qquad [4.12]$$

If it holds, Bose–Einstein condensation occurs at sufficiently low temperatures. Unfortunately no calculations of f, indicating for which parameters this condition would be fulfilled, are available at present. Moreover, the whole theory breaks down if the excitons are bound into molecules. Keldysh and Kozlov claim, however, that a density range should exist where molecules are mostly dissociated whereas excitons remain stable. On the other hand, Bose–Einstein condensation of excitonic molecules could also be possible.

A representation of excitons as structureless bosons has been given in Refs. [41] and [42]. The internal structure is taken into account as an effective boson–boson interaction. A similar method for the case of He^4 has been developed in Ref. [43]. It turns out that even in He^4 the internal structure arising from the fermion character of electrons and nucleons is not negligible.

Macroscopic quantum effects connected with Bose–Einstein condensation of excitons have been treated very recently by Hanamura and Haug.[44]

Mott Limit

In an ideal Bose gas all particles are in the state of lowest energy at zero temperature irrespective of the density. In an interacting Bose system, however, there is a depletion of the condensate. This depletion increases with density and becomes complete at a certain value ρ_m. To estimate this maximum density we represent the excitons as structureless bosons and choose the scattering length equal to the Bohr radius. From Eqs. [3.13] and [3.14] it is obvious that the condensate vanishes (at $T = 0$) if

$$\rho = \rho_m = \frac{1}{(2\pi)^3}\int \frac{\epsilon_k + \rho v(k) - E_k}{2E_k} d^3k, \qquad [4.13]$$

or if all particles are involved in the zero-point motion. By using Eq. [4.11] together with [4.9], the integration can be performed and one obtains a maximum density

$$\rho_m a_0^3 = \frac{9\pi}{64}. \qquad [4.14]$$

This result should not be taken too seriously because it represents an extrapolation of a low-density theory to the high-density limit. In addition there exists another limit determined by the dissociation of excitons into electrons and holes. This so-called Mott limit may be slightly different from the depletion limit Eq. [4.14].

Indirect Semiconductors

Two effects must be considered if, for example, the conduction band minimum is at the Γ-point and the valence band maximum at the L-point of the Brillouin zone. First, there are four equivalent energy gaps in the Brillouin zone, and therefore the exciton states have an additional four-fold degeneracy. Second, the hole mass is anisotropic.

We shall not dwell on the problem of degeneracy and suppose merely that the sum over the momenta is multiplied by some factor. The second problem has recently been discussed for the ideal Bose gas model by introducing *ad hoc* an anisotropic effective mass tensor into the free-particle spectrum.[45] However, a consequent treatment must start from the center of mass kinetic energy for an exciton given by Eq. [4.5]. One obtains for the critical temperature

$$k_B T_c = \left(\frac{1+\alpha}{\zeta\left(\frac{3}{2}\right)}\right)^{2/3} \frac{2\pi\hbar^2}{M_\parallel} \rho^{2/3}, \qquad [4.15]$$

where

$$\alpha = \frac{M_\parallel - M_\perp}{M_\perp}$$

This expression is different from the formula given in Ref. [45]. In both cases, however, the critical temperature differs very little from the value that would result from the ideal gas formula with an average mass M given by

$$\frac{1}{\overline{M}} = \frac{1}{3}\left(\frac{2}{M_\perp} + \frac{1}{M_\parallel}\right).$$

Optical Spectrum

Excitons are most easily generated and detected by optical means. Therefore it is not surprising that all experiments concerning Bose–Einstein condensation reported so far are optical experiments, predominantly emission studies. Let us assume that excitons are generated by an external light source and decay by radiative recombination in a stationary way. Furthermore we suppose that the excitons are ideal bosons occupying the different momentum states according to the thermal distribution function n_p. The intensity of the emitted light with frequency ω is then given by

$$I(\omega) \sim \frac{1}{N}\sum_{\mathbf{p}} n_p \delta\left(\omega - \frac{1}{\hbar}\left(E_0 + \frac{p^2}{2M}\right)\right), \qquad [4.16]$$

where E_0 is the ground-state energy of the exciton. For indirect semiconductors, the phonon energy needed for momentum conservation is also included in E_0. Eq. [4.16] must be compared with the scattering cross section Eq. [3.23]. Contrary to inelastic neutron scattering, exciton luminescence directly measures the density of states (and thus the momentum distribution). In fact, in the presence of a condensate we obtain ($\hbar\omega \geq E_0$)

$$I(\omega) \sim \frac{N_0}{N}\delta\left(\omega - \frac{E_0}{\hbar}\right) + \frac{(2M)^{3/2}}{4\pi^2\rho\hbar^2}\,\frac{(\hbar\omega - E_0)^{1/2}}{\exp\left\{\dfrac{\hbar\omega - E_0}{\kappa_B T}\right\} - 1}\,. \qquad [4.17]$$

This spectrum consists of two parts—an infinitely sharp line at E_0 with intensity proportional to N_0, and a high-energy tail originating from the thermal motion of the excitons whose integrated intensity is $N - N_0$.

For exciton temperatures $T > T_c$, the sharp line disappears and the high-energy tail goes over into a Boltzmann distribution, since the chemical potential is different from zero (see Eq. [2.3]) and becomes large compared to $k_B T$ at temperatures $T \gg T_c$.

The optical spectrum for an interacting exciton system at $T = 0$ has been discussed in Ref. [46] and [47]. The condensate line is still sharp but lowered in intensity and shifted to higher energies, since the ground-state energy of an exciton increases due to the interaction (see Eq. [4.10]). An additional feature at the low-energy side of the condensate line appears to result from the zero-point fluctuations in the exciton system.

4.2 Experiments

4.2.1 The General Situation

In 1970 Akopyan, Gross, and Razbirin[48] reported having observed Bose–Einstein condensation of free excitons in CdSe. Later, in addition to luminescence studies, reflectivity and absorption experiments were performed in the strongly excited system by the same group.[49] However, the evidence presented so far is not sufficiently detailed in our opinion to rule out other explanations. Kuroda, Shionoya, Saito, and Hanamura[50,51] have published evidence for Bose–Einstein condensation of excitonic molecules in CdSe. Some of the experimental facts given by this group are rather convincing, although doubts have been raised as to the validity of their interpretation on both theoretical and experimental grounds by Johnston and Shaklee.[45] However, in our opinion these objections are not all very important since they depend very critically on the numerical value of a number of parameters not all of which are sufficiently well known. Therefore we believe that the interpretation of Kuroda et al still may be correct.

Insufficient information is available on Bose–Einstein condensation of excitons in CuCl,[52] and it would be premature to comment on the above observations.

Czaja and Schwerdtfeger published the observation of a peculiar free-exciton emission in AgBr, which they have interpreted as being due to the radiative recombination of Bose–Einstein condensed free excitons.[53,54] Contrary to the papers referred to above, the experimental difficulties seem to be less drastic in this material. Therefore it was possible to investigate various aspects of this emission line. Based on these results we believe that the data published actually give good evidence for Bose–Einstein condensation of free excitons in AgBr.

4.2.2. Luminescence in Silver Bromide

Apparatus

In our experiments, photoluminescence is observed by exciting pure AgBr crystals with light of energy of 3.5, 3.4, and 2.8 eV, which lies between the indirect and direct bandgap energies (see Appendix 1). The excitation power varies between 20 and 100 mW cw. The crystals are immersed in liquid helium and the bath temperature is monitored with a mechanical vacuum gauge calibrated against both a Ge resistor and a carbon resistor thermometer. The temperature readings below the λ-transition of liquid helium are accurate to ±0.05°K at least down to 1.4 K.

The light emitted from the sample is analysed by a 2 m grating spectrometer having a dispersion of 4 Å/mm and detected by a photomultiplier with an S20 cathode using a photon counting system that provides a linear intensity scale. Typical dark count rates are 0.2–0.5 per sec. With some care the background signal was of the order of 10 counts per second or smaller. The spectrum is finally plotted on a recorder.

The crystals under investigation were the purest available. The residual impurity content was about 1 ppm or less. The samples were annealed before they were measured. This proved to be necessary in order to reduce—as we believe—the influence of point defects on the spectra observed. Only crystals that exhibited a proper emission due to the residual impurity iodine, as explained in Appendix 2, have been used in our experiments.

Spectrum Observed

Fig. 3 shows the "TA" (L_3^-)-phonon replica of the indirect free exciton emission of AgBr. The simultaneous emission of a momentum-conserving "TA" (L$_3^-$)- or LA(L$_1^-$)-phonon is required by symmetry for dipole-allowed radiative recombination of free excitons. The phonon energies obtained from emission and absorption experiments,[53,55] and given in Appendix 1, agree well with those resulting from inelastic neutron scattering.[56,57] It is remarkable that the LA-phonon replica has only about one tenth of the intensity of the "TA"-phonon replica. This drastic intensity difference and the almost ideal Boltzmann line shape shown in Fig. 3 was also observed by von der Osten and Weber.[58] The Boltzmann line shape indicates that these excitons are in thermal equilibrium among themselves. The line-shape analysis yields an exciton temperature of about 10 K in good agreement with Ref. [58], which means that these excitons are not in thermal equilibrium with the bath. Furthermore, we observe that neither a change in bath temperature nor a change in excitation density or in excitation energy alters this exciton temperature markedly. We interpret this finding by assuming that the lifetime of these excitons is shorter than the relaxation time necessary to establish equilibrium with the lattice.

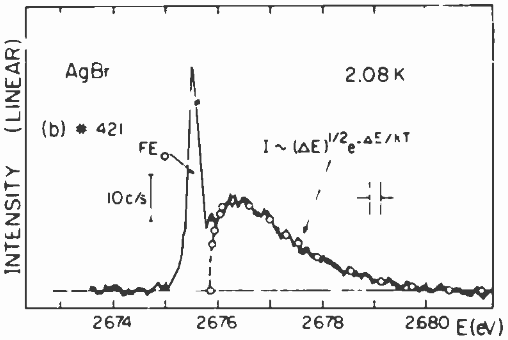

Fig. 3—Exciton spectrum observed in AgBr following Hg-lamp excitation (50 mW at 3.44 eV).

The important feature in Fig. 3 is the sharp symmetric line at the low energy side of the Boltzmann-shaped exciton emission. This line is observed for the "TA"- and LA-phonon replica as well[53] and is removed from the extrapolated $K = 0$ free exciton emission edge by 0.34 meV to lower energies. Its half-width is 0.14 meV, which is about the width expected for the momentum-conserving phonon.* This means that the width of the electronic transition is much smaller.

---

* The TO(Γ)-phonon halfwidth observed in Ref. [59] is only a factor of 2 larger.

Neither the half-width of this line nor its shape nor its energetic postion was influenced by changing experimental parameters. However, its intensity changes quite drastically and exhibits a number of unusual properties discussed later on.

Excitonic State

Matsushita[60] has demonstrated by analysing magneto-absorption experiments that the four-fold degenerate indirect L-point exciton in AgBr is split due to exchange interaction. The lowest state is a doubly degenerate pure (spin) triplet state and thus, its optical recombination is dipole forbidden. The higher one is a doubly degenerate (spin) singlet–triplet mixed state. The energy separation between these states is found to be 0.33 meV. However, as can be shown, Matsushita's analysis is incomplete.* Given the band symmetries, group theory requires that *both* excitons can recombine via a dipole-allowed transition with simultaneous emission of momentum-conserving phonons. This can be understood by the admixture of d-wave functions to the valence-band states at the L-point as is known from band-structure calculations.[61,62] The dipole transition probability for the recombination of the pure triplet excitons must be small because it is due to this d-wave function admixture. Therefore it is to be expected that the lifetime of the triplet excitons is considerably longer than the lifetime of the singlet–triplet mixed excitons. As a consequence the triplet excitons have sufficient time to thermalize with the lattice. However, since the singlet–triplet and the triplet excitons have the same symmetry, both are observed within the same phonon replica.[53]

Bose–Einstein Condensation of Triplet Excitons

Knowing the excitonic states, the spectrum shown in Fig. 3 can be interpreted in the following way. The broad Boltzmann-shaped emission is due to the recombination of singlet–triplet mixed excitons. Because of their high temperature these excitons cannot show Bose–Einstein condensation. The temperature of triplet excitons, however, is close to the bath temperature and therefore Bose–Einstein condensation seems to be possible. The recombination radiation of these excitons gives rise to the sharp line removed to lower energies by the exchange splitting of 0.34 meV. Position and width of this line imply that these triplet excitons belong to a highly occupied state with zero kinetic energy, suggesting that in fact, the triplet excitons show Bose–

---

* We are grateful to Prof. F. Bassani for a clarifying discussion about this point.

Einstein condensation. Therefore we expect from Eq. [4.17]†

$$I(\mathrm{FE}_0) \sim N_0.$$

Strong support to this model will be given by the temperature, density, and magnetic-field dependence of this emission intensity, which is discussed next.

Temperature Dependence

In Fig. 4 the dependence of $I(\mathrm{FE}_0)$ on temperature is shown.[53] The practically linear decrease of this intensity with increasing temperature justifies the linear extrapolation to the intensity zero, which defines the critical temperature T_0. In the temperature range accessible to experimental investigation so far, the results shown in Fig. 4 suggest

$$N_0 \sim 1 - \left(\frac{T}{T_0}\right)^{\alpha}, \qquad \alpha \approx 1. \qquad [4.18]$$

This is qualitatively the form expected for an ideal gas (see Eq. [2.10]).

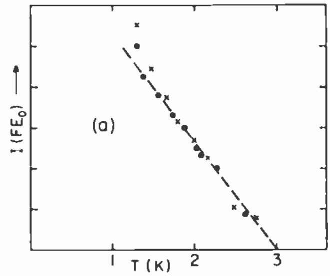

Fig. 4—Temperature dependence of the intensity $I(\mathrm{FE}_0)$.

Excitation Density Dependence

In these experiments, the crystal has been excited using the UV emission of an Ar-ion laser where the total laser power has been kept constant. The variation of the excitation density has been achieved by varying the position of the focusing lens. Fig. 5 shows the dependence of $I(\mathrm{FE}_0)$ on excitation density combined with the temperature varia-

---

† The high-energy tail predicted by Eq. [4.17] was not resolved, mainly due to the broadening related to the momentum-conserving phonon.

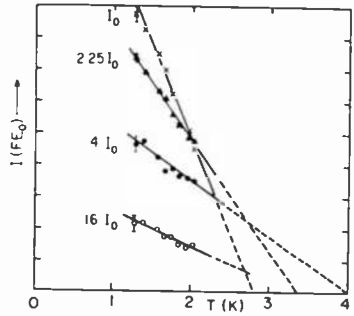

Fig. 5—$I(\mathrm{FE}_0)$ as function of temperature and excitation density. The relative excitation densities are given in the figure.

tion.[54] We notice in particular that experimentally a crossover of two curves, obtained for different excitation densities, has been observed that excludes an increased lattice temperature as the reason for the effect shown in Fig. 5. If we assume that the total triplet exciton density is proportional to the excitation density, then we obtain from Fig. 5, (a) an increase of T_0 with increasing ρ and (b) a decrease of N_0 with increasing ρ. Both properties are expected from the theory of a weakly interacting Bose gas (see Fig. 1) and are discussed in more detail later.

Magnetic Field Dependence

Finally, $I(\mathrm{FE}_0)$ also depends on an external magnetic field as shown[54] in Fig. 6. It should be pointed out specifically that neither a shift nor a broadening of the FE_0 emission is detectable for magnetic fields up to 25 kOe. However, a definite splitting of the zero phonon line due to the exciton bound to iodine impurities has been observed at these

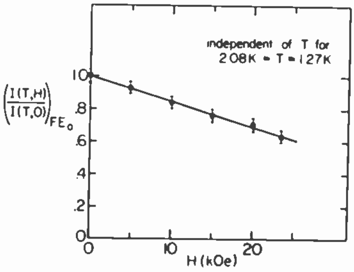

Fig. 6—Normalized intensities $I(\mathrm{FE}_0)$ as a function of temperature and magnetic field. Note the independence of the normalized intensities on temperature.

field strengths. From the experimental data of Fig. 6,

$$I_{FE_0}(H,T) \approx I_1(H)\cdot I_2(T), \qquad [4.19]$$

where $I_2(T)$ is given by Eq. [4.18] and $I_1(H)$ has the form

$$I_1(H) \sim 1 - \text{const}\cdot H. \qquad [4.20]$$

Discussion of Results

The temperature dependence of $I(FE_0)$ shown in Figs. 4 and 5 is similar to the calculated behavior for an ideal Bose gas. In addition we obtain from the data shown in Fig. 5 the variation of the critical temperature T_0 with the total exciton density ρ. The result is shown in Fig. 7. In the low-density limit, T_0 increases with ρ following a power law

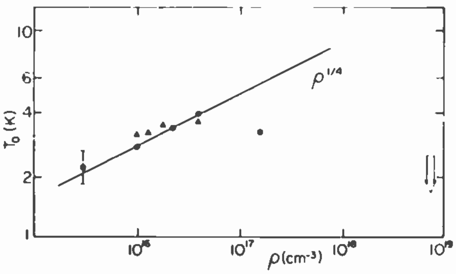

Fig. 7—Extrapolated critical temperatures T_0 as function of total triplet exciton density ρ. The arrow points to the Mott limit.

$$T_0 \sim \rho^{\alpha'}, \alpha' \approx \frac{1}{4}, \qquad [4.21]$$

in qualitative agreement with the behavior of the critical temperature of an ideal Bose gas, Eq. [2.9].

With a further increase of ρ, however, T_0 starts to decrease. This behavior is expected qualitatively as a consequence of the interaction. In order to apply the more quantitative argument of Eq. [4.14], one must know the exciton densities at least within an order of magnitude. In Appendix 3 exciton densities are estimated and used for the absolute ρ-scale in Fig. 7. In approaching the Mott limit $\rho a_0{}^3 \approx 1$ (corresponding to $\rho \approx 10^{19}$ cm^{-3} in AgBr) the properties of our system resemble increasingly those of a dense electron–hole plasma, where the exciton is no longer well defined. It is interesting to note that the ρ-dependence of the λ-temperature in liquid helium fits into this general scheme. The appropriately scaled densities fall into the high-density region of Fig. 7, where T_0 decreases with increasing ρ. This same dependence of T_λ on ρ is actually well known for liquid He^4 (see Ref. [34]), in support of our argument.

The decrease of the condensate fraction with density at low temperatures ("depletion") is obtained by analyzing Fig. 5. The behavior can be fitted to

$$N_0 \sim \rho^{-1/2}. \quad [4.22]$$

The dependence of N_0 on a magnetic field has no analog in liquid He^4 and therefore must be related to some specific properties of the exciton system. For excitons in AgBr the low field limit applies because the parameter γ_H (see Ref. [63]),

$$\gamma_H = \frac{\hbar\omega_c}{2E_b},$$

where ω_c, the cyclotron resonance frequency, varies linearly with H and is 0.16 for a field of 100 kOe. Therefore in the exciton Hamiltonian the magnetic field terms are small.

Singlet and triplet excitons are only weakly coupled without a magnetic field. Their temperatures are determined by the individual generation and recombination processes. A weak magnetic field increases drastically the triplet exciton concentration ρ, since transitions from the singlet to the triplet state become dipole-allowed and can take place without phonon cooperation. The increase in ρ will lead to a decrease in N_0 according to Eq. [4.22]. This mechanism seems to be the only one that qualitatively explains the data, yielding a second independent indication that the excitons that show Bose–Einstein condensation are in a (spin) triplet state.

Up to now the main emphasis has been to prove that Bose–Einstein condensation of excitons has been observed in AgBr. Now we discuss why AgBr is actually well suited for this observation. The following properties are found to be essential:

(1) The *exciton lifetime* is long enough to reach low exciton temperatures, $T_{exc} = 2°K$ for instance, since the recombination transition is only weakly allowed.

(2) In order to have Bose–Einstein condensation at a given temperature, say 2°K, T_c must be equal or larger, which defines a *critical exciton density* ρ_c (see Eq. [2.9]). This critical density must satisfy

$$\rho_c a_0^3 \ll 1$$

for two reasons. First, the interaction energy must be small compared to the exciton binding energy

$$\rho_c v(0) \ll E_b,$$

in order to be sufficiently far from the Mott limit, or, by using Eq. [4.9],

$$\rho_c a_0^3 \ll \frac{1}{4\pi}\frac{M}{m}.$$

The right-hand side is equal to 0.45 for AgBr. Second, as has been shown in Sec. 4.1.2, to ensure a small depletion,

$$\rho_c a_0^3 \ll \frac{9\pi}{64}.$$

For AgBr $\rho_c = 1.6 \times 10^{16}$ cm^{-3} and $\rho_c a_0^3 = 1.2 \times 10^{-3}$, where we have used $a_0 = 42$ Å from Appendix 1. Large exciton binding energies E_b and small exciton radii a_0 are obviously favorable.

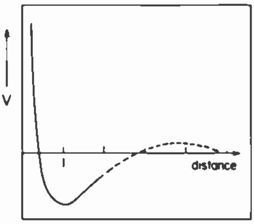

Fig. 8—Exciton-exciton interaction potential as a function of separation for a polar substance.

(3) *Band structure and exciton–exciton interaction* prevent the formation of electron–hole droplets. On the one hand, valence band and conduction band are reversed compared to Ge, and it appears in the simple Hartree–Fock approximation that such a situation does not favor droplet formation. On the other hand, Tosatti has recently shown that the exciton–exciton interaction in polar crystals like AgBr is repulsive on the average,[64] leading to an interaction potential of the form shown in Fig. 8 (from Ref. [53]). As a consequence the stability

criterion Eq. [3.12] is satisfied. Moreover this interaction would not favor the formation of excitonic molecules which in any case are not very likely to occur in AgBr due to the relatively small difference between the electron and hole mass and, probably, the influence of electron–hole exchange.[65]

These properties of AgBr may be necessary conditions for Bose–Einstein condensation of excitons and give a hint as to the types of materials in which this phenomenon might be observed.

5. Conclusions

We have tried in the present article to give a review on different aspects of Bose–Einstein condensation in both liquid He^4 and exciton systems. In particular, we have discussed extensively the luminescence experiments in AgBr. Because of the complexity of this system, we did not attempt to predict the experimental spectrum from first principles; we merely tried to draw an internally consistent picture. It turns out that excitons in AgBr as well as liquid He^4 can be fitted into the same general scheme. This result is rather surprising, and we believe that future work continuing on this line will give some new insight into the old and challenging problem of Bose–Einstein condensation.

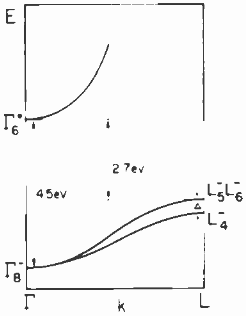

Fig. 9—Schematic band structure of AgBr. The symbols denote band symmetries at the Γ- and L-point, Δ = spin orbit splitting.

Appendix 1—Some Material Parameters of AgBr

AgBr has an indirect bandgap of 2.70 eV at the L-point in the Brillouin zone. Fig. 9 gives a schematic band structure according to* Ref.

---

* We use the notations for irreducible representations in agreement with G. F. Koster, J. O. Dimmock, R. C. Wheeler, and H. Statz, *Properties of the 32 Point Groups*, MIT-Press, Cambridge, Mass. (1963).

Table 1

	Polaron Mass		Band Mass
Electron Ref. [66]	$m_e = 0.2897 \pm 0.006\ m_0$	$\alpha_e = 1.57$	$m_e = 0.221$
	$m_{h\perp} = 0.79 \pm 0.01\ m_0$		$m_{h\perp} = 0.52\ m_0$
Hole		$\alpha_h = 2.8$	
Ref. [67]	$m_{h\parallel} = 1.71 \pm 0.06\ m_0$		$m_{h\parallel} = 1.25\ m_0$

[62]. The spin orbit splitting of the valence band at the L-point amounts to $\Delta = 0.15$ eV.[61,62] Electron- and hole-polaron masses in units of the free electron mass m_0 and the Fröhlich coupling constants α defined in Eq. [4.7] are collected in Table 1.

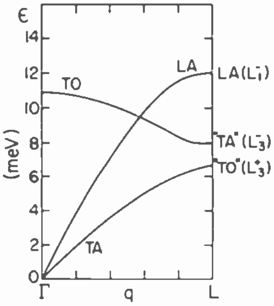

Fig. 10—Phonon dispersion at about 4°K. The symbols denote phonon symmetries.

The phonon dispersion is known from inelastic neutron scattering experiments[56,57] and is shown in Fig. 10. It is important to realize that the symmetries of TO and TA are interchanged at the L-point due to a mode–mode interaction along the Λ-line close to the L-point. Some optically determined phonon energies are given in Table 2; they are in good agreement with the energies from neutron scattering.

Table 2

Phonon	Energy (meV)
“TA_L” (L_3^-)	8.3*
LA_L (L_1^-)	12.3*
TO (Γ)	11.4†
LO (Γ)	17.3†

* Ref. [53].
† Ref. [59].

The free indirect (L-point) exciton binding energy has been determined experimentally E_{exc} = 16.3 meV.[68] An effective exciton Bohr radius a_0 can be obtained from the binding energy by applying Eq. [4.5], which yields $a_0 \approx 42$ Å. This value should be a reasonable lower limit, since the static dielectric constant $\kappa_0 = 10.60$ has been used.[66] Polaron effects are found to be sizable, and they would tend to increase a_0 due to a reduction of the coulomb attraction.[69]

Appendix 2—The Emission Spectrum of Iodine in AgBr

Iodine substituting for Br in AgBr is an isoelectronic trap[70] with a characteristic emission spectrum consisting of a zero phonon line at 2.640 eV (4694.9 Å) and up to 10 LO phonon replica superimposed upon a broad emission band. Although in our purest crystals the iodine content was only 0.2 ppm* (~5 × 10^{15} cm^{-3}) the emission following optical band-to-band excitation was still dominated by the spectrum originating from the isoelectronic trap iodine. However, the typical iodine spectrum, as shown in Fig. 11, was obtained for our unintentionally doped crystals only after annealing in vacuum at 200°C for 24 hours and slowly cooling to room temperature over a period of 24 hours. Only then was the zero phonon line with a half-width of less than 0.1 Å observed, and the yellow emission centered around 2.12 eV

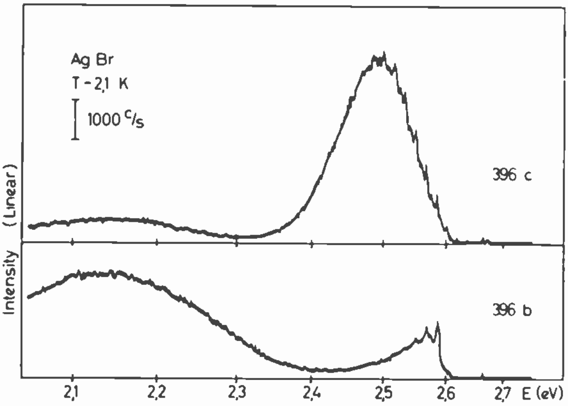

Fig. 11—Emission spectrum due to iodine impurities, measured on the same sample, before heat treatment (396b) and after heat treatment (396c). Note that the intensity scales are identical; however, they are not corrected for photomultiplier response.

---

* Based on a mass-spectrometric analysis.

(5700 Å), which has been ascribed to the influence of point defects,[71] was virtually nonexistent. In experimenting with a crystal by excitation with the strongly absorbed 3600 Å near-UV radiation (penetration depth ~30 μm) of about 100 mW intensity, the iodine spectrum gradually changes to the "atypical" shape within a period of two or more weeks. The bulk of the crystal still shows the original spectrum as can be observed by excitation with more penetrating (~0.1 cm) light of 4416 Å wavelength. An additional heat treatment normally brings the sample back to the original "good" condition. This cycle can often be repeated 3 to 4 times until finally the change is irreversible. Although it is tempting to ascribe the observed behavior to the generation of point defects (e.g., Ag Frenkel defects have an activation energy of 0.85 eV[72]) during illumination with bandgap light and a subsequent formation of interstitial (or vacancy) iodine impurity clusters, we have as yet no proof for this suggestion. However, the intrinsic spectra described in this paper have been observed exclusively under conditions of "well behaved" samples as monitored by the frequent observation of the iodine spectrum.

Furthermore, an additional doping with iodine (1 ppm added to the melt) yields a more pronounced iodine spectrum; however, the free-exciton emission has disappeared under our excitation conditions.* Also, at these higher iodine concentrations, no sensitivity to heat treatment was observed. A similar experience has been found for AgBr crystals of different origin and grown in a different process. Only by reducing the iodine content has the exciton emission become visible.†

Appendix 3—Estimation of Exciton Concentration

Until luminescence decay times are measured, one is forced to estimate the order of magnitude of the exciton concentration indirectly. First an estimate of the concentration of electron–hole pairs generated is given. Subsequently, by a completely different method, the exciton concentration is estimated yielding a reasonable value as can be seen by comparison with the electron–hole concentration.

(1) In the crystals used in our experiment, the iodine concentration is 5×10^{15} cm^{-3} (*c.f.* Appendix 2). Our experiments indicate that the recombination of charge carriers via the iodine impurities is dominant. Furthermore, the luminescence due to this impurity is nearly

---

* We thank Dr. P. Junod from CIBA-GEIGY, Photochemie, Fribourg (Switzerland) for the high purity AgBr-crystals used in these experiments.

† We are grateful to Prof. J. Malinovski from the Bulgarian Academy of Sciences in Sofia, Bulgaria, for his cooperation.

saturated for the lowest excitation used. These observations have two consequences. First, the lifetime of electron–hole pairs is close to the time constant of luminescence decay and not to the time constant for free carrier capture. Second, the concentration of electrons and holes generated must be larger than the iodine concentration.

(2) The luminescence decay time constant for the iodine-related emission has been measured[73] and found to be $\tau \approx 50\ \mu s$. For an excitation power of 50 mW with an energy of 3.44 eV (penetration depth $\sim 30\ \mu m$) focused on a sample area of 10^{-2} cm^2, we obtain under steady-state conditions (assuming 100% quantum efficiency) an electron–hole concentration of[54]

$$\rho_{e,h} \approx 10^{17}\ \mathrm{cm}^{-3},$$

which, in fact, is larger than the iodine concentration.

(3) At an excitation power of 50 mW, the extrapolated critical temperature $T_c \approx 3°$K (Fig. 4). From this value, applying Eq. [2.9] we obtain

$$\rho_{exc} \approx 3 \times 10^{16}\ \mathrm{cm}^{-3}.$$

This value is reasonable in view of the other concentrations estimated and is taken as a calibration for the ρ-scale in Fig. 7 with the further assumption that ρ is proportional to the excitation density.

References:

[1] S. A. Moskalenko, "Reversible Optico-Hydrodynamic Phenomena in a Nonideal Exciton Gas," *Sov. Phys. Solid State*, **4**, p. 199 (1962); J. M. Blatt, K. W. Böer, and W. Brandt, "Bose-Einstein Condensation of Excitons," *Phys. Rev.*, **126**, p. 1691 (1962); and R. C. Casella, "On the Possibility of Observing a Bose-Einstein Condensation of Excitons in CdS and CdSe," *J. Phys. Chem. Solids*, **24**, 19 (1963).

[2] S. N. Bose, "Plancks Gesetz und Lichtquantenhypothese," *Z. Physik*, **26**, 178 (1924).

[3] A. Einstein, "Quantentheorie des Einatomigen Idealen Gases," *Sitzungsber preuss. Akad. der Wissensch., phys.-math. Kl.*, **22**, 261 (1924), **23**, 3 (1925).

[4] *Physics Today*, "Obituary for S. N. Bose," April (1974), p. 129.

[5] F. London, "On the Bose-Einstein Condensation," *Phys. Rev.*, **54**, p. 947 (1938).

[6] K. Huang, *Statistical Mechanics*, John Wiley and Sons, New York (1963).

[7] F. London, *Superfluidity*, Vol. II, John Wiley and Sons, New York (1954).

[8] P. T. Landsberg, "On Bose-Einstein Condensation," *Proc. Cambridge Phil. Soc.* **50**, p. 65 (1954), and references cited therein.

[9] N. N. Bogoliubov, *Izv. Akad. Nauk SSSR, Ser. Fiz.*, **11**, p. 77 (1947); see also, N. N. Bogoliubov, *Lectures in Quantum Statistics*, Gordon and Breach, New York (1967).

[10] O. Penrose and L. Onsager, "Bose-Einstein Condensation and Liquid Helium," *Phys. Rev.*, **104**, p. 576 (1956).

[11] For a review of the subject, see G. V. Chester, "Topics in the Theory of Liquid Helium Four," in *Lectures in Theoretical Physics*, **XI-B**, ed. by K. J. Mahanthappa and W. B. Brittin, Gordon and Breach, New York (1969), p. 253.

[12] W. P. Francis, G. V. Chester, and L. Reatto, "Ground State of Liquid He^4," *Phys. Rev. A*, **1**, 86 (1970).

[13] W. L. Mc Millan, "Ground State of Liquid He^4," *Phys. Rev.*, **138**, p. A442, (1965).

[14] D. Schiff and L. Verlet, "Ground State of Liquid Helium -4 and Helium -3," *Phys. Rev.*, **160**, p. 208 (1967).

[15] M. H. Kalos, D. Levesque, and L. Verlet, "Helium at Zero Temperature with Hard-Sphere and Other Forces," *Phys. Rev. A*, **9**, p. 2178 (1974).

[16] J. de Boer and A. Michels, "Contribution to the Quantum-Mechanical Theory of the Equation of State and the Law of Corresponding States. Determination of the Law of Force of Helium," *Physica*, **5**, p. 945 (1938).

[17] See, for instance: H. Fröhlich, "The Connection Between Macro- and Microphysics," *Riv. del Nuovo Cim.*, **3**, p. 490 (1973).

[18] O. Penrose, "On the Quantum Mechanics of Helium II," *Phil. Mag.*, **42**, p. 1373 (1951).

[19] C. N. Yang, "Concept of Off-Diagonal Long-Range Order and the Quantum Phases of Liquid He and of Superconductors," *Rev. Mod. Phys.*, **34**, p. 694 (1962).

[20] J. S. Bell, "On a Conjecture of C. N. Yang," *Phys. Lett.*, **2**, p. 116 (1962).

[21] A. Miller, D. Pines, and P. Nozières, "Elementary Excitations in Liquid Helium," *Phys. Rev.*, **127**, p. 1452 (1962).

[22] P. C. Hohenberg and P. M. Platzman, "High-energy Neutron Scattering from Liquid He^4," *Phys. Rev.*, **152**, p. 198 (1966).

[23] V. F. Sears, "High-Energy Scattering from Liquid He^4," *Phys. Rev.*, **185**, p. 200 (1969).

[24] H. A. Gersch and P. N. Smith, "High-Energy Neutron Scattering in the Impulse Approximation," *Phys. Rev. A*, **4**, p. 281 (1971).

[25] R. A. Cowley and A. D. B. Woods, "Neutron Scattering from Liquid Helium at High Energies," *Phys. Rev. Lett.*, **21**, p. 787 (1968).

[26] O. K. Harling, "High-Energy Neutron Scattering Measurements on Liquid Helium and Bose Condensation in He II," *Phys. Rev. A*, **3**, p. 1073 (1971).

[27] H. A. Mook, R. Scherm, and M. K. Wilkinson, "Search for Bose-Einstein Condensation in Superfluid ^{4}He," *Phys. Rev. A*, **6**, p. 2268 (1972).

[28] R. D. Puff and J. S. Tenn, "High-Energy Neutron-Liquid He^4-Scattering and the He^4 Condensate Density," *Phys. Rev. A*, **1**, p. 125 (1970).

[29] F. W. Cummings, G. J. Hyland, and G. Rowlands, "Proposal for Measurement of Helium-II Condensate," *Phys. kond. Mat.*, **12**, p. 90 (1970).

[30] W. C. Kerr, K. N. Pathak, and K. S. Singwi, "Neutron Scattering from Liquid Helium II at Large Momentum Transfer and the Condensate Fraction," *Phys. Rev. A*, **2**, p. 2416 (1970).

[31] H. A. Gersch, L. J. Rodriguez, and P. N. Smith, "Corrections to the Impulse Approximation for High-Energy Neutron Scattering from Liquid Helium," *Phys. Rev. A*, **5**, p. 1547 (1972).

[32] L. J. Rodriguez, H. A. Gersch, and H. A. Mook, "Analysis of Experimental Data on Neutron Scattering from Superfluid Helium at Large Momentum Transfers," *Phys. Rev. A*, **9**, p. 2085 (1974).

[33] H. W. Jackson, "Reexamination of Evidence for a Bose-Einstein Condensate in Superfluid He^4," *Phys. Rev. A*, **10**, p. 278 (1974).

[34] J. Wilks, *The Properties of Liquid and Solid Helium*, Clarendon Press, Oxford (1967).

[35] G. H. Wannier, "The Structure of Excitonic Levels in Insulating Crystals," *Phys. Rev.*, **52**, p. 191 (1937); see, e.g., R. S. Knox, "Theory of Excitons," Suppl. 5 of *Solid State Phys.*, ed. Seitz and Turnbull, Acad. Press N.Y. (1963), J. O. Dimmock, "Introduction to the Theory of Exciton States in Semiconductors," in *Semiconductors and Semimetals*, ed. Willardson and Beer, Acad. Press N.Y. (1967), Vol. 3, p. 259.

[36] N. O. Lipari and A. Baldereschi, "Energy Levels of Indirect Excitons in Semiconductors with Degenerate Bands," *Phys. Rev.*, **B3**, p. 2497 (1971).

[37] G. Dresselhaus, "Effective Mass Approximation for Excitons," *J. Phys. Chem. Solids*, **1**, p. 14 (1956); J. J. Hopfield and D. G. Thomas, "Fine Structure and Magneto-Optic Effects in the Exciton Spectrum of CdS," *Phys. Rev.*, **122**, p. 35 (1961).

[38] J. G. de Vooght and K. K. Bajaj, "Ground-State Energy of a Wannier Exciton in a Polar Crystal," *Phys. Rev.*, **B7**, p. 1472 (1973); K. K. Bajaj, "Effect of Electron-Phonon Interaction on the Binding Energy of a Wannier Exciton in a Polarizable Medium," *Solid State Comm.*, **15**, p. 1221 (1974).

[39] T. D. Lee, K. Huang, and C. N. Yang, "Eigenvalues and Eigenfunctions of a Bose System of Hard Spheres and its Low-Temperature Properties," *Phys. Rev.*, **106**, p. 1135 (1957).

[40] L. V. Keldysh and A. N. Kozlov, "Collective Properties of Excitons in Semiconductors," *Sov. Phys. JETP*, **27**, p. 521 (1968).

[41] E. Hanamura, "Theory of the High Density Exciton," *J. Phys. Soc. Japan*, **29**, p. 50 (1974).

[42] T. Nagashima and C. Horie, "Condensation of Excitons in a Highly Excited State of Semiconductors," *J. Phys. Soc. Japan*, **37**, p. 614 (1974).

[43] M. D. Girardeau and S. Y. Yoon, "Condensation and Momentum Distribution in a Simplified Liquid ^{4}He Ground State," *Phys. Rev. A*, **8**, p. 2009 (1973).

[44] E. Hanamura and H. Haug, "Will a Bose-Condensed Exciton Gas Be Superfluid," *Solid State Comm.*, **15**, p. 1567 (1974); E. Hanamura and H. Haug, "Derivation of the Two-Fluid Model for Bose-Condensed Excitons," to be published.

[45] W. D. Johnston and K. L. Shaklee, "Considerations Relevant to Bose Condensation of Excitonic Molecules in CdSe," *Solid State Comm.*, **15**, p. 73 (1974).

[46] E. Hanamura, "Optical Response of Many Exciton System," *Solid State Comm.*, **11**, p. 485 (1972).

[47] V. A. Gergel', R. F. Kazarinov, and R. A. Suris, "Optical Properties of an Exciton Condensate in a Semiconductor," *Sov. Phys. JETP*, **26**, p. 354 (1968).

[48] I. Kh. Akopyan, E. F. Gross, and B. S. Razbirin, "Bose–Einstein Condensation of Excitons in a CdSe crystal," *Sov. Phys. JETP Lett.*, **12**, p. 251 (1970).

[49] I. Kh. Akopyan and B. S. Razbirin, "Emission, Absorption, and Reflection Spectra of High-Density Excitons in a CdSe Crystal," *Sov. Phys. Solid State*, **16**, p. 113 (1974).

[50] H. Kuroda, S. Shionoya, H. Saito, and E. Hanamura, "Observation of the Bose Condensation of Excitonic Molecules in CdSe," *Solid State Comm.*, **12**, p. 533 (1973); same authors, "Bose Condensation of Excitonic Molecules in CdSe," *J. Phys. Soc. Japan*, **35**, p. 534 (1973).

[51] S. Shionoya, "Bose Condensation of High Density Exciton System in Semiconductors," *Proc. XII Int. Conf. Physics of Semicond.*, Stuttgart, 1974, p. 113.

[52] T. Goto, T. Anzai, and M. Ueta, "The Possibility of the Bose Condensation of Excitons in CuCl," *J. Phys. Soc. Japan*, **35**, p. 940 (1973).

[53] W. Czaja and C. F. Schwerdtfeger, "Evidence for Bose-Einstein Condensation of Free Excitons in AgBr," *Solid State Comm.*, **15**, p. 87 (1974).

[54] W. Czaja and C. F. Schwerdtfeger, "On the Bose-Einstein Condensation of Free Excitons in AgBr," *Proc. XII Int. Conf. Physics of Semicond.*, Stuttgart, 1974, p. 142.

[55] H. Kanzaki and S. Sakuragi, "Optical Absorption and Luminescence of Excitons in Silver Halides Containing Isoelectronic Impurities. II," *J. Phys. Soc. Japan*, **27**, p. 924 (1969).

[56] H. Kanzaki, S. Sakuragi, S. Hoshino, G. Shirane, and Y. Fujii, "Neutron Scattering Study of Phonons Associated with Indirect Band-Gap Transition in AgBr," *Solid State Comm.*, **15**, p. 1547 (1974).

[57] W. von der Osten and B. Dorner, "Phonon Dispersion in AgBr and Exchange of the Transverse Mode Eigenvectors at L," preprint.

[58] W. von der Osten and J. Weber, "Exciton Recombination in AgBr," *Solid State Comm.*, **14**, p. 1133 (1974).

[59] R. P. Lowndes, "Anharmonicity in the Silver and Thallium Halides: Far-Infrared Dielectric Response," *Phys. Rev. B*, **6**, p. 1490 (1972).

[60] M. Matsushita, "Magnetoabsorption of Indirect Exciton in AgCl and AgBr," *J. Phys. Soc. Japan*, **35**, p. 1688 (1973).

[61] F. Bassani, R. S. Knox, and W. B. Fowler, "Band Structure and Electronic Properties of AgCl and AgBr," *Phys. Rev.*, **137** p. A1217 (1965).

[62] P. M. Scop, "Band Structure of Silver Chloride and Silver Bromide," *Phys. Rev.*, **139** p. A934 (1965).

[63] F. Bassani and A. Baldereschi, "Theory of Magnetic Field Effects on Critical Points," *Surface Science*, **37**, p. 304 (1973).

[64] E. Tosatti, "Lattice-Induced Forces between Excitons," *Phys. Rev. Lett.*, **33**, p. 1092 (1974).

[65] J. J. Forney, A. Quattropani, and F. Bassani, "Structure of the Biexciton Molecule and Optical Selection Rules in Zincblende and Wurtzite Materials," *Proc. XII Int. Conf. Physics of Semicond.*, Stuttgart 1974, p. 128.

[66] J. W. Hodby, J. G. Crowder, and C. C. Bradley, "Polaron Cyclotron Resonance in AgBr at Microwave and Infrared Frequencies," *J. Phys. C*, **7**, p. 3033 (1974).

[67] H. Tamura and T. Masumi, "Cyclotron Resonance of Positive Holes in AgBr," *Solid State Comm.*, **12**, p. 1183 (1973).

[68] G. Ascarelli, "Dynamic Piezo-Optic Study of Exciton and Polaron States in AgBr," *Phys. Rev.*, **179**, p. 797 (1969).

[69] H. Haken, *Quantenfeldtheorie des Festkörpers*, B. G. Teubner, Stuttgart, 1973.

[70] For a review, see: W. Czaja, "Isoelectronic Impurities in Semiconductors," *Festkörperprobleme*, **11**, p. 65 (1971).

[71] F. Moser and S. Lyu, "Luminescence in Pure and I-Doped AgBr Crystals," *J. Lumin*, **3**, p. 447 (1971).

[72] M. Roulet, H. Huber, and C. Jaccard, "Etude du Désordre Thermique dans AgBr par Canalisation de Protons de 100 keV," Fall meeting of the Swiss Phys. Soc. 1974, to be published in *Helv. Phys. Acta.*

[73] M. Tsukakoshi and H. Kanzaki, "Radiative Decay-Time of Bound Excitons in Silver Bromide," *J. Phys. Soc. Japan*, **30**, p. 1423 (1971).

Optical Properties of Layer Structure Compounds

G. Harbeke

Laboratories RCA Ltd., Zurich, Switzerland

E. Tosatti

GNSM-CNR, Istituto di Fisica, University of Rome, Italy

Abstract—Layer structure crystals represent an example of nearly two-dimensional solids. We investigate the influence of the strong structural anisotropy on the elementary excitations of such crystals. The main emphasis is on electronic interband transitions and exciton effects in PbI_2, CdI_2, and their alloys. The optical spectra of these materials are discussed in terms of the electronic band structure.

1. Quasi-Two-Dimensional Structures

Dimensionality effects in solids have recently attracted a great deal of interest, particularly with respect to phase transitions and to conduction phenomena in quasi-one-dimensional solids. A quasi-one-dimensional structure consists of parallel linear chains, or strands, of atoms or molecules where the interaction within the strand is far larger than between neighboring strands. In quasi-two-dimensional structures the system is either strongly confined in the third dimension or the atoms are arranged in parallel layers where the interaction within the layers is far larger than between neighboring layers. There exist several examples of both types of quasi-two-dimensionality. A strongly confined electron gas can be created, for example, in inversion layers of MOS devices,[1] as shown in Fig. 1 for the case of p-type Si. By applying a field at the gate electrode, one can induce a depletion region of majority carriers and, close to the surface, even an inversion layer containing only minority carriers (electrons in this case). The thickness of the inversion layer is of the order of 100 Å or less. Because of this strong confinement, the motion of the electrons in the *z*-direction is quantized while they can move freely parallel to the surface. Many properties of this two-dimensional electron gas, such as energy levels, electronic transport, and magnetoconductivity, have been studied during the last few years. More recently, the quantum levels associated with the confinement of carriers in very thin semiconductor layers in multiple heterostructures produced by molecular-beam epitaxy have also been investigated by tunneling experiments and optical spectroscopy.[2]

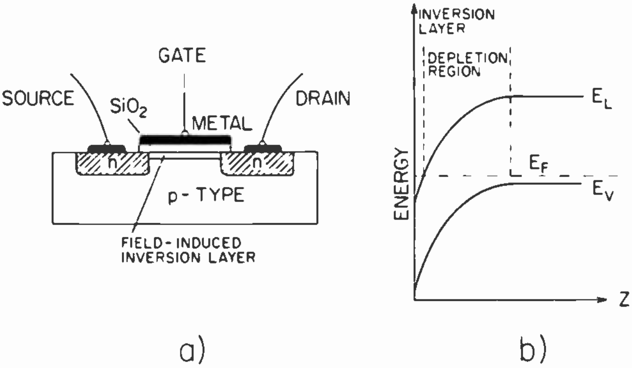

Fig. 1—(a) Schematic diagram of an insulated-gate field-effect transistor. (b) Energy-level diagram in the presence of a surface field. E_L, E_v, and E_F are conduction band, valence band, and Fermi level, respectively.

Another example of a quasi-two-dimensional structure is the solid surface. Due to the termination of the periodic structure there is a rearrangement of the atoms over the depth of a few atomic layers. This leads to changes in the spectrum of magnetic, electronic, and lattice excitations as compared to the bulk.

Finally, there is one example of "bulk two-dimensionality" in the crystals that have layer structures. These crystals can be regarded approximately as a linear array of compact planes made of atoms or of molecules. A classic example is crystalline graphite, where the carbon atoms are arranged in planar layers which are then loosely piled up to form the crystal. The nearest-neighbor distance within the plane is about 2.5 times smaller than the smallest separation of two atoms in adjoining planes. The simplest layer compound is hexagonal BN, which has the same structure as (and indeed is isoelectronic with) graphite. Conceptually similar are the layer compounds where we find layers with constituent atoms usually arranged in a three-dimensional structure. As an example Fig. 2 illustrates the CdI_2 structure. The cadmium atoms represented by empty circles are arranged in atomic sheets perpendicular to the c-axis of the trigonal structure. The Cd sheet is sandwiched between two atomic sheets of iodine. Such a three-sheet package constitutes one layer unit, the building block of the crystal. As can be seen, the distance to the next layer is again much larger than the separation of atomic sheets within a layer. The binding between the layers is therefore weak and predominantly of the van der Waals type. Within the layer, on the other hand, one has covalent or ionic binding of the usual kind.

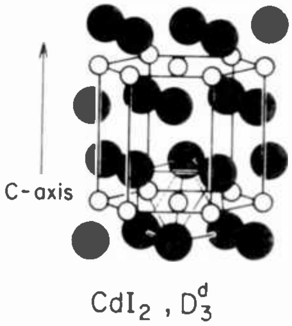

Fig. 2—CdI_2 structure. Full and empty circles denote iodine and cadmium atoms, respectively.

A large group of materials crystallize in the CdI_2 structure of point symmetry group D_{3d}, among them PbI_2, SnS_2, $SnSe_2$. All these materials are semiconductors or insulators. Another interesting group, based on a three-sheet layer, is that of the transition-metal dichalcogenides, which contains both semiconductors (e.g., MoS_2, $ZrSe_2$) and metals (e.g., $NbSe_2$, TaS_2), some of them being superconducting. A somewhat related structure occurs in GaSe and GaS, where the layer is formed by four sheets Se–Ga–Ga–Se, the Ga–Ga pair replacing the metal of the previous compounds.

Common features to all these materials are the van der Waals gap and a strong structural anisotropy with unusual consequences in terms of many macroscopic properties. In the first place, cleavage is extremely easy along the layer plane (basal plane). One can obtain thin crystals down to a thickness of the order of a few unit cells. This is useful when one is interested in the effect of spatial confinement, e.g., on excitons, or in the question of superconductivity in nearly two-dimensional crystals.

Foreign atoms or molecules can diffuse very easily into layer structures and the diffusion occurs practically only inside the van der Waals gap. Using this effect one can fill the gap by a complete layer of foreign atoms or molecules. This process, called intercalation,[3] generally produces an increase of the interlayer distance and changes the properties of the original crystal in a very pronounced way. Semiconducting compounds can be made metallic by intercalating with alkali metals; nonmagnetic compounds can be made ferromagnetic by introducing transition metals. Interesting work has been done on superconducting layer compounds intercalated with organic molecules. It turned out to be possible to separate the layers by distances of 50 to 60 Å, and thus to study, essentially the properties of a two-dimensional superconductor and to compare the results with those obtained from extremely thin cleaved samples.

A third consequence of the weak interlayer binding is the existence of numerous polytypes for every given compound, which differ only in the stacking of the fundamental layer along the c-axis. The resulting unit cells have identical x,y-size but are multiples of the basic cell along z. The left half of Fig. 3 shows two identical unit cells of the basic 2H-CdI_2 containing one CdI_2 molecule each. Let us call the stacking, from bottom to top, AcB AcB. In the next possible polytype, 4H, shown in the right half of Fig. 3, the stacking is instead AcB CaB, corresponding to a rotation of the upper layer by 180° around the c-axis going through site B. Since the energy difference between the two types of stacking is rather small, the occurrence of higher polytypes, sometimes with large periodicity distances, is fairly frequent. In general, the interlayer interaction is weak enough to leave the gross physical properties unchanged. There are some differences in the details, however, that are discussed in a later section.

We can now pose the question—how important is the effect of this peculiar anisotropy on the elementary excitations of the electron and of the lattice system? Experimentally, optical spectroscopy has been the most useful method for studying the excitations in ordinary nonlayer materials. We concentrate in this paper on a discussion of the electronic excitations of layer-structure semiconductors as measured by optical techniques. Mainly, we studied the materials PbI_2 and CdI_2.

2. The Dielectric Function

The complex dielectric function $\epsilon(\omega) = \epsilon_1(\omega) + i\epsilon_2(\omega)$ describes the response of the medium to the driving electromagnetic field, $\mathbf{D} = \epsilon \cdot \mathbf{E}$. It is the square of the complex refractive index $N(\omega) = n(\omega) + ik(\omega) = \epsilon(\omega)^{1/2}$ where n is the real refractive index and k the attenuation index. We have thus $\epsilon_1 = n^2 - k^2$ and $\epsilon_2 = 2nk$. The optical constants n and k are real and positive numbers that can be determined by optical measurements. In practice, one often uses the absorption coefficient K, defined by the relative decrease of the intensity (rather than that of the field) per unit distance through $I = I_0 \exp(-Kx)$. We have $K = 4\pi k/\lambda$, where λ is the wavelength in vacuum. Another quantity, which is easily obtained by experiment, is the normal incidence reflectivity

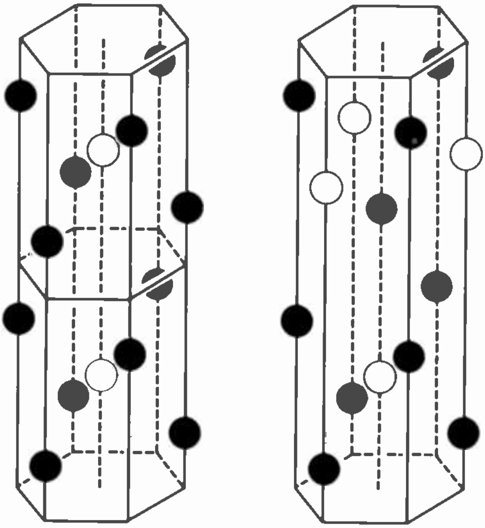

Fig. 3—Crystal structures of $2H-\mathrm{CdI_2}$ (left) and $4H-\mathrm{CdI_2}$ (right). Full and empty circles denote iodine and cadmium atoms, respectively.

$$R = \frac{(n-1)^2 + k^2}{(n+1)^2 + k^2}.$$

Only cubic crystals are isotropic in the linear optical response. The optical properties of noncubic crystals, which include birefringence and dichroism, are described by a tensor dielectric function. Since all the layer structures mentioned in Sec. 1 are uniaxial, the tensor reduces to the two elements $\epsilon_\perp$ for polarization in the basal plane and $\epsilon_\parallel$ for polarization along the c-axis.

The dielectric function contains contributions due to excitations of lattice vibrations, mainly in the infrared region of the spectrum, and to electronic excitations of both the intraband and interband type. In semiconductors, intraband transitions give only small contributions since the concentration of free carriers is small compared to that in metals. Interband transitions occur between filled valence-band states and empty conduction-band states, mainly in the visible and ultraviolet region of the spectrum. We can use them to illustrate the influence of dimensionality on the dielectric function. The imaginary part of $\epsilon(\omega)$ is proportional to the joint (valence and conduction band) density of states function $J_{vc}(\omega)$ and to the square of the matrix element for the transition M_{vc}.

$$\epsilon_2(\omega) \propto \frac{1}{\omega^2} J_{vc}(\omega) \cdot M_{vc}^2. \qquad [1]$$

The joint density of states function $J_{vc}(\omega)$ or $J_{vc}(E)$ (since the photon energy $E = \hbar\omega$) has pronounced features at critical points in the energy versus wave-vector function $E(\mathbf{k})$, i.e., at points where the condition $\nabla_{\mathbf{k}}(E_c - E_v) = 0$ in the function of the vertical energy difference between conduction and valence bands $E_{vc} = E_c - E_v$ is fulfilled.

The function $J_{vc}(E)$ depends strongly on dimensionality; at the onset energy for transitions corresponding to the bandgap E_0, it starts (for parabolic bands $E_0 \propto k^2$) with a square-root behavior for $d = 3$, with a step function for $d = 2$, and with a singularity for $d = 1$. This behavior, illustrated in the left half of Fig. 4, can be expected to show up in $\epsilon_2(\omega)$ provided the matrix element M_{vc} does not vary strongly in the region of E_0. Corresponding features should be observed in the real part $\epsilon_1(\omega)$, which is connected with $\epsilon_2(\omega)$ through dispersion relations, and in the optical constants n and k as well as in the reflectivity. Pronounced differences should also occur in the shape of spectral lines arising from saddle points in the $E(\mathbf{k})$ function, i.e., points where the energy bands have an upward curvature in some directions of $\mathbf{k}$ and a downward curvature in others. Fig. 4 shows J_{vc} for M_1 type (curvature negative in one direction) saddle points. We note the sharp logarithmic singularity for $d = 2$. It can, for example, be found in the experimental ϵ_2 curve of graphite for the electric vector $\mathbf{E}$ of the incident light perpendicular to the c-axis, as shown in the dashed line in Fig. 5. The solid line is calculated from the electronic band structure, which contains two saddle points and

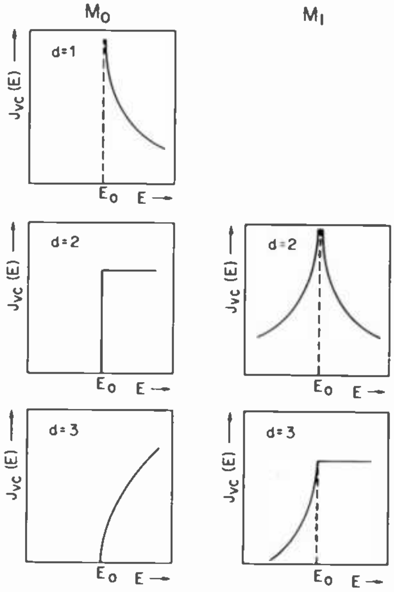

Fig. 4—Joint density of states function at M_0- and M_1-type critical points for different dimensions.

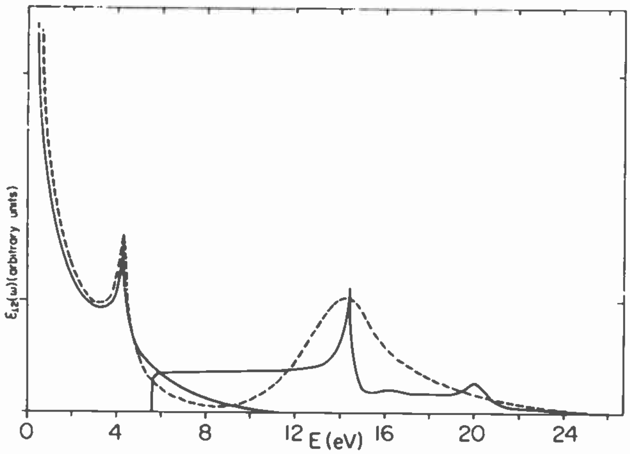

Fig. 5—Imaginary part of the dielectric function of pyrolytic graphite versus photon energy for E⊥c. Dashed line indicates experiment and the solid line theory.

one M_0 type onset in the region from 0.5 to 24 eV. At the 15 eV peak, the experimental line is broadened by strong final state electron–electron interaction (which increases with the distance from the Fermi level), but there is good agreement in the line shape at the 4-eV saddle point. Graphite is thus an excellent example for near two-dimensionality of the electronic excitations in a layer structure. This is also apparent in the **E**‖**c** spectrum, which is determined by the same bands and joint density of states function but by different matrix elements; the selection rules for optical transitions are not the same for both configurations. Thus $\epsilon_{2\parallel}$ just in the 4-eV region, where $\epsilon_{2\perp}$ reaches the sharp maximum, is nearly zero.[4]

The step function onset in J_{vc} for $d = 2$ has never been clearly observed in the measured $\epsilon_2(\omega)$ of any layer structure material. This is largely due to reasons outside of our discussion of the density of states. Graphite is not a good candidate since it is a semimetal with zero energy gap. In semiconducting materials the $\epsilon_2(\omega)$ onset is often strongly modified by the coulomb interaction between the electron excited to the conduction band and the hole left behind in the valence band. If this electron–hole interaction is strong enough, then not only are the quasi-continuum transitions above E_0 modified, but observable band states are formed at energies below E_0, so called exciton states. In the three-dimensional case the exciton energy levels are simply derived from the Rydberg series of atomic hydrogen by replacing the proton by the hole, screening the coulomb interaction, and using the effective-mass approximation. One obtains a series of levels

$$E_n = E_0 - \frac{e^4 m^*}{2\hbar^2 \epsilon_1{}^2} \cdot \frac{1}{n^2}, \qquad n = 1, 2, 3 \ldots \qquad [2]$$

where m^* is the reduced effective mass, $1/m^* = (1/m_e) + (1/m_h)$.

In the anisotropic case the line spectrum is definitely modified in terms of the anisotropy parameter

$$\gamma = \frac{m_\perp{}^* \cdot \epsilon_{1\perp}}{m_\parallel{}^* \cdot \epsilon_{1\parallel}}.$$

In layer structures the effective mass for motion within the plane, $m_\perp{}^*$, is generally expected to be smaller than $m_\parallel{}^*$, the mass for motion along the axis, due to the weaker electronic overlap between layers. If this is not overcompensated by the ratio of the dielectric constants (as is usually the case), we expect $\gamma < 1$. Fig. 6 shows the position of the three lowest levels as a function of γ as calculated by

Baldereschi and Diaz.[5] It can be seen that the levels differ markedly from the isotropic values, not just by a scaling factor. The larger the relative increase, the smaller n is. The binding is increased since we now have an elliptical envelope wave function such that the effective electron–hole distance becomes smaller. The exciton spectra of several layer-structure compounds have been analyzed to yield their respective γ-values. The relative oscillator strengths react more sensitively than exciton energies on the anisotropy. For a detailed evaluation, however, a knowledge of the wave function is required; calculations providing the wave functions are not yet available.

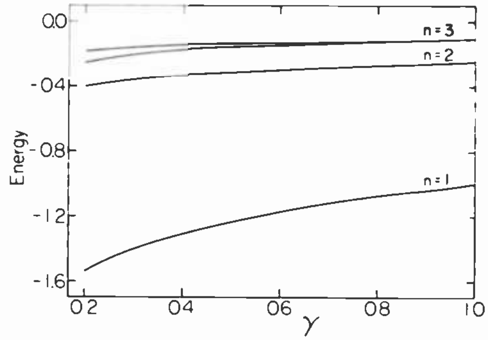

Fig. 6—Exciton energy levels of anisotropic excitons in units of isotropic binding energy versus $\gamma = m_\perp{}^* \mathrm{E}_{1\perp} / m_\parallel{}^* \epsilon_{1\parallel}$. The $n = 3$ state splits into a 3*s* and a 3*d* level.

Just as the lower dimension causes a sharpening of the critical-point features in the optical spectrum of electronic interband transitions, there is also a structure enhancement in the phonon density of states. This should lead to line-shape sharpening in the infrared absorption due to lattice vibrations as well as in the Raman scattering spectra.

3. Sample Preparation and Experimental Procedure

$2H - PbI_2$ and $2H - CdI_2$ crystallize in the trigonal CdI_2-structure of space group $D_{3d}{}^3$. The lattice spacings are rather similar ($a = 4.24$ Å, $c = 6.84$ Å in CdI_2; $a = 4.54$ Å, $c = 6.90$ Å in PbI_2). In PbI_2, the nearest-neighbor distance between lead atoms in the layer is thus about 1.5 times smaller than between lead atoms in adjoining layers.

Crystals of PbI_2 and CdI_2 were grown by a number of methods. Bridgman growth from the melt gave single crystals of up to 10 mm diameter and 20 mm length with a small mosaic spread (~1°) of the

c-direction. Hexagonal platelets of up to 5 mm diameter and 0.5 mm thickness with the plane perpendicular to the c-axis were grown by the silica-gel method as described by Henisch et al[6] or by slowly cooling a saturated aqueous solution from 100°C to room temperature. The latter technique, as well as sublimation growth from PbI_2 powder in closed ampoules, also yielded very thin platelets of a few 1000 Å thickness that were used for transmission measurements.

It is well known that both CdI_2 and PbI_2 exist in more than twenty polytypes. The distribution of polytypes depends on the growth process. Polytypes for gel-grown PbI_2 have been discussed by Hanoka and Vand.[7] We have used only PbI_2 crystals of the $2H$ and $4H$ polytype for our optical measurements. The polytype of individual crystals was first determined by zero layer (and in some cases first layer) Weissenberg photographs of the a^*-c^*-plane. Once a correlation between the two polytypes and their band-edge exciton energies had been set up in this way, it was possible to identify the polytype of a sample directly from its optical spectrum. This is particularly useful for large Bridgman-grown crystals, which can consist of regions of different polytypes. We found that, in contrast to the wide distribution observed in gel growth,[7] Bridgman crystals mainly contain just $2H$ and $4H$.

The occurrence of a large variety of polytypes indicates that only small differences in the thermodynamic energy exist between them. For the same reason it is easy to induce polytypic phase transformations at elevated temperatures and retain the crystals in the transformed state after going back to room temperature. We found that such transformations always go in the direction of disorder. A $2H$-crystal, e.g., can be transformed to $4H$ by annealing in vacuum at 170°C for 12 hours and then cooling to room temperature over a period of three hours. Annealing at higher temperatures, say at 300°C, leads generally to a mixture of $4H$ and higher polytypes. It is generally believed that the polytypic phase transformations result from the creation, propagation, and redistribution of stacking faults. The final distribution of stacking faults may then be ordered such that an ordered structure with a high identity period in the stacking along the axis results. Back transformation from $4H$ to $2H$ at room temperature has been reported to occur partly over a period of months. We have also seen some indications of back transformation in the optical spectra, but the effects seem to be strongly sample dependent. This is easy to understand in terms of a sample-dependent density and distribution of stacking faults.

Optical measurements were carried out on faces obtained by cleaving from the Bridgman crystals or from thick crystals grown by other methods. Cleavage along the layers gives surfaces of high optical quality, and no further treatment was given to them. Cleavage along any other crystal plane is impossible. Therefore, reflectivity measurements with $\mathbf{E}\|\mathbf{c}$ have been performed on small as-grown crystal faces containing the c-axis, which occurred inside polycrystalline Bridgman crystals. The transmission of thin samples down to a few 100 Å thickness was measured on gel- or sublimation-grown crystal platelets with as-grown surfaces.

Transmission and reflectivity measurements between 2 eV and 6 eV were done with a double-beam optical spectrometer with a dispersion of 16 Å/mm. At higher photon energies up to 11 eV, a 1-meter-focal-length Seya–Namioka-type vacuum spectrometer fitted with a low pressure ($\cong$1 Torr) hydrogen gas discharge as light source was used. Since we have a windowless connection between the discharge lamp and the main vacuum chamber, a vacuum of no better than 10^{-4} Torr can be maintained. In order to prevent condensation on the sample surface during low-temperature measurements, the sample chamber is sealed off from the main spectrometer by an LiF window for measurements at liquid nitrogen or helium temperatures. This limits the working range to wavelengths larger than 1100 Å, equivalent to 11 eV. Inside the sample chamber we use ion getter pumping down to 10^{-7} Torr. In the sample chamber a small part of the beam cross section is reflected into a reference beam by an LiF-coated aluminum mirror. Two RCA 1P21 photomultipliers in conjunction with glass plates coated with sodium salicylate phosphor are used to detect the ultraviolet radiation in the reference and sample beams. The samples are fixed to the "cool finger" of a liquid-helium cryostat extending into the sample chamber.

4. Optical Spectra and Electronic Band Structure of PbI_2 and CdI_2

Fig. 7 shows the overall $\mathbf{E}\perp\mathbf{c}$ reflectivity spectrum of PbI_2 between 2 eV and 10 eV at 77°K and 300°K, measured under near normal incidence on a cleaved basal-plane surface. At first sight one could be tempted to associate some of the sharp features, e.g., at 4.5 eV, with the logarithmic singularities that are to be expected at saddle points in two-dimensional crystals, which we have seen in Fig. 5 for graphite. It should, however, be noted that the sharp structure is very temperature dependent. That means that the line shape is strongly enhanced by final state electron–hole interaction. Such excitonic peaks are seen at 2.5 eV (associated with the absorption edge), 3.3 eV, 4.5 eV, 5.7 eV, and possibly at 8.4 and 9.2 eV. Since the electron–hole interaction is strongest at critical points in E(**k**), we might try to associate all these peaks with such M_0- or M_1-type critical points. By definition it will be an M_0-type at the absorption edge at 2.5 eV, and the oscillator strength indicates that we are dealing with direct transitions (i.e., practically without change of wave vector **k**) at the band edge. Exciton states at higher conduction bands are degenerate with continua of scattering states in other bands. In spite of this interaction, the exciton lines are still observable in the spectrum (typically with asymmetric line shapes) provided the dielectric screening of the coulomb interaction is not too strong. Exciton effects therefore predominate over continuum interband transitions in the spectra of low-dielectric-constant materials such as the alkali halides, where $\epsilon_1(\omega = 0)$ is about 5. Continuum interband transitions, on the other hand, largely determine the spectra of semiconductors with high dielectric constants, such as germanium ($\epsilon_1(\omega = 0) = 16$). The values in PbI_2 are intermediate between these two cases; $\epsilon_{1\perp}$ is 6.25 in the transparent optical region, $\epsilon_{1\parallel}$ is about the same; for the static value $\epsilon_{1\parallel}(\omega = 0)$ again the same value has been reported.[8] This result would indicate that there is virtually no ionicity that is hard to reconcile with the observation of infrared active lattice vibrations. Disregarding the question of the

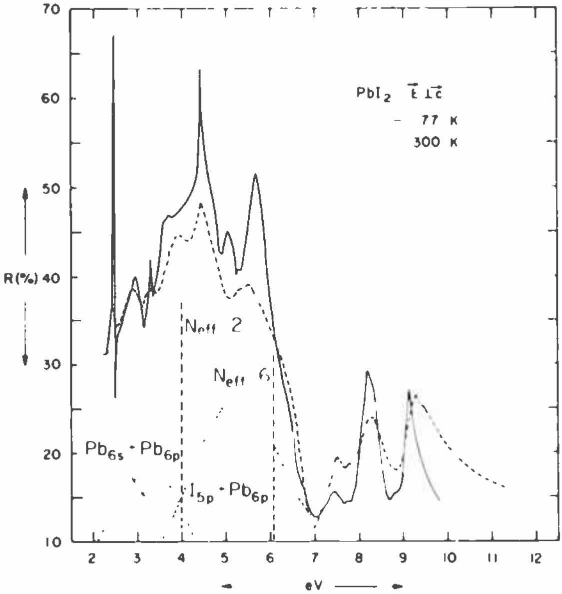

Fig. 7—Reflectivity spectrum of PbI_2 at 300°K and 77°K, $E \perp c$, cleaved surface.

exact values, the dielectric screening will be of medium strength. As a result, we see in Fig. 7 a mixture of exciton peaks and broad, rather temperature insensitive, interband continuum lines, for example around 3 eV and 4 eV.

Before we discuss fine details of the spectra and assignments to the electronic band structure, we should try to make use of the additional information that can be had from measurements with linearly polarized light under different orientations of the electric vector with respect to the optic axis. Since the selection rules for electric dipole transitions, straightforwardly derived from the crystal symmetry, depend on the orientation, we have one more parameter at hand than in cubic, optically isotropic systems. Fig. 8 shows the 4.2°K reflectivity spectrum of PbI_2 between the band edge and 5 eV. Since the spectrum was obtained on an as-grown surface parallel to the *c*-axis, the reflectivity for $\mathbf{E} \perp \mathbf{c}$ is not as high as in Fig. 7 from a cleaved surface. The band-edge region to 2.55 eV is discussed in more detail in Section 5. We note that some of the broad structure is either independent of polarization (near 3.5 eV) or slightly shifted (near 3 eV). There are a few more details in the sharp structure as compared to Fig. 7 due to the lower temperature, but of interest is the pronounced polarization dependence found for the exciton lines. The band-edge exciton at 2.5 eV is about 4 times weaker for $\mathbf{E} \| \mathbf{c}$ than for $\mathbf{E} \perp \mathbf{c}$ (for quantitative details see below) and the exciton peaks at 3.3 eV and

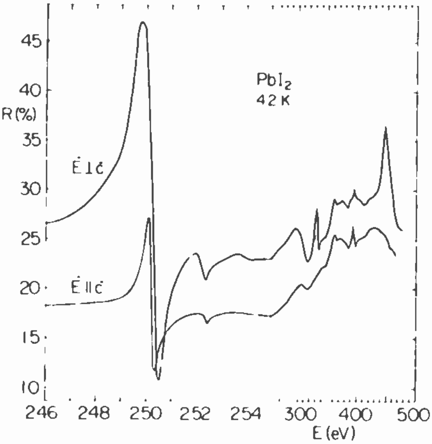

Fig. 8—Reflectivity spectrum of PbI_2 at 4.2°K for $\mathbf{E} \perp \mathbf{c}$ and $\mathbf{E} \| \mathbf{c}$, as-grown surface. Note the change of change of scale on the abscissa at 2.55 eV.

4.5 eV are completely absent for $\mathbf{E}\|\mathbf{c}$. For $\mathbf{E}\|\mathbf{c}$, we find an excitonic peak at 3.95 eV that is only weakly present for $\mathbf{E}\perp\mathbf{c}$, where it rides on a broader background structure. Thus, in the region from 2.5 to 4 eV, we have three excitons, one strongly for $\mathbf{E}\perp\mathbf{c}$, one only for $\mathbf{E}\perp\mathbf{c}$ and one strongly for $\mathbf{E}\|\mathbf{c}$.

Band-structure calculations have been performed by two methods that start from opposing approximations. One was done by Schlüter and Schlüter[9] using the pseudopotential method, which has its origin in the free-electron approximation. The other approach, used by Doni et al,[10] starts from the tight-binding approximation, where the wave functions are built from atomic functions. It is comforting to see that both methods give essentially the same results. We show in Fig. 9 the results of the tight-binding approximation without spin–orbit interaction taken into account. We note that the valence bands occur in groups well separated from each other. They can be traced back to the atomic levels, which are given on the left hand side. The two lowest bands arise from I_{5s}, the next higher group of six bands mainly from I_{5p}, the uppermost valence band mainly from Pb_{6s} and the three lowest conduction bands mainly from Pb_{6p} functions. This correlation has also been demonstrated very clearly by charge-density calculations in the pseudopotential approach.

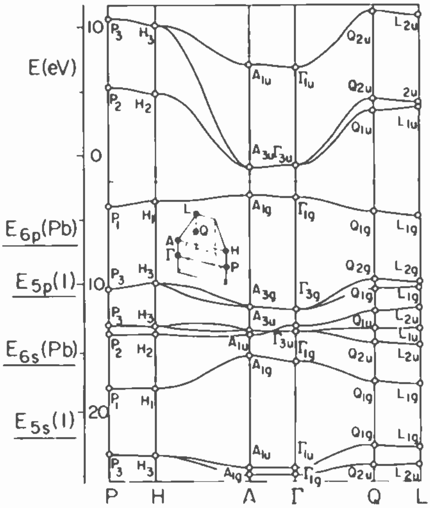

Fig. 9—Electronic band structure of PbI_2 in the main symmetry directions of **k**. The inset shows the elementary section of the hexagonal Brillouin zone.

The calculated band structure can now be compared with the optical results in terms of gross separations. The two dashed vertical lines in Fig. 7 indicate the energies at which the total number of electrons, which have been effective in the transitions up to that energy, reaches 2 and 6, respectively, according to[11]

$$N_{eff} = \frac{2mV_0}{e^2h^2}\int_0^E \epsilon_2 \cdot E \cdot dE, \qquad [3]$$

where V_0 is the volume of the unit cell, and m, e, and h are fundamental constants. We find that at 4 eV, most of the transitions from the uppermost valence band are exhausted (2 electrons per band) and that at about 6 eV most of the transitions from the two next lower I_{5p} bands have taken place, as indicated by the dotted lines in Fig. 7. In terms of the bands in Fig. 9 it means that the Γ_{1u} conduction band should be shifted downwards by 5 to 6 eV and that the I_{5p} bands should be shifted upwards by abot 2 to 3 eV. The latter conclusion is also supported by recent photoemission measurements[12] which have essentially mapped the valence-band density of states, and by the pseudopotential calculation. These corrections are not surprising in view of the fact that the calculation is an *a priori* one, performed without fitting any parameter to the experiment.

One further aspect that meets the eye, is the extreme anisotropy in the curvature of the conduction bands. The bands are very flat along the A-Γ direction (the same is true for the valence bands) which corresponds to the c-direction in real space. (This is in agreement with the expectation of large effective masses for motion of carriers across the layers as a consequence of the strong anisotropy in the electronic bonds.) There should be a large density of states available for transitions at points all along the A-Γ direction. It is thus to be expected that most of the spectral structure can be explained by transitions at critical points at the points A and Γ, which are equivalent (symmorphous point groups). We have therefore proposed the band model in Fig. 10 for transitions from the Pb_{6s} valence band to the Pb_{6p} conduction band at the point A where Fig. 9 shows the minimum gap.[13] The model begins with two conduction bands split by the crystal field anisotropy. In the next step spin–orbit interaction is initiated. In the first order, this splits the p_x,p_y band A_{3u} into A_{4u} and $A_{5u} + A_{6u}$ and, in the second order mixes this A_{4u} state with the other state originating from A_{1u}. This mixing causes the transitions from the A_{4g} valence band to be allowed for both polarizations of light, one of them strongly allowed and the other weakly, as indicated by the solid and dashed lines, respectively. In the final step, the electron–hole interaction is introduced, leading to the three *s*-envelope excitons produced in transitions between the A_{4g} valence band and the conduction bands. The calculated relative oscillator strengths for both polarizations are in excellent agreement with the results for the exciton peaks at 2.5, 3.3, and 3.95 eV shown in Fig. 8. In correspondence with these three sharp, exciton-enhanced M_0-type peaks there should also be three broader structures with similar polarization behavior due to M_1 type saddle point transitions at Γ. The first one at about 3 eV is indeed much stronger for $\mathbf{E} \perp \mathbf{c}$ and should therefore be assigned to $\Gamma_{4g} \rightarrow \Gamma_{4u}$ transitions. Similar arguments can be made for the broad peaks at 3.9 eV (⊥) and 4.3 eV (∥), but in this region there may also be contributions from transitions at other points in **k**-space. In conclusion, we can say that the band model in Fig. 10 gives a very good description of the optical properties of PbI_2 up to 4 eV. We see later that it has been confirmed by further calculations and experiments on different polytypes.

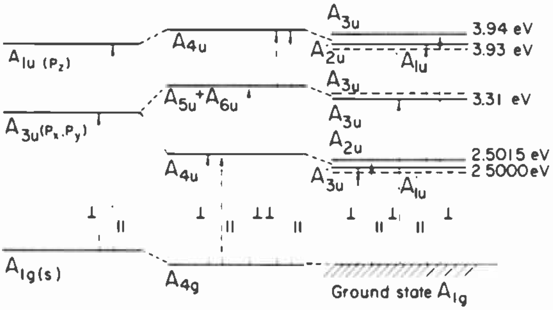

Fig. 10—Valence- and conduction-band model for 2*H*-PbI_2. Strongly and weakly allowed transitions are denoted by continuous and dashed lines, respectively. Numerical values for the exciton energies are taken from experiment.

CdI_2 has basically the same band scheme as PbI_2, but the Cd atom possesses two valence electrons fewer than the Pb atom to fill the bands. Consequently, the Fermi level in CdI_2 is below the Cd_{5s} band, whereas in PbI_2 it is above the corresponding Pb_{6s} band in Fig. 9. Thus, the optical absorption begins with indirect transitions at about 3.5 eV,[14,15] so that no pronounced exciton structure occurs at the edge. Fig. 11 shows a section of the reflectivity spectrum in order to demonstrate the existence of narrow, strongly temperature-dependent lines (X_1 and X_2) at fairly high energies: At 77°K additional structure occurs on the high-energy side of X_1 and X_2, which has been interpreted as being due to the higher exciton states according to Eq. [2].[16] The sharp structures are thus certainly partly due to excitonic effects, but the 300°K line shape of X_1 suggests also a strong bunching of density of states, probably again due to rather flat and parallel valence and conduction bands along A-Γ. The quasi-two-dimensionality in the bonding of both materials expresses itself thus in the optical properties via the anisotropy of the curvature of the electron bands.

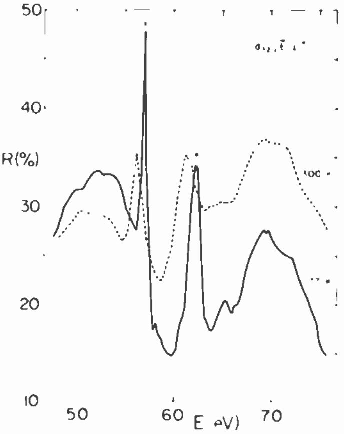

Fig. 11—Reflectivity spectrum of CdI_2 between 4.8 and 7.5 eV at 300°K and 77°K, **E** ⊥ **c**, cleaved surface.

5. Cationic Excitons in PbI_2

The band-edge exciton series of PbI_2 has in the past given rise to many interpretations and controversies. First reports came from Nikitine and Perny[17] who described an absorption spectrum with four lines in front of the absorption edge. It was explained in terms of an isotropic Wannier exciton series according to Eq. [2] with $E_0 = 2.567$ eV and $R = e^4 m^*/(2\hbar^2 \epsilon_1^2) = 142$ meV. The $n = 1$ line, however, did not follow this law but was shifted by 82 meV to higher energies. Later the spectrum was identified as that of the 4*H*-polytype; the 2*H*-type gave the same kind of spectrum with $E_0 = 2.552$ eV and $R = 127$ meV.[11] Baldini and Franchi[18] then gave an interpretation in terms of two overlapping series, one allowed for **E** ⊥ **c** and one for **E**∥**c**. This conjecture was disproved by the polarization-dependent results[19] in the edge region up to 2.55 eV shown in Fig. 8. These results show clearly that all the lines belong to one and the same Wannier series and that the intensity ratio $I_\perp / I_\parallel$ is about the same for all lines. Quantitative values are obtained from $\epsilon_2(E) = \mathrm{Im}\epsilon(E)$ and $-\mathrm{Im}(\epsilon^{-1})$ derived from the reflectivity by Kramers–Kronig analysis up to 2.53 eV and shown in Fig. 12. The positions of transverse excitons are given by peaks in Imϵ, while those of longitudinal excitons are given by peaks in $-\mathrm{Im}(\epsilon^{-1})$. These positions have been indicated above the curves. The longitudinal–transverse splittings are different for $\mathbf{E}\perp\mathbf{c}$ (6.2 meV) and $\mathbf{E}\|\mathbf{c}$ (1.5 meV). Their ratio of about 4 should be the same as that of the oscillator strengths, i.e., the integrated areas under the peaks in ϵ_2 for $\perp$ and $\|$ as is indeed the case. The dashed lines mark the centers of gravity of the $\mathbf{E}\perp\mathbf{c}$ and $\mathbf{E}\|\mathbf{c}$ excitons, respectively, which are found as the lowest A_{3u} and A_{2u} exciton levels in the band scheme in Fig. 10.

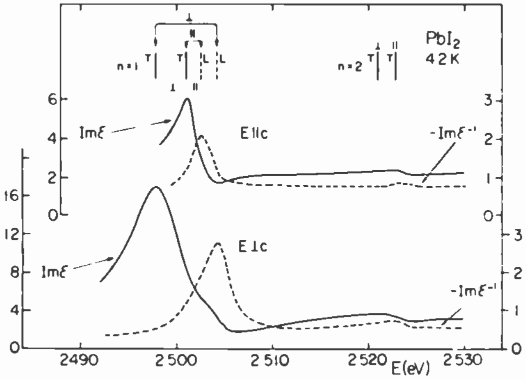

Fig. 12—Imaginary part Imϵ of the dielectric function and $-\mathrm{Im}(\epsilon^{-1})$ of 2*H*-PbI_2 in the band-edge exciton region for $\mathbf{E}\perp\mathbf{c}$ and $\mathbf{E}\|\mathbf{c}$.

The conclusion that there is one single exciton series leaves again the problem of the large $n = 1$ anomaly to be solved. We can first consider the ellipticity of the wave function expressed by the parameter γ in Sec. 2 as one possible cause of perturbation of a Wannier series in a layer structure. This will certainly not be without influence, but we have seen in Fig. 6 that for $\gamma < 1$ the relative binding of the $n = 1$ exciton increases, whereas in PbI_2 it is decreased. A value of $\gamma > 1$ is rather unlikely in view of the band structure, and does not give a fit to the spectrum for a wide range of γ either. A rough estimate of γ can be obtained from the ratios of the oscillator strengths f_n of the lines. Fig. 13 shows the absorption coefficient in the exciton region as derived from reflectivity by Kramers–Kronig analysis. The ratio f_1/f_2 is about 13, in agreement with earlier results,[17] whereas the ratio f_2/f_3

is difficult to evaluate because of the uncertainty about the exact shape of the background. In an isotropic Wannier series the intensity varies as n^{-3}, and for a strictly two-dimensional case as $[n - (\frac{1}{2})]^{-3}$. Our experimental value of 13 for f_1/f_2 is thus in between these two extreme cases, markedly different from isotropy.

There are a few other corrections to the Wannier series that we must also consider. Binding energies of excitons in small-bandgap semiconductors are usually calculated in the *effective mass approximation* (EMA), where free electrons and holes are assumed to be plane-wave states with effective masses replacing the real masses. In larger-band gap materials, this approximation becomes poorer, and it is important to take into account various corrections, most of which act to change the electron–hole interaction at small distances. They are thus usually called "central cell corrections." One of these corrections that we must consider here is required by the fact that valence and conduction states become rather localized in space. In the Wannier representation[20] the electron–hole interaction is built up from matrix elements

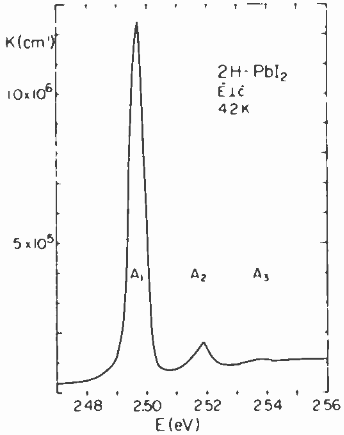

Fig. 13.—Absorption coefficient of $2H$-PbI$_2$ in the band-edge exciton region for $\mathbf{E} \perp \mathbf{c}$.

$$\left\langle \psi_l(r)\psi_m(r') \left| \frac{-e^2}{\epsilon|r - r'|} \right| \psi_n(r)\psi_0(r') \right\rangle . \qquad [4]$$

First of all one can neglect multicenter integrals and restrict consideration to $l = n$ and $m = 0$. Then the matrix element takes the simple form of a coulomb interaction between sites *l* and *m:*

$$\int |\psi_l(r)|^2 \left(\frac{-e^2}{\epsilon(r - r')} \right) |\psi_m(r')|^2 dr^3 dr'^3 \approx \frac{-e^2}{\epsilon |R_l - R_m|}. \qquad [5]$$

This is a good approximation for large $|R_l - R_m|$, but obviously wrong for $l = m$. That is, when electron and hole sit on the same site, their interaction cannot be taken as coulombic.

It follows that by assuming, as is done in the EMA, a coulomb interaction, one overestimates, as far as this aspect is concerned, the attraction at small distances. One must therefore consider an additional central cell correction that is *repulsive* and thus bound to reduce the binding energy of the exciton from its EMA value. This correction was discussed for the first time by Hermanson and Phillips.[21] Although not considered by other authors, it is in a sense very basic, as it accounts for the smooth transition found in nature between Wannier excitons in small-bandgap materials and Frenkel excitons in large-bandgap materials. It is in fact clear that, because the EMA binding energy is $R = e^4 m^*/2\hbar^2\epsilon_1{}^2$, the limiting case of extreme tight binding (flat bands, i.e., $m^* \rightarrow \infty$, and $\epsilon_1 \cong 1$) produces an infinite binding energy in the EMA rather than (as happens in reality) a well-behaved, moderately bound Frenkel exciton. All other corrections to the EMA considered previously[22] go in the opposite direction, i.e., they increase the binding over the EMA value, and thus sharpen the contradiction. The Wannier–Frenkel transition is, in fact, only accounted for if one considers the repulsive correction just described. The reason is clear—in the tight binding limit the exciton radius becomes as small as the lattice parameter, until eventually the matrix element $l = m = n = 0$ becomes the one that dominates. This is precisely the matrix element, ill-behaved in the EMA, that makes R infinite, while it is in fact finite and calculable from atomic states. In the opposite limit of small bandgaps, of course, the contribution of this single matrix element to the exciton binding energy becomes unimportant, and the EMA is valid.

In Fig. 14, we present a rough sketch of what the valence- and conduction-band state wave functions look like in PbI_2. They both originate, as discussed in Sec. 4, from the same atom, the cation, and the bound electron–hole pair state is thus a *cationic* exciton. The similarity to solid rare gases[21] is strong, though in this case accidental.

For an electron and hole sitting on the same atom, the interaction matrix element is very strongly cancelled by the *s* and *p* nature of the two orbitals. How important a correction to the EMA this will bring, depends in a very critical fashion on the geometry and on the actual

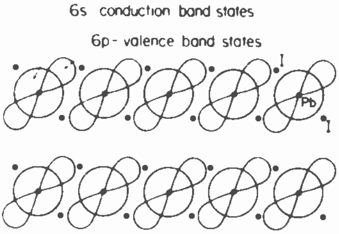

Fig. 14—Schematic view of the valence- and conduction-band wave function in PbI_2.

envelope function shape and size. We do not attempt here a detailed calculation, but simply outline the reasoning that shows how, despite the Bohr radius being still fairly large (of the order of 15 to 20 Å), cationicity and layer geometry conspire to make the anomaly particularly large.

In the first place, the Pb atoms are rather close-packed in their plane; the 6*s*-valence wave functions form a sort of sheet of charge whose thickness is of the order of twice the Pb atomic radius, i.e., $2r_0 \cong 4$ Å. The conduction states largely overlap this sheet although they have a node on the Pb nucleus. An electron and hole can in this case interact only very poorly over whole two-dimensional layers of thickness $2r_0$. The resulting correction to the EMA is much larger than in the isotropic case, as one can see, for example, by reformulating Eqs. [4] and [5] in terms of sheets and layers.

Given an exciton envelope function of a generally elliptical shape but roughly characterized by a radius a_0, the electron–hole coulomb interaction is hindered over a fraction of order r_0/a_0 of the total exciton volume, as indicated by Fig. 15. Because the electron–hole potential energy is on the average $2R$ (from the virial theorem), a *decrease* of the binding energy of order $2R(r_0/a_0)$ is predicted. A calculation of this correction energy, performed by assuming complete cancellation of the electron–hole interaction over a single layer of thickness $2r_0$ at $z = 0$ gives, for a spherical hydrogen *s*-state of principal quantum

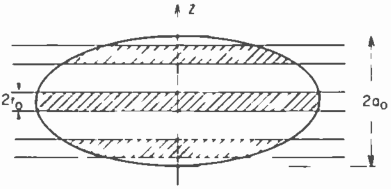

Fig. 15—Elliptical envelope wave function in a layer structure.

number n, the similar result

$$\delta R = -4Rn^{-3}(r_0/a_0).$$

The magnitude obtained for this correction in PbI_2 is of the order of $R/2$. The effect of the cationic central cell repulsion is considerably enhanced by the dimensionality effects caused by layer geometry and close packing of Pb atoms.

Experimentally, the observed anomaly of about 70 meV for R = 127 meV is in good agreement with the above estimates, particularly since the anisotropy discussed above and the exchange interaction, which can be estimated to give roughly 0.1 R decrease of binding, are also of influence.

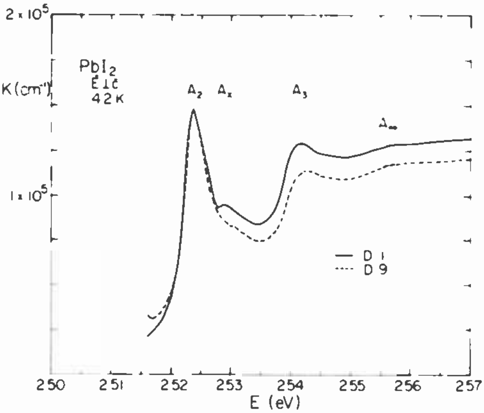

Fig. 16—Absorption coefficient of PbI_2 derived from transmission data of two thin crystals. The absorption of sample D_9 has been normalized to that of D_1 at the peak value of A_2.

Recently Levy et al[23] have reported the observation of a new line in reflection at an energy between those for n = 2 and n = 3 in Fig. 13. It has been used to give a new interpretation in terms of an isotropic Wannier series with a binding energy of about 30 meV. Since transmission measurements on samples of appropriate thickness can provide more accurate values of the absorption coefficient than Kramers–Kronig processed reflection data, we have measured the transmission of as-grown crystal platelets of a few thousand Å thickness. Fig. 16 shows the absorption coefficient from the n = 2 line on into the continuum obtained from two such crystals. The line reported by Levy et al., called A_x, is strongest in D_1, weak in D_9 and not observable in the majority of crystals.[17] It should also be noted that A_x is in a very different way sample-dependent compared with the other exciton lines. Fig. 16 shows that the widths of A_2 as well as of A_3 are nearly the same in both samples, whereas A_x is almost completely absent in D_9. These findings make it hard to believe that the line A_x forms as exciton series together with A_1 and A_2. Besides this, the line A_3 and the kink at the series limit A_∞ would not find an interpretation. There are no interband transitions[23] to be expected from the band structure in this region as we have discussed *in extenso*, and the absorption is definitely too high for phonon-assisted exciton transitions. Although we do not offer an explanation of A_x in terms of an intrinsic excitation, we believe that our previous conclusions concerning the exciton series are valid, particularly in view of the explanation of the $n = 1$ anomaly in terms of the layer-enhanced, cationic central-cell correction.

6. Interlayer Interaction in PbI_2—Polytypes

We have seen that the band-edge exciton series in the two lowest polytypes of PbI_2 illustrated in Fig. 3 differ only by about 10 meV in energy. This is an example of small changes of physical properties generated by polytypism. It is nevertheless difficult to establish general rules that give a correspondence between microscopic properties of polytypes, because the space group of the higher polytype is in general not a subgroup of the basic one. This situation holds also for $2H$- and $4H$-PbI_2 since the group of $4H$ is $C_{6v}{}^4$. It means that the electronic band structure of $4H$ cannot simply be derived from that of $2H$ by a perturbational approach, but that rather the symmetry properties of $4H$ and the interlayer interaction have to be considered in a separate calculation. This was done by Doni et al[24] in a tight-binding approach; the results are shown in Fig. 17. For comparison, the results for $2H$, improved by including spin–orbit interaction and fitting the uppermost band to experiment, at the points Γ and A are also given. Going to $4H$, the intralayer interaction was not changed but all meaningful details of the different interlayer interactions were taken into account. As a result, no essential changes occur in the k_x, k_y plane from the $2H$-results in Fig. 9. The extension of the Brillouin zone in the k_z-direction Γ-A′ is half of Γ-A in $2H$, since the unit cell in real space is doubled along the c-axis. At the point A′ on the face of the $4H$-Brillouin zone, a twofold degeneracy is required by the symmetry properties of the group $C_{6v}{}^4$; bands can therefore intersect at A′ with non-vanishing slope. No critical points with high density of

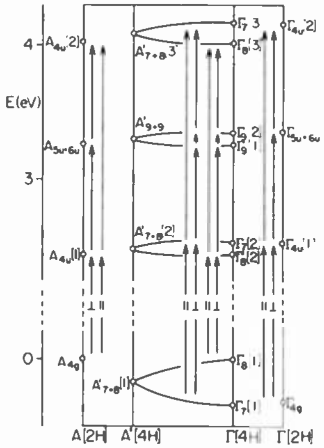

Fig. 17—Energy bands of $4H$-PbI_2 along the Γ-A′ line of the Brillouin zone. Energy levels of $2H$-PbI_2 at the points Γ and A are also reported for comparison. The arrows indicate allowed transitions for the specific polarization.

states are then to be expected at A′, and many interesting features of the optical spectrum should be explainable in terms of transitions at Γ.

We compare in Fig. 18 the reflectivity spectra of both polytypes measured with light polarized in the cleavage plane. The corresponding features in the two spectra can easily be found. There is only a

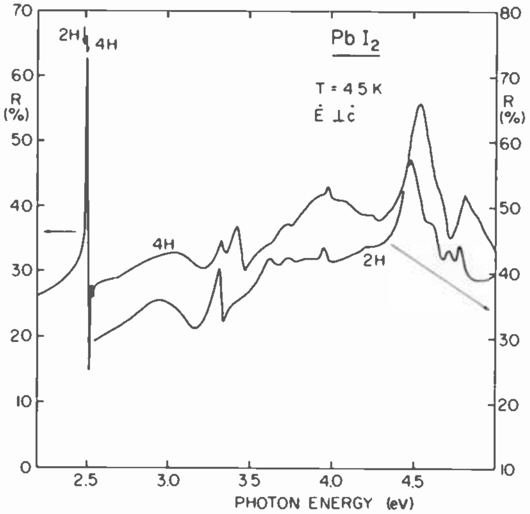

Fig. 18—Reflectivity spectra of $4H$-PbI_2 and $2H$-PbI_2 for $\mathbf{E} \perp \mathbf{c}$.

shift of 10 meV and no line splitting at the band-edge excitons at 2.5 eV. At the 3.3-eV peak we note a splitting into a doublet with 0.1 eV separation, the oscillator strength being mainly transferred into the higher-energy component. Some further changes appear between 3.6 and 4.1 eV and at higher energies.

It will now be shown that the main features are in agreement with the band structure in Fig. 17. The 2.5-eV excitons are related to the $\Gamma_8(1) \rightarrow \Gamma_8(2)$ transition (double group notation for C_{6v} states); no peak is expected for $\Gamma_8(1) \rightarrow \Gamma_7(2)$ since the transition is forbidden. There is thus only a 10 meV increase of the energy bandgap in good agreement with the experiment.

Around 3.3 eV there are now two critical point transitions allowed, $\Gamma_8(1) \rightarrow \Gamma_9(1)$ and $\Gamma_8(1) \rightarrow \Gamma_9(2)$. The calculated splitting is quantitatively borne out by the experiment. It also illustrates how narrow the conduction bands along k_z in both polytypes are, since the states $\Gamma_9(1)$ and $\Gamma_9(2)$ correspond to A_{5u+6u} and Γ_{5u+6u} in 2*H*, a clear demonstration of small effective masses for motion across the layers.

In conclusion, our results show that the change of interlayer interaction preserves the individuality of narrow bands. The bands in Fig. 17 look as if the 2*H* bands along k_z had just been folded around the point A′, although it is not required by the symmetry. It means then that interlayer interaction energies are small compared to band–band separations. This pseudo-correspondence can, however, not be carried through to the intensities and wave functions. It would predict the higher-energy component of the 3.3-eV doublet to be unobservable, since it would be derived from the indirect $A_{4g} \rightarrow \Gamma_{5u+6u}$ transition in 2*H*. Experiment shows that it is actually the stronger component. This means that interlayer interaction energies are of the order of the conduction bands, i.e., 0.01 to 0.1 eV, such that considerable mixing of the wave functions in the 4*H* band occurs. This example shows again that wave functions and transition probabilities are far more sensitive to a perturbation than are the eigenvalues.

7. The Non-Isoelectronic Alloy System $Pb_{1-x}Cd_xI_2$

PbI_2 and CdI_2 form stable alloys over the whole range of concentrations. Like the constituent compounds, the alloys are semiconductors. The Cd atom has two valence electrons ($5s^2$), while Pb has four ($6s^26p^2$). We have thus a non-isoelectronic system. Pb impurities in CdI_2 should therefore tend to donate electrons to the empty Cd_{5s}-like conduction band, while Cd impurities in PbI_2 are expected to accept electrons from the full Pb_{6s}-like valence band. Hypothetical impurity

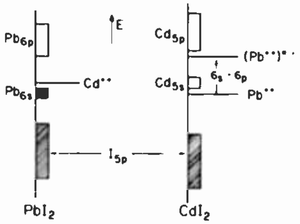

Fig. 19—Schematic energy level diagram for Cd impurities in PbI_2 and Pb impurities in CdI_2.

levels corresponding to these two situations are sketched in Fig. 19. We discuss the details of this "impurity limit" below. As the concentration of either Cd in PbI_2 or Pb in CdI_2 increases, the impurity level acquires more and more states, becoming an impurity band. At the same time, the host metal s-band is gradually depleted and shrinks and flattens in **k**-space.

There must exist critical concentrations x_1 and x_2 at which Mott–Anderson-type transitions from localized impurity states to extended band states occur. The fact that one cannot detect appreciable numbers of free carriers in the whole concentration range should mean that the two metal s-bands are essentially nonoverlapping for all x. On the whole, we expect a situation like that shown qualitatively in Fig. 20.

Preliminary reflectivity measurements at 77°K have been performed on $Pb_{1-x}\,Cd_xI_2$ over the whole concentration range.[25] Since the fundamental bandgap is rather different in the two limits (2.5 eV direct gap in PbI_2, 3.5 eV indirect bandgap in CdI_2), the spectra look different in the low-energy region. Also, sharp structures occur only in the two limits; the extra broadening at intermediate concentrations is probably due to random disorder in the alloy. Many of the

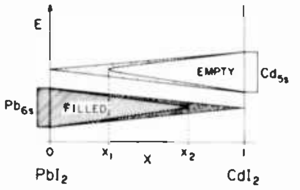

Fig. 20—Schematic energy diagram of the metal s-bands in $Pb_{1-x}\,Cd_xI_2$ alloys. The dotted area indicates localized states.

peaks can nevertheless be followed unambiguously as a function of x, their behavior being sketched in Fig. 21.

A quantitative interpretation of these results will have to be based on a band-structure calculation for the mixed crystal. Simple physical considerations, however, already provide some understanding, particularly in the impurity limits. First of all, it should be expected that the electronic properties of this system are mainly governed by the fact that it is not an isoelectronic one. In an isoelectronic system such as, for example, $GaAs_{1-x}P_x$, every state is well defined for all x and can be followed in a continuous manner from $x = 0$ to $x = 1$. Here, it is also a matter of band formation, band shrinkage, and disappearance of bands; it is thus not surprising to find transitions in Fig. 21 that seem to exist only for certain ranges of x. Let us look first at the 2.5-eV excitons series of PbI_2 for small x. Increasing quantities of Cd represent for the excitons first of all a scattering agent that reduces the lifetime when the average spacing becomes comparable with the exciton radius. It follows that exciton states of larger radius should disappear from the spectrum one after the other with increasing x. This is indeed the case[19]; the $n = 3$ line disappears at $x \cong 0.03$, the $n = 2$ line for $x \cong 0.15$, whereas the $n = 1$ line persists (though with increasing width) all the way to $x = 1$. (This result gives support again to the assignment of the $n = 3$ line A_3 in Fig. 16 as a member of the exciton series of 130 meV binding energy). It is very interesting that in this limit the "$n = 1$ exciton" peak goes into a sharp impurity line, observed in absorption at 3.2 eV, about 0.3 eV below the indirect bandgap of CdI_2.[25,26] It could also be identified by its temperature coefficient in the linear regime ($d E_0/dT = -2.1 \times 10^{-4}$ eV/K), which is very similar to that of the exciton in pure PbI_2 (-2.5×10^{-4} eV/K) and different from that of the indirect band edge of CdI_2 (-11×10^{-4} eV/K). Based on these findings, the peak was attributed to an inter-

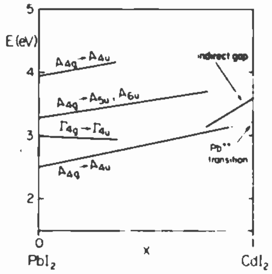

Fig. 21—Energy versus composition of some optical transitions in $Pb_{1-x}Cd_xI_2$.[25]

nal transition of a Pb^{++} impurity. For $\mathbf{E}\|\mathbf{c}$, a similar peak is found at about 25-meV lower energy. The splitting is qualitatively explained by the octahedral crystal field surrounding the substitutional Pb impurity,[26] although a quantitative calculation has not been attempted.

The fact that the $n = 1$ exciton goes continuously over to a Pb^{++} impurity line on alloying provides again strong evidence that the exciton itself is strongly "cationic," as we have discussed in the previous sections. It is essentially an internal $6s \rightarrow 6p$ transition of Pb, except for the screening provided by the crystal matrix. The decrease of screening in going from the PbI_2 to the CdI_2 environment should account for the increase in energy from 2.5 ($x = 0$) to 3.2 eV ($x = 1$). The other effect of alloying is a continuous change of (a) the lattice parameters and (b) the average effective potential to be attributed to the metal in a virtual-crystal band-structure calculation.

We notice that on increasing the concentration of Pb impurities, the CdI_2 indirect band edge decreases steeply; and that the PbI_2 saddle-point transition $\Gamma_{4g} \rightarrow \Gamma_{4u}$ at 3.0 eV decreases gently on increasing the Cd concentration in PbI_2. The energy difference between $\Gamma_{4g} \rightarrow \Gamma_{4u}$ and $A_{4g} \rightarrow A_{4u}$, which is a direct measure of the Pb_{6s} bandwidth, shrinks and extrapolates to zero at $x = 0.6$. This value can be taken as a rough estimate of the concentration x_2 at which the Pb_{6s} band becomes just an assembly of impurity levels. Reduced overlap and disorder act together to reduce bandwidth and to destroy the extended character of the states. No similar evidence for the shrinking of the Cd_{5s} band seems to be present. The decrease of the indirect-bandgap energy can be tentatively associated with the increase of lattice parameter for decreasing x; the Cd_{5s} conduction band is expected to lower its energy relative to I_{5p} as the average lattice parameter is increased by adding Pb.

As a final remark, we notice that the excitonic transitions at 3.3 and 3.9 eV in PbI_2 shift to higher energies with increasing x, with slopes very similar to that of the 2.5-eV exciton. This provides another confirmation that these three exciton groups belong to the same original $6s \rightarrow 6p$ transition of atomic Pb, the p-band being split by spin–orbit interaction and crystal field, as discussed in Sec. 4.

8. Summary

We have described a few realizations of nearly two-dimensional solid-state systems, particularly various layer structures. It was shown that the low dimensionality has a great influence on the joint density of states available for interband transitions and thus on the optical properties. Experimental results of reflection and absorption measurements have been reported for the layer-structure compounds PbI_2, CdI_2, and their respective alloys. The dielectric function of these materials in the interband region is strongly exciton exhanced but also determined by the quasi-two-dimensionality of the bonding via the anisotropy of the effective masses.

Interpretation of the PbI_2 spectra leads to an electronic-band-structure model in which the direct-bandgap transitions are essentially derived from internal $6s \rightarrow 6p$ transitions of atomic Pb. The binding anomaly of the bandgap exciton series of PbI_2 is explained in terms of a central cell correction for cationic excitons. The resulting correction is far larger than in the isotropic case due to the layer geometry and the elliptical envelope wave function. Optical spectra of different polytypes have been discussed in terms of interlayer interaction. Both these results and data of the nonisoelectronic alloy system Pb_{1-x} CdI_2 give support to the proposed band-structure model.

Acknowledgments

We are indebted to F. P. Emmenegger, K. Frick, and G. Lang for providing the samples, to F. Bassani for many stimulating discussions and to D. L. Greenaway and E. Meier for communicating unpublished results.

References:

[1] G. Dorda, "Surface Quantization in Semiconductors," p. 215, in *Advances in Solid State Physics*, H. J. Queisser ed., Pergamon Press, 1973.

[2] L. L. Chang, L. Esaki, A. Segmüller, and R. Tsu, "Resonant Electron Transport in Semiconductor Barrier Structures," *Proc. 12th Intern. Conf. on the Physics of Semiconductors*, Stuttgart 1974, p. 688. R. Dingle, W. Wiegmann, and C. H. Henry, "Quantum States of Confined Carriers in Very Thin $Al_xGa_{1-x}As - GaA_s - Al_xGa_{1-x}As$ Heterostructures," *Phys. Rev. Lett.*, **33**, p. 827, 1974.

[3] F. R. Gamble, F. J. DiSalvo, R. A. Klemm, and T. H. Geballe, "Superconductivity in Layered Structure Organometallic Crystals," *Science*, **168**, p. 568, 1970.

[4] D. L. Greenaway, G. Harbeke, F. Bassani, and E. Tosatti, "Anisotropy of the Optical Constants and the Band Structure of Graphite," *Phys. Rev.*, **178**, p. 1340, 1969.

[5] A. Baldereschi and M. G. Diaz, "Anisotropy of Excitons in Semiconductors," *Nuovo Cimento B*, **68**, p. 217, 1970.

[6] H. K. Henisch, J. Dennis, and J. I. Hanoka, "Crystal Growth in Gels," *J. Phys. Chem. Solids*, **26**, p. 493, 1965.

[7] J. I. Hanoka and V. Vand, "Further Studies of Polytypism in Lead Iodide," *J. Appl. Phys.*, **39**, p. 5288, 1968.

[8] A. E. Dugan and H. K. Henish, "Dielectric Properties and Index of Refraction of Lead Iodide Single Crystals," *J. Phys. Chem. Solids*, **28**, p. 971, 1967.

[9] I. Chr. Schlüter and M. Schlüter, "Electronic Structure and Optical Properties of PbI_2," *Phys. Rev. B*, **9**, p. 1652 (1974).

[10] E. Doni, G. Grosso, and G. Spavieri, "Band Structure and Absorption Edge of PbI_2," *Solid-State Commun.*, **11**, p. 493 (1972).

[11] Ch. Gähwiller and G. Harbeke, "Excitonic Effects in the Electroreflectance of Lead Iodide," *Phys. Rev.*, **185**, p. 1141, 1969.

[12] F. R. Shepherd and P. M. Williams, private communication.

[13] G. Harbeke, F. Bassani, and E. Tosatti, "Excitons in PbI_2," *Proc. 11th Int. Conf. on the Physics of Semiconductors*, Warsaw, 1972, p. 163.

[14] G. Grosso and E. Doni, private communication.

[15] D. L. Greenaway and R. Nitsche, "Preparation and Optical Properties of Group IV-VI_2 Chalcogenides Having the CdI_2 Structure," *J. Phys. Chem. Solids*, **26**, p. 1445, 1965.

[16] D. L. Greenaway and G. Harbeke, "Metastable Excitons in CdI_2 and PbI_2," *Proc. Int. Conf. on the Physics of Semiconductors*, Kyoto, 1966, p. 151.

[17] S. Nikitine and G. Perny, "Etude du spectre de raies d'absorption de PbI_2 aux très basses températures," *C. R. Acad. Sci., Serie A, B*, **240**, p. 64, 1955.

[18] G. Baldini and S. Franchi, "Exciton Magnetic Circular Dichroism of PbI_2," *Phys. Rev. Letters*, **26**, p. 503, 1971.

[19] G. Harbeke and E. Tosatti, "Band Edge Excitons in PbI_2: A Puzzle?," *Phys. Rev. Letters*, **28**, p. 1567, 1972.

[20] R. S. Knox, "Theory of Excitons," *Solid-State Physics*, Suppl. 3, New York, 1963.

[21] J. Hermanson and J. C. Phillips, "Pseudopotential Theory of Exciton and Impurity States," *Phys. Rev.* **150**, p. 652, 1966.

[22] W. Kohn, "Shallow Impurity States in Silicon and Germanium," *Solid State Physics*, **5**, p. 257, 1957.

[23] F. Levy, C. Depeursinge, Le Chi Thanh, A. Mercier, E. Mooser, and J. P. Voitchovsky, "Optical Absorption Edge and Luminescence of PbI_2," *Proc. 12th Int. Conf. on the Physics of Semiconductors*, Stuttgart 1974, p. 1237; Le Chi Thanh, C. Depeursinge, F. Levy, and E. Mooser, "The Band Gap Excitons in PbI_2," *J. Phys. Chem. Solids*, to be published.

[24] E. Doni, G. Grosso, G. Harbeke, E. Meier, and E. Tosatti, "Interlayer Interaction and Optical Properties of Layer Semiconductors: 2H- and 4H-Polytypes of PbI_2," to be published in *Phys. Stat. Sol. (b)*, **68**.

[25] D. L. Greenaway and E. Meier, unpublished results.

Coupled Lattice Modes in Light Scattering

R. K. Wehner and E. F. Steigmeier

Laboratories RCA Ltd., Zurich, Switzerland

Abstract—The effects of mode coupling in the light-scattering spectra of phonon excitations in solids are discussed. The fluctuations of the dielectric (electronic) susceptibility, giving rise to light scattering, are related to the lattice vibrations and their interactions. A general formulation is presented in terms of the microscopic dynamical theory of interacting phonons. For two modes the equations reduce in a classical approximation to an eight-parameter model. A discussion of the analysis of experimental spectra in terms of this model is given, emphasizing some important points that previously have led to considerable confusion in the literature.

1. Introduction

The phenomenon of mode coupling is of general interest in many areas of solid-state physics. The effects of coupled lattice modes, in particular, are of importance in such areas as, e.g., piezoelectricity, sound attenuation, etc. In most cases, the term lattice mode means a lattice normal vibration, or single-phonon mode, which is characterized by its frequency and displacement eigenvector (polarization). The term mode, however, is not necessarily restricted to this narrow sense. Occasionally, it is convenient to adopt a phenomenological point of view and to consider two-phonon bands and collective phonon excitations, such as thermal fluctuations, as vibrational modes in a more general sense. In any case, the precise specification of a mode must always be given within lattice dynamical theory.

In light-scattering studies, one very frequently observes mode coupling in the spectrum and can study the interactions between the modes, which result in line shifts, interferences, and line-shape anomalies. Very often one is interested in one special mode and its behavior as an uncoupled, free mode, the properties of which are obscured by interactions with other modes. This is the case, for example, near structural phase transitions when a strongly temperature-dependent lattice vibration, or soft mode, crosses a temperature-independent, or hard, mode. Interest can also be directed toward two coupled modes, such as, e.g., the coupling of the soft mode with the mode of temperature fluctuation, where the response of the system, in approaching the transition, changes from the soft mode to the mode of temperature fluctuation. In all these cases it is important to know how to analyze the interactions and to be able to extract information about the individual free modes. This paper presents a review of these problems and gives selected examples for the different cases.

2. Theory of Light Scattering

2.1. Phenomenological Foundation

In a homogeneous loss-free dielectric medium, a plane wave of visible light propagates with a velocity that depends on the dielectric tensor $\epsilon_{\alpha\beta}(\omega)$ taken at the light frequency. Specifying the light wave by a joint index $\rho = (\mathbf{q}r)$ for wave vector $\mathbf{q}$ and polarization type r, we denote its frequency by ω_ρ and its polarization vector by $\mathbf{e}(\rho)$. For given wave number $q \equiv |\mathbf{q}|$ and polarization the dispersion relation

$$\omega_{\mathbf{q},r}{}^2 = \frac{(cq)^2}{\sum_{\alpha\beta} e_\alpha(\rho)\epsilon_{\alpha\beta}e_\beta(\rho)} \qquad [2.1]$$

determines the frequency (c is velocity in vacuum).

In a real crystal, the motion of the atoms gives rise to local time-dependent variations of the dielectric tensor. Their effect on the propagation of light is described here in terms of space- and time-dependent fluctuations of the electronic susceptibility $\chi_{\alpha\beta}(\omega)$

$$\epsilon_{\alpha\beta}(\omega|\mathbf{r},t) = \epsilon_{\alpha\beta}(\omega) + 4\pi\delta\chi_{\alpha\beta}(\omega|\mathbf{r},t). \qquad [2.2]$$

The variations relevant for light scattering are very smooth within lattice-cell dimensions; they must have a range over **r** comparable to the wavelength of the light. The time dependence induced by the atomic vibrations is generally slow compared to the oscillations of the radiation field.

In the presence of fluctuations $\delta\chi$, light will no longer propagate as perfect plane waves. The fluctuations result in changes of direction of propagation and also in slight changes of frequency. Assuming the radiation field to be confined to a narrow spectral range around the frequency ω_i of an incident wave, the energy of the radiation changes by the amount

$$H' = \frac{1}{2}\int d^3r \sum_{\alpha\beta} \delta\chi_{\alpha\beta}(\omega_i|\mathbf{r},t)\, E_\alpha(\mathbf{r})\, E_\beta(\mathbf{r}). \qquad [2.3]$$

Here, $\mathbf{E}(\mathbf{r})$ is the macroscopic electric field related to the propagating light.

The phenomenological concept of the perturbation energy of Eq. [2.3] leads to a detailed quantitative theory of light scattering by two steps. First the fluctuations of the electronic susceptibility and their dynamics must be related to the atomic vibrational modes. Second, from Eq. [2.3], one can derive a general expression for the scattering rate.

2.2 Susceptibility Fluctuations in Crystal Lattices

For a crystal volume V that is large compared to the wavelength of light, it is meaningful to decompose the susceptibility fluctuations into Fourier components (ignoring the dependence on the light frequency)

$$\delta\chi_{\alpha\beta}(\mathbf{r}) = \frac{1}{V}\sum_{\mathbf{q}} \delta\chi_{\alpha\beta}(\mathbf{q})\exp\{i\mathbf{q}\cdot\mathbf{r}\}. \qquad [2.4]$$

Here, the wave vectors **q** are restricted to a very small region around the Brillouin zone center. If all atoms of the crystal are resting at the positions of an ideal lattice, the fluctuations $\delta\chi$ are zero. The motion of the atoms produces the fluctuations through deformations of the electronic charge distribution. This effect is generally small, so that $\delta\chi(\mathbf{q})$ can be represented, following Born and Huang,[1] by a Taylor expansion in terms of atomic displacements. Using the phonon normal coordinates $A(\lambda)$, we write

$$\begin{aligned} \delta\chi_{\alpha\beta}(\mathbf{q}) &= \sum_{j} P_{1,\alpha\beta}(\mathbf{q}j)A(\mathbf{q}j) \\ &+ \frac{1}{2}\sum_{\lambda_1\lambda_2} P_{2,\alpha\beta}(\lambda_1\lambda_2)A(\lambda_1)A(\lambda_2) + \ldots \end{aligned} \qquad [2.5]$$

Here, the phonon index $\lambda = (\mathbf{q}j)$ denotes wave vector and branch. The normal coordinates $A(\lambda)$ differ from the complex normal coordinates $Q(\lambda)$ of Born and Huang[1] by a factor containing the phonon frequency ω_λ

$$Q(\lambda) = \left(\frac{\hbar}{2\omega_\lambda}\right)^{1/2} A(\lambda) \qquad [2.6]$$

By this definition, the matrix elements of $A(\lambda)$ are dimensionless and depend only on the quantum numbers.

The first term in Eq. [2.5] is the most important one in practice; it is related to first-order Raman and Brillouin scattering. For optical phonons the coefficients P_1 (Raman tensors) cannot be related to macroscopic phenomenological quantities, but for acoustic phonons they can be connected with the elasto-optic (or Pockels') coefficients p_{ik}. If in a cubic crystal, for example, the light is polarized in z-direction and λ is the LA phonon in x-direction, then[2]

$$P_{1,zz}(\lambda) = \frac{\epsilon^2}{4\pi}\, p_{12}q \left(\frac{\hbar}{2\omega_\lambda V\rho}\right)^{1/2}. \qquad [2.7]$$

where ρ is mass density. The second-order terms in Eq. [2.5] lead to direct scattering of light by pairs of phonons and by collective phonon excitations. These terms must be summed over the Brillouin zone under the condition that $\mathbf{q}_1 + \mathbf{q}_2 = \mathbf{q}$, i.e., the sum of wave vectors is practically zero. The thermal motion of the atoms leads to a nonvanishing thermal expectation value of $\delta\chi_{\alpha\beta}(\mathbf{q} = 0)$, which in the free-phonon approximation is given by

$$\langle\delta\chi_{\alpha\beta}(\mathbf{q} = 0)\rangle^{(0)} = \frac{1}{2}\sum_{\lambda} P_{2,\alpha\beta}(\lambda\bar{\lambda})[2n_\lambda + 1]. \qquad [2.8]$$

Here, $\bar{\lambda}$ denotes $(-qj)$ and $n_\lambda = [\exp(\hbar\omega_\lambda/kT) - 1]^{-1}$ is the thermal phonon occupation number. The derivative of Eq. [2.8] with respect to temperature, at constant volume, relates the thermo-optic coefficients $(\partial\epsilon_{\alpha\beta}/\partial T)_V$ to a sum over the second-order coefficients with $j_1 = j_2$. For cubic materials this has been discussed in some detail by Wehner and Klein.[2]

The dynamics of the susceptibility fluctuations is governed by the equations of motion of the normal coordinates. In the free-phonon approximation the solutions of these equations represent an ensemble of harmonic oscillators. For the study of linear (e.g., piezoelectric) and nonlinear (anharmonic) interactions we refer to the general dynamical theory of interacting phonons.[3–5] Results are quoted here in terms of the retarded phonon Green function.[6–8] These are solutions of the equations of motion that have the appropriate initial conditions built in and also ensure proper thermal averaging.

2.3 Photon Scattering Rate

The effects of the interaction of Eq. [2.3] are discussed here in terms of scattering of photons. The scattering of an incident photon ρ_i into a different photon mode ρ_s will occur with a transition probability that is related to a partial lifetime $\tau_{\rho_i \to \rho_s}$ of the incident photon. If the material is not absorbing, the lifetime of the incident photon is exclusively an effect due to the scattering processes

$$\frac{1}{\tau_{\rho_i}} = \sum_{\rho_s} \frac{1}{\tau_{\rho_i \to \rho_s}}. \qquad [2.9]$$

The theoretical result for the transition probability can be expressed by the spectral density function of the susceptibility fluctuations[2] ($\bar{\rho}_i = -\mathbf{q}_i r_i$)

$$\frac{1}{\tau_{\rho_i \to \rho_s}} = J_\omega(\delta\chi_{\bar{\rho}_i\rho_s} | \delta\chi_{\rho_i\bar{\rho}_s}). \qquad [2.10]$$

Here, $\omega \equiv \omega_i - \omega_s \gtrless 0$ denotes the transfer of energy to the crystal. The operator $\delta\chi_{\bar{\rho}_i\rho_s}$ is related to the susceptibility fluctuations of Eq. [2.5] by

$$\delta\chi_{\bar{\rho}_i\rho_s} = 2\pi \frac{\omega_i^3}{c^2 q_i q_s} \sum_{\alpha\beta} e_\alpha(\bar{\rho}_i) e_\beta(\rho_s) \delta\chi_{\alpha\beta}(\mathbf{q}) \qquad [2.11]$$

Here, $\mathbf{q} = \mathbf{q}_i - \mathbf{q}_s$ denotes the momentum transfer in the scattering process ($\mathbf{q}_i$ and $\mathbf{q}_s$ relate to the photons in the dielectric). The spectral density function in Eq. [2.10] is generally defined for two operators A and B as the Fourier transform of the correlation function

$$J_\omega(A|B) \equiv \int_{-\infty}^{\infty} dt\, e^{i\omega t} \langle A(t)B(0)\rangle; \qquad [2.12]$$

it is linear in both A and B.

Eq. [2.10] is evaluated by inserting the expansion Eq. [2.5] and by calculating the phonon spectral density functions $J_\omega(A(\lambda)|A(\lambda'))$, $J_\omega(A(\lambda)|A(\lambda_1)A(\lambda_2))$, etc.

3. Spectra of Coupled Modes

The relations introduced in the foregoing sections define a general frame for detailed quantitative calculations of first- and second-order spectra on the basis of lattice dynamical models, e.g., anharmonic shell models.[9,10] Here, we are putting emphasis on the effects of mode coupling; we therefore consider the second-order coupling P_2 to a two-phonon band or to a collective phonon excitation only insofar as it can phenomenologically be described by an effective first-order coupling to a single mode in a wider sense.

An appealing representation[11] of the effect of coupled modes is given in Fig. 1, which shows the Raman spectra of ferro- and paraelectric SbSI for $T \to T_c^-$ and $T \to T_c^+$. The soft ferroelectric mode is clearly seen to undergo a mode coupling[12] with a hard mode at about 30 cm^{-1} at $T_c - T \approx 22°$. A second mode coupling is effective as the soft ferroelectric mode further approaches zero frequency; at $T_c - T \lesssim 10°$ it interferes with the upcoming mode of phonon density fluctuations[13] (central mode), which is manifested by the broad background line of increasing intensity on which the soft mode rides. Both of these mode couplings have been successfully analyzed[12,14] in terms of coupled modes.

3.1 The General Spectrum of Two Modes

Restricting the discussion to two modes, we simplify Eq. [2.5] to the form

$$\delta\chi = P_1 A_1 + P_2 A_2, \qquad [3.1]$$

where now the subscripts denote the modes, $A_i \equiv A(\mathbf{q}j_i)$, $P_i \equiv P(\mathbf{q}j_i)$ real. Expressing the spectral density function of Eq. [2.10] by the retarded Green function, G_ω, the spectrum is conveniently written

$$J(\omega) = 2[n(\omega) + 1]\,\mathrm{Im}\,G_\omega(\delta\chi|\delta\chi), \qquad [3.2a]$$

$$= 2[n(\omega) + 1]\,\mathrm{Im}\sum_{i,k} P_i P_k G_{ik}(\omega), \qquad [3.2b]$$

where $n(\omega) \equiv [\exp(\hbar\omega/kT) - 1]^{-1}$ denotes the Bose–Einstein function and $G_{ik}(\omega) \equiv G_\omega(A_i|A_k)$. Eqs. [3.2] hold for Stokes ($\omega > 0$) and anti-Stokes ($\omega < 0$) scattering since $n(-\omega) + 1 = -n(\omega)$ and $\mathrm{Im}G(-\omega) = -\mathrm{Im}G(\omega)$, a fact which frequently is not recognized in the literature.

In the approximation of free undamped modes with frequencies ω_i we have

$$G_{ik}^{(0)}(\omega) = G_i^{(0)}(\omega)\delta_{ik}, \qquad [3.3a]$$

$$G_i^{(0)}(\omega) = \frac{2\omega_i}{\omega_i^2 - (\omega + i\epsilon)^2}, \qquad [3.3b]$$

and the spectrum simply consists of sharp Stokes and anti-Stokes lines

$$J^{(0)}(\omega) = 2\pi \sum_i P_i^2 \{(n_i + 1)\,\delta(\omega - \omega_i) + n_i\delta(\omega + \omega_i)\}. \qquad [3.4]$$

Here,

$$n_i \equiv n(\omega_i).$$

In general, the spectrum exhibits complicated line shapes that arise microscopically from anharmonic phonon–phonon interactions. We do not discuss these in detail but introduce a few concepts and approximations commonly used in dealing with interacting modes.

Within the general dynamical theory of anharmonic lattices one obtains from the equations of motion of the phonon normal coordinates $A(\lambda)$ the Dyson (matrix) equation for the retarded phonon Green functions

$$G_{ik} = G_{ik}^{(0)} - \sum_{l,m} G_{il}^{(0)}\Pi_{lm}G_{mk}. \qquad [3.5]$$

Here, the so-called self-energy matrix Π contains elements that are complex functions of frequency

$$\Pi_{ik}(\omega) = \Delta_{ik}(\omega) - i\Gamma_{ik}(\omega); \qquad [3.6]$$

they represent the effects of interactions.

In the case of two modes the solution of Eqs. [3.5] can be given by simple expressions. Separating the self-energy matrix first into the diagonal and non-diagonal parts, $\Pi_{ik} = \Pi_{ii}\delta_{ik} + \Pi_{ik}^{nd}$, one finds

$$G_{ik} = G_{ik}^{(1)} - \sum_{l \neq m} G_{il}^{(1)} \Pi_{lm} G_{mk}, \qquad [3.7]$$

where $G_{ik}^{(1)} = G_i^{(1)}\,\delta_{ik}$ is the solution of the Dyson equation containing only the diagonal part of the self-energy

$$G_i^{(1)} = G_i^{(0)} - G_i^{(0)}\Pi_{ii}G_i^{(1)}, \qquad [3.8a]$$

$$= \frac{2\omega_i}{\omega_i^2 - \omega^2 + 2\omega_i\Pi_{ii}}. \qquad [3.8b]$$

This solution in two steps holds for any number of modes. The explicit solution for two modes is given by[7] ($ik = 12$ or 21)

$$G_{ii} = \frac{2\omega_i}{\omega_i^2 - \omega^2 + 2\omega_i\,[\Pi_{ii} - \Pi_{ik}G_{kk}^{(1)}\Pi_{ki}]}, \qquad [3.9]$$

$$G_{ik} = -G_{ii}^{(1)}\Pi_{ik}G_{kk} = -G_{ii}\Pi_{ik}G_{kk}^{(1)}. \qquad [3.10]$$

For the analysis[13] of experimental spectra, a simple parametrization of the self-energy is sometimes sufficient, which we discuss in the following.

3.2 Renormalization of Individual Modes

Neglecting the off-diagonal elements of Π_{ik}, we arrive in a first step at the individual mode Green functions

$$G_i^{(1)}(\omega) = \frac{2\omega_i}{\omega_i^2 - \omega^2 + 2\omega_i[\Delta_{ii}(\omega) - i\Gamma_{ii}(\omega)]} \qquad [3.11]$$

Here, the diagonal elements of the self-energy can be seen to renormalize the individual mode resulting in a frequency shift of approximately $\Delta_{ii}(\omega_i)$, and allowing for a general line shape with a half-width of approximately $\Gamma_i \equiv \Gamma_{ii}(\omega_i)$. In order to avoid unnecessary discussions of frequency shifts we assume that the frequencies ω_i have been chosen self-consistently so that $\Delta(\omega_i) = 0$.

Classical oscillators with "viscous" damping are introduced by inserting in Eq. [3.11]

$$\Delta_{ii}(\omega) = \Delta_{ii}(\omega_i) = 0, \qquad \Gamma_{ii}(\omega) = \frac{\omega}{\omega_i}\gamma_i, \qquad [3.12]$$

so that

$$G_i^{(1)}(\omega) = \frac{2\omega_i}{\omega_i^2 - \omega^2 - i2\omega\gamma_i}. \qquad [3.13]$$

In this individual-mode approximation, the spectrum (Eqs. [3.2]) consists of superimposed Lorentzians.

Overdamped modes, $\gamma_i \gg \omega_i$, play an important role in treating relaxation processes. Introducing the relaxation time $\tau_i = 2\gamma_i/\omega_i^2$ and neglecting the term ω^2 in the denominator of Eq. [3.11] one arrives at the relaxation Green function

$$G_i^{(1)}(\omega) = G_i^{(0)}(0)\frac{1}{1 - i\omega\tau_i}. \qquad [3\cdot14]$$

This relaxation approximation[15] is used in many discussions of central modes.

If, in the case of two modes, one is dominant over the other or plays a particular role, we may use Eqs. [3.9] and [3.10] to write the symmetric form of the spectrum Eq. [3.2b] in asymmetric ways[2]

$$J(\omega) = 2[n(\omega) + 1] \text{ Im } \{\tilde{P}_1^2(\omega)G_{11}(\omega) + P_2^2 G_{22}^{(1)}(\omega)\}. \qquad [3.15]$$

Here, the mode numbers 1 and 2 may be interchanged; it is assumed that $\Pi_{12} = \Pi_{21}$. The second term on the right-hand side represents the mode 2 as individual uncoupled mode, whereas the first term can be considered as the individual mode 1 renormalized by the coupling. Not only does G_{11} differ from $G_{11}^{(1)}$ by an additional term in the denominator (Eq. [3.9]), but also the coupling to the light appears renormalized insofar as

$$\tilde{P}_1(\omega) = P_1 - P_2 G_{22}^{(1)}(\omega)\Pi_{21}(\omega) \qquad [3.16]$$

Subdivisions of the spectrum into two parts as in Eq. [3.15] can be helpful for interpretations.[2]

3.3 Integrated Intensity and Susceptibility

The total intensity I scattered into the same direction is obtained by integrating Eq. [2.10] over ω, at constant direction $\hat{\mathbf{q}}_s \equiv \mathbf{q}_s/q_s$,

$$I \equiv \frac{1}{2\pi}\int_{-\infty}^{\infty} d\omega\, J_\omega(\delta\chi|\delta\chi), \qquad [3.17a]$$

$$= \langle\delta\chi\delta\chi\rangle. \qquad [3.17b]$$

The factor $1/2\pi$ arises from $\tau_{\rho_i \to \rho_s}$ in Eq. [2.10] being an inverse circular frequency. For J_ω given by Eqs. [3.2] this integral is easily evaluated in the classical limit, $kT \gg \hbar\omega$, by applying a Kramers–Kronig relation

$$I = \frac{kT}{\hbar} G_{\omega=0}(\delta\chi | \delta\chi), \qquad [3.18a]$$

$$= \frac{kT}{\hbar} \sum_{i,k} P_i P_k G_{ik}(\omega = 0). \qquad [3.18b]$$

Here, the Green functions G at zero frequency have the physical meaning of static isothermal response coefficients. In the literature[16–21] the quantities in Eqs. [3.18] and [3.2] have often been referred to rather loosely as 'susceptibilities' and sometimes they have been related in a confusing way to the *dielectric* susceptibility. The relation between these distinct quantities shall be clarified in the following.

If the ionic contributions to the dielectric susceptibility dominate over the electronic ones, we obtain the dielectric susceptibility from an expansion of the crystal dipole moment in terms of the phonon normal coordinates,[1]

$$M = \sum_i M_i A_i. \qquad [3.19]$$

The coefficients M_i have the physical meaning of electric charges. The dynamic dielectric susceptibility is then given by a form[7] analogous to the scattered intensity

$$\chi(\omega) = \frac{1}{V\hbar} G_\omega(M|M) \qquad [3.20a]$$

$$= \frac{1}{V\hbar} \sum_{i,k} M_i M_k G_{ik}(\omega). \qquad [3.20b]$$

The static isothermal susceptibility χ_T must be calculated from Eqs. [3.20] in the limit $\omega \to 0$ ($\mathbf{q}$ = const.). It may be combined with Eq. [3.18b], to give

$$\frac{I}{V} = kT\chi_T \frac{\sum_{i,k} P_i P_k G_{ik}(0)}{\sum_{i,k} M_i M_k G_{ik}(0)}. \qquad [3.21]$$

This relation between I and $kT\chi_T$ must be considered rather artificial if no simple proportionality between P_i and M_i happens to exist (in which case the phonon response coefficients $G_{ik}(0)$ would drop out). Such a circumstance cannot be expected a priori since the coefficients M_i have the physical meaning of ionic charges, whereas the P_i's have the meaning of changes of electronic susceptibility per atomic displacement.

For a single mode that is infrared active as well as Raman active, we have

$$\frac{I}{V} = kT\chi_T \frac{P_1^2}{M_1^2}, \qquad [3.22]$$

where the ratio P_1/M_1 represents an electro-optic coefficient. Even in this simple and also in more extended[22] model cases one must question whether these coefficients can be assumed as temperature-independent constants, particularly for soft modes. An obvious example where this is not the case is demonstrated in Fig. 1, where in the ferroelectric phase of SbSI[11] P_{soft} goes to zero for $T \rightarrow T_c^-$, while M_{soft} stays finite. Thus the proportionality of I to $kT\chi_T$ is certainly violated in this case. In concluding this section it should be emphasized, therefore, that the use of a relation $I \propto kT\chi_T$ is senseless, particularly in the case for coupled modes, if the coefficients P_i and M_i are not sufficiently well known.

3.4 Interferences and Line Shape Anomalies

The coupling of two modes produces a twofold possibility for the excitation of everyone of the modes. This can be seen immediately for mode 2 from Eqs. [3.15] and [3.9]. Mode 2 is excited by direct scattering through P_2^2 and, in an indirect way, through P_1^2 making use of the coupling Π_{12} in G_{11}. The excitation of a mode by two different interaction mechanisms generally raises the question of interferences, which in fact are contained in Eq. [3.15]. This problem is elucidated in the following for the case of weak coupling.

Iterating Eq. [3.7] twice we obtain

$$G_{11} = G_1^{(1)} + G_1^{(1)}\Pi_{12}G_2^{(1)}\Pi_{21}G_1^{(1)}. \qquad [3.23]$$

Inserting this into Eq. [3.15] and retaining only terms of order Π^2 we arrive, in the weak coupling limit, at ($\Pi_{12} = \Pi_{21}$)

$$\begin{aligned} J(\omega) = {} & 2[n(\omega) + 1]\,\mathrm{Im}\{P_1^2 G_1^{(1)}(\omega) \\ & + [P_2 - P_1 G_1^{(1)}(\omega)\Pi_{12}(\omega)]^2 G_2^{(1)}(\omega) \\ & + P_2^2[G_2^{(1)}(\omega)\Pi_{21}(\omega)]^2 G_1^{(1)}(\omega) + O(\Pi^3)\}. \end{aligned} \qquad [3.24]$$

This expression is symmetric in both modes. The second term on the right-hand side is of a typical form containing interference effects; they appear here in the form of a frequency-dependent coupling of the mode 2 to the light, which leads to line-shape anomalies. If $G_2^{(1)}(\omega)$ represents a broad band forming a background to mode 1, then mode 1 will induce an antiresonance. Examples for this are seen in Fig. 2 for the case of BaTiO$_3$.[23] The interference is found to depend considerably on the photon and phonon polarization. This type of anomaly is often named after Fano[24] who studied an analogous situation in the context of electronic transitions. The system investigated by Fano is in no way more fundamental than phonon systems.

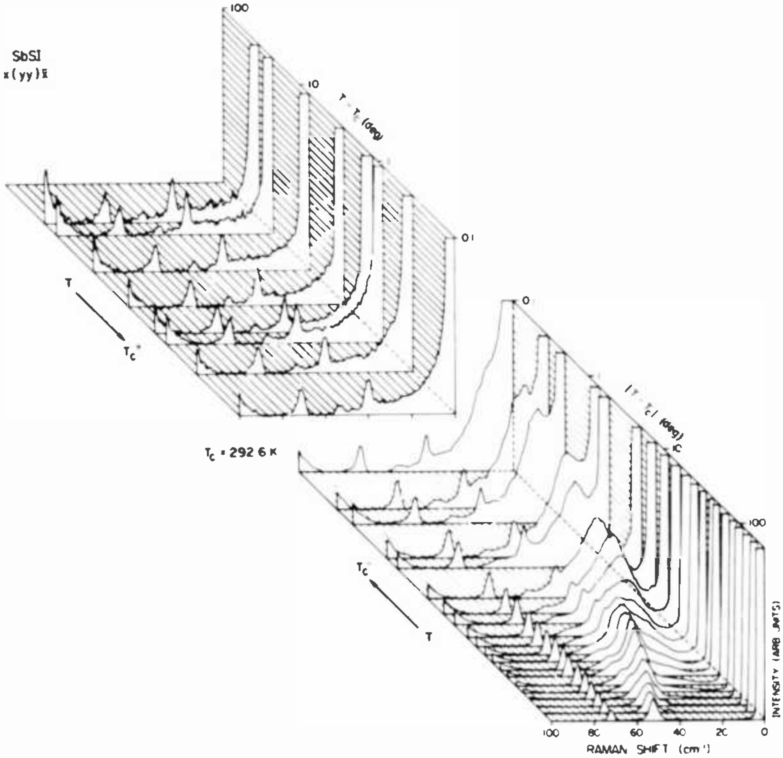

Fig. 1—Raman spectra of SbSI for the ferroelectric ($T < T_c$) and paraelectric phase ($T > T_c$) showing the modes of A_1 and A_1^+ symmetries, respectively. (According to Ref. (11); Note the difference of scale of the two figures in Ref. (11), as seen from the intensity of the reference line.)

In the past, it has rarely been recognized that the essential features of the interference of a discrete transition with a continuous band had been treated for phonon systems by Szigeti[25] before Fano's work. Szigeti's expression for the two-phonon bands in infrared absorption corresponds to the second term in Eq. [3.24].

If mode 1 is dominating, $P_2 \ll P_1$, we can omit the third term. The spectrum can then be considered as a superposition of the individual modes 1 and 2, where mode 2 is affected by the interferences; under certain circumstances the latter may result in an extinction of the second mode.[2]

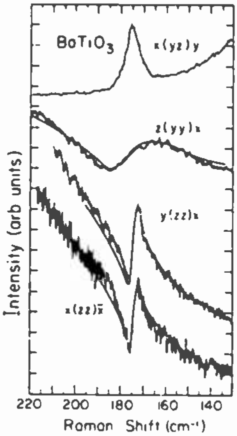

Fig. 2—Raman spectra of ferroelectric $BaTiO_3$ for different configurations showing antiresonances (according to Rosseau and Porto[23]).

4. The Eight-Parameter Model

4.1 Two Classical Oscillators with Linear Coupling

Experimentally observed spectra of coupled modes are mostly analyzed in terms of classical oscillators that are linearly coupled. For the individual oscillators with velocity-dependent damping, the Green functions are given by Eq. [3.13]. The coupling of two or several oscillators by the self-energy matrix Π in the Dyson Eq [3.5] is formally a linear coupling; this is independent of the question whether the self-energy matrix elements Eq. [3.6] arise microscopically from harmonic or anharmonic interactions.

Simple forms of linear coupling between two oscillators can be included into the self-energy either by an effective 'force constant' Δ_{12}, corresponding to an elastic interaction force, or by a 'viscous' damping constant γ_{12} accounting for a velocity-dependent dissipation of energy through the coupling mechanism. These quantities can be taken to set up a parametrized form of self-energy

$$\Pi = \begin{pmatrix} -i\dfrac{\omega}{\omega_1}\gamma_1 & \Delta_{12} - i\dfrac{\omega}{\sqrt{\omega_1\omega_2}}\gamma_{12} \\ \Delta_{12} - i\dfrac{\omega}{\sqrt{\omega_1\omega_2}}\gamma_{12} & -i\dfrac{\omega}{\omega_2}\gamma_2 \end{pmatrix} \qquad [4.1]$$

The four parameters ω_1, ω_2, P_1, and P_2, introduced earlier and the four parameters entering here, γ_1, γ_2, Δ_{12}, and γ_{12} define an eight parameter model of two coupled classical oscillators.

Here, we do not discuss the calculation of the self-energy from the microscopic lattice potential in terms of phonon–phonon interactions; for that purpose the notation used up to now is very convenient. Therefore, we switch over to a more classical notation but retain the parameters characterizing the phonons. This enables easier comparison with other work based on purely phenomenological views.[26] Defining

$$g_{ik}(\omega) \equiv (4\omega_i\omega_k)^{-1/2}G_{ik}(\omega), \qquad [4.2]$$

$$\pi_{ik}(\omega) \equiv (4\omega_i\omega_k)^{1/2}\Pi_{ik}(\omega), \qquad [4.3]$$

and

$$p_i \equiv \left(\frac{\hbar}{2\omega_i}\right)^{-1/2} P_i, \qquad [4.4]$$

we are led to

$$J(\omega) = 2\hbar[n(\omega) + 1] \sum_{i,k} p_i p_k \operatorname{Im} g_{ik}(\omega), \qquad [4.5]$$

where

$$g_{ii} = \frac{1}{\omega_i^2 - \omega^2 + \pi_{ii} - \pi_{ik} g_k^{(1)} \pi_{ki}}, \qquad (i \neq k) \qquad [4.6]$$

$$g_{ik} = -g_i^{(1)}\pi_{ik}g_{kk} = -g_{kk}\pi_{ki}g_i^{(1)}, \qquad (i \neq k) \qquad [4.7]$$

$$g_i^{(1)} = \frac{1}{\omega_i^2 - \omega^2 + \pi_{ii}}, \qquad [4.8]$$

and

$$\pi_{ik} = \begin{pmatrix} -i2\omega\gamma_i & 2\sqrt{\omega_i\omega_k}\,\Delta_{ik} - i2\omega\gamma_{ik} \\ 2\sqrt{\omega_i\omega_k}\,\Delta_{ik} - i2\omega\gamma_{ik} & -i2\omega\gamma_{ik} \end{pmatrix}. \qquad [4.9]$$

The equations of motion now have the form

$$\sum_l \{D_{il}(\omega) - \omega^2\delta_{il}\} g_{lk}(\omega) = \delta_{ik}, \qquad [4.10]$$

where the (non-hermitian) matrix

$$D_{ik}(\omega) = \omega_i^2\delta_{ik} + \pi_{ik}(\omega) \qquad [4.11]$$

is a generalization of the dynamical matrix as known in lattice dynamics.[1]

The resonances of the spectrum are obtained from the eigenvalues of the matrix D of Eq. [4.11]. For vanishing damping we have[12]

$$\omega_\pm^2 = \frac{1}{2}\{\omega_1^2 + \omega_2^2 \pm \sqrt{(\omega_1^2 - \omega_2^2)^2 + 16\omega_1\omega_2\Delta_{12}^2}\}. \qquad [4.12]$$

In general the eigenvalues of the matrix D are complex.

4.2 Indeterminacy of the Eight-Parameter Model

In analyzing an experimental spectrum in terms of the eight-parameter model, Eqs. [4.5] to [4.9], one must recognize that the model contains one parameter more than can be determined uniquely from the spectrum. This is evident, in the infinite-lifetime approximation, from Eq. [4.12]; for two experimental frequencies ω_+ and ω_- there is no unique set of parameters ω_1, ω_2, and Δ_{12}. This indeterminacy is due to the arbitrariness in subdividing the total energy of the system into a free-mode energy and an interaction energy. In other words, this reflects the freedom in defining the noninteracting modes.

Barker and Hopfield[26] have discussed the fact that the coordinates of a pair of coupled classical oscillators can be transformed by a 2 × 2 rotation leaving the spectrum unchanged. The classical coordinates corresponding to the phonon normal coordinates A_i are given by (Eq. [2.6])

$$Q_i = \left(\frac{\hbar}{2\omega_i}\right)^{1/2} A_i. \qquad [4.13]$$

In terms of these classical coordinates, we have

$$\delta\chi = p_1Q_1 + p_2Q_2 \qquad [4.14]$$

and

$$g_{ik}(\omega) = \frac{i}{\hbar}\int_0^\infty dte^{i\omega t}\langle[Q_i(t), Q_k(0)]\rangle \qquad [4.15]$$

Under a orthogonal transformation

$$T = \begin{pmatrix} \cos\varphi & \sin\varphi \\ -\sin\varphi & \cos\varphi \end{pmatrix} \qquad [4.16]$$

of the coordinates, leaving $\delta\chi$ and J (Eq. [4.5]) invariant, we have

$$Q_i = \sum_l T_{il} Q_l', \qquad [4.17]$$

$$p_i = \sum_l T_{il} p_l', \qquad [4.18]$$

and, in matrix notation,

$$T^{-1}DT = D'. \qquad [4.19]$$

Obviously, it is always possible to find values of the angle φ so that either Δ_{12}' or γ_{12}' is transformed to zero. That means that for a given spectrum of two coupled classical oscillators, the model parameters can always be chosen so that the coupling is either real or imaginary.

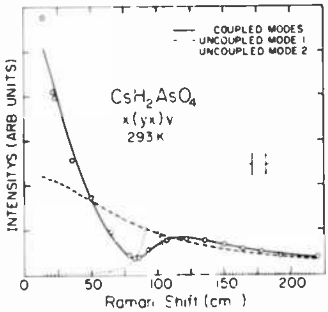

Fig. 3—Raman spectra of CsH_2AsO_4. The dashed curves correspond to the choice $\gamma_{12} = 0$. The full curve is the fitted coupled-mode intensity (according to Katiyar et al[16]).

The ambiguity of the model parameters is elucidated, e.g., by the analysis by Katiyar et al[16] of the Raman spectrum of CsH_2AsO_4 shown in Fig. 3. These authors explicitly give the two equivalent parameter sets for either $\gamma_{12} = 0$ or $p_1 = 0$, which produce the measured spectrum given by the experimental points. Mode 1 is here considered to be the tunneling-proton mode. The dashed curves give the individual modes obtained from the set $\gamma_{12} = 0$. This choice of purely real coupling is preferred by the authors since they find that it produces a simple temperature dependence for some of the parameters in analyzing spectra of different temperatures. Other authors[16,19,21] widely follow this simple argument for choosing a meaningful set out of an infinite number of possible sets. It is felt, however, that this does not represent a sufficient physical justification. It seems that additional physical arguments are badly needed to resolve the problem, as presented, e.g., by Peercy[27] for KH_2PO_4 and RbH_2PO_4.

From the second parameter set, $p_1 = 0$, considered by Katiyar et al for CsH_2AsO_4 one cannot draw conclusions about Kobayashi's model,[28] which implies $M_{z,1} = 0$. It follows from our arguments in Sect. 3.3 that the latter condition cannot be related to the condition $P_{xy,1} = 0$ for the Raman spectrum without specifying further assumptions.

It is obvious that a model with three or more oscillators, as studied, e.g., by Lagakos and Cummins[20] for KH_2PO_4, represents an even larger ambiguity, and the *ad hoc* assumptions required in such an analysis can at best be considered as a working hypothesis. In order to determine a coupled-mode system completely, it is necessary to have a priori more information than the light-scattering spectrum.

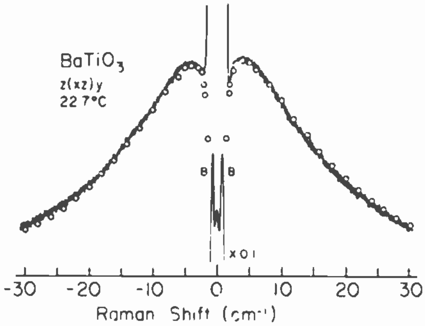

Fig. 4—Raman spectrum of $BaTiO_3$. The curves show the experimental data; they are reduced by a factor 10 in the inset, which gives the Brillouin peaks. The circles represent the coupled-mode fit for the coupling of the light to the soft mode only and not to the acoustic mode (according to Fleury and Lazay[30]).

Successful attempts to find additional physical arguments to choose a set of parameters for two coupled modes were made by several authors.[14,22,29,30] The additional information mostly results from using temperatures for which the mode coupling is no longer appreciable or from using different polarisations where one of the mode is not effective.

An example of this is shown in Fig. 4 for $BaTiO_3$.[30] The mode coupling is here between a strongly damped soft ferroelectric mode and an acoustic mode, and the coupling is of the piezoelectric kind. Again a strong line-shape anomaly with an antiresonance is observed as described above. It is found that the light coupling is to the soft mode only ($p_{\text{opt.}} \neq 0$) and not to the acoustic mode ($p_{\text{ac}} = 0$). The circles in Fig. 4 represent the coupled-mode fit resulting for this.

It is nice to find that the inverse case to $BaTiO_3$ occurs in KH_2PO_4,[29] where it is found that the light couples solely to the acoustic mode (i.e., $p_{\text{ac}} \neq 0$ and $p_{\text{opt}} = 0$).

An interesting case is SbSI[14] (see Fig. 1), where one of the mode couplings (as mentioned in Sect. 3.1) is between the ferroelectric soft mode and the mode of phonon density fluctuations (or central mode). It is found in SbSI that the two modes are both present in the ferroelectric phase and both absent in the paraelectric phase (where the central mode would be permitted but the soft mode prohibited by symmetry). From this it is concluded, and used for the analysis, that the light coupling in SbSI is to the soft mode only ($p_{\text{soft}} \neq 0$) and only indirectly to the central mode ($p_{\text{central}} = 0$).

5. Conclusions

Discussing coupled modes in light-scattering spectra, we have put emphasis on demonstrating how the phenomenological model of two coupled classical oscillators emerges from the microscopic dynamical theory. The two-oscillator spectrum involves eight parameters, which renders flexibility and richness to this model. Unfortunately, these eight parameters cannot be determined uniquely from the spectrum, a point to which the literature has not always paid sufficient attention. For each spectrum an infinity of eight-parameter sets, i.e., special models, exist. Future work should concentrate on removing this ambiguity by using additional experimental information or microscopic models.

To relate the dielectric susceptibility to the light-scattering spectra one must clarify the relations between the expansion coefficients M_i and P_i (Raman tensor) of the dipole moment and electronic susceptibility, respectively, on the basis of detailed models or on grounds of microscopic theory. Much work in the literature is based on hidden assumptions that sometimes are questionable. Further progress can be expected using anharmonic shell models, which enable a unified treatment of the ionic susceptibility and of the fluctuations of the electronic susceptibility.

References

[1] M. Born and K. Huang, *Dynamical Theory of Crystal Lattices*, Oxford University Press, London, (1954).

[2] R. K. Wehner and R. Klein, "Scattering of Light by Entropy Fluctuations in Dielectric Crystals," *Physica*, **62**, p. 161 (1972).

[3] W. Ludwig, "Recent Developments in Lattice Theory," *Springer Tracts in modern Physics*, **43**, Berlin-Heidelberg-New York (1967).

[4] R. A. Cowley, "Anharmonic Crystals," *Reports on Progress in Physics*, **XXXI**, p. 123 (1968).

[5] W. Götze, "Phonons in Bravais Lattices," *Phys. Rev.*, **156**, p. 951 (1967).

[6] A. A. Maradudin and A. E. Fein, "Scattering of Neutrons by an Anharmonic Crystal," *Phys. Rev.*, **128**, p. 2589 (1962).

[7] R. K. Wehner, "On the Infra-Red Absorption of Crystals Due to Lattice Vibrations," *Phys. Stat. Sol.*, **15**, p. 725 (1966).

[8] R. K. Wehner, "Phonon Green Functions by Functional Methods," *Phys. Stat. Sol.*, **22**, p. 527 (1967).

[9] A. D. Bruce and R. A. Cowley, "The Two-Phonon Raman Spectra of Alkali Halide Crystals," *J. Phys. C (GB)*, **5**, p. 595 (1972).

[10] M. Buchanan, H. Bilz, and R. Haberkorn, "Second-Order Raman Effect in Alkaline Earth Oxides," *J. Phys. C (GB)*, 7, p. 439 (1974).

[11] E. F. Steigmeier, "Light Scattering near Structural Phase Transitions," *Ferroelectrics*, **7**, p. 65 (1974).

[12] G. Harbeke, E. F. Steigmeier, and R. K. Wehner, "Soft Phonon Mode and Mode Coupling in SbSI," *Sol. State Comm.*, **8**, p. 1765 (1970); ibid. **9**, p. 174 (1971).

[13] E. F. Steigmeier, G. Harbeke, and R. K. Wehner, "Soft-Mode Coupling and Critical Rayleigh Scattering in Ferroelectric SbSI," in *Light Scattering in Solids*, ed. by M. Balkanski (Flammarion, Paris, 1971) p. 396.

[14] E. F. Steigmeier, H. Auderset, and G. Harbeke, "The Central Peak in SbSI," *Phys. Stat. Sol.*, to be published.

[15] See, e.g., R. A. Cowley, G. J. Coombs, R. S. Katiyar, J. F. Ryan, and J. F. Scott, "Dielectric Response in Piezoelectric Crystals," *J. Phys. C (GB)*, **4**, p. L203 (1971); R. Klein, "Theory of Rayleigh and Brillouin Scattering near the Phase Transition," *J. Phys. (Paris)*, **33**, p. C2-11 (1972); or S. M. Shapiro, J. D. Axe, G. Shirane, and T. Riste, "Critical Neutron Scattering in $SrTiO_3$ and $KMnF_3$," *Phys. Rev. B*, **6**, p. 4332 (1972).

[16] R. S. Katiyar, J. F. Ryan, and J. F. Scott, "Proton-Phonon Coupling in CsH_2AsO_4 and KH_2AsO_4," in *Light Scattering in Solids*, ed. by M. Balkanski (Flammarion, Paris, 1971) p. 436, and *Phys. Rev. B*, **4**, p. 2635 (1971).

[17] C. Y. She, T. W. Broberg, L. S. Wall, and D. F. Edwards, "Effect of Proton-Phonon Coupling on the Ferroelectric Mode in KH_2PO_4," *Phys. Rev. B*, **6**, p. 1847 (1972).

[18] J. F. Scott, "Soft-Mode Spectroscopy: Experimental Studies of Structural Phase Transitions," *Rev. Mod. Phys.*, **46**, p. 83 (1974).

[19] R. P. Lowndes, N. D. Tornberg and R. C. Lenng, "Ferroelectric Mode and Molecular Structure in the Hydrogen-Bonded Ferroelectric Arsenates and Their Deuterated Isomorphs," *Phys. Rev. B*, **10**, p. 911 (1974).

[20] N. Lagakos and H. Z. Cummins, "Preliminary Observation of a Central Peak in KH_2PO_4," *Phys. Rev. B*, **10**, p. 1063 (1974).

[21] P. S. Peercy and G. A. Samara, "Pressure and Temperature Dependences of the Dielectric Properties and Raman Spectra of RbH_2PO_4," *Phys. Rev. B*, **8**, p. 2033 (1973).

[22] R. L. Reese, I. J. Fritz and H. Z. Cummins, "Light-Scattering Studies on the Soft Ferroelectric and Acoustic Modes of KO_2PO_4," *Phys. Rev. B*, 7, p. 4165 (1973).

[23] D. L. Rousseau and S. P. S. Porto, "Auger-like Resonant Interference in Raman Scattering From One- and Two-Phonon States of $BaTiO_3$," *Phys. Rev. Lett.*, **20**, p. 1354 (1968).

[24] U. Fano, "Effects of Configuration Interaction on Intensities and Phase Shifts," *Phys. Rev.*, **124**, p. 1866 (1961).

[25] B. Szigeti, "The Infra-Red Spectra of Crystals," *Proc. Roy. Soc. A*, **258**, p. 377 (1960).

[26] A. S. Barker and J. J. Hopfield, "Coupled-Optical-Phonon-Mode Theory of the Infrared Dispersion in $BaTiO_3$, $SrTiO_3$, and $KTaO_3$," *Phys. Rev.*, **135**, p. A1732 (1964).

[27] P. S. Peercy, "Evaluation of the Coupled Proton-Optic-Mode Model for KH_2PO_4 and RbH_2PO_4," *Phys. Rev.*, **9**, p. 4868 (1974).

[28] K. K. Kobayashi, "Dynamic Theory of the Phase Transition in KH_2PO_4-Type Crystals," *J. Phys. Soc. Japan*, **24**, p. 497 (1968).

[29] E. M. Brody and H. Z. Cummins, "Brillouin-Scattering Study of the Ferroelectric Transition in KH_2PO_4," *Phys. Rev. Letters*, **21**, p. 1263 (1968).

[30] P. A. Fleury and P. D. Lazay, "Acoustic-Soft-Optic Mode Interactions in Ferroelectric $BaTiO_3$," *Phys. Rev. Lett.*, **26**, p. 1331 (1971).

Some Recent Developments in Brillouin Scattering

J. R. Sandercock

Laboratories RCA Ltd., Zurich, Switzerland

Abstract—A very-high-contrast interferometer has been developed that extends the scope of Brillouin scattering to cases where the very large amount of elastically scattered light would otherwise have made measurement impossible. Some aspects of the construction of the instrument are discussed. The wealth of information that can be obtained on elastic properties is illustrated with measurements on some layer compounds, opaque materials, liquid crystals, and materials undergoing structural phase transitions. It is shown that measurements are now possible on spin waves in magnetic materials. This is illustrated with reference to measurements on YIG and $CrBr_3$.

1. Introduction

Although Brillouin scattering is a long-established phenomenon, it required the high spectral purity of the laser to reduce it to practical usefulness. Brillouin scattering is the result of an interaction in a material between sound waves and light. An acousto-optic modulator is nothing other than a practical demonstration of Brillouin scattering. In very simple terms the interaction can be understood with reference to Fig. 1. A longitudinal sound wave propagating through a material has associated with it regions of compression and rarefaction. Since these density changes produce corresponding variations in the refractive index, the sound wave may be thought of as a three-dimensional phase grating moving with the velocity of sound through the medium. Incident light may be Bragg reflected from this phase grating, provided that the normal Bragg condition is satisfied;

$$\lambda_1 = 2\Lambda \sin\frac{\varphi}{2}. \qquad [1]$$

Here, λ_1 and Λ are, respectively, the wavelengths of the light and the sound, and the scattering angle φ is defined in Fig. 1. However, since the grating is moving with the velocity of sound v, the scattered light experiences a Doppler frequency shift $\Delta\omega$ given by

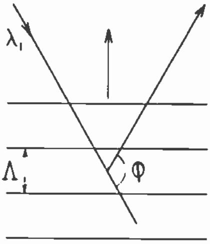

Fig. 1—Bragg scattering of light of wavelength λ_1 through an angle φ by a sound wave of wavelength Λ.

$$\Delta\omega = \pm\frac{v}{c}\frac{\lambda_1}{\Lambda}\omega_1 \qquad [2]$$

where ω_1 is the frequency of the incident light and c the velocity of light.

Quantum mechanically, Brillouin scattering describes an event in which an incident photon with wave vector $\mathbf{k}_1$ and frequency ω_1 is scattered into a state with wave vector $\mathbf{k}_2$ and frequency ω_2 by emission or absorption of a phonon with wave vector $\mathbf{K}$ and frequency Ω. The requirements of conservation of momentum and energy,

$$\mathbf{k}_1 - \mathbf{k}_2 = \mathbf{k} \qquad [3]$$

and

$$\omega_1 - \omega_2 = \pm\Omega \qquad [4]$$

are the direct equivalents, respectively, of the classical expressions Eqs. [1] and [2].

Since the velocity of sound v is always very much less than the velocity of light c, it follows that $|\mathbf{k}_1| \simeq |\mathbf{k}_2|$ and so $0 \leq |\mathbf{K}| \leq 2|\mathbf{k}_1|$. The corresponding phonon frequencies, $\Omega = Kv$, have an upper limit of about 100 GHz for $\mathbf{k}_1$ in the visible region.

Although the idea of Brillouin scattering has been introduced as light scattering from an externally produced sound wave, the normal application is in scattering from thermal phonons. The thermal atomic vibrations in a solid are synthesized of phonons in all directions, spanning the entire phonon frequency spectrum. However, the momentum-conservation requirement Eq. [3] is so selective that by specifying the directions of $\mathbf{k}_1$ and $\mathbf{k}_2$ and the magnitude $|\mathbf{k}_1|$, only phonons in one particular direction with a particular momentum may contribute to the scattering.

A typical experimental arrangement is shown in Fig. 2. The choice of laser and the scattering angle completely determines the wave vector $\mathbf{K}$. The scattered light has frequency components ω_2 shifted both downward and upward from the incident frequency ω_1 and corresponding to emission and absorption of phonons, respectively. The frequency shift is equal to the phonon frequency Ω. In general, a solid will show three such doublets due to scattering from a single longitudinal- and two transverse-phonon branches. The width of a peak $\Delta\omega$ is determined by the phonon lifetime $\tau = 2/\Delta\omega$. A typical Brillouin measurement thus determines the frequency Ω and lifetime τ of a phonon of predetermined wave vector $\mathbf{K}$. The ratio $\Omega/\mathbf{K}$ is equal to the sound velocity v. Measurements of the sound velocity as a function of direction in a material yield the elastic constants. It should be emphasized that the light wave vector $\mathbf{k}_1$ is the wave vector inside the material. It is related by $\mathbf{k}_1 = n_0\mathbf{k}_0$ to the vacuum wave vector $\mathbf{k}_0$, where n_0 is the refractive index. Introducing the scattering angle φ

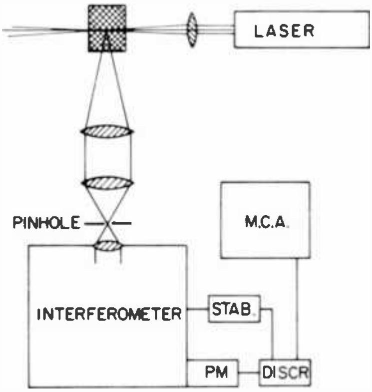

Fig. 2—A typical light-scattering arrangement showing collection and analysis of light scattered through 90° from a transparent solid.

into Eq. [3], we obtain with Eq. [4]

$$v = \frac{\Omega}{\mathbf{K}} = \frac{\omega_1 - \omega_2}{2|\mathbf{k}_1| \sin\frac{\varphi}{2}} = \frac{\omega_1 - \omega_2}{2n_0|\mathbf{k}_0| \sin\frac{\varphi}{2}}. \qquad [5]$$

Normally, therefore, the Brillouin scattering experiment determines the product $n_0 v$ rather than v alone. An exception to this is seen in the measurements on layer compounds described in Sec. 3.

The spectrometer shown in Fig. 2 must be able not only to resolve frequency shifts of approximately 1 to 100 GHz but must also be able to measure line widths down to a few MHz. Such high resolution can only be achieved by using a Fabry–Perot interferometer. In a commonly used form, this consists of two plane mirrors mounted accurately parallel to one another with a spacing L. One mirror may be scanned by means of a piezoelectric crystal as shown in Fig. 3. The output of the instrument for monochromatic incident light is a series of peaks wherever $L = n\lambda/2$, for integral n. The instrument acts as a tunable filter whose peak transmission is close to unity over a narrow spectral interval. Outside this interval the transmission is low, typically of order 10^{-3} to 10^{-4}. The frequency range between neighboring

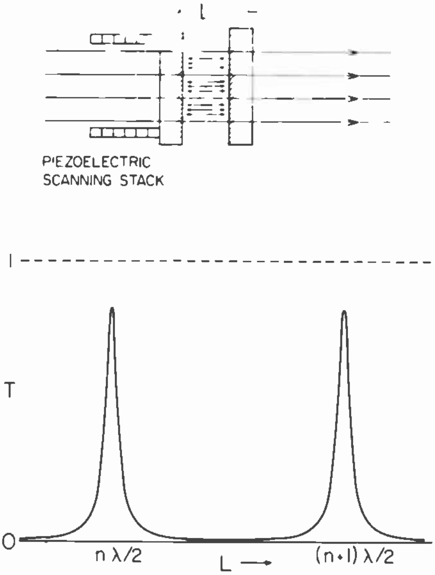

Fig. 3—Practical arrangement and transmission function of a Fabry–Perot interferometer.

orders, known as the free spectral range (FSR), is equal to $(2L)^{-1}$ cm^{-1}. The FSR divided by the width of the transmission peak is called the finesse. The FSR divided by the finesse thus gives the resolution of the instrument. The determination of finesse in terms of mirror reflectivity, mirror flatness, and aperture is discussed in many reviews (see, e.g., Jacquinot[1]).

For an experiment of the type shown in Fig. 2 involving a measurement on a large transparent crystal, the Fabry–Perot is a satisfactory instrument. When the crystal is opaque or small and imperfect, however, it is found that the light scattered elastically from defects, particularly at the surfaces, may be more intense than the Brillouin peaks by four to nine or more orders of magnitude. Under such conditions it is clear that a filter with a cutoff of 10^{-4} (a contrast of 10^4) is quite inadequate for resolving the Brillouin peaks, which will be completely swamped by the tail of the elastic peak.

To overcome this problem, a new spectrometer has been developed with a much improved contrast (close to 10^{10}). This spectrometer has opened up a whole range of new applications in the field of Brillouin scattering. In the next section, this instrument is described and some of the practical problems are discussed. In Sec. 3 a short survey of some of the applications of this spectrometer are given. It is shown that not only scattering from phonons may be detected, but also scattering from spin waves in magnetic systems. In the concluding section, some of the advantages and disadvantages of Brillouin scattering spectroscopy are discussed.

2. Experimental Technique

The Fabry–Perot interferometer is an excellent instrument for the high-resolution analysis of light. However it possesses two drawbacks which in the present situation are serious. The first is the limited contrast, as mentioned above, which for reasons of mirror quality cannot greatly exceed 10^4. The second stems from the tolerance required in the mirror alignment. Typically the parallelism must be maintained to the order of 0.1 sec of arc and the spacing must be controllable to about 50 Å. As a result, the instrument is relatively unstable. The low contrast makes measurement impossible in the presence of a strong elastic peak, and the instability is troublesome if long measuring times are required (for weak Brillouin signals). Both these problems are overcome in the present instrument.

The problem of low contrast was also encountered in the grating spectrometers used for Raman scattering. In that case, the contrast was improved by taking two (or sometimes three) synchronously scanned gratings in series. The transmission function for the instrument is the product of the transmission functions of the individual gratings, the contrast the product of the individual contrasts. Unfortunately, an arrangement of two or more interferometers in series, although it has been used,[2] is not a satisfactory solution. The difficulty of synchronizing the scans of two interferometers to within the required 50 Å, even using pressure scanning techniques,[1,2] is very great.

A neat solution to the problem has been achieved by passing the light several times through one interferometer. This is indicated schematically in Fig. 4. Corner cube reflectors are used to return the light parallel to itself. The arrangement shown is equivalent to having five identical interferometers in series, except that the separate passages are automatically synchronized as long as the mirrors remain parallel, which in itself is necessary in any case. The design parameters for such an instrument have been discussed previously.[3] It turns out that five passes are about optimum for high contrast with low losses and moderate finesse. Greater simplicity and higher finesse are achieved using three passes, but the losses become greater. Figures that can be practically achieved in a five-pass system are a contrast approaching 10^{10}, a finesse of 50, and a peak transmission as high as 50%.

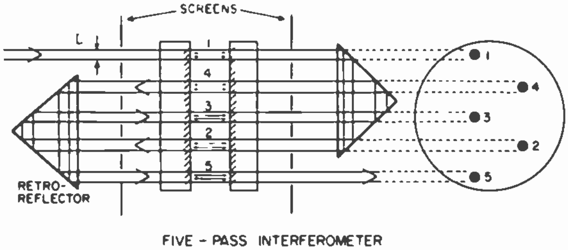

Fig. 4—Schematic arrangement for a multipass Fabry–Perot. The beam diameter has been reduced for clarity; in practice, a greater fraction of the mirror area may be used.

A demonstration of the increase in contrast achieved can be seen in the spectra of SbSI taken using a one- and two-pass interferometer.[3] This system was a rather lossy forerunner of the five-pass system but, as can be seen in Fig. 5, produced a remarkable improvement in contrast. The upper curve shows the back-scattered spectrum of SbSI using a single-pass conventional interferometer. The longitudinal phonon peak is just resolved in the wing of the elastic peak. The lower curve shows the same spectrum after two passes through the same interferometer. The transverse modes are now resolved in addition to the longitudinal modes. The wings of the elastic peak are seen to be drastically cut back. Compared to this two-pass system, the five-pass interferometer offers still greater contrast and significantly lower losses.

Two points regarding the operation of the instrument that have not been previously discussed are of interest.

The first point is that, in any system of tandem interferometers, care must be taken to avoid coupling between the separate interferometers, since otherwise the external cavities formed will seriously complicate the operation of the instrument. The finesse of the external cavities may be reduced, i.e., decoupling may be achieved, in three different manners:

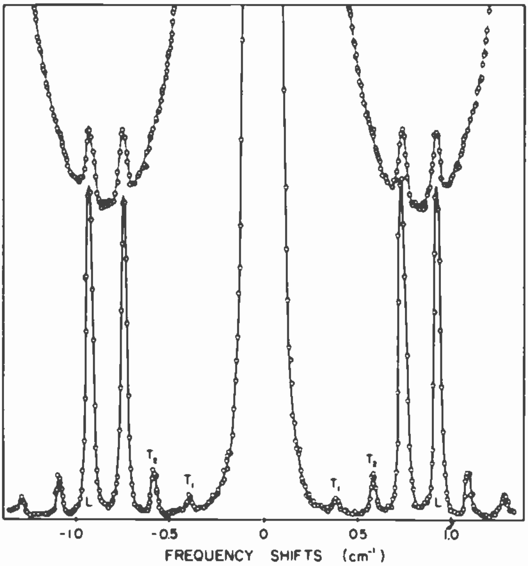

Fig. 5—Brillouin backscattering spectrum of SbSI using a double-pass interferometer. The longitudinal peaks *L* from neighboring orders are overlapped. The upper recording (base line the same) shows the same spectrum obtained using a single pass through the same interferometer.

(1) an attenuator may be placed between the cavities,
(2) a polarization decoupler may be used, or
(3) the separate interferometers may be slightly misaligned with respect to each other.

It is the last possibility that applies in the case of the multipass instrument. As previously mentioned, an alignment of roughly 0.1 sec of arc is required to achieve the full finesse. Thus, the external cavity will only be in good alignment if the retroreflectors are accurate to within 0.1 sec of arc. On the other hand, the acceptance angle of the interferometers is typically several minutes of arc, and thus it is quite unnecessary to use retroreflectors that are more accurate than about 1 minute. Interference in the external paths is thereby completely eliminated. It would indeed be a mistake to use retroreflectors of too high a quality.

The second point concerns the distribution of the five passes over the available mirror area. The simple reflector system of Fig. 4 has two disadvantages.

(1) Pass 2 is close to pass 5, which increases the possibility that the overall contrast will be reduced by crosstalk between the separate passes. In a better reflector design, it would be advantageous to separate passes 1 and 2 as much as possible from pass 5.

(2) The second problem is that, in practice, mirrors are never completely flat. As a first approximation the gap between the mirrors is likely to show a spherical distortion. In this case the mirror spacings for passes 1, 3, and 5 of Fig. 4 are no longer identical, and a serious loss of transmission may result. In such a case a distribution of the passes on a circle (which would be a contour of equal mirror spacing) will give much better results. Furthermore, the more ideal use of the available mirror area will allow larger beam areas to be used with consequently greater light throughput. The beams may be arranged to lie on a circle by making use of two special retroreflectors, as shown in Fig. 6. The reflectors consist of a normal corner cube retroreflector, on the front surface of which has been mounted a small-angle biprism. Without the biprism, light would be reflected parallel to itself but displayed by inversion through the point P. The effect of the biprism is to form two virtual inversion points P_1 and P_3 for light entering and leaving through the upper or lower halves of the biprism, respectively. The line X_1Y_1 is the ridge of the biprism. This reflector replaces the right-hand reflector of Fig. 4. An identical reflector with inversion points P_2 and P_4 and ridge X_2Y_2 replaces the left-hand reflector. The relative orientation of the two reflectors is shown in Fig. 6(c), the two ridges being set at an angle of 36° to each other. The separation of the virtual inversion points is chosen to suit the available mirror diameter and may be set by

a suitable choice of biprism angle or, alternatively, by use of a spacer of suitable thickness l. The successive passes through the interferometer, labeled 1 to 5 in Fig. 6(c), occur by successive inversions of the beam about the points P_1 to P_4. It is seen that by this arrangement, not only do the passes lie on a circle but also the early passes are separated as much as possible from the later ones, thus solving both the problems discussed above.

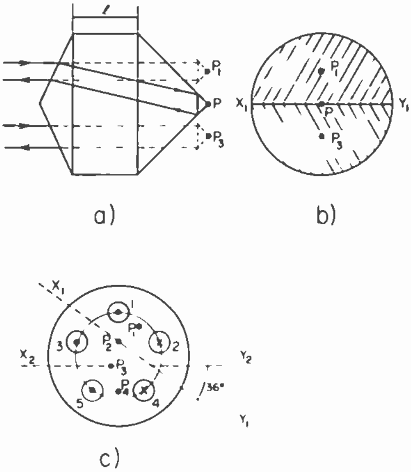

a)

b)

c)

Fig. 6—The design of a modified corner cube reflector that permits ideal usage of the available interferometer mirror area.

It should be emphasized that the retroreflectors should be used as total internal reflection devices. Some commercial reflectors have metallic coatings to increase the acceptance angle of the reflector. These coatings introduce intolerably large losses since each inversion involves three reflections. Such coatings must be removed.

The multipass spectrometer described above can be operated up to quite high resolution by increasing the mirror spacing. It has been used with spacings between 0.25 and 60 mm, corresponding to an FSR between 20 and $\frac{1}{12}$ cm^{-1}. With the greater spacing a resolution of about 60 MHz has been achieved, but care is required to avoid degrading the contrast. Reduced contrast can be avoided by using correct apertures to limit the beam divergence both in front of and after the interferometer. The size of aperture is a function of the resolving power and is discussed in Ref. [1].

The throughput of a Fabry–Perot is a function of the beam area and the resolving power. It is clear that a multipass interferometer must have a lower throughput than a single-pass instrument of the same finesse, since the beam area is reduced. This is discussed in Ref. [3], which shows that for typical light-scattering experiments, particularly on opaque materials, the loss in throughput is unimportant. It is also shown that the throughput of a multipass interferometer *of a given contrast* is considerably greater than that of a single-pass interferometer of the same contrast (assuming that such an instrument were practically possible).

The general properties of the multipass interferometer as compared to a single-pass interferometer of the same finesse may be summarized as follows:

(1) Contrast five or six orders of magnitude better.
(2) Transmission comparable or better.
(3) Throughput an order of magnitude lower (although for many situations in laser scattering this does not represent a loss of signal).
(4) Maximum resolving power comparable.
(5) Stability comparable.

On the last point, as mentioned previously, synchronization of the separate passes is equivalent to requiring that the mirrors be parallel. The degree of parallelism required is comparable to that required in a single-pass interferometer in which the same area of the mirror is utilized. The maintenance of parallelism may be achieved either passively through good, thermally compensated, stable design or actively by a feedback mechanism. The latter method has clear advantages where very long recording times are required. A feedback system has been described[4] that operates to maximize the intensity of the transmitted elastic scattered peak. The system will maintain full stability over an indefinite period and operates equally well on a single-pass or multipass interferometer.

For experiments where the highest resolution is required, it becomes necessary to use a spherical Fabry–Perot. This interferometer has been well described by Hercher.[5] A resolution as high as 1 MHz is possible with high light throughput. The limitations on contrast are similar to those on the plane Fabry–Perot described above. Furthermore, the instrument does not lend itself to multipassing, although a two-pass system may be operated.[6] If high resolution is required combined with high contrast, for example to analyze the line width of a narrow Brillouin component, a tandem arrangement of a multipass interferometer and a spherical one may be successfully employed, although the synchronization problems inherent in a tandem system are inevitably present.

Some interesting applications of the multipass spectrometer are given in the next section.

3. Measurements

The early Brillouin scattering experiments were restricted, because of the low instrumental contrast, to measurements of phonon velocity and lifetime in liquids, gases, and large transparent crystals. With the development of the high-contrast interferometer many new fields, particularly in solid-state physics, were opened up. It is the purpose of this section to describe some experiments to illustrate these new fields and to discuss the type of information that can be obtained from the measurements. The section is not intended to be a review of the current state of Brillouin scattering, but rather to indicate some of the new regions that have become accessible. These include scattering from phonons in layer compounds, opaque semiconductors, liquid crystals, and materials undergoing phase transitions and scattering from spin waves in magnetic materials.

3.1 Layer Compounds

Layer compounds generally form as small flaky crystals. As a result, there have been very few reported determinations of the elastic properties of these materials—neutron scattering measurements require large crystals in order to get sufficient signal, while Brillouin scattering measurements previously required large crystals so that the flare, or elastic scattered light, at the crystal surfaces could be arranged to lie outside the entrance aperture of the interferometer. The multipass interferometer is capable of completely rejecting the flare, even on 1-μm-thick crystals where the ratio of flare to Brillouin intensity may be as high as 10^8 and where all the flare light inevitably enters the spectrometer.

The measurements reported here were made for a scattering angle φ of 180° (backscattering) on crystals of CdI_2, GaSe, and SnS_2. Fig. 7 shows the scattering geometry for the experiment. It is seen that two distinct scattering events are recorded simultaneously. The upper process is backscattering from a phonon traveling across the crystal, while the lower process results from light reflected from the back surface of the crystal being forward scattered from a phonon traveling precisely in the plane of the crystal. If the incident light makes an angle β with the c-axis (the normal to the surface), then applying Eq.

[3] to the two cases we have:
(1) for the backscattering,

$$|\mathbf{K}| = 2n_0|\mathbf{k}_0|$$

with **K** making an angle $\theta = \arcsin([\sin\beta]/n_0)$ with the c axis; (2) for the forward scattering,

$$|\mathbf{K}| = 2|\mathbf{k}_1|\frac{\sin\beta}{n_0} = 2|\mathbf{k}_0| \sin\beta$$

and **K** travels in the plane of the crystal. This case is interesting in that **K** is determined entirely by $\mathbf{k}_0$ and the external angle β and is independent of the refractive index n_0.

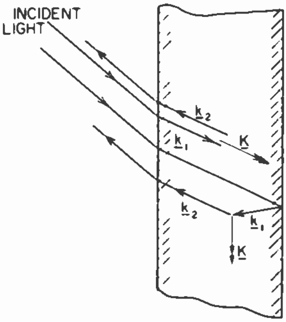

Fig. 7—Experimental arrangement for backscattering from a thin parallel-sided crystal, showing simultaneous measurement of a forward-scattering and a backscattering event.

From the Brillouin shifts as a function of angle β, the sound velocity as a function of angle θ in the crystal may be determined. The values obtained for GaSe are shown in Fig. 8. (For this crystal, some additional measurements were made on a crystal face making an angle to the c direction.) The curves in the figure are best fits obtained in terms of five elastic constants appropriate to a hexagonal structure. The elastic constants thus obtained for CdI_2, GaSe, and SnS_2 are shown in Table 1. (Of these three materials, only GaSe is always hexagonal. CdI_2 and SnS_2 have a similar structure in which the lowest polytype is trigonal while the second polytype is hexagonal. For the measured crystal of SnS_2, the sound velocity was observed to be completely isotropic within the c plane, implying hexagonal symmetry. For the CdI_2 crystal, the symmetry has not yet been deter-

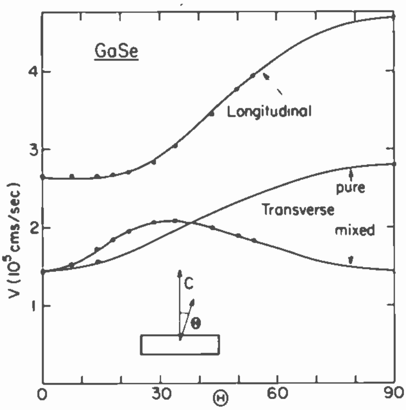

Fig. 8—Sound velocities in GaSe as a function of propagation direction θ relative to the c axis. The points are experimental; the curves are best fits in terms of five elastic constants describing a hexagonal crystal.

mined, but the sound velocity measurements would be well fitted with the assumption of hexagonal symmetry, i.e., $C_{14} = 0$.)

Of interest is the remarkable lack of elastic anisotropy in these, in other respects, very anisotropic materials. The ratio of the longitudinal sound velocities perpendicular and parallel to the c axis is shown in the last row of Table 1. Such a low anisotropy is at first sight surprising in view of the very weak van der Waals bonding between layers compared to the strong covalent bonding within the layers. Even graphite, which shows an extreme two-dimensional type behavior, has been shown by neutron scattering[7] to have only a ratio six in

Table 1—The elastic constants derived for CdI_2, GaSe, and SnS_2 together with the ratio of longitudinal sound velocity for propagation perpendicular and parallel to the c axis.

Elastic Constants (10^{10} dynes/cm^2)	CdI_2	GaSe	SnS_2
C_{11}	43	111	144
C_{33}	22.6	35	27.3
C_{44}	5.2	10.5	8.3
$(C_{11} - C_{12})/2$	11.4	39	53
C_{13}	9	12.5	12.5
Sound-Velocity Ratio $(V_L(\perp c)/V_L(\|c))$	1.38	1.78	2.30

the sound velocities. The underlying reason for this lack of anisotropy can be seen from Fig. 9 in which an oversimplified layer structure is depicted. The force constant k_0 within the plane is assumed to be much greater than k_1 between the planes. It is correspondingly assumed that c is greater than a. It is straightforward to derive the ratio of the sound velocities as shown in Fig. 9. It is seen that the anisotropy in the lattice parameter can, to a large extent, compensate the anisotropy in the force constants. This very simple argument is borne out by more detailed calculations involving the true lattice structures.[8]

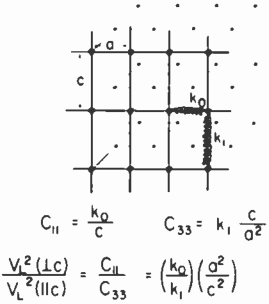

Fig. 9—The elastic constants C_{11} and C_{33} for a simple layer structure in terms of the inter- and intra-layer force constants k_1 and k_0.

3.2 Opaque Materials

Measurements on opaque semiconductors are possible using the backscattering technique. When the optical absorption coefficient α is less than about 10^3 cm^{-1}, the Brillouin spectrum appears the same as that of a transparent material and yields the sound velocity (multiplied by the refractive index) and the phonon life time. However, when the absorption coefficient is so high that the light penetrates only a few wavelengths into the material, a broadening effect occurs that is a direct result of the high optical absorption. The effect can be understood simply as follows. Because of the high absorption coefficient α, the scattering event must have occurred within a distance $\simeq 1/\alpha$ from the surface. The uncertainty principle then states that the phonon momentum $\hbar\mathbf{K}$ can only be determined to within an accuracy $\hbar|\Delta\mathbf{K}| \simeq h\alpha$. Thus all phonons with momentum in this range $|\Delta\mathbf{K}|$ around the value $\mathbf{K}$ determined by Eq. [3] may contribute to the scattering and since the phonon frequency $\Omega = v|\mathbf{K}|$, there is a corresponding width $\Delta\Omega$ in the Brillouin scattered peak. In terms of the imaginary part n_0'' of the refractive index,

$$\Delta\Omega \simeq v.2\pi\alpha = v.4\pi k_0 n_0''.$$

An exact calculation gives

$$\Delta\Omega = 4vk_0 n_0'' \qquad [5]$$

for the FWHM.

The phonon frequency Ω for back scattering is the usual

$$\Omega = 2k_0 v n_0', \qquad [6]$$

where n_0' is the real part of the refractive index. For $\alpha \gg 10^3$ cm^{-1}, such that the Brillouin width is dominated by this absorption effect, the measurement of the Brillouin spectra yields $n_0''v$ from the width and, as in the normal case, $n_0'v$ from the shift.

Some measurements on silicon and germanium[9] are shown in Fig. 10. The optical absorption increases from about 10^4 cm^{-1} for the upper spectrum to about 6×10^5 cm^{-1} for the lowest. The increase in line width with absorption is very noticeable. Since the velocity of sound in both silicon and germanium is well known, the spectra were interpreted to yield the values n_0' and n_0''. The values have been compared[9] with those obtained by other techniques and it has been shown that the method is capable of yielding reliable information on the optical constants in this high-absorption region.

Dresselhaus and Pine[10] have considered the detailed line shape and have shown that when $n_0'' \sim n_0'$ the line shape is no longer Lorentzian, but becomes asymmetrical. They have shown that the above measurements on germanium (lowest spectrum in Fig. 10) can be fitted much better by the asymmetric function than by the Lorentzian, although without an appreciable effect on the deduced value of n_0''.

3.3 Liquid Crystals

Interest in liquid crystals has been stimulated by their potential as display devices. From the elastic point of view, their crystalline character is reflected in the existence of shear propagating sound waves, which are otherwise absent in liquids. Brillouin scattering measurements of the elastic properties can thus yield important information on the liquid-crystal structure.

Some measurements with a double-pass interferometer of smectic A and smectic B phases in a liquid crystal have been reported by Liao and coworkers.[11] Both longitudinal and transverse propagating modes were observed, in agreement with the theoretical predictions.

3.4 Structural Phase Transitions

The study of materials undergoing structural phase transitions has developed in the last few years into one of the more lively fields in solid-state physics. The distortion occurring at a phase transition is characterised by an order parameter that couples to a greater or lesser extent to static strains in the system. For the case of linear coupling between strain and order parameter, an elastic constant is driven to zero at the phase transition. For weaker coupling, a correspondingly weaker elastic anomaly will appear. The subject is too extensive to enter into here (a good review of this field has been given

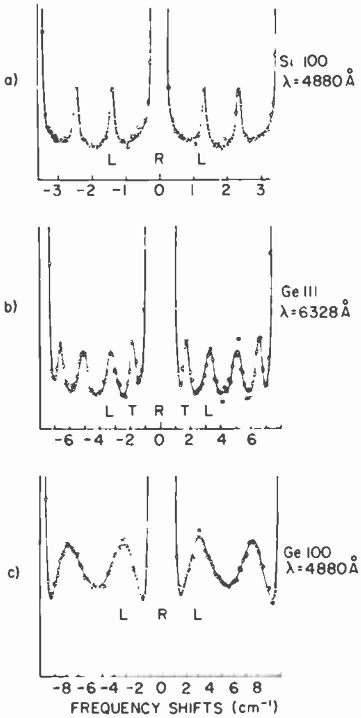

Fig. 10—Some Brillouin spectra of silicon and germanium. In (a) the peaks are observed in the first neighboring order, in (b) and (c) in the zero order.

by Rehwald[12]). It is clear that Brillouin scattering determinations of the anomalous elastic constants can be helpful in increasing our understanding of the mechanisms underlying the phase transition. Pioneering measurements of the transition in KDP (which is an example of linear coupling between strain and order parameter) by Cummins and Brody[13] have demonstrated the power of the Brillouin scattering technique in its application to phase transitions.

With the development of the high-contrast interferometer, the measurements are no longer limited to large and perfect crystals, as has been demonstrated by measurements on small flux-grown crystals of $DyVO_4$ and $TbVO_4$.[14]

Brillouin scattering measurements at phase transitions are limited to relatively transparent materials, since otherwise the incident laser energy is absorbed in such a small volume that temperature gradients exist that smear out the effects of the transition.

3.5 Light Scattering from Spin Waves

The discussion so far has been limited to the case of scattering from acoustic phonons. Magnetic materials also exhibit, apart from phonons, propagating acoustic spin wave modes. In this section we discuss some examples of scattering from spin waves.

Strong coupling via the exchange interaction exists between neighboring spins with the result that a fluctuation in one spin is felt by its neighbors and leads to a propagating fluctuation in the spin, rather similar to the case of phonons. Light can couple to the spin waves and so it is possible to perform light-scattering measurements of the spin-wave frequencies. The coupling mechanism is not, as might be supposed, a direct coupling between the spin and the magnetic vector of the light, but is rather an indirect coupling via the lattice as a result of the spin–orbit interaction.

Since most magnetic materials are rather opaque in the visible, it had not previously proved possible to observe light scattering, except from externally generated intense spin waves. With the new spectrometer, we can now observe light scattering from thermally excited acoustic spin waves. The first measurements[15] were made on YIG, a typical spectrum being shown in Fig. 11. It is seen that the spin-wave and phonon peaks are roughly similar in intensity, but whereas the upward and downward shifted phonon peaks are equally intense, the spin-wave peaks are not. The underlying reason for this is the precessional nature of the spin waves as compared to the linear nature of the phonons. It has been shown[16] that the intensity of the peaks may be interpreted in terms of the magnetic birefringence and dichroism and thus it is possible to determine the magnitude of these separate effects.

The dispersion equation for spin waves in an isotropic ferromagnet may be expressed as

$$\omega = \gamma(H + DK^2)$$

on the oversimplification that dipole–dipole interactions may be ignored. Here γ is the gyromagnetic ratio, H the magnetic field allowing for demagnetization effects, D the exchange constant and $\mathbf{K}$ the spin-wave vector. Measurements of ω as a function of H and $\mathbf{K}$ can thus determine both γ and D, as was demonstrated[15] for the case of YIG.

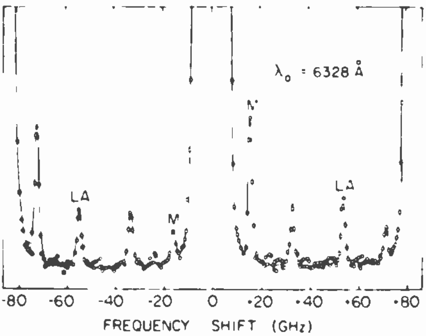

Fig. 11—Spectrum of YIG obtained for λ_0 = 6328 Å in a field of 3.5 kOe showing both LA phonon and spin wave peaks (M). The unlabeled peaks belong to the neighboring interference orders.

An investigation[17] of the low-temperature ferromagnet $CrBr_3$ ($T_c = 32.5°K$) demonstrated that light scattering may be observed not only in the ferromagnetic phase but also in the paramagnetic phase under the influence of an external magnetic field. Light scattering was observed for temperatures as high as nearly $8T_c$. Measurements of the spin-wave energy as a function of crystal orientation were shown to predict a single anisotropy coefficient, in agreement with earlier spin-resonance determinations.

4. Conclusion

An improved Fabry–Perot interferometer has been described that considerably extends the scope of Brillouin-scattering investigations. Some examples have been given from solid-state physics of how new information has been obtained using this spectrometer. Measurements of sound velocity and phonon lifetime on small and rather opaque materials may be performed and the spectra of very opaque materials may be analyzed to yield the optical constants. Applications in the fields of liquid crystals and structural phase transitions have been briefly discussed. Light scattering may also yield a wealth of information on magnetic systems in terms of magneto-optic effects, exchange interaction, gyromagnetic ratio, anisotropy, and spin-wave lifetime.

Light-scattering measurements have the general advantage that measurements may be made on extremely small samples—a volume of 1 mm^3 is quite adequate. On the other hand, for very opaque materials, heating of the scattering volume presents a limitation, particularly near phase transitions where the effects to be measured are very temperature dependent.

References:

[1] P. Jacquinot, "Recent Developments in Interference Spectroscopy," *Rep. Prog. Phys.*, **23**, p. 268, 1960

[2] A. S. Pine, "Thermal Brillouin Scattering in Cadmium Sulfide," *Phys. Rev.*, **5**, p. 2997, 1972

[3] J. R. Sandercock, "The Design and Use of a Stabilised Multipassed Interferometer of High Contrast Ratio," *Proc. 2nd Int. Conf. Light Scattering in Solids*, p. 9, 1971

[4] J. R. Sandercock, "Brillouin Scattering Study of SbSI using a Double-Passed Stabilised Scanning Interferometer," *Opt. Comm.*, **2**, p. 73, 1970

[5] M. Hercher, "The Spherical Mirror Fabry-Perot Interferometer," *Appl. Opt.*, **7**, p. 951, 1968

[6] D. S. Cannel, J. H. Lunacek, and S. B. Dubin, "A Simple Double-Pass Spherical Fabry-Perot Interferometer," *Rev. Sci. Instr.*, **44**, p. 1651, 1973; D. Beysens, "Etude des Phenomènes de Diffusion de la Lumière par Spectroscopie Fabry-Perot à haute Resolution et grande Sensibilité," to be published.

[7] R. Nicklow, N. Wakabayashi, and H. G. Smith, "Lattice Dynamics of Pyrolytic Graphite," *Phys. Rev. B*, **5**, p. 4951, 1972

[8] P. Schmid, private communication

[9] J. R. Sandercock, "Brillouin Scattering Measurements on Silicon and Germanium," *Phys. Rev. Letters*, **28**, p. 237, 1972.

[10] G. Dresselhaus and A. S. Pine, "Light Scattering Lineshape in opaque Materials," *Sol. State Comm.*, to be published.

[11] Y. Liao, N. A. Clark, and P. S. Pershan, "Brillouin Scattering from Smectic Liquid Crystals," *Phys. Rev. Letters*, **30**, p. 639, 1973.

[12] W. Rehwald, "The Study of Structural Phase Transitions by Means of Ultrasonic Experiments," *Adv. in Phys.*, **22**, p. 721, 1973.

[13] E. M. Brody and H. Z. Cummins, "Brillouin Scattering of the Ferroelectric Transition in KDP," *Phys. Rev. Lett.*, **21**, p. 1263, 1968.

[14] J. R. Sandercock, S. B. Palmer, R. J. Elliott, W. Hayes, S. R. P. Smith, and A. P. Young, "Brillouin Scattering, Ultrasonic and Theoretical Studies of Acoustic Anomalies in Crystals showing Jahn-Teller Phase Transitions," *J. Phys. C*, **5**, p. 3126, 1972.

[15] J. R. Sandercock and W. Wettling, "Light Scattering from Thermal Acoustic Magnons in YIG," *Sol. State Comm.*, **13**, p. 1729, 1973.

[16] W. Wettling, M. G. Cottam, and J. R. Sandercock, "The Relation between One-Magnon Light Scattering and the Complex Magnetooptic Effects in YIG," *J. Phys. C*, **8**, p. 211 (1975).

[17] J. R. Sandercock, "A Light Scattering Study of the Ferromagnet $CrBr_3$," *Sol. State Comm.*, **15**, p. 1715, 1974.

Optical Properties of Polystyrene Suspension in Water (Latex)

Hiizu Fujita, Kohei Ametani, and Michiko Inoue

RCA Research Laboratories, Inc., Tokyo

Abstract—Some optical properties of the ordered state of a latex, i.e., polystyrene spheres in a lattice structure in water, are summarized. The aligned micropolystyrene particles in water exhibit Bragg reflection and diffraction, and are iridescent in visible light. The results for the Bragg reflection spectrum and diffraction pattern obtained in the visible range are reported and the order–disorder phase-transition phenomena and stability problem of the ordered system are briefly summarized. A novel phenomenon, the electro-optical effects due to the ordered latex lattice system, are reported for the first time.

1. Introduction

The term "latex" was originally used to describe the milky liquid taken from rubber trees in which the rubber molecules (mostly polyisoprene) formed a colloidal dispersion in water. This term has been extended to aqueous dispersions of synthetic polymers prepared by emulsion polymerization. The word latex as used in this paper refers to a colloidal suspension of polystyrene (or polystyrene-butadiene) spheres in water. The diameter of the spheres ranges from about 500 Å to a few μm, depending on the chemical conditions for the synthesis. As an intermediate raw material for synthetic rubber, latex is well known to the rubber industry and its synthesis and chemical properties have been extensively studied.[1] In this review article, the authors do not become involved with much of the colloidal chemistry and rheology of latexes, but instead, confine their discussion to topics relating to novel phenomena in latexes that open up avenues for further investigations.

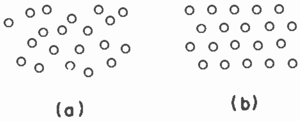

Fig. 1—Schematic views (a) of disordered and (b) of ordered states of latex dispersion.

Fig. 1(a) illustrates the latex particles dispersed in water. As is true for usual colloidal suspensions, the latex particle positions and particle-to-particle distances are randomly distributed. The feature of the latex suspension in water that distinguishes it from other colloidal suspensions is its formation of a well-ordered crystalline structure under certain conditions (Fig. 1(b)). Fig. 1(b) illustrates a crystal plane of a hexagonal close-packed (hcp) structure. The latex-particle suspension makes a phase transition from its disordered state (random phase, Fig. 1(a)) to an ordered state (Fig. 1(b)) when specific ionic conditions in the water are satisfied. As a consequence of the ordering and spacing of these microparticles, Bragg-reflection (diffraction) in the visible spectrum[2–4] occurs due to the optical-refractive-index discontinuity at the particle–water interface. This reflected light is iridescent. Fig. 2(a) shows the Bragg condition for visible light and Fig. 2(b) illustrates the macroscopic conditions to obtain monochromatic light by the use of a plane-parallel cell. In all respects, the ordered latex in a plane-parallel cell is similar to a 3-dimensional grating.

The reason for the "crystallization" of the latex particles in water is quite unique. The polystyrene particles have bound negative charges at the surface that originate from the end groups of the polymer chains. The end groups are due to the monomer polymerization process.[5–9] The negatively charged particles repel each other in water

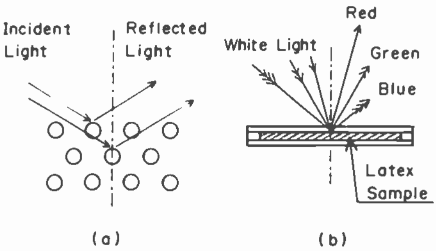

Fig. 2—(a) Bragg-reflection condition in a microparticle dispersion and (b) macroscopic condition to obtain monochromatic light.

and crystallize if the ionic conditions in the water are favorable.[10] Two factors that facilitate crystallization of the latex particles are simple geometrical shape and monodispersed size distribution. Because of the spherical shape of the particle, the electrical potential field around a latex particle is spherically symmetric and the latex suspension crystallizes more easily than colloidal suspensions with particles of complex geometrical shape.

Latex particles are grown in water and the particle suspension is called a monodispersed latex when the particle-size distribution has a single sharp maximum. If the size distribution were broad or multiple peaked it would be called a polydispersed latex. It is easy to see that a sharp Bragg reflection would not occur for a polydispersed latex suspension. Details of the synthesis and particle growth are described in the Appendix. Very briefly however, the polymerization process is started by an initiator and continues within a soap-micelle-form surfactant that is dispersed within water. In order to obtain a good monodispersed suspension, the growth-rate difference between varying particle sizes is utilized; the growth rate for small particles is faster than that for large particles. After synthesis, impurities such as unused monomers, surfactant and impurity ions are removed from the water. If the synthesized latex suspension shows iridescence, the sample is ready for experiments.

We divide the physical properties of the latex into two categories—the static physical properties and the dynamical properties. The static properties deal with the ordered latex lattice with little (or no) external perturbations. The Bragg-reflection analysis and the phase-transition problems fall into this category and are described in Part 2, below. The dynamical properties refer to the lattice-formation dynamics and phenomena involving significant external perturbations to the ordered lattice. Observations that relate to lattice dynamics, such as lattice-imperfection formation and/or phonon and light scattering, and electro-optical phenomena, are described in Part 3.

2. Static Properties of Latex

2.1 Crystal Structure

2.1.1 Brag-Reflection of Visible Light

The extraordinary fact that the polystyrene particles form a lattice structure in water was confirmed by careful measurements of the reflected spectra.[3,4] Fig. 3(a) shows an example of the reflected light spectra taken with the setup shown in Fig. 3(b). In Fig. 3(a), three spectra of different colors are shown; each has a sharp maximum depending on the incidence angle to the normal of the sample cell. The lattice constant d, as determined from the simple Bragg equation, $2d\cos\theta = n\lambda$, was 3135 Å (using the green peak data), where θ is the incidence angle to the normal of the cell, n is an integer for the ordering number of the diffraction, and λ is the wavelength. However, the index of refraction of the sample is different from unity in the visible wavelength range, and corrections must be taken into account in the simple Bragg equation; this is a point of departure from x-ray analysis, and more detailed equations are found in the literature.[4] It is easy to see that all the studies normally carried out by x-ray analysis, such as determinations of structure factor, atomic-scattering factor, and intensity ratios between different orders, can be readily extended to latexes using visible light. To the authors' knowledge, how-

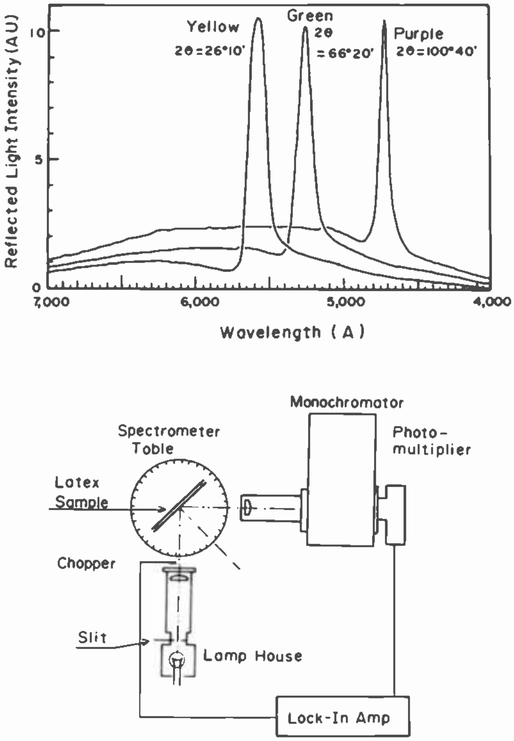

Fig. 3—(a) Bragg-reflection spectra of latex and (b) instrument layout for the measurements. Angle θ is the incidence angle to the sample-cell normal.

ever, very little has been reported, to date,[11,12] and much work remains for future investigation.

2.1.2 *Diffraction Pattern*

In order to verify that the particles are in an ordered state, not only in a few hundred layers near the surface but in the bulk sample as well, a transmission-diffraction pattern was taken using an He-Ne laser beam. A pin-hole plate, 10 μm in diameter, a beam expander, and a lens were used, so that the final spot diameter on the sample would be of the order of 10 μm. As a matter of fact, the entire cell becomes rather transparent, like a transmission grating, when the latex in a cell is well ordered. Fig. 4 is an example of the diffraction pattern, taken by the method described above, that shows hexagonal symmetry.

Fig. 4—Transmission-diffraction pattern of a latex plane-parallel cell using an He-Ne laser.

2.2 Phase Transition

At present two models are used to describe the latex system. One, the Kirkwood model, is used to explain the order–disorder transition while the other, the Wigner lattice model, describes the stability of the ordered state of the latex. Both models are briefly described in this section.

2.2.1 Kirkwood–Alder Transition

One important question regarding the latex and its behavior is the mechanism that gives rise to the order–disorder phase transition.[13] Before describing this phase-transition phenomenon, let us first look closely at the ion distribution in the water around the latex particles. Fig. 5(a) schematically represents the ion distribution near the particle surface. Because of the bound negative charges on the particle surface, positive ions in water are attracted to the particle (negative free ions are repelled) and, in effect, the particle is "clothed" by an excess positive-ion cloud. Latex particles interact with their mutually repulsive forces via the surrounding ion cloud. The thickness of the ion cloud or the "electric double layer" depends on the charge density of the bound charges on the particle surface and the ion concentration in the surrounding water. The repulsive force between two spherical particles can be represented, to a reasonable approximation, by[14]

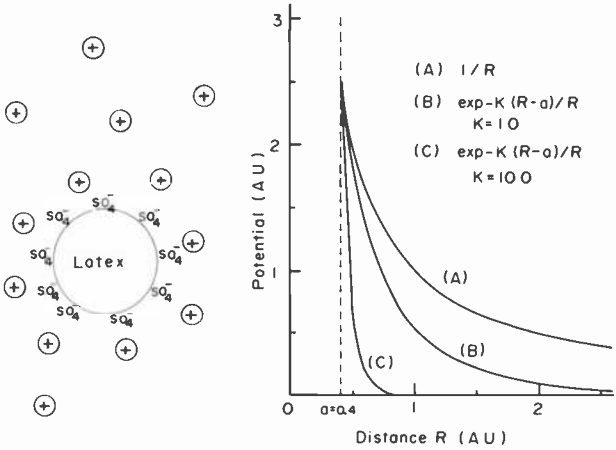

(a) (b)

Fig. 5—(a) Schematic view of ion distribution around a latex particle and (b) coulomb and screened coulomb potential curves versus distance from the latex particle surface.

$$V_R = (Ze)^2 \frac{\exp\{-K(R-2a)\}}{D(1+2Ka)R}, \quad \text{for } R \geq 2a,$$

where R is the distance between the centers of two particles with diameter of $2a$, Ze is the total particle charge, and D is the dielectric constant of the solvent. K is the Debye screening constant, and roughly gives the order of the width of the electric double layer. For a hard (undistorted) layer, we have $K^2 = 8\pi n(Ze)^2/Dk_BT$, where n is the ion concentration. Fig. 5(b) shows the screened coulomb potentials with different values of ion concentration, and for comparison, the coulomb potential as a function of distance. One sees clearly from Fig. 5(b) that the screened coulomb potential gives a short-range interaction as compared to the long-range coulomb potential, and it decreases sharply at a given distance as the ion concentration n and the charge Ze increases.

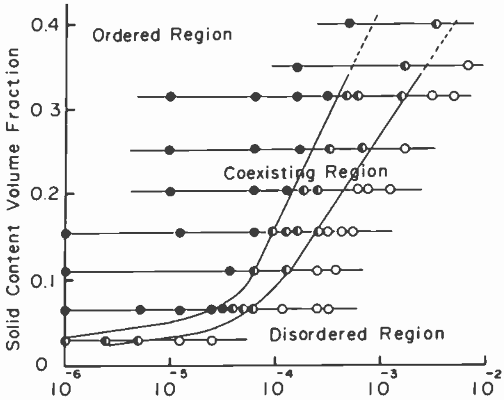

Fig. 6—Order–disorder phase diagram of polystyrene latex (courtesy of S. Hachisu, Y. Kobayashi and A. Kose).

In colloidal chemistry van der Waals attractive force, together with the particles repulsive force, play a major role in determining the stability of coagulation of lyophobic sols. In a latex, however, van der Waals force seems to play a minor role compared with the repulsive force in the order–disorder transition. Fig. 6 shows an example of the order–disorder phase diagram of a latex suspension in water.[10] Similar experiments were performed with a latex particle suspension in an organic solvent,[15] where the double-layer thickness is of negligible magnitude and the van der Waals force between latex particles is negligible. In this case the hard-sphere model should certainly hold. By analyzing the ion-concentration dependence of the latex system phase-transition diagram, it was concluded that the mechanism that controlled this phase transition was nothing more than the Kirkwood–Alder mechanism,[16] i.e., a phase transition from the disordered to ordered state that occurs in a system of hard spheres and purely repulsive forces when the packing fraction of particles increases above a critical range of values. This result, as predicted by Kirkwood, was confirmed by computer experiments.[17,18]

2.2.2 Wigner Lattice

The Wigner lattice is a famous and interesting theoretical subject in solid-state physics that predicts that low-density electrons in a metal will form a lattice structure.[19,10] Wigner[19] first pointed out that for a dilute electron gas in the background of uniform positive charges, the kinetic energy can be neglected compared to the coulomb potential energy of the system and the ground state of the electron lattice is a body-centered cubic (bcc) structure. Later theoretical work[20] revealed that the bcc structure is favored over other structures, such as face-centered cubic (fcc) or hexagonal close-packed (hcp) structures, which differ by only a small amount of energy. One can consider that a latex system is similar to a dilute gas system, particularly when the thickness of the electric double layer is increased. Support for this hypothesis arises from the observed Debye–Scherrer powder pattern obtained using an He-Se laser beam in the visible range. The lattice structures are found to be fcc or bcc depending on the particle density.[12]

3. Dynamical Properties

3.1 Individual Particle Motion

A polystyrene particle is commonly used to study Brownian motion of a particle in water because the particle shape is perfectly spherical and its size well controlled. Rayleigh scattering of light due to the Brownian motion of an individual particle was studied using a laser beam, and correlation time measurements were reported.[21–23] For Rayleigh-scattering experiments, the latex particle suspension must be extremely dilute so that no two particles appear in the observed area within the correlation time. When a polystyrene sphere in a latex is under forced oscillation by an ac electric field, as discussed in Sec. 3.3, it excites a sound wave in the surrounding water. It is known in fluid dynamics that the motion of a fluid caused by the oscillation of a sphere is rotational in a region around the sphere and the amplitude decays exponentially with distance.[24] The decay length is given by $\delta = (\eta/\rho\omega)^{1/2}$, where η is the viscocity, ρ the density of the fluid, and ω the radian frequency. For water, δ falls in the range of $10^{-3} - 10^{-4}$ cm for frequencies between 1 kHz and 1 MHz. Thus, in an ordered latex where the interparticle distance is smaller than δ, a stable mode of shear wave, in addition to the ordinary longitudinal waves, is expected. Such an excitation can be detected by light-scattering techniques. However, the authors are unaware of any reported Brillouin- or Raman-scattering experiments for the ordered latex.

3.2 Lattice and Defect Formations

The direct observation of the ordered latex particles in water was performed using a metallurgical optical microscope.[25] By observing the individual particle motion, the condensation of the latex particles from a gaseous-phase to a solid phase, i.e., a motion of the boundaries between the two phases, was seen and reported. Dislocations in a crystal-lattice plane and a stacking fault between crystal planes were also observed. In some cases, the motion of the domain wall and a phonon-like wave in a crystal plane were seen and reported. All of the experiments were performed under high-particle-density conditions (highly iridescent samples), which are different from the Wigner-lattice condition (Sec. 2.2.2).[12] The point defect of a latex crystal, where a latex particle at a lattice site is missing, was observed. However, it is worth noting that the number of voids in the hcp structure is equal to the number of lattice sites, and they may play a role as trapping sites for negative foreign ions. However, no physical or optical experiments on the trapped ion cloud or trapped ions have been reported.

3.3 Electro-Optical Properties

When the viewing angle is fixed, a color change is observed if a dc electric field is applied across the sample cell (Fig. 2(b)). This is due to the lattice-parameter change caused by electrophoresis of the latex particles. The color change is reversible and electric-field-polarity dependent. This color change is also observed when an ac electric field is applied, and if the frequency is sufficiently low (below about 30 Hz), the change can be observed by eye. Fig. 7 illustrates schematically the instruments used to measure this change. Fig. 8(a) shows the typical signal taken at a low applied electric frequency (15 Hz). The proposed origin of the measured signal in Fig. 8(a) is schematically indicated in Fig. 8(b). In Fig. 8(b), the shift of the spectrum is due to the applied electric field, as indicated. If the spectrum-shift takes place without changing the spectrum shape (rigidly), then the signal

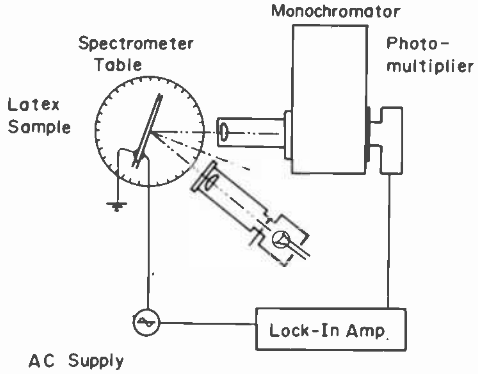

Fig. 7—Schematic layout of the instrument for the electro-optical measurements.

output, which is modulated by the electric field, is shown in Fig. 8(a). The modulation signal is a result of a change in the lattice parameter of the latex particle crystal. Another feature of the electric-field response signal shows up when the applied electric frequency is increased. Fig. 9(a) is a typical representation of the measured signal at high frequency (750 Hz). Fig. 9(b) represents the proposed origin of

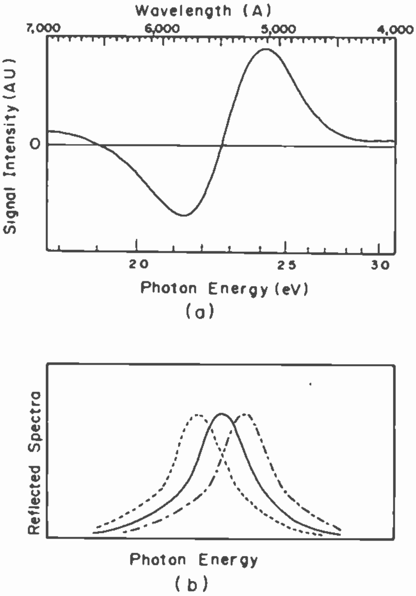

Fig. 8—(a) Electro-reflectance spectrum of a Bragg reflection measured at a 15-Hz modulation frequency and (b) schematic curves to explain the above effect.

the signal, following the same approach as for Fig. 8(b). In this case, the original spectrum is not shifted rigidly, but becomes "soft" when the electric field is applied. Fig. 10 is a plot of the signal height at a fixed wavelength relative to the applied electric frequency. The spectrum change from Fig. 8(a) to Fig. 9(a) takes place gradually between 100 and 400 Hz.

It is difficult to believe that the crystallized latex particles, about 2,000 Å in diameter, are able to keep up with the external electric field, through 100 kHz. Considering the results shown in Figs. 8, 9, and 10, it is more reasonable to assume the following. At low frequency, say from 10 Hz to about 100 Hz, the latex particles and surrounding ion cloud are forced to oscillate as a whole. The distortion of the surrounding charge distribution by the external electric field changes the lattice parameter of the latex system and results in a light-intensity modulation. When the frequency of the external electric field is sufficiently high, the latex particles are no longer able to follow the forcing oscillation. However, the charge cloud (ions and possibly oriented water around the particles) can keep up with the frequency, because their mobilities in water are higher than that of the latex parti-

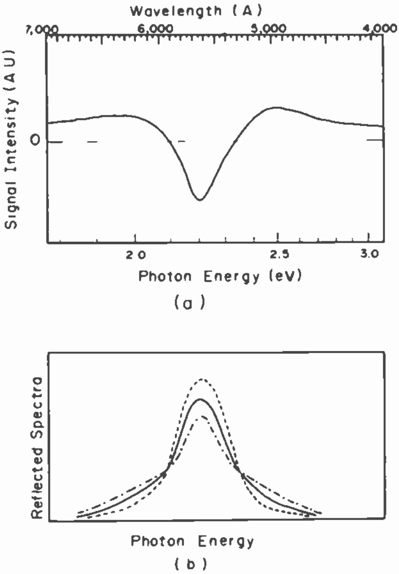

Fig. 9—(a) Electro-reflectance spectrum of a Bragg reflection measured at a 750-Hz modulation frequency and (b) schematic curves to explain the above effect.

cles. An elementary calculation shows that if the optical refractive index of the bound water that contains the charge cloud differs from that of the rest of the pure water by about 0.5%, the photoresponse due to the bound cloud movement would be of the order of magnitude obtained at 20 kHz (Fig. 10). In that event, the light intensity is not modulated by the latex-particle movement, but rather by the movement of the ion cloud generated by the latex lattice. The frequency dependence of the phase shift between the applied electric field and the response of the reflected light intensity was observed. A fairly large phase shift, almost 90°, was observed when the frequency was elevated from 10 to 300 Hz, and this fact supports the likelihood of the above-mentioned model.

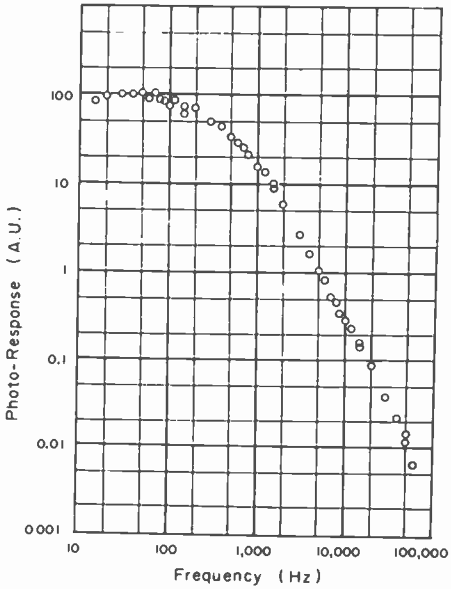

Fig. 10—Frequency dependence of the electro-reflectance intensity. The measurements were performed at a fixed wavelength of 6170 Å, and the output was adjusted for a maximum of this frequency.

4. Remarks

As described above in Sec. 2 and 3, the polystyrene sphere suspension in water (latex) offers for study a wide variety of interesting subjects, such as crystallography, lattice dynamics, Brownian motion and electro-optical phenomena. In the latex system, especially in the ordered state, a large amount of fundamental solid-state physics research remains to be done. The strongest and most attractive feature of the system is that all the parameters necessary for analysis, i.e., particle size, particle density, and ion concentration, can be controlled. It should be mentioned that the interesting aspects of this system are not limited to the simulative experiments only. Finally, it must be pointed out that other avenues of investigation also exist for latex systems that are suspended in organic solvents, rather than water, and that also crystallize.

Acknowledgments

The authors are anxious to express their sincere thanks to Drs. A. Kose and S. Hachisu, Institute for Optical Research, Tokyo University of Education, for their generous supply of latex samples in early stage of experiments. The authors gratefully acknowledge the support and encouragement of B. Hershenov of RCA, Tokyo, and many helpful discussions with Dr. Hirota, currently at Ritsumeikan University, and formerly at RCA and associated with this program.

Appendix

The latexes are prepared either by a conventional emulsion-polymerization technique or by a seed technique. The seed technique, which is not described here, employs latex particles that were previously polymerized. The polymerization technique uses a mixture of water, surfactant, monomer, and initiator. The monomers usually used are styrene, butadiene, or divinyl benzene; all of these compounds have vinyl groups. The surfactant is used as an emulsifier, while potassium persulfate and hydrogen peroxide are the initiators that are frequently used. When heated, these compounds undergo cleavage at the oxygen–oxygen bond and form two free radicals.

Fig. 11 shows the reaction-vessel apparatus. (Different types of reaction vessels, such as capped bottles or stainless reactors, have been used.[5,9]) All aqueous reagents are purged by nitrogen gas to remove dissolved oxygen before the reaction in order to avoid oxidation of polymers during the polymerization reaction.[26-28] The monomer is purified with a washing agent to remove the inhibitor. (Pyrogallol-NaOH solution is used for styrene.) The reactants are charged into the stirring reactor and warmed to temperatures between 40° and 90°C. Nitrogen gas is continuously bubbled through during the reaction process. In the solution, the monomer is emulsified with a micelle-form surfactant. As the reaction proceeds, a part of the monomer molecule is distilled out and condensed back into the vessel by the condenser. The polymerization reaction is completed when the distillation of monomers is terminated, a time period of several hours to one day.

The reaction is known as "addition polymerization" of vinyl monomers, which are catalyzed by free radicals produced from the initiator. The theory of the mechanism of emulsion polymerization was first proposed qualitatively by Harkins.[29] Ever since Smith and Ewart put the theory into a quantitative form,[30] discussions on the mechanism of emulsion polymerization have taken place.[9,31,32] The general understanding of the process is summarized below.

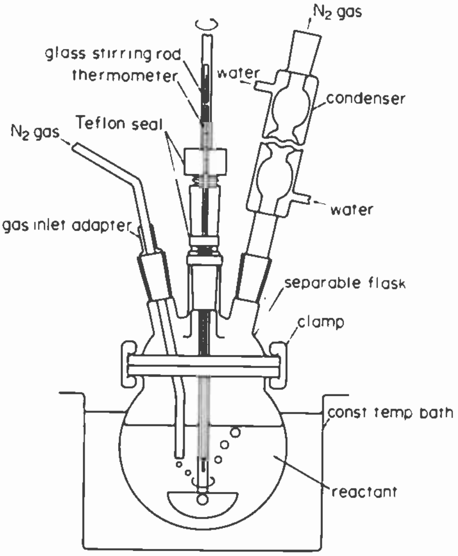

Fig. 11—Schematic view of the apparatus of reaction vessel.

The free-radical polymerization is a chain reaction and consists of three stages; initiation, propagation, and termination. In the initiation stage, styrene monomers are swollen by a soap-micelle-form surfactant and dissolved in the aqueous phase. The surfactant molecules or ions are, in turn, adsorbed on the monomer droplet. Meanwhile, the initiator, potassium persulfate for example, is dissolved in the aqueous phase. When the reaction solution is heated, the initiator (persulfate ions in the aqueous phase) decomposes and generates free radicals as represented by

$$S_2O_8^{2-} \longrightarrow 2SO_4^{-\bullet}.$$

The free radicals, $SO_4^{-\bullet}$, react with the monomer molecules and the polymerization is initiated in the monomer-swollen surfactant micelles. In the propagation stage, the primary radicals are augmented up to surface-active "oligostyrene-sulfate" radicals in the micelles; addition of a primary sulfate radical to a styrene molecule produces a new styrene radical, which reacts with another styrene molecule to form more macro-polystyrene radicals. The growth of polymeric radicals continues until a second radical is captured by the same micelle. At this stage, the polymerization is terminated by the combination of two polymeric radicals with each polymer molecule having two sulfate end groups.

The resulting latex is an aqueous dispersion of spherical polymer particles that are stabilized by surfactant molecules or initiator fragments located at the water–polymer interface. The latex solution also contains ionic and nonionic water-soluble impurities. The removal of impurities and surfactant molecules adsorped on the surface is performed by the use of an ion-exchange resin[8] or dialysis against distilled (or deionized) water. A combination of both techniques, ion-exchange resin and dialysis, removes all water-soluble impurities.

Monodispersity is attained by limiting the number of micelles. The total surface of a micelle is determined by the amount of ionic surfactant, while the volume of the micelle is determined by the nonionic surfactant content.[5] Monodispersed latexes are obtained by the coexistence of both ionic and nonionic surfactants in a certain mixing ratio; the absence of either one results in a polydispersed latex.[5] A particle size of 0.08 to 0.50 μm in diameter is available by conventional techniques.[5]

Most of the end groups on the persulfate-initiated latexes are strongly acidic sulfate groups. However, in the initiation of polymerization, the sulfate-ion radical can react in a way different from that described above, i.e.,

$$SO_4^{-\bullet} + H_2O \longrightarrow HSO_4^{-} + OH^{\bullet}.$$

In this case, an appreciable number of hydroxyl or carboxyl end groups may combine with the polymer; carboxyl groups are generated by the oxidation of hydroxyl groups. Lowering the reaction-solution pH from 10 to 2 increases the number of hydroxyl-end groups and decreases the number of the sulfate groups.[9] No carboxyl groups are detected in a latex prepared in a nitrogen atmosphere,[9] but they are incorporated into a latex when the reaction is carried out in an air atmosphere.[7] A single sphere consists of many polymer molecules, and the charge density of sulfate groups is one charge for every 200 to 3,100 Å^2 of surface.[8,9]

Different particle size latex can be prepared by controlling concentrations of initiator and surfactant and reaction temperature at a constant pH while the total surface charge remains constant. On the other hand, it is also possible to change the surface-charge density on a given latex particle size by varying the pH at a constant surfactant concentration.[9]

References

[1] See, for example, *Polymer Colloids*, Ed. R. M. Fitch, Plenum Publishing, New York (1971).

[2] T. Alfrey, Jr., E. B. Bradford, and J. W. Vanderhoff, "Optical Properties of Uniform Particle-Size Latexes," *J. Opt. Soc. Amer.*, **44**, p. 603 (1954).

[3] Von Werner Luck, M. Klier, H. Wesslau, "Über Bragg-Reflexe mit sichtbarem Licht an monodispersen Kunststofflatices," *Berichte der Bunsengesellschaft*, **67** (1962) (Part 1, p. 75; Part II, p. 84); "Kristallisation ubermolekularer Bausteine, "*Naturmissenschaften*, **50**, p. 485 (1963).

[4] P. A. Hiltner and I. M. Krieger, "Diffraction of Light by Ordered Suspensions," *J. Phys. Chem.*, **73**, p. 2386 (1969).

[5] M. E. Woods, J. S. Dodge, I. M. Krieger, and P. E. Pierce, "Emulsion Polymerization with Mixtures of Anionic and Nonionic Surfactants," *J. Paint Technol.*, **40**, p. 541 (1968).

[6] P. Ghosh, S. C. Chadha, A. R. Mukherjee, and S. R. Palit, "Endgroup Studies in Persulfate-Initiated Vinyl Polymer by Dye Techniques. Part I. Initiation by Persulfate Alone," *J. Polymer Sci.*, **A2**, p. 4433 (1964).

[7] R. H. Ottewill and J. N. Shaw, "Studies on the Preparation and Characterization of Monodisperse Polystyrene Latices. Part 2: Electrophoretic Characterization of Surface Groupings," *Z. Polymere*, **218**, p. 34 (1967).

[8] H. J. Van den Hul and J. W. Vanderhoff, "Well Characterized Monodispersed Latexes," *J. Colloid and Interface Sci.*, **28**, p. 336 (1968).

[9] H. J. Van den Hul and J. W. Vanderhoff, "Inferences on the Mechanism of Emulsion Polymerization of Styrene from Characterization of the Polymer End-Groups," *Brit. Polymer J.*, **2**, p. 121 (1970).

[10] S. Hachisu, Y. Kobayashi, and A. Kose, "Phase Separation in Monodisperse Latexes," *J. Colloid and Interface Sci.*, **42**, p. 342 (1973).

[11] F. Robillard and A. J. Patitsas, "Diameter Measurement of Dow Latexes EP-1358-38 by Three Optical Methods," *Can. J. Phys.*, **51**, p. 2395 (1973).

[12] R. Williams and R. S. Crandall, "The Structure of Crystallized Suspensions of Polystyrene Spheres," *Phys. Lett.*, **48A**, p. 225 (1974).

[13] S. Hachisu and Y. Kobayashi, "Kirkwood-Alder Transition in Monodispersed Latexes, II. Aqueous Latexes of High Electrolyte Concentration," J. Colloid and Interface Sci., 46, p. 470 (1974).

[14] E. J. W. Verway and J. T. G. Overbeek, Theory of the Stability of Lyophobic Colloids, Elsevier (1948).

[15] A. Kose and S. Hachiso, "Kirkwood-Alder Transition in Monodispersed Latexes, I. Nonaqueous Systems," *J. Colloid and Interface Sci.*, **46**, p. 460 (1974).

[16] M. Wadati and M. Toda, "An Evidence for the Existence of Kirkwood-Alder Transition," *J. Phys. Soc. Japan*, **32**, p. 1147 (1972); M. Wadati, A. Kose, and M. Toda, *Kagaku*, **42**, p. 646 (1972) (in Japanese).

[17] B. J. Alder and T. E. Wainright, "Phase Transition in Elastic Disks," *Phys. Rev.*, **127**, p. 359 (1962).

[18] B. J. Alder, W. G. Hoover, and D. A. Young, "Studies in Molecular Dynamics. V. High-Density Equation of State and Entropy for Hard Disks and Spheres," *J. Chem. Phys.*, **49**, p. 3688 (1968).

[19] E. Wigner, "Effects of the Electron Interaction on the Energy Levels of Electrons in Metals," *Trans. Far. Soc.*, **34**, p. 678 (1938).

[20] K. Fuchs, *Proc. Foy. Soc. (London)*, **A151**, p. 585 (1935); W. J. Carr, Jr., "Energy, Specific Heat, and Magnetic Properties of the Low-Density Electron Gas," *Phys. Rev.*, **122**, p. 1437 (1961).

[21] H. Z. Cummins, N. Knable, and Y. Yeh, "Observation of Diffusion Broadening of Rayleigh Scattered Light," *Phys. Rev. Lett.*, **12**, p. 150 (1964).

[22] R. Pecora, "Doppler Shifts in Light Scattering from Pure Liquids and Polymer Solutions," *J. Chem. Phys.*, **40**, p. 1604 (1964).

[23] F. T. Arecchi, M. Giglio, and U. Tartari, "Scattering of Coherent Light by a Statistical Medium," *Phys. Rev.*, **163**, p. 186 (1967).

[24] L. D. Landau and E. M. Lifshitz, *Fluid Mechanics*, Pergamon Press (1963).

[25] A. Kose, M. Ozaki, K. Takano, Y. Kobayashi, and S. Hishisu, "Direct Observation of Ordered Latex Suspension by Metallurgical Microscope," *J. Colloid and Interface Sci.*, **44**, p. 330 (1973).

[26] A. A. Miller and F. R. Mayo, "Oxidation of Unsaturated Compounds. I. The Oxidation of Styrene," *J. Amer. Chem. Soc.*, **78**, p. 1017 (1956).

[27] F. R. Mayo, "The Oxidation of Unsaturated Compounds. V. The Effect of Oxygen Pressure on the Oxidation of Styrene," *J. Amer. Chem. Soc.*, **80**, p. 2465 (1958).

[28] A. G. Parts, "Polymerization Kinetics of Acrylonitrile," *J. Polymer Sci.*, **37**, p. 131 (1959).

[29] W. D. Harkins, "A General Theory of the Mechanism of Emulsion Polymerization," *J. Amer. Chem. Soc.*, **69**, p. 1428 (1947).

[30] W. V. Smith and R. H. Ewart, "Kinetics of Emulsion Polymerization," *J. Chem. Phys.*, **16**, p. 592 (1948).

[31] R. M. Fitch, "The Homogeneous Nucleation of Polymer Colloids," *Brit. Polymer J.*, **5**, p. 467 (1973).

[32] Y. Toyooka and T. Imoto, "Continuous Emulsion Polymerization of Styrene," *Nippon Kagaku Kaishi*, p. 1762 (1974) (in Japanese).

The Nephelauxetic Effect in Divalent Rare Earth Ions

R. Casanova Alig

RCA Laboratories, Princeton, N. J. 08540

Abstract—Recent measurements of the optical spectra of divalent rare earth impurities in alkaline earth halide hosts cannot be explained using only crystal field theory, i.e., by a description of the host as a lattice of point charges. To account for the nephelauxetic effect (the reduction of the electrostatic interaction of the impurity electrons) found in these spectra, it must be assumed that the impurity electrons and the nearby halide electrons form molecular orbitals. The work leading to these conclusions is reviewed here.

1. Introduction

An atom or an ion in free space consists of a group of electrons interacting among themselves and with a positive nucleus. The major interactions among the electrons are the electrostatic repulsion between electrons and the spin-orbit interaction of each electron. When an ion is an impurity in a crystal, the crystal field interaction frequently must be added to the above two interactions. This interaction occurs between the electrons on the impurity ion and the ions of the host crystal, called ligands, which surround it. For example, the local environment of an impurity might be described by a cube centered on the impurity with 8 negative ions at its corners that interact electrostatically with the impurity electrons. However, real ligands have electronic orbitals that interact with those on the impurity and thus change the electrostatic and spin-orbit interactions of the impurity electrons from their free-ion values. This change is called the nephelauxetic (cloud-expanding in Greek) effect. It is not surprising that such a change should occur, for the impurity resides in a cavity in a dielectric.

The optical spectra of rare earth impurities have been important in phosphor research,[1] in the development of solid state lasers,[2] and of other research tools.[3] The rare earth, or lanthanide, series is a group of 14 elements characterized by a partially-filled $4f$ electronic shell. This shell is shielded from the outside world by other filled electronic shells, e.g., the $6s$ and $5p$ shells. Thus, the field of the ligands perturbs the $4f$ electrons on a rare-earth impurity only slightly. It follows then, that if we want to examine the interaction between the impurity and the crystal, we should consider electrons outside the $4f$ shell. Unfortunately in the most common valence state of the rare-earth impurity ions, +3, the optical transitions involving electrons outside the $4f$ shell all lie to the UV side of the visible, where they are not easily studied. However, these impurities also exist in the divalent state and transitions between the $4f^n$ and $4f^{n-1}\,5d$ configurations (where n lies between 1 and 14) frequently result in the emission or absorption of visible light. Hence, only divalent rare-earth impurities will be considered here.

2. The Nephelauxetic Effect

One of the most important conclusions deduced from the existence of a nephelauxetic effect is that the description of the crystal field by a distribution of fixed charges is not sufficient, for if the ligands were only point charges, then the interaction of two electrons on the impurity ion would be unperturbed by the presence of the ligands. In the crystal field theory as proposed by Bethe[4] in 1929, the ligands were regarded as point charges. This theory has proved to be very powerful because the point symmetry of the impurity environment can be used to express the optical properties in terms of a few integrals of the radial parts of the electronic wave functions. These integrals then become parameters in fitting the experimental observations to the theory. Since the parameters obtained in this way are sometimes as much as an order of magnitude larger than those estimated by regarding the ligands as point charges (we don't know exactly what the radial wave functions are), the Bethe theory is thought to be only part of the truth.[3,5] A more general description of the crystal field using molecular orbitals was proposed by Mulliken[6] in 1935; in this description the wave functions on the impurity and on the ligands become mixed. Thus while the observed crystal field parameters lead us to suspect that a molecular orbital description is necessary, the observation of a nephelauxetic effect virtually demands it. In addition, the amount of delocalization of the impurity wave function can be inferred from the magnitude of the nephelauxetic effect, as we shall see.

Jorgensen has studied the nephelauxetic effect extensively in the transition metal complexes.[5,7] (A complex is a chemical unit consisting of a central ion with several ligands arranged symmetrically about it.) Just as the rare earths are characterized by a partially-filled $4f$ shell, the transition metals are characterized by a partially-filled d shell. However, the shielding of this d shell frequently is not strong enough to prevent strong interactions between the d electrons and the ligands. Reductions of the electrostatic interaction to less than 50% of its free-ion magnitude are not uncommon in transition-metal complexes, especially those containing ions from the third transition series.

There are two accepted explanations for the nephelauxetic effect in transition metal complexes; these are called central-field covalency and symmetry-restricted covalency.[8] Central-field covalency refers to the extension of the ligand electrons into the region between the central atomic core and the outer electrons. This reduces the effective positive charge on the atomic core from z for the free-ion to z_* for the impurity ion; this modification in the charge on the central core changes the wave function of the outer electron. Then when the electrostatic interaction energy of two electrons is calculated quantum-mechanically, it is altered by a factor z_*/z from the free-ion value.[9] Symmetry restricted covalency refers to the formation of molecular orbitals ψ_{mo} from the impurity and ligand electronic orbitals, ψ_{imp} and ψ_{lig}; i.e.

$$\psi_{\mathrm{mo}} = a\,\psi_{\mathrm{imp}} + b\,\psi_{\mathrm{lig}}$$

where a and b are the delocalization coefficients. Thus, if both interacting electrons are described by this wave function, the electrostatic interaction is reduced by a factor a^4 from its value in the free ion.

When central-field covalency and symmetry-restricted covalency are combined, the magnitude of the electrostatic interaction of the electrons on the impurity is a factor $a^4 z_*/z$ smaller than that of the electrons on the free-ion. But how can the experimental data be used to distinguish between these two explanations? When the values of the nephelauxetic ratio (i.e., the ratio of the electrostatic interaction calculated from the impurity-ion spectrum to that calculated from the free-ion spectrum) are equated to this factor, it becomes obvious that central-field covalency alone is not responsible for the nephelauxetic effect (z_* is ridiculously small). Separate calculations of a and z_* could be made if the nephelauxetic reduction in the spin-orbit interaction were available; unfortunately, the values of this interaction are very uncertain in the transition metal complexes.

3. The Divalent Rare Earth Ions

Although it had been known that some rare earths can exist as divalent impurities, McClure and Kiss[10] first demonstrated in 1963 that the entire series can exist as divalent impurities in CaF_2. They also presented evidence that indicated that these impurities reside in sites of cubic symmetry, e.g., at the center of a cube of 8 F^- ions. Many of the impurities were shown to have optical absorption bands in the visible region; however, the detailed analysis of these spectra has been slow and difficult. This is due mainly to the exceedingly complicated spectra that partially-filled f shells permit. Hence, only the ions at the ends and center of the series can be studied for only these systems can be analyzed as two- or three-electron spectra.

Piper, Brown, and McClure[11] made the first detailed study of the optical absorption spectrum of a divalent rare earth impurity in 1966; they examined Yb^{2+} in $SrCl_2$. This analysis, as well as those to be described, was made possible by the spectroscopic studies of the free ions being done at the Johns Hopkins University and the National Bureau of Standards almost concurrently.[12] These authors found that the observed spectrum arose from transitions between a filled $4f^{14}$ shell and levels of an excited $4f^{13}5d$ configuration and that it could be described quite well with crystal field theory. That is, there seemed to be no need to modify the parameters of the electrostatic interaction from their free-ion values.

Several years later Alig, Kiss, Brown, and McClure[13] examined the spectrum of Ce^{2+} in CaF_2. This ion is unusual in that the ground state of the free ion lies on the $4f^2$ configuration while the ground state of the impurity ion lies in the $4f5d$ configuration. Because of this, however, the transitions responsible for the optical absorption of the impurity terminate on levels of the $4f^2$ configuration and yield little information about the $4f5d$ configuration. Once again the crystal field theory seemed to be adequate. Some predictions however, especially those associated with the $4f5d$ configuration,[14] were not in accord with experiment.

More years passed before Weakliem[15] examined the optical spectrum of Eu^{2+} in CaF_2. This spectrum results from transitions between the ground state in the $4f^7$ configuration and excited states of the $4f^6 5d$ configuration. The analysis is simplified because the $4f^7$ core behaves, in many respects, like a filled shell. It is complicated, however, by the absence of an analysis of the free ion. Nevertheless it is possible to interpolate the free-ion data for the ions at the ends of the rare earth series to obtain a fairly accurate estimate of the electrostatic interaction between the $4f$ and $5d$ electrons.[16] Weakliem found it was impossible to fit the calculated spectrum to the observed spectrum unless this electrostatic interaction was halved. This was the first[17] indication that a large nephelauxetic effect existed among the rare-earth ions and the first time it had occurred in the interaction between electrons on different shells. However, because the free-ion electrostatic interaction was not known, because this interaction was only one of several commensurate interactions contributing to the splitting of the $4f^6 5d$ configuration, and because other descriptions based on the crystal field theory which existed in the literature,[18] the evidence for the existence of this nephelauxetic effect was not overwhelming.

The inadequacy of the crystal field theory was substantiated a short time later by the work of Alig, Duncan, and Mokross[19] on Tm^{2+} in $SrCl_2$. This absorption spectrum results from transitions between a ground state in the $4f^{13}$ configuration and excited states of the $4f^{12}5d$ configuration. Fortuitously, a small group of the 364 possible levels in the $4f^{12}5d$ configuration lie at much lower energies than the rest of the levels and are responsible for absorption bands in the visible. Furthermore the splitting within this small group of levels is due almost entirely to the electrostatic interaction between the $4f$ and $5d$ electrons. These authors found that the calculated energies were in agreement with the experimental data only when the electrostatic interaction was multiplied by the factor 0.6.

It would appear that a large nephelauxetic effect is a common property of the divalent rare earths were it not for the example of Yb^{2+} in $SrCl_2$ mentioned above. Recently this impurity system has been re-examined.[20] Although the work is incomplete, it is already apparent that with a reduction in the electrostatic interaction spectra can be calculated that are in good agreement with much of the experimental data given in Ref. [11]. This is illustrated in Fig. 1 which shows the spectra calculated with and without a nephelauxetic effect together with the experimental spectrum. Clearly, both calculated spectra are in good agreement with the experimental spectrum, yet the ratios of the electrostatic, the $5d$-electron crystal field, and the

5*d*-electron spin-orbit interactions for the lower and upper calculated spectra are 0.75, 1.29, and 0.69, respectively.

Thus, there seems to be substantial evidence for a large nephelauxetic effect associated with the 4*f* and 5*d* electrons on divalent rare-earth impurities. Since the 4*f* shell is well shielded and does not exhibit large nephelauxetic effects by itself,[7] we are led to associate this phenomenon with the 5*d* electron. The reduction in the electrostatic interaction of the 4*f* and 5*d* electrons could be due to an increased separation of the two electrons, i.e., central-field covalency, or to the formation of molecular orbitals from the 5*d* and ligand electronic orbitals. Thus, if only the 5*d* electronic wave function changes significantly, we expect the electrostatic interaction to be reduced by a fac-

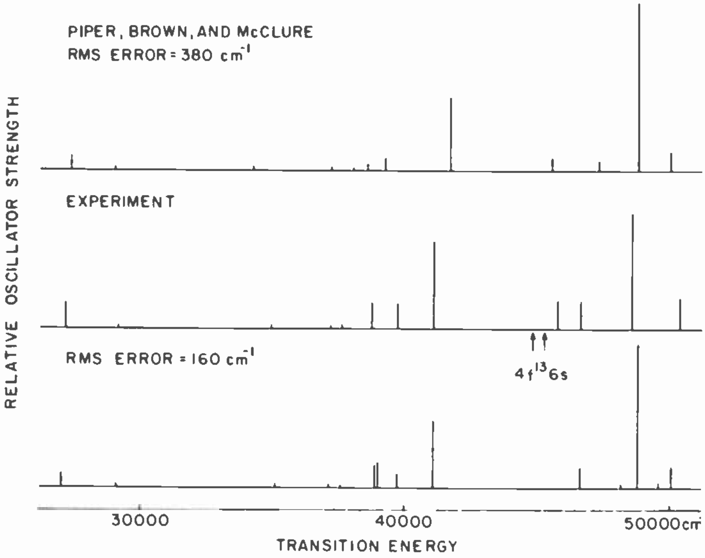

Fig. 1—The relative oscillator strengths of the optical transitions between the ground and excited states of Yb^{2+} in SrCl$_2$ are plotted versus the energy of the transition. The experimental absorption spectrum from Ref. [11] is shown in the center diagram. The spectrum calculated by Piper, et al.,[11] using crystal field theory alone, is shown at the top; a spectrum calculated[20] with a nephelauxetic effect is shown at the bottom. The root-mean-square error between the calculated and experimental absorption energies is shown for both calculated spectra. In calculating the lower spectrum, it was assumed that the absorption line observed near 46000 cm^{-1} is due to admixture of the $4f^{13}5d$ configuration with the $4f^{13}6s$ configuration by the crystal field. The free-ion absorption to the $4f^{13}6s$ levels is marked by arrows in the experimental spectrum.

tor $a^2 z_*/z$ (instead of $a^4 z_*/z$)* from the free-ion value. We expect, also that the spin-orbit interaction of the $5d$ electron will be changed† by the factor $a^2(z_*/z)^4$. For Yb^{2+} in $\mathrm{SrCl_2}$, described above, these factors, 0.75 and 0.69, are quite similar—this would suggest that the nephelauxetic effect arises from the formation of molecular orbitals with the ligands.

References

[1] A. Bril, W. L. Wanmaker, and C.D.J.C. de Laat, "Flourescent Properties of Red-Emitting Europium-Activated Phosphors with Cathode Ray Excitation," *J. Electrochem. Soc.*, **112**, p. 111 (1965).

[2] W. V. Smith and P. P. Sorokin, *The Laser*, McGraw-Hill Book Co., N. Y. (1966).

[3] C. Anderson, *The Physics of Fluorite Compounds*, p. 281, ed. by W. Hayes, Clarendon Press, Oxford (1974).

[4] H. Bethe, "Termaufspaltung in KRISTALLEN=" *Ann. Physik*, **3**, p. 133 (1929).

[5] G. C. Allen and K. D. Warren, "The Electronic Spectra of the Hexafluro Complexes of the First Transition Series," *Structure and Bonding*, **9**, p. 49 (1971).

[6] R. S. Mulliken, "Electronic Structures of Molecules. XI. Electroaffinity, Molecular Orbits and Dipole Moments," *J. Chem. Phys.*, **3**, p. 573 (1935).

[7] C. J. Jorgensen, "The Nephelauxetic Series," *Prog. in Inorganic Chem.*, **4**, p. 73, (1962).

[8] C. K. Jorgensen, "Recent Progress in Ligand Field Theory," *Structure and Bonding*, **1**, p. 3 (1966).

[9] If the radial wave functions are hydrogenic, the electrostatic interaction is linear in the central positive charge. See E. U. Condon and G. H. Shortley, *Theory of Atomic Spectra*, Univ. Press, Cambridge, U. K. (1967).

[10] D. S. McClure and Z. J. Kiss, "Survey of the Spectra of the Divalent Rare-Earth Ions in Cubic Crystals," *J. Chem. Phys.*, **39**, p. 3251 (1963).

[11] T. S. Piper, J. P. Brown and D. S. McClure, "fd and $f^{13}d$ Configurations in a Crystal Field and the Spectrum of Yb^{++} in Cubic Crystals," *J. Chem. Phys.*, **46**, p. 1353 (1967).

[12] G. H. Dieke, *Spectra and Energy Levels of Rare Earth Ions in Crystals*, Interscience Pub., New York (1968), and J. Sugar and J. Reader, "Ionization Energies of Doubly and Triply Ionized Rare Earths," *J. Chem. Phys.*, **59**, p. 2083 (1973).

[13] R. C. Alig, Z. J. Kiss, J. P. Brown and D. S. McClure, "Energy Levels of Ce^{2+} in $\mathrm{CaF_2}$," *Phys. Rev.*, **186**, p. 276 (1969).

[14] A. Kiel and J. F. Scott, "Impurity Raman Scattering from $\mathrm{CaF_2}$:Ce," *Phys. Rev.*, **B6**, p. 2033 (1970).

[15] H. Weakliem, "Electronic Interactions in the $4f^6\,5d$ Configuration of Eu^{2+} in Crystals," *Phys. Rev.*, **B6**, p. 2743 (1972).

[16] A calculation of this interaction on the free Eu^{2+} ion was recently done by J. Sugar and N. Spector, "Spectrum and Energy Levels of Doubly Ionized Europium (Eu III)," *J. Opt. Soc. Am.*, **64**, p. 1484 (1974).

[17] Both A. Yanase and T. Kasuya, "Magneto-Optical Effect due to Eu^{2+} Ion," *Progr. Theoret. Phys.* (Kyoto) Suppl., **46**, p. 388 (1970); and H. A. Weakliem, C. H. Anderson and E. S. Sabisky, "Magnetic Circular Dichroism Spectra of Divalent Lanthanide Ions in Calcum Fluoride," *Phys. Rev.*, **B2**, p. 4354, (1970), had previously noted that the electrostatic interaction of the $4f$ and $5d$ electrons on the Eu^{2+} ion appeared to be smaller in an crystalline environment than in the free ion.

[18] M. V. Eremin, "The $4f^{n-1}$-$5d$ Electrostatic Interaction of Tm^{2+} in $\mathrm{SrCl_2}$," *Optics and Spect. (USSR)*, **26**, p. 317 (1969).

[19] R. C. Alig, R. C. Duncan, Jr., and B. J. Mokross, "Reduced $4f$-$5d$ Electrostatic interaction of Tm^{2+} in $\mathrm{SrCl_2}$," *J. Chem. Phys.*, **59**, p. 5837 (1973).

[20] R. C. Alig, *Bull. Am. Phys. Soc.*, **19**, p. 258 (1974).

---

* If the charge distributions represented by the $4f$ and $5d$ wave functions are replaced by spherical shells at the radii of maximum electronic density, then by Gauss' law, the interaction energy is inversely proportional to the radius of the larger shell. From Ref. [9], the change in the radius of the $5d$ electronic wave function is proportional to z/z_*.

† For hydrogenic radial wave functions, see Ref. [9].

Two Dimensional Phase Transitions of Mobile Ions at SiO_2–Si Interfaces

Peter J. Wojtowicz

RCA Laboratories, Princeton, N.J. 08540

Abstract—The possibility of phase transitions involving the distribution of mobile positive ions at SiO_2–Si interfaces is examined. A theoretical model is constructed based on the image force interaction of the ions at the interface. The model is found to exhibit phase transitions from states in which the ions are condensed into patches of high concentration to states in which the ions are uniformly distributed. At high concentrations of ions at the interface the transitions are first order, while for low concentrations the transitions are third order. The critical temperatures are found to decrease with increasing average ionic concentration. Estimates of the magnitudes of the critical temperatures and accompanying thermal anomalies are made.

1. Introduction

Phase transitions in physical systems of less than three dimensions have attracted the attention of numerous investigators. Examples of much current interest include two dimensional ferromagnetism and antiferromagnetism in layer structures[1] and one dimensional metal-insulator and Peierls transitions in certain salts and organic compounds.[2] Mathematical models of phase transitions in one or two dimensions have also been popular since these are sometimes exactly soluble.[3] In this paper we examine the possibility of a new and different kind of two dimensional phase transition, the condensation of mobile positive ions at the SiO_2–Si interface.

Mobile positive ions in SiO_2 have been the subject of extensive research because of their importance in the instability of devices composed of Si–SiO_2 or Si–SiO_2–metal layers. The appropriate literature is cited in References (4)–(6). The main features of interest to the present study are as follows. Mobile positive ions, usually sodium ions or protons, can be present in SiO_2 layers as natural impurities or as purposely introduced species. Depending on the history of the samples the ions can be found concentrated at either the SiO_2–Si or the SiO_2–metal interface. The mobility of the ions is relatively high and transport through the SiO_2 layer from one interface to the other is possible upon application of suitable electric potentials. High concentrations of positive ions near the silicon interface are found to enhance the internal photoemission of electrons from the silicon into the SiO_2 layer. Measurements of the enhancement of the photoemission as a function of position on the silicon interface have demonstrated[4,5] that the positive ions are aggregated into patches of relatively high concentration, rather than being uniformly distributed over the interface. This last finding is particularly significant. The aggregation into patches of high concentration constitutes a state of low entropy. Since for sufficiently high temperatures equilibrium states are always those of high entropy, there must be some temperature or range of temperatures where the ions disperse over the entire interface. Thus, as already suggested by Williams and Woods,[6] it is of interest to inquire into the possible existence and nature of a phase transformation involving the distribution of mobile positive ions at the SiO_2–Si interface.

In the ensuing sections we will investigate this question by constructing a simple mathematical model of the behavior of positive ions at the SiO_2–Si interface. The essential element of the model is the image force interaction of the ions as discussed by Williams and Woods.[6,7] The model is found to exhibit phase transitions of rather unusual character depending on the concentration of ions present. The nature of these transitions will be described along with estimates of the temperatures at which they might be observed in real SiO_2–Si interfaces.

2. Image Force Interactions

The behavior of positive ions in SiO_2 layers has been rationalized by Williams and Woods[6,7] in terms of the classical electrostatic image force interaction. The potential energy $U(z)$ of an ion in SiO_2 a distance z from a plane interface with another medium is given by the classical formula

$$U(z) = \left(\frac{q^2}{4\epsilon_1 z}\right)\left(\frac{\epsilon_1 - \epsilon_2}{\epsilon_1 + \epsilon_2}\right). \qquad [1]$$

where q is the electronic charge, ϵ_1 is the dielectric constant of silica (3.8), and ϵ_2 is the dielectric constant of the medium on the other side of the interface. The characteristics of this function are displayed in Fig. 1a for three important cases. When silica interfaces with vacuum ($\epsilon_2 = 1$) the image force interaction is repulsive. For an interface with intrinsic silicon ($\epsilon_2 = 11.7$) the image force is attractive, while in the case of a metal ($\epsilon_2 \rightarrow \infty$) the image force is even more strongly attractive. The final term in parenthesis in Eq. [1] shows in fact that, for a given distance, the binding of an ion to an interface with a metal is twice that for intrinsic silicon. At a distance, z of about 1 Å the potential depth is about 1 eV at a metal interface and about 0.5 eV at an interface with silicon.

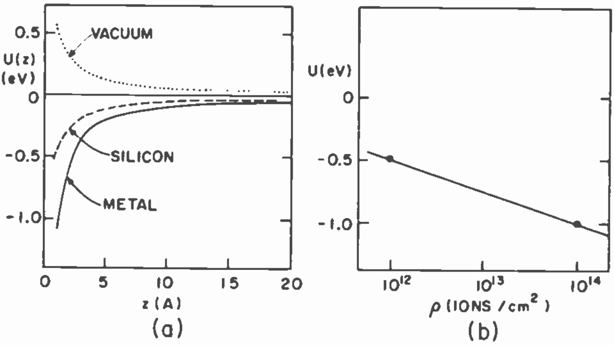

Fig. 1—(a) Potential energy of an ion in SiO_2 a distance z from a plane interface with another medium (after Ref. [6]). (b) Potential energy of an ion in SiO_2 a distance of 1 Å from a plane interface, with Si as a function of the surface concentration ρ of other ions in its neighborhood.

As described by Williams and Woods,[6] the most interesting feature of the image force interaction is the behavior at the SiO_2–Si interface. For intrinsic silicon, Eq. [1] is valid as displayed if ϵ_2 is set equal to 11.7. However, each ion in the silica induces a matching free electron (image charge) in the silicon. As the number of ions in the silica increases, the number of electrons in the silicon also increases. The silicon becomes n type, then degenerate n type, and eventually must behave as a metal. For example, at a surface concentration of 10^{12} ions/cm^2, the volume concentration of image charges is 10^{18} electrons/cm^3; the Debye length corresponding to this electron density in silicon is

40 Å and the silicon behaves as a dielectric. At a surface concentration of 10^{14} ions/cm^2, the volume concentration of image charges rises to 10^{21} electrons/cm^3 and the screening length is reduced to 1.2 Å; the silicon is now behaving as a metal. Thus, as the concentration of ions at the interface increases from 10^{12}/cm^2 (or less) to 10^{14}/cm^2, the binding energy of each of the ions to the interface increases by approximately a factor of two. If we assume that the ions reside at a distance of about 1 Å from the SiO_2–Si interface, the binding energy changes from 0.5 eV to 1 eV over the aforementioned concentration range. A substantial decrease in the energy of the system is therefore possible if (as has been observed) the ions cluster into patches of locally high concentration.

3. The Theoretical Model

The construction of the theoretical model begins with the deduction of an approximate potential energy function for each ion in terms of the local concentration of other ions in its neighborhood. We assume that the positive ions in the silica are situated within about an Angstrom of the plane SiO_2–Si interface. The considerations of the previous section then provide two points in the concentration range of interest. For a local surface concentration ρ of 10^{12} ions/cm^2, the energy binding the ion to the interface U is about 0.5 eV; for $\rho = 10^{14}$ ions/cm^2, $U = 1$ eV. These data are displayed in Fig. 1b as the two points. Binding energies at ionic concentrations intermediate to these points will be approximated by the straight line drawn through these points. The functional relationship between the binding energy per ion and the local concentration of ions is then simply

$$U = U_0 - U_1 \ln \rho. \qquad [2]$$

where U_0 and U_1 are constants. For the situation shown in Fig. 1b, $U_0 = 2.5$ eV and $U_1 = 0.11$ eV. If the ions reside at a distance greater than 1 Å from the interface then, according to Eq. [1], U_0 and U_1 will scale down with the inverse of the distance. The energy relationship, Eq. [2], is simple and convenient and closely approximates the results that would be obtained from Eq. [1] using an explicit model[7] for the dependence of ϵ_2 on ρ. It can, however, be in error for local concentrations outside the range shown in Fig. 1b. For $\rho < 10^{12}$ ions/cm^2 the magnitude of U will be underestimated while for $\rho > 10^{14}$ ions/cm^2 the magnitude of U will be overestimated. In the development that follows we will find that these problems are of no great consequence. The model will preclude the existence of regions of very high ρ by including an upper bound for this quantity (which in the real system is determined by lateral repulsive forces between the ions[7]). At the opposite end of the range, the terms in the free energy that represent the regions of low local ionic concentration will be seen to make relatively small contributions, so that errors introduced by the simplicity of Eq. [2] will not be serious.

The energy and entropy of the system of N positive ions at the SiO_2–Si interface can now be derived. We divide the interface into an assembly of N_A elementary areas of area A containing a number N_S of sites in which positive ions can reside. The size of an elementary area is chosen to be large enough to contain enough sites so that a local surface concentration of ions can be defined, yet small enough that each area can be considered an individual element in a system upon which statistical mechanics is to be performed. It seems reasonable that the areas should be chosen such that $N_A \approx N_S$, the number of areas is approximately the number of available sites within an area. The introduction of the number of available sites per area N_S serves to place an upper limit on the local concentration of ions at the interface. Though not of critical importance in these calculations, the actual magnitude of N_S can be established from the lateral repulsive forces acting between the ions;[7] a value of about 1 to 3×10^{14} per cm^2 is indicated.

We label each area with the index α; $\alpha = 1, 2, \ldots, N_A$. For each α we define an occupation parameter n_α which gives the number of ions actually contained in area α; $0 \leq n_\alpha \leq N_S$. Since the total number of ions at the interface is conserved the n_α must satisfy the condition, $\Sigma_\alpha \, n_\alpha = N$. In the special case where the ions are distributed uniformly across the interface all areas are equally occupied and $n_\alpha = \bar{n} = N/N_A$ for all α. This will be called the disordered state. The ordered state of the system will be that in which the ions are as well condensed into patches of as high concentration as possible. That is, N/N_S areas will have $n_\alpha = N_S$, the maximum occupation, while the remaining $N_A - (N/N_S)$ areas will have $n_\alpha = 0$. The introduction of the concepts of elementary areas and occupation parameters is particularly convenient because it permits the problem of the condensation of the ions to be treated as an order–disorder phenomenon.

The energy of an ion in area α can be computed using the relationship between image force potential and local ion concentration, Eq. [2], deduced in the previous section:

$$U_\alpha = U_0 - U_1 \ln(n_\alpha / A). \qquad [3]$$

The energy of the entire elementary area α containing n_α ions is then

$$E_\alpha = n_\alpha U_\alpha = n_\alpha[U_0 - U_1 \ln(n_\alpha/A)], \qquad [4]$$

while the energy for the total number of ions at the interface is

$$E = \sum_\alpha E_\alpha = \sum_\alpha n_\alpha[U_0 - U_1 \ln(n_\alpha/A)]. \qquad [5]$$

Collecting constant terms,

$$\begin{aligned} E &= E_0 - U_1 \sum_\alpha n_\alpha \ln n_\alpha, \\ E_0 &= N(U_0 + U_1 \ln A). \end{aligned} \qquad [6]$$

The entropy of the ions in area α is given in terms of the number of ways n_α ions can be permuted among the N_S equivalent sites in α:

$$S_\alpha = k \ln \frac{N_S!}{n_\alpha!(N_S - n_\alpha)!}, \qquad [7]$$

where k is the Boltzmann constant. Using Stirling's approximation,

$$S_\alpha = k[N_S \ln N_S - n_\alpha \ln n_\alpha - (N_S - n_\alpha)\ln(N_S - n_\alpha)]. \qquad [8]$$

The entropy of the total number of areas on the interface is

$$S = \sum_\alpha S_\alpha. \qquad [9]$$

Separating out constant terms,

$$\begin{aligned} S &= S_0 - k\sum_\alpha [n_\alpha \ln n_\alpha + (N_S - n_\alpha)\ln(N_S - n_\alpha)], \\ S_0 &= k N_A N_S \ln N_S. \end{aligned} \qquad [10]$$

The free energy, $F = E - TS$, is

$$\begin{aligned} F = {} & F_0 - U_1 \sum_\alpha n_\alpha \ln n_\alpha \\ & + kT \sum_\alpha [n_\alpha \ln n_\alpha + (N_S - n_\alpha)\ln(N_S - n_\alpha)], \end{aligned} \qquad [11]$$

where $F_0 = E_0 - TS_0$.

The computation of the free energy of the ions, Eq. [11], involved a number of approximations. First is the use of the simple formula Eq. [2] for the potential energy of the ions. Next is the neglect of the energy of interaction of the ions in the lateral direction; this is partially accounted for, however, by setting a limit N_S on the number of ions that can occupy a given elementary area. Except for the conservation of total ion number, the elementary areas are treated as independent; the energy of interaction between neighboring areas is neglected as are any additional entropy terms coming from the permutation of the areas among themselves. Both of these contributions are small, however, compared to those included in Eq. [11].

4. Reduction to a Single Order Parameter

The determination of the equilibrium distribution of ions at the SiO_2–Si interface for any given temperature T and number of ions present N requires the minimization of the free energy, Eq. [11], with respect to the N_A occupation parameters n_α. This is an essentially impossible task because of the large number of variables involved. A simplifying approximation will now be made that permits the free energy to be written in terms of a single order parameter. With only this one variable present, the determination of the minima of the free energy becomes straightforward and the equilibrium distributions of the ions are easily found.

At the highest temperatures, the equilibrium state of the system is that having the maximum entropy, Eq. [10]. This is the disordered state with all $n_\alpha = \bar{n}$. At very low temperatures the equilibrium state is that having the lowest energy, Eq. [6]. This is the ordered state with N/N_S of the n_α equal to N_S, and the remaining $N_A - (N/N_S)$ of the n_α equal to zero. We now make the simplifying assumption that all N/N_S of the n_α which must increase from $\bar{n}$ to N_S as the system orders will do so uniformly. That is, all these n_α will have the common value n_I $(\bar{n} \leq n_I \leq N_S)$ as the temperature is lowered and the ions redistribute into patches of high concentration. Likewise, all $N_A - (N/N_S)$ of the n_α which must decrease from $\bar{n}$ to zero as the system orders will also do so uniformly; all these n_α will have the common value n_D $(0 \leq n_D \leq \bar{n})$ as the temperature is lowered. In terms of these two variables the free energy becomes

$$
\begin{aligned}
F = F_0 &- U_1\left\{\frac{N}{N_S} n_I \ln n_I + \left(N_A - \frac{N}{N_S}\right) n_D \ln n_D\right\} \\
&+ kT\left\{\frac{N}{N_S}\left[n_I \ln n_I + (N_S - n_I)\ln(N_S - n_I)\right]\right. \\
&\left. + \left(N_A - \frac{N}{N_S}\right)\left[n_D \ln n_D + (N_S - n_D)\ln(N_S - n_D)\right]\right\}. \qquad [12]
\end{aligned}
$$

The variables n_D and n_I are not independent. Because of the conservation of the total number of ions,

$$\frac{N}{N_S}n_I + \left(N_A - \frac{N}{N_S}\right)n_D = N. \qquad [13]$$

This relation permits the introduction of a single variable, an order parameter, to describe the distribution of the ions. We define the order parameter as the reduced difference between the occupation of those areas that are increasing and the occupation of those that are decreasing:

$$s = (n_I - n_D)/N_S. \qquad [14]$$

In the completely ordered state ($n_I = N_S$, $n_D = 0$), $s = 1$ while in the completely disordered state ($n_I = n_D = \bar{n}$), $s = 0$. The order parameter s thus plays the same role as the reduced magnetization in a ferromagnet. Combining Eq. [13] and [14],

$$\begin{aligned} n_I &= (1 - s)\bar{n} + sN_S, \\ n_D &= (1 - s)\bar{n}. \end{aligned} \qquad [15]$$

The substitution of Eq. [15] into Eq. [12] gives the free energy as an explicit function of the order parameter s. Because it is more convenient in the actual computation, however, we will display instead the free energy per site, $\mathfrak{F} = F/(N_A N_S)$. In terms of s this function is

$$\begin{aligned} &\mathfrak{F}(s) = \mathfrak{F}_1 - fU_1[g_1 \ln g_1 + g_2 \ln g_3] + kT[f(g_1 \ln g_1 \\ &+ g_2 \ln g_2) + (1 - f)(g_3 \ln g_3 + g_4 \ln g_4)]. \qquad [16] \\ &\mathfrak{F}_1 = f[U_0 - U_1 \ln(N_S/A)], \\ &g_1 = (1 - s)f + s, \quad g_2 = (1 - f)(1 - s), \\ &g_3 = (1 - s)f, \quad g_4 = 1 - (1 - s)f, \end{aligned}$$

where $f = N/(N_A N_S)$ is the fraction of the total number of available sites actually occupied by ions (a measure of the total concentration of ions present at the interface). If we set $s = 1$ in $\mathfrak{F}$ we find $\mathfrak{F}(1) = \mathfrak{F}_1$; $\mathfrak{F}_1$ is thus the free energy per site in the perfectly ordered state. For the completely disordered state, $s = 0$, and

$$\mathfrak{F}(0) = \mathfrak{F}_1 - U_1 f \ln f + kT[f \ln f + (1 - f)\ln(1 - f)]. \qquad [17]$$

The determination of the distribution of the ions at the interface and the exploration of possible phase transitions between these distributions is now reduced to finding the values of the order parameter

s which minimize $\mathfrak{F}(s)$ for various given temperatures T and concentrations of the ions f. The detailed examination of Eq. [16] reveals that the behavior of $\mathfrak{F}$ is qualitatively different depending on whether f is greater or less than ½. We will therefore consider the cases of high and low concentrations separately.

5. Phase Transitions: $f \geq \frac{1}{2}$

The search for the values of the order parameter which minimize the free energy begins with the solution of the equation obtained by setting the partial derivative of $\mathfrak{F}$ with respect to s equal to zero. The derivative of $\mathfrak{F}$, Eq. [16] is

$$\frac{\partial \mathfrak{F}}{\partial s} = f(1 - f)\left[-U_1 \ln\frac{g_1}{g_3} + kT \ln\frac{g_1 g_4}{g_2 g_3}\right]. \qquad [18]$$

For $f \geq \frac{1}{2}$, however, the equation, $\partial\mathfrak{F}/\partial s = 0$ yields only trivial solutions. The solution $s = 0$ exists at all temperatures; for some temperatures it gives a minimum in $\mathfrak{F}$, while at other temperatures it represents a maximum. Solutions with finite s exist in some range of temperatures but these always give a maximum in $\mathfrak{F}$. This unusual situation can be understood by examining plots of $\mathfrak{F}(s)$ versus s for various temperatures and values of f. Fig. 2 displays the curves of $\mathfrak{F}(s) - \mathfrak{F}(0)$ versus s for $f = 0.75$ at a variety of temperatures. At low temperatures the minima of $\mathfrak{F}(s)$ in the domain, $0 \leq s \leq 1$ occur at $s = 1$ (with a non-vanishing slope, $\partial\mathfrak{F}/\partial s$). At temperatures above $kT/U_1 = 0.38369$, the minima of $\mathfrak{F}(s)$ occur at $s = 0$ (with vanishing slope). The temperature dependence of the equilibrium order parameter for the case $f = 0.75$ is shown in Fig. 3. Perfect order (ions condensed into patches of the highest possible local concentration, N_S/A) exists up to the critical temperature, $kT_c/U_1 = 0.38369$. At this temperature a *first order* phase transition takes place and the system becomes completely disordered (ions uniformly distributed over the entire interface).

The same behavior is found for all values of f between ½ and 1. The critical temperature as a function of f may be obtained analytically by solving the equation, $\mathfrak{F}(1) - \mathfrak{F}(0) = 0$:

$$\frac{kT_c}{U_1} = \frac{f \ln f}{f \ln f + (1 - f)\ln(1 - f)}, \quad \left(f \geq \frac{1}{2}\right). \qquad [19]$$

The behavior of T_c versus f for $f \geq \frac{1}{2}$ is shown as the solid curve in Fig. 4. We note that the critical temperature *decreases* with *increas-*

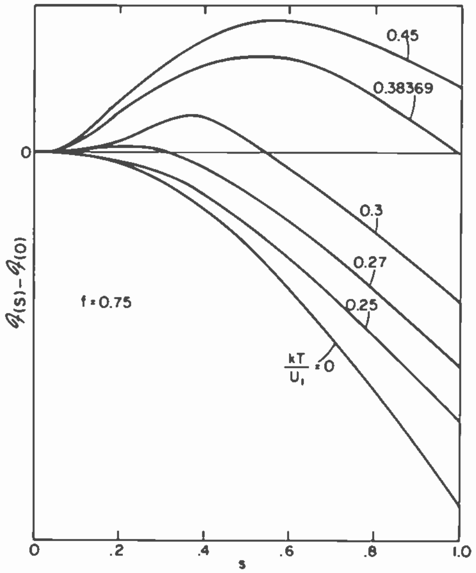

Fig. 2—Schematic representation of free energy (per site) versus order parameter at various temperatures for $f = 0.75$.

ing concentration of the ions on the interface. At first sight this result seems strange since in other cooperative phenomena, such as ferromagnetism, the critical temperature decreases with decreasing concentration of the active species. This feature of the transition is a consequence of the form of the responsible interaction, Eq. [2]. The

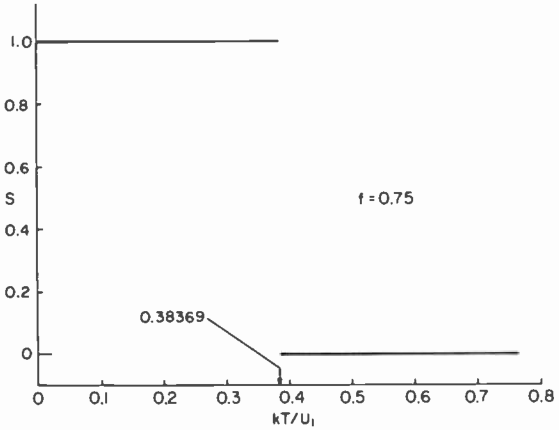

Fig. 3—Temperature dependence of the order parameter for $f = 0.75$.

energy to be gained by each ion upon condensation into patches of high concentration is greatest when the collection of ions condenses from an initially very dilute uniform distribution. The energy gained by condensing from an already concentrated uniform dilution on the other hand is much lower; as a consequence the critical temperature will be reduced.

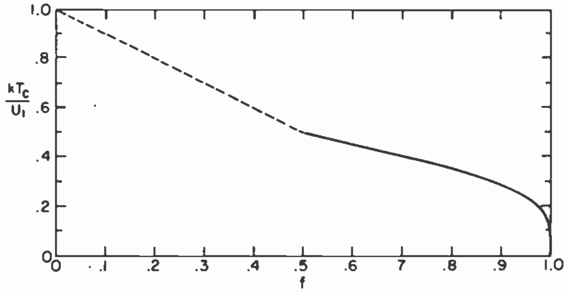

Fig. 4—Concentration dependence of the critical temperatures.

The internal energy per site is obtained from the free energy, Eq. [16] by differentiation: $\varepsilon = \partial(\mathcal{F}/T)/\partial(1/T)$. The latent heat (per site) of the transition is then

$$\Delta\varepsilon = \varepsilon(0) - \varepsilon(1) = -U_1 f \ln f. \qquad [20]$$

The latent heat per ion, on the other hand, is

$$\frac{\Delta E}{N} = \frac{N_A N_S}{N}\Delta\varepsilon = -U_1 \ln f. \qquad [21]$$

In keeping with the discussion of the previous paragraph, the latent heat is also seen to decrease with increasing f. The entropy (per ion) of the transition is obtained from Eqs. [19] and [21]:

$$\frac{\Delta S}{N} = \frac{\Delta E}{NT_c} = -k[\ln f + f^{-1}(1 - f)\ln(1 - f)]. \qquad [22]$$

For $f = \frac{1}{2}$, this entropy change amounts to $2k\ln 2$ per ion; the entropy change vanishes as f approaches unity.

The phase transformation exhibited by this model for $f \geq \frac{1}{2}$ is unusual in that the perfectly ordered state is maintained for a finite range of temperature before any disorder sets in. Though unusual, it is not, however, unique. Similar behavior has been observed by Lieb[8] in his exact solution of the two dimensional Slater KDP model of ferroelectrics. In the present model this feature results from the imposition of a rigid boundary condition concerning the ultimate concentration (N_S/A) to which the ions will condense. If this ultimate concentration was permitted to be established naturally by including the lateral repulsive forces explicitly, this feature would presumably be softened. The order parameter would be everywhere determined by the condition $\partial \mathfrak{F}/\partial s = 0$, and would have values less than unity for finite values of T.

6. Phase Transitions: f < ½

For $f < ½$, the behavior of the free energy $\mathfrak{F}(s)$, Eq. [16], is quite different from that found in the previous section. Fig. 5 displays the curves of $\mathfrak{F}(s) - \mathfrak{F}(0)$ versus s for $f = 0.25$ at a variety of temperatures. As in the previous case, at low temperatures the minima in $\mathfrak{F}(s)$ in the domain $0 \le s \le 1$ occur at $s = 1$ (with nonvanishing slope). At temperatures above $kT/U_1 = 0.5$, however, the minima in $\mathfrak{F}(s)$ occur at values of s less than one and are determined by the usual condition,

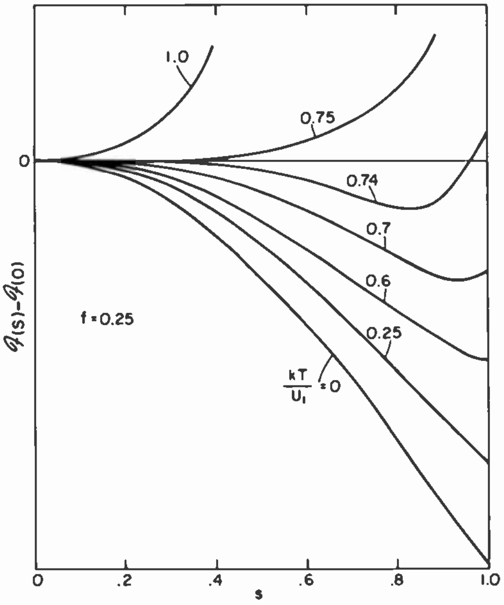

Fig. 5—Schematic representation of free energy (per site) versus order parameter at various temperatures for $f = 0.25$.

the vanishing of $\partial \mathfrak{F}/\partial s$, Eq. [18]. The temperature dependence of the equilibrium order parameter for three cases, $f = 0.25$, 0.10, and 0.01, respectively, are shown in Fig. 6. Perfect order exists up to the temperature $kT/U_1 = 0.5$ independent of the concentration f (as can be verified by solving the equation $\partial \mathfrak{F}/\partial s = 0$ with $s \rightarrow 1$). The order parameter s then decreases continuously to zero. The critical temperature is determined analytically by the condition $\partial \mathfrak{F}/\partial s = 0$ with $s \rightarrow 0$:

$$\frac{kT_c}{U_1} = (1 - f), \quad (f < 1/2). \qquad [23]$$

Again, the critical temperature is found to decrease with increasing concentration f; the behavior of T_c versus f for $f < ½$ is shown as the dashed line in Fig. 4.

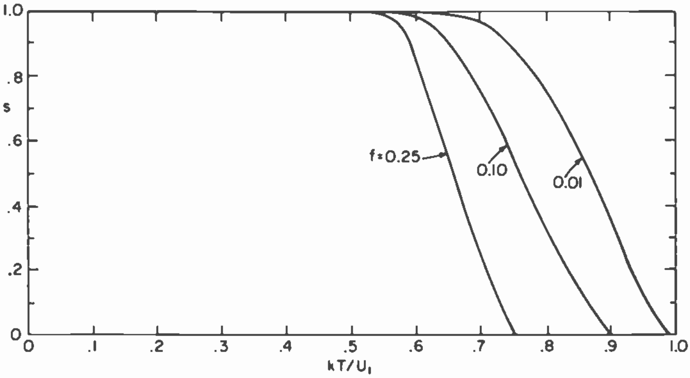

Fig. 6—Temperature dependence of the order parameter for $f = 0.25$, 0.10, and 0.01.

The phase transformations which occur at the critical temperatures given by Eq. [23] are *third order* phase transitions. This can be demonstrated by examining the critical behavior of the thermodynamic functions at temperatures near T_c. At temperatures close to the critical point the order parameter is very nearly zero and the free energy (per site), Eq. (16) can be expanded in a power series in s:

$$\begin{aligned}\mathfrak{F}(s) - \mathfrak{F}(0) &= -U_1\left[\frac{1}{2}(1 - f)s^2 \right. \\ &\left. - \frac{(1 - f)(1 - 2f)}{6f}s^3 + \ldots\right] \\ &+ kT\left[\frac{1}{2}s^2 - \frac{(1 - 2f)^2}{6f(1 - f)}s^3 + \ldots\right]. \qquad [24]\end{aligned}$$

where, as before, $\mathcal{F}(0)$ is the free energy (per site) of the completely disordered state. Collecting terms, Eq. [24] can be re-expressed as an explicit expansion in the parameter s:

$$\mathcal{F}(s) - \mathcal{F}(0) = \frac{1}{2}[kT - (1-f)U_1]s^2 - \frac{(1-2f)^2}{6f(1-f)}\left[kT - \frac{(1-f)^2}{(1-2f)}U_1\right]s^3 + \dots . \qquad [25]$$

The temperature dependence of s near T_c is determined by taking $\partial\mathcal{F}/\partial s = 0$ and solving for s:

$$s = \frac{(kT/U_1) - (1-f)}{\frac{1}{2}(1-2f)}. \qquad [26]$$

As suggested by the curves of Fig. 6, s is a linear function of T near T_c. The actual value of T_c is obtained from Eq. [26] by setting $s = 0$ and is in agreement with Eq. [23]. The internal energy (per site) is obtained from Eq. [25] by differentiation. Keeping only the first term and substituting Eqs. [23] and [26],

$$\mathcal{E} - \mathcal{E}(0) = \frac{-2U_1(1-f)}{(1-2f)^2}\left[\frac{kT_c}{U_1} - \frac{kT}{U_1}\right]^2. \qquad [27]$$

The internal energy just below T_c is thus quadratic in the temperature difference from T_c. The heat capacity (per site) is obtained from Eq. [27] by differentiation:

$$C = \frac{d\mathcal{E}}{dT} = \frac{4k(1-f)}{(1-2f)^2}\left[\frac{kT_c}{U_1} - \frac{kT}{U_1}\right]. \qquad [28]$$

The heat capacity just below T_c is thus a linear function of the temperature difference from T_c. Eqs. [25] through [28] reveal that $\mathcal{F}(s)$, $\mathcal{E}(s)$ and $C(s)$ are all continuous functions of the temperature through the phase transition. The temperature derivative of $C(s)$, however, is discontinuous at T_c (a negative constant below and zero above). This combination of properties is, of course, the major characteristic of a third-order phase change. Phase transitions of the third order are rather rare but do occur in various theoretical models. Two examples are the Bose–Einstein condensation[9] and the two-dimensional hard-square lattice model.[10]

The complete curve of heat capacity (per site) versus temperature is obtained by differentiating the complete free energy function, Eq. [16]:

$$\begin{aligned} C &= kf(1-f)\left(\ln\frac{g_3}{g_1}\right)\left(\frac{C_1}{C_2-C_3}\right), \\ C_1 &= \ln\frac{g_2g_3}{g_1g_4}, \\ C_2 &= \frac{kT}{U_1}\left[\frac{(1-f)}{g_1}+\frac{f}{g_3}+\frac{f}{g_4}+\frac{(1-f)}{g_2}\right], \\ C_3 &= \frac{(1-f)}{g_1}+\frac{f}{g_3}. \end{aligned} \qquad [29]$$

Fig. 7 shows the temperature dependence of C for the case of $f = 0.45$. At temperatures below $kT/U_1 = 0.5$ the system is in a constant state of perfect order and C vanishes. Above this temperature disordering begins and the heat capacity rises, eventually having a broad maximum at a temperature well below the critical point. The heat capacity then declines, falling to zero at $kT_c/U_1 = 0.55$. The discontinuity in the slope of C at T_c is evident, reaffirming the conclusion that this is a third-order phase change.

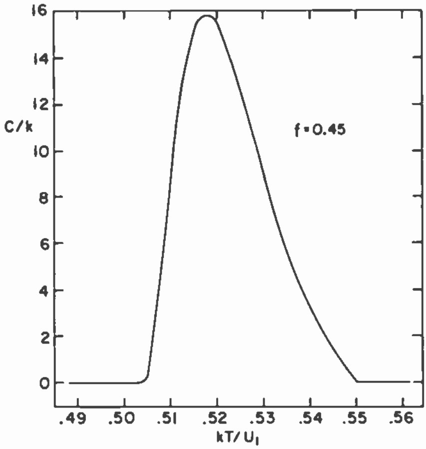

Fig. 7—Temperature dependence of the heat capacity (per site) for $f = 0.45$.

7. Conclusions

The question of the existence of phase transformations involving the distribution of mobile positive ions at the SiO_2–Si interface has been examined. A theoretical model was constructed based on a simplified form of the image force interaction of the ions at the interface. Approximations to the energy and entropy were constructed by introducing the concept of elementary areas containing a fixed number of sites in which ions could reside. The description of the distribution of ions was then simplified by the introduction of a single order parameter. This simplification was made, however, at the expense of fluctuations in the behavior of different elementary areas; by requiring the uniform behavior of the areas, the theory has been in effect reduced to a mean-field or Bragg-Williams type of treatment.

The resulting free energy of the model was examined in detail and two kinds of unusual phase transitions were found. For situations in which more than half the available sites at the interface were occupied by ions, a first-order phase transition was observed to take place from a fully condensed state to a completely uniform distribution. For situations in which less than half of the available sites were occupied, a third-order phase transition is observed. In this case the distribution of ions changes continuously from fully condensed to perfectly uniform over a range of temperatures. In both regimes the critical temperature was found to decrease with increasing average concentration of the ions at the interface.

Eqs. [19] and [23] can be used to estimate the order of magnitude of the phase transition temperatures that can be expected to be found in real systems. If we take the coverage of the interface to be about a half, either formula gives the result that T_c is of the order of $U_1/2k$. In the discussion of the image force interactions leading to Eq. [2], we estimated that U_1 was about a tenth of an electron volt. The critical temperature should therefore be about 600°K. The actual value in any real system could, of course, be less than or greater than this according to whether f is greater or less than a half. The value of U_1 could also be somewhat different in a real situation. The estimate of 600°K is very encouraging, however. In the systems studied to date[4,5] the mobile ions have been found to be condensed into patches of high concentration at room temperature, in agreement with this estimate of T_c.

It is very unlikely that the phase transitions predicted here will ever be seen using the usual classical calorimetric techniques. The heats involved are extremely minute because of the basic two-dimensional nature of the interface system. Eq. [21] gives the latent heat of representative first-order transitions as about $U_1/2$ per ion. Using our estimate of 0.1 eV for U_1 gives latent heats in the range of 0.05 eV/ion $\approx 10^{-6}$ cal/cm^2 (assuming a few times 10^{14} ions/cm^2 at the interface).

The magnitude of the heat capacity peaks of the third-order phase transitions can be estimated from Fig. 7. The maximum in C is about $16\ k$ per site or about $30\ k \times 10^{14} \approx 10^{-8}$ cal/°K per cm^2 (again assuming a few times 10^{14} sites per cm^2). Thus it is quite clear that a non-calorimetric search must be made for these phase transitions. Techniques that are capable of probing the local ionic concentration at the interface (such as the internal photoemission measurements[4,5]) as a function of the temperature are the most likely to be successful.

Acknowledgements

I wish to express my appreciation to Richard Williams for bringing this interesting problem to my attention. I also wish to thank Richard Williams and Roger Cohen for several helpful discussions during the course of this research.

References:

[1] L. J. de Jongh and A. R. Miedema, "Experiments on Simple Magnetic Model Systems," *Adv. in Physics*, **23**, p. 1 (1974); A. R. Miedema, P. Bloembergen, J. H. P. Colpa, F. W. Gorter, L. J. de Jongh and L. Noordermeer, "Heisenberg Ferromagnetism in Two Dimensions: An Experimental Study," *AIP Conf. Proc.*, **18**, p. 806 (1974); also references in both these papers.

[2] H. J. Deiseroth and H. Schulz, "Evidence for Ordered Layers of K^+ in KCP ($K_2[Pt(CN)_4]Cl_{0.3} \cdot 3H_2O$)," *Phys. Rev. Lett.*, **33**, p. 963 (1974); J. M. Williams, J. L. Petersen, H. M. Gerdes and S. W. Peterson, "New Structural Findings from a Neutron Diffraction Study of One-Dimensional $K_2Pt(CN)_4Br_{0.3} \cdot 3H_2O$," *Phys. Rev. Lett.*, **33**, p. 1079 (1974); D. B. Tanner, C. S. Jacobsen, A. F. Garito and A. J. Heeger, "Infrared Conductivity of Tetrathiofulvalene Tetracyanoquinodimethane (TTF-TCNQ) Films," *Phys. Rev. Lett.*, **32**, p. 1301 (1974); P. A. Lee, T. M. Rice and P. W. Anderson, "Fluctuation Effects at a Peierls Transition," *Phys. Rev. Lett.*, **31**, p. 462 (1973); and references in these papers.

[3] For an introduction and further references, see H. E. Stanley, Introduction to Phase Transitions and Critical Phenomena, Oxford University Press, New York (1971).

[4] T. H. DiStefano, "Barrier Inhomogenieties on a Si–SiO_2 Interface by Scanning Internal Photoemission," *Appl. Phys. Lett.*, **19**, p. 280 (1971).

[5] R. Williams and M. H. Woods, "Laser-scanning Photoemission Measurements of the silicon-silicon dioxide Interface," *J. Appl. Phys.*, **43**, p. 4142 (1972).

[6] R. Williams and M. H. Woods, "Image Forces and the Behavior of Mobile Positive Ions in Silicon Dioxide," *Appl. Phys. Lett.*, **22**, p. 458 (1973).

[7] R. Williams, "Image Force Interactions at the Interface between an Insulator and a Semiconductor," *J. Appl. Phys.*, **45**, p. 1239 (1974).

[8] E. H. Lieb, "Exact Solution of the Two-Dimensional Slater KDP Model of a Ferroelectric," *Phys. Rev. Lett.*, **19**, p. 108 (1967).

[9] F. London, "The λ-Phenomenon in Liquid Helium and the Bose-Einstein Degeneracy," *Nature*, **141**, p. 643 (1938).

[10] F. H. Ree and D. A. Chesnut, "Phase Transition of a Hard-Square Lattice with Second Neighbor Exclusions," *Phys. Rev. Lett*, **18**, p. 5 (1967).

Optical Properties of $SrTiO_3$ and $LiNbO_3$

H. A. Weakliem, W. J. Burke, D. Redfield, and V. Korsun

RCA Laboratories, Princeton, N.J. 08540

Abstract—The fundamental optical absorption and reflectance due to electronic transitions in $SrTiO_3$ and $LiNbO_3$ are reviewed in the context of their importance as members of the class of ionic compounds ABO_3 and some new data are added. Marked similarities exist in the reflectivity spectra of many of these compounds, including these two, in spite of significant differences in crystal structure. The optical absorption edges occur in the energy range 3–4 eV, although there are major differences in other properties of these edges. Detailed temperature-dependent absorption spectra of $SrTiO_3$ exhibit clearly a phonon-assisted fundamental transition, as well as an anomalous sign and magnitude of the temperature dependence of the energy gap. $LiNbO_3$ displays a very broad, structureless edge at all temperatures and shows almost no dichroism in spite of the anisotropy in its crystal structure and in its near UV reflectance. Interpretations of these various observations are discussed in relation to the other known properties and theoretical electron energy-band calculations.

1. Introduction

The ABO_3 class of oxide compounds, where A is an alkali or alkaline earth metal and B is a transition metal, is of great current interest because of the wide range of physical phenomena that members of this family exhibit and because of existing and potential applications of particular members of the class. Alloys of these compounds are also of interest for tailoring a material for a particular application. Although members of the class exist in a wide variety of structural modifications, the compounds are almost always insulators. They can, however, be made to exhibit semiconducting or metallic characteristics,[1] and even superconductivity in $SrTiO_3$, by doping with impurities or altering the stoichiometry by heat treatment.[2] We are concerned here with the fundamental optical properties of two members of this class, $SrTiO_3$ and $LiNbO_3$, and with the relationship of these properties to their crystal structures, phase changes, and electronic structures.

In the ABO_3 class with which we are concerned, the B ion is at the center of an octahedral array of oxygen ions. In many compounds of the class, A is a large ion having a size comparable to oxygen, B is much smaller, and the materials crystallize in the perovskite structure which is cubic, space group $Pm3m$. In the perovskite structure the octahedra are linked by sharing corners in all three orthogonal directions. Various structural modifications have been observed that may be described as ordered sets of small ionic displacements. In $BaTiO_3$ and $KNbO_3$, a sequence of phases from cubic to lower symmetries is observed with decreasing temperature, and the lower symmetry phases are usually ferroelectric or anti-ferroelectric.[3] $SrTiO_3$ has the cubic perovskite structure down to 106°K, where it undergoes a transition[4] to a tetragonal phase having space group $I4/mcm$. The phase change is not accompanied by an anomaly in the dielectric constant. The structural change at 106°K has been shown to arise from a softening of a zone center (R point) phonon, and consists of a rotation of the oxygen atoms about the new tetragonal axis, the sense of rotation being reversed in adjacent octahedra so that the unit cell is doubled and the Brillouin zone is halved.[5] Transitions to a trigonal lattice phase on application of a [111] stress[6] and to a ferroelectric phase on application of a [100] stress[7] have been observed. In the absence of [100] stress, $SrTiO_3$ remains paraelectric at all temperatures.

$LiNbO_3$ has a rhombohedral structure,[8] space group $R3c$, and is ferroelectric[9] at all temperatures up to ~1100°C, which is only slightly below the growth temperature of 1250°C. The structure consists of planar sheets of oxygen atoms approximately in hexagonal close packing with both Li and Nb occupying octahedral interstices. The octahedra are irregular and the Nb-containing octahedron shares a face with a vacant octahedron on one side and with an Li-containing one on the other side. Both Li and Nb lie closer to one plane of oxygen atoms than the other.

The stoichiometry of $LiNbO_3$ is sensitive to melt composition and temperature, and large departures from stoichiometry (Li deficiency) have been found.[10] The Curie temperature and the optical birefringence are known to be influenced by these variations in composition.[11] Stoichiometric crystals can be grown from a melt containing excess Li, but crystals grown at the congruent melting point (5% Li deficiency) are most commonly used.

The nature of the electronic states of such oxides has been the subject of many investigations, and it is not possible to describe them within a single framework. Several electronic energy-band-structure calculations for perovskites have been done,[12–14] the earliest being that of Kahn and Leyendecker[12] for $SrTiO_3$. There is agreement that the lowest energy interband transition is from a valence band comprised primarily of oxygen $2p$ orbitals to a conduction band comprised of crystal field split orbitals of transition-metal $3d$ orbitals. A fundamental, recurring problem in all the calculations made to date is that the predicted bandgaps range from 10 to 15 eV, far larger than the observed 3 to 4 eV. It is possible that the influence of correlation effects on band-structure calculations[15] may account for this discrepancy. Thus the tight-binding band structure calculations provide a qualitative model for describing the optical absorption and reflectivity spectra, but detailed interpretation is not possible. No energy-band calculation has been done for the more complicated case of $LiNbO_3$, but we shall show why it is reasonable to describe the fundamental edge as also being due to transitions of electrons from filled oxygen $2p$ bands to empty niobium $4d$ bands.

In this paper we describe the fundamental optical properties of $SrTiO_3$ and $LiNbO_3$ in the visible and UV. $SrTiO_3$ is of particular interest because it is the most thoroughly studied and best understood member of the ABO_3 class and often serves as a model system. In the case of $LiNbO_3$, interest in its fundamental optical properties is stimulated by its increasing technological importance for surface-wave and optical waveguide devices, and as an optical modulator and frequency converter. We shall refer to both the similarities and differences in the optical properties of the members of the class. Specifically, we discuss the optical reflectivity and absorption spectra. Detailed results on the temperature dependence of the absorption spectra are also presented; the experimental techniques are not discussed except for a brief comment on materials. Refractive indexes of $SrTiO_3$[16] and $LiNbO_3$[17] are well known and are also not presented here.

The $SrTiO_3$ samples used in these studies were cut from several crystals of the highest available purity purchased from National Lead Company. These samples were mechanically polished to a window-glass finish. Further polishing with a chemical etchant (hot phosphoric acid) produced no change in the measured absorption. The $LiNbO_3$ samples used were cut from crystals grown at RCA Laboratories by W. Phillips or from Linobate grade crystal grown by Crystal Technology Corp. The samples were mechanically polished to a window-glass finish. Chemical polishing had a significant effect in reducing the extra absorption due to surface damage.

In Sec. 2 the reflectivity spectra of both $SrTiO_3$ and $LiNbO_3$ are described. The absorption edges of $SrTiO_3$ and $LiNbO_3$ are discussed separately in Sec. 3 and 4, respectively.

2. Reflectivity

The room-temperature, near-normal-incidence reflectivity spectrum of $SrTiO_3$ was measured by Cardona[16] and is shown in Fig. 1. There is a strong peak (A) centered about 5 eV, a moderate peak (C) centered about 10 eV, and a weak peak (D) near 12.4 eV. The peaks A and C are slightly split and some weak maxima occur between them. There are distinct minima in the reflectivity near 7.5 eV and 15 eV.

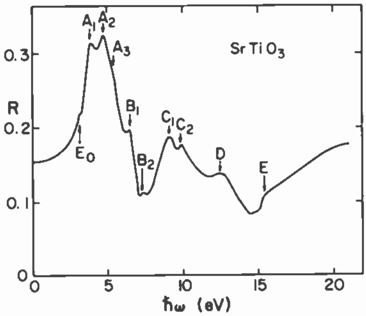

Fig. 1—Reflectivity spectrum of $SrTiO_3$ at room temperature (from Ref. [16]).

The near-normal-incidence reflectivity spectrum of $LiNbO_3$ at room temperature was recently measured using both polarized[18] and unpolarized[19] light. The unpolarized spectrum is shown in Fig. 2 and represents an average suitable for comparison with the isotropic spectrum of cubic $SrTiO_3$. Although the two crystal structures are quite different, and thus the electronic band structures have no required similarity, the two reflectivity spectra are remarkably similar. This similarity extends to other members of this class, including $BaTiO_3$[16] and $KNbO_3$.[18] The $LiNbO_3$ spectrum is less structured than that of $SrTiO_3$, but it also has a strong peak at an energy slightly higher than the fundamental absorption edge (*vide infra*), a weaker peak at about twice the energy of the first, and a third, still weaker, peak as well as two distinct minima.

Only the lowest energy peak (A) of $LiNbO_3$ shows significant polarization effects. The individual polarized spectra are very similar in shape and position, the principal difference being that the π spectrum is 10–20% weaker than the σ spectrum. A Kramers–Kronig analysis shows that the observed reflectivity anisotropy of band (A) completely explains the observed birefringence of the visible refractive indices and the near coincidence of the polarized absorptivities just above the onset of the fundamental edge.[18]

In spite of the anisotropy found in $LiNbO_3$, the average spectrum (Fig. 2) closely resembles the isotropic $SrTiO_3$ spectrum over a wide energy range. Notwithstanding the difference in crystal structures, the gross spectral features must be independent of the details of the energy band structure. This supports the view that the transitions are basically of the charge transfer type involving electrons making transitions from the filled oxygen 2*p* orbitals to the empty *d* orbitals of Nb or Ti. Theoretical estimates place the band arising from the *s* orbitals of Li or Sr at considerably higher energy than the *d* bands. Sum rule calculation of the effective number of valence electrons in $LiNbO_3$ indicates that the 2*s* band of Li begins at 12 eV.[19]

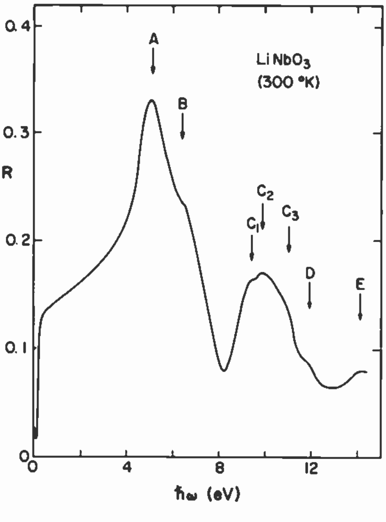

Fig. 2—Unpolarized reflectivity spectrum of $LiNbO_3$ at room temperature.

The 0.8 eV splitting of the bands in $SrTiO_3$ has been attributed to the crystal field and coulomb splitting of the oxygen 2*p* valence band.[16] There could be further splitting of these bands in the case of $LiNbO_3$ because the symmetry is lower. However, in each case, the transition metal is coordinated to six oxygens in an octahedral array; thus, to a first approximation, both have the same set of bonding molecular orbitals (MO). The departure from regularity of the octahedron of (NbO_6) in $LiNbO_3$ arises from a trigonal distortion, and trigonal splitting of cubic states is usually small. Thus, the (MO) states in both cases may be expected to be similar, so the width of the reflectivity peaks is a measure of the splitting of the (MO) levels. The extra symmetry selection rules imposed by the higher translational symmetry of $SrTiO_3$ makes transitions from some of the (MO) states to the 3*d* states forbidden, which may account for the slightly better resolution of the peaks in $SrTiO_3$.

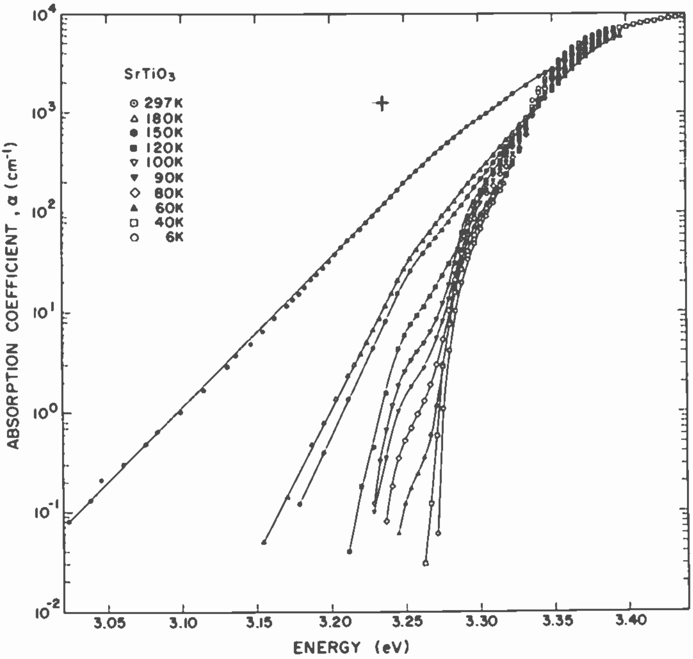

Fig. 3—Temperature dependence of the absorption edge of $SrTiO_3$ for temperatures up to ~300°K. Each curve is a composite of data from samples of 5 thicknesses.

3. Absorption Edge of $SrTiO_3$

The fundamental optical absorption edge of $SrTiO_3$, as measured by transmission methods, has several features that distinguish it from other members of the ABO_3 class of materials. It should be remarked that this material is the most studied one of this class and probably has the best quality with respect to purity and freedom from physical defects. We present first the dc measurements of absorption coefficient, then the wavelength-modulated measurements, and finally a discussion of other related data.

The temperature dependence of the absorption coefficient has been measured by several groups.[20–22] Fig. 3 shows an extension of the work of Redfield and Burke[22] and is the most detailed set of data available for temperatures up to 300°K. Most of the significant features are apparent in this figure. First is the temperature dependence of the energy gap, which should appear as an overall shift of the curves. This is generally obtained by measuring the shift with temperature of the highest portion of the curves because that is where the *shape* is nearly unchanged with temperature. It is evident from Fig. 3 that there is very little temperature shift of the gap up to room temperature. In fact, the curves cross near 10^3 cm^{-1}, which is very unusual. These upper portions of these curves are shown with expanded scales in Fig. 4. Taking the shift in energy gap as the change in photon energy at fixed absorption coefficient between 4,000 and 6,000 cm^{-1}, it is clear that the gap *increases* at higher temperatures—a nearly unique result. Furthermore, the magnitude of this shift, 16 meV up to 180°K, is much less than that of most other materials (for example, it is ~½ that of $LiNbO_3$). The weakness of the temperature dependence of the gap is also confirmed by the analysis of the data at low α as discussed next.

A second principal feature of the data of Fig. 3 is the structure between 3.22 and 3.32 eV, especially the very strong temperature dependence near 3.25 eV. There seems little doubt that these effects are evidences of phonon assisted optical transitions across an indirect energy gap, notwithstanding some theoretical conclusions to the contrary.[14] This interpretation is supported not only by the independent analyses of two groups using conventional transmission measurements[20–22] but also by wavelength-modulated transmission[23] and by electro-absorption at 80°K.[24] Phonon-assisted transitions of this sort lead to the relation $\alpha \sim (\hbar\omega - E_i)^2$ where E_i is the threshold for a particular process. This relation was verified in all the above-mentioned experiments. As an illustration, the derivative spectrum of α is shown in Fig. 5, where the expected linear relation between $\alpha^{1/2}$ or $(\Delta\alpha/\Delta E)$ is seen as a function of energy for the lower portion of the absorption edge.[23]

This phonon participation in the low-energy transitions provides the explanation for the strong temperature dependence of α near 3.25

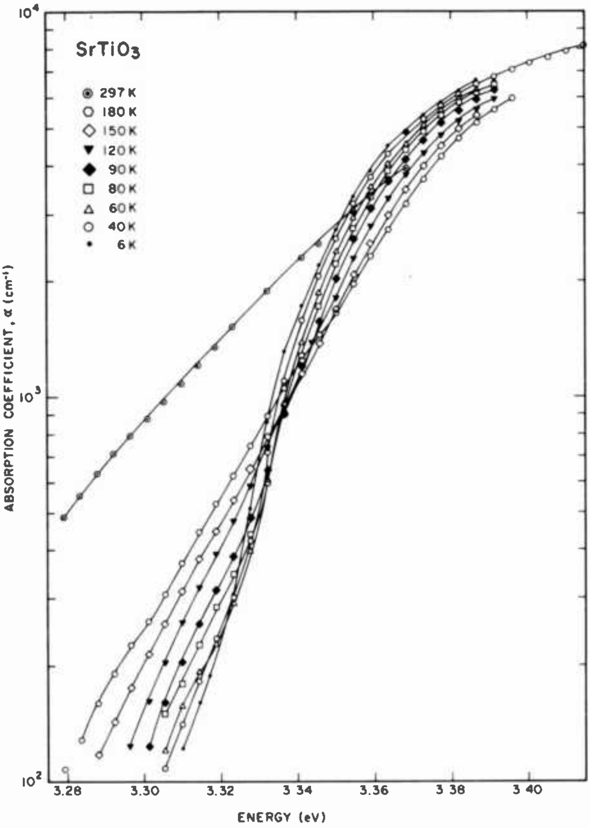

Fig. 4—Enlarged display of the upper portions of the curves of Fig. 3.

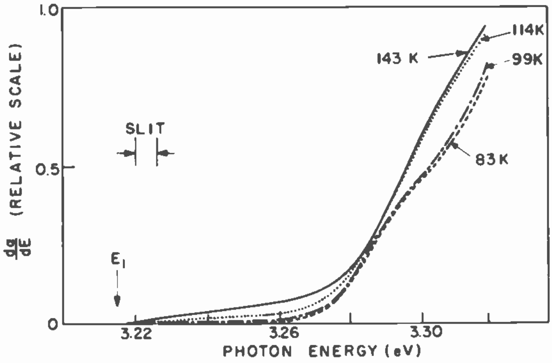

Fig. 5—Photon energy modulation spectra of SrTiO$_3$ at two temperatures above and two below the 106°K phase transition (from Ref. [23]).

eV, the range in which phonon absorption from the lattice is required for momentum conservation in the optical transition. Another aspect of this analysis is the identification of 3 threshold energies—the lowest at 3.22 eV for phonon absorption, the highest at 3.32 eV for phonon emission, and an inadequately explained[24] threshold at 3.27 that is normally unexpected. One significant property of these thresholds is their apparent invariance with temperature up to ~150°K (the highest temperature at which they can be measured).[22] This invariance confirms the very weak temperature dependence of the energy gap inferred from the highest values of α.

There are several other interesting features of the absorption edge of $SrTiO_3$. One is the apparent absence of excitons, which may simply be due to the very high static dielectric constant ($\epsilon_0 \simeq 300$ at 300°K and $\simeq 18{,}000$ at 4°K).[25] A second is the evolution of the structured edge at low temperatures into a smoothly exponential shape at higher temperatures, as shown in Fig. 3. This behavior is also seen in a number of other materials and has been explained by broadening effects of electric microfields associated with polar modes of lattice vibration.[26] Third is the effect of the 106°K phase transition on the absorption edge. This effect has been difficult to observe, presumably because of the second-order nature of the transition and the small distortion characterizing the tetragonal structure. However, thermomodulation absorption measurements for photon energies up to 3.32 eV have recently succeeded in displaying such effects.[27] In view of the crossings of the absorption spectra shown in Figs. 3 and 4, thermodulation measurements for photon energies above 3.35 eV would be of interest.

The clarity and detail of the data on $SrTiO_3$ appear to be the best of any ionic material reported. Therefore, in addition to characterizing the material, they have been used in attempts to deduce the electronic energy-band structure. In view of the similarities to other materials of this class mentioned in the introduction and the close resemblances among the UV reflectivity spectra, it is widely felt that an energy-band structure of $SrTiO_3$ would be applicable in some degree to the other materials.

In spite of all the information available, however, only a rather limited number of reliable conclusions can be drawn about the energy-band structure. The principal one is that the energy gap is indirect, as described above in connection with the structure in the edge. Beyond that, it seems probable that one of the participating band edges is located at an X point of the Brillouin zone. This assignment is supported by analysis of electroreflectance[21] and by phonon energies and symmetries,[23] and is consistent with the original band-structure calculation.[12] In keeping with that calculation, it is generally believed that the valence band maximum is at Γ and the conduction band minimum is at X, and this identification is confirmed by transport measurements.[28] All other aspects of the band structure appear to be conjectural.

4. Absorption Edge of $LiNbO_3$

In spite of the similarity of the reflectivity spectra of $SrTiO_3$ and $LiNbO_3$, the fundamental optical absorption edges are significantly different. Fig. 6 shows the only detailed study[29] of this edge, made between 10°K and 667°K. The temperature dependence of the energy gap was determined from the systematic shift of the upper portions of the curves. The results were quite comparable[29] with those of most other materials, with $SrTiO_3$ remaining exceptional.[22] (Note the compressed scale of photon energy as compared with the corresponding plot of Fig. 3 for $SrTiO_3$.)

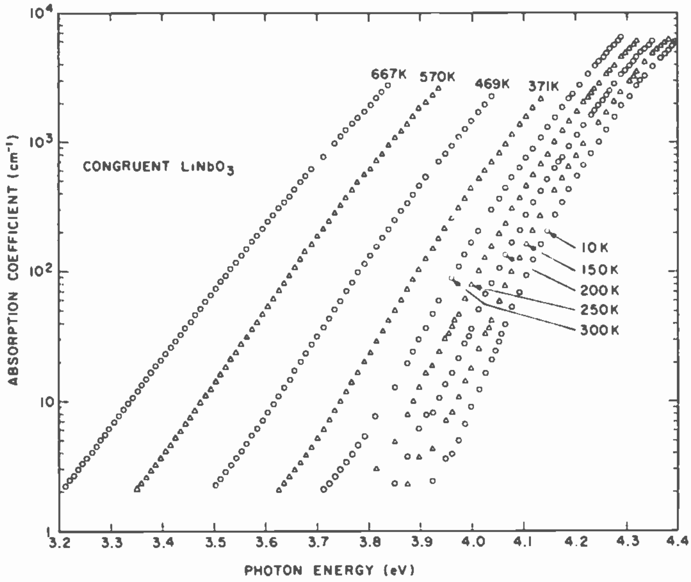

Fig. 6—Temperature dependence of the absorption edge of congruent $LiNbO_3$ (from Ref. [29]). Each curve is a composite of data from samples of 5 thicknesses.

An unusual feature of the edge of $LiNbO_3$ is its great breadth and its smooth curvature at low temperatures. The structure at low absorption coefficients (2–5 cm^{-1}) is believed to be extrinsic. $LiNbO_3$ has the broadest edge at low temperatures of any crystalline material, although above room temperature its breadth is very similar to those of other ionic crystals. An effort has been made to explain[29] this breadth in terms of the broadening effects of electric microfields produced by the defects known to be prevalent in most $LiNbO_3$. These defects are principally point defects associated with the deficiency of Li and O in $LiNbO_3$ crystals grown with the congruent composition.

It is possible, however, to grow crystals with a stoichiometric composition (i.e., equal Li and Nb concentrations), and measurements made of the absorption edge of such a crystal are shown in Fig. 7. The edge at room temperature is ~0.1 eV higher in energy than that of the congruent composition but the shapes are comparable. (The same is true at 80°K.)[29] This similarity in shapes lead to the conjecture, which can be supported by thermodynamic arguments, that stoichiometric $LiNbO_3$ also contains many defects whose nature is unknown.[29]

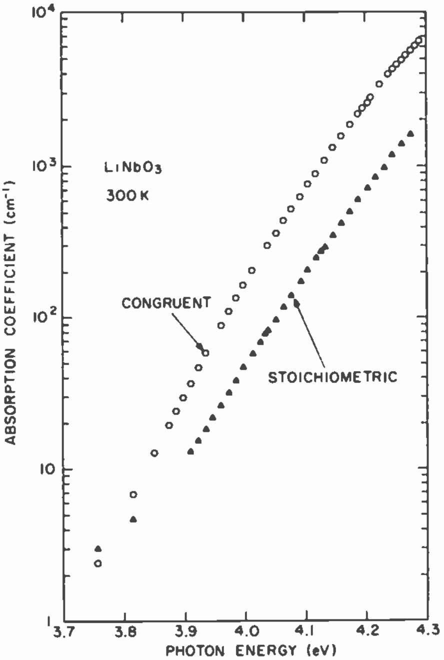

Fig. 7—Comparison of the room temperature absorption edges of congruent and stoichiometric $LiNbO_3$ crystals.

An additional feature of $LiNbO_3$ is the near absence of dichroism in the absorption edge. This is quite unexpected for several reasons: (1) the crystal structure is anisotropic, (2) there is pronounced birefringence in the visible and anisotropic reflectance in band A in the UV, and (3) a comparable material, $BaTiO_3$, has a marked dichroism in the ferroelectric state.[30] Detailed measurements of the dichroism in the edge of $LiNbO_3$ are illustrated in Fig. 8 for two temperatures.

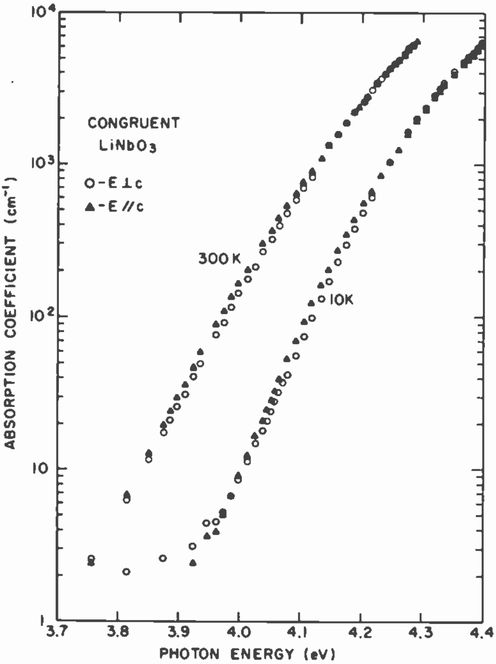

Fig. 8—Effects of polarization of the light on the absorption edge of congruent $LiNbO_3$ at two temperatures.

Not only is the maximum separation of a given pair of curves less than 10 meV, but the curves actually cross at $\alpha \simeq 10^3$ cm^{-1}. There is no apparent explanation for this property but the following facts seem relevant. First, the Kramers–Kronig analysis of the reflectivity of $LiNbO_3$ leads to absorption spectra for the two polarizations that merge at the absorption edge.[18] The electrical conductivity of $LiNbO_3$ is also found to be isotropic.[31] In another comparable material, $KNbO_3$, there is an orthorhombic ferroelectric phase in which all three directional degeneracies should be lifted but two polarization directions have essentially the same absorption edge.[32]

Acknowledgments

We appreciate the help of W. Phillips who provided the $LiNbO_3$ crystals along with an understanding of their physical properties. We have benefited from discussions about electronic states and defects with A. Miller and J. D. Dow.

References:

[1] H. P. R. Frederikse, W. R. Thurber, and W. R. Hosler, "Electronic Transport in Strontium Titanate," *Phys. Rev.*, **134**, p. A442, (1964).
[2] J. F. Schooley, W. R. Hosler, and M. L. Cohen, "Superconductivity in Semiconducting $SrTiO_3$," *Phys. Rev. Lett.*, **12**, p. 474, (1964).
[3] F. Jona and G. Shirane, *Ferroelectric Crystals*, Pergamon Press, New York (1962).
[4] F. W. Lytle, "X-ray Diffractometry of Low-Temperature Phase Transformations in Strontium Titanate," *J. Appl. Phys*, **35**, p. 2212, (1964).
[5] P. A. Fleury, J. F. Scott, and J. M. Worlock, "Soft Phonon Modes and the 110K Phase Transition in $SrTiO_3$," *Phys. Rev. Lett.* **21**, p. 16, (1968).
[6] W. J. Burke, R. J. Pressley, and J. C. Slonczewski, "Raman Scattering and Phase Transitions in Stressed $SrTiO_3$," *Solid State Comm.*, **9**, p. 121, (1971).
[7] W. J. Burke and R. J. Pressley, "Stress Induced Ferroelectricity in $SrTiO_3$," *Solid State Comm.*, **9**, p. 191, (1971).
[8] S. C. Abrahams, J. M. Reddy, and J. L. Bernstein, "Ferroelectric Lithium Niobate. 3. Single Crystal X-ray Diffraction Study at 24°C," *J. Phys. Chem. Solids*, **27**, p. 997, (166).
[9] K. Nassau, H. J. Levinstein, and G. M. Loiacona, "Ferroelectric Lithium Niobate. 1. Growth, Domain Structure, Dislocations and Etching," *J. Phys. Chem. Solids*, **27**, p. 983, (1966).
[10] J. R. Carruthers, G. E. Peterson, M. Grasso, and P. M. Bridenbaugh, "Non-Stoichiometry and Crystal Growth of Littium Niobate," *J. Appl. Phys.*, **42**, p. 1846, (1971).
[11] J. G. Bergman, A. Ashkin, A. A. Ballman, J. M. Dziedzic, H. J. Levinstein, and R. G. Smith, "Curie Temperature, Birefringence, and Phase-Matching Temperature Variations in $LiNbO_3$ as a Function of Melt Stoichiometry," *Appl. Phys. Lett.*, **12**, p. 92, (1968).
[12] A. H. Kahn and A. J. Leyendecker, "Electronic Energy Bands in Strontium Titanate," *Phys. Rev.*, **135**, p. A1321, (1964).
[13] T. F. Soules, E. J. Kelly, D. M. Vaught, and J. W. Richardson, "Energy Band Structure of $SrTiO_3$ from a Self-Consistent-Field Tight Binding Calculation," *Phys. Rev.*, **B6**, p. 1519, (1972).
[14] L. F. Mattheiss, "Energy Bands for $KNiF_3$, $SrTiO_3$, $KMoO_3$, and $KTaO_3$," *Phys. Rev.*, **B6**, p. 4718, (1972).
[15] S. T. Pantelides, D. J. Mickish, and A. B. Kunz, "Correlation Effects in Energy-Band Theory," *Phys. Rev. B*, **10**, p. 2602, (1974).
[16] M. Cardona, "Optical Properties and Band Structure of $SrTiO_3$ and $BaTiO_3$," *Phys. Rev.*, **140**, p. A651, (1965).
[17] G. D. Boyd, R. C. Miller, K. Nassau, W. L. Bond, and A. Savage, "$LiNbO_3$: An Efficient Phase Matchable Non-Linear Optical Material," *Appl. Phys. Lett.*, **5**, p. 234, (1964).
[18] E. Wiesendanger and G. Güntherodt, "Optical Anisotropy of $LiNbO_3$ and $KNbO_3$ in the Interband Transition Region," *Solid State Comm.*, **14**, p. 303, (1974).
[19] K. Bärner, R. Braunstein, and H. A. Weakliem, "The Optical Properties of $LiNbO_3$," (to be published).
[20] M. Capizzi and A. Frova, "Optical Gap of Strontium Titanate (Deviation from Urbach Tail Behavior)," *Phys. Rev. Lett.*, *25*, p. 1298, (1970).
[21] M. Capizzi and A. Frova, "Determination of the Nature of the Optical Gap of $SrTiO_3$," *Il Nuovo Cimento*, **5B**, p. 181, (1971).
[22] D. Redfield and W. J. Burke, "Fundamental Absorption Edge of $SrTiO_3$," *Phys. Rev. B*, **6**, p. 3104, (1972).
[23] H. A. Weakliem, R. Braunstein, and R. Stearns, "Wavelength Modulation Spectra of $SrTiO_3$," *Solid State Comm.*, **15**, p. 5, (1974).
[24] Y. Yacoby and O. Naveh, "Differential Optical Spectra and Band Structure of $SrTiO_3$," *Phys. Rev. B*, **7**, p. 3991, (1973).

[25] H. E. Weaver, "Dielectric Properties of Single Crystals of $SrTiO_3$ at Low Temperatures," *J. Phys. Chem. Solids*, **11**, p. 274, (1959).
[26] J. D. Dow and D. Redfield, "Toward a Unified Theory of Urbach's Rule and Exponential Absorption Edges," *Phys. Rev. B*, **5**, p. 594, (1972).
[27] M. Capizzi, Q. Taccetti and A. Frova, "Thermomodulation Experiments at the Cubic-to-Tetragonal Phase Transition in $SrTiO_3$," *Surface Science*, **37**, p. 258, (1973).
[28] H. P. R. Frederikse, W. R. Hosler, W. R. Thurber, J. Babiskin, and P. G. Siebenmann, "Shubnikov-de Haas Effect in $SrTiO_3$," *Phys. Rev.*, **158**, p. 775, (1967).
[29] D. Redfield and W. J. Burke, "Optical Absorption Edge of $LiNbO_3$," *J. Appl. Phys.*, **45**, p. 4566, (1974).
[30] S. H. Wemple, "Polarization Fluctuations and the Optical Absorption Edge in $BaTiO_3$," *Phys. Rev. B*, **2**, p. 2679, (1970).
[31] W. Bollmann and M. Gernand, "On the Disorder of $LiNbO_3$ Crystals," *Phys. Stat. Sol. (a)*, **9**, p. 301, (1972).
[32] E. Wiesendanger, "Dielectric, Mechanical and Optical Properties of Orthorhombic $KNbO_3$," *Ferroelectrics*, **6**, p. 1, (1974).

Optical Properties of GaN

J. I. Pankove and S. Bloom

RCA Laboratories, Princeton, N.J. 08540

G. Harbeke

Laboratories RCA Ltd., Zurich, Switzerland

Abstract—This article reviews the optical properties of GaN including absorption, reflection, and photoluminescence and summarizes the theoretical calculations leading to a description of the band structure of GaN. The various luminescent transitions are tabulated.

1. Introduction

Of all the semiconducting III–V compounds, GaN has received comparatively little attention. The apparent lack of research interest is due to the difficulty in growing large homogeneous single crystals and in obtaining p-type material. Yet, GaN has a large direct energy gap, can be an efficient light emitter over a wide spectral range including the visible,[1,2] has been made to lase in the ultraviolet,[3] and has exhibited negative electron affinity.[4,5] All these properties have been revealed in a rather short span of time and by a relatively small number of investigators.

The purpose of this article is to present the known optical properties of GaN in a review form with emphasis on three areas: (1) phenomena that concern the energy gap, (2) optical transitions within the gap, and (3) transitions involving higher energy states, which are used to determine the band structure of the material.

2. Nonoptical Properties

Although GaN can be synthesized by a variety of techniques involving Ga compounds (or Ga metal) and either ammonia or ionized nitrogen, the most successful approach has been that of Maruska and Tietjen.[6] This technique consists of reacting GaCl with NH_3 at about 950°C over a sapphire substrate. The resulting material appears as a single crystal per x-ray diffraction. It has a wurtzite structure and its orientation depends on the crystallographic orientation of the substrate. When undoped, the material is n-type conducting, with an electron concentration of usually about 2×10^{18} electrons/cm^3 and a mobility of about 130 cm^2/Vsec (the highest mobility reported is 440 cm^2/Vsec).[7] The donors, which are believed to be nitrogen vacancies, can be compensated by the addition of Zn,[8] Mg,[9] Li,[10] or Be.[10,11] When the material is compensated, it becomes semi-insulating. Table 1 summarizes the nonoptical properties of GaN.

Table 1—Properties of GaN

Crystal Structure	Wurtzite	Zinc Blende
Lattice Constants (Å)	$a = 3.18$ $c = 5.185$	4.51
Expansion Coefficients (10^{-6}/°K)[6]	$5.59 \parallel a$ $3.17 \parallel c$ 300–700°K $7.5 \parallel c$ 700–900°K	
Energy of Formation (kcal/mole)[12]	24.9 (1.10 eV)	
Energy of Dissociation (eV)[13]	3.24	
Dissociation Temperature (K)[13]	1250	
Effective Mass Electrons[14,15]	0.22 ± 0.03	
Effective Mass Holes[14,15]	0.8 ± 0.2	
Phonon Energy (meV)[16]		
LO	95.4, 99.2	
TO	66, 69	

3. Properties Characterizing the Energy Bandgap

3.1 Absorption and Reflectance

The fundamental transition from the valence band to the conduction band determines the value of the energy gap and reveals whether or not momentum conservation needs the mediation of phonons. The first measurement on a large-area single crystal[6] revealed that the absorption spectrum above 3.4 eV varies approximately with the square root of the photon energy in excess of the gap energy, E_g—more precisely as $(h\nu - 3.39)^{0.63}$. This nearly square-root dependence was the first indication that the energy gap of GaN is direct, and a value of $E_g = 3.39$ eV was derived for the energy gap. Later results[17] showed the exponential nature of the absorption edge at energies lower than bandgap, an Urbach tail[18] resulting from the perturbation of the band edges.[19] Such an exponential edge is observed in all direct bandgap semiconductors and, therefore, supports the conclusion that the energy gap of GaN is direct. The extent of the exponential tail to lower energies depends on the strains in the crystal. The strain effect is most severe in very thin GaN layers,[14] leading to an erroneous evaluation of the energy gap.

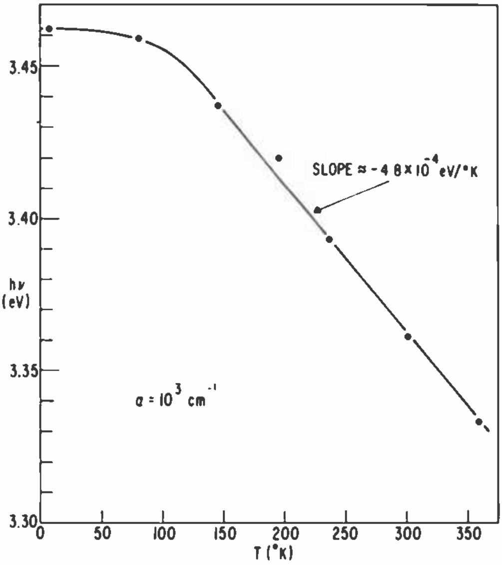

Fig. 1. Temperature dependence of the absorption edge of GaN at $\alpha = 10^3$ (cm^{-1}).

From the temperature dependence of the absorption edge, Fig. 1, one can deduce a temperature dependence of the energy gap. Above 100°K, the energy gap has, in the linear approximation, a temperature coefficient of -4.8×10^{-4} eV/°K. This value is intermediate between the two previously reported values of -3.9×10^{-4} eV/°K of Kauer and Rabenau[20] and -6.7×10^{-4} eV/°K of Camphausen and Connell.[21] A good fit to the energy gap is given by the expression $3.503 + (5.08 \times 10^{-4}\ T^2)/(T - 992)$ of Lagerstedt and Monemar.

The pressure dependence of the absorption edge was measured up to 10 kbars by Camphausen and Connell[21] who find a pressure coefficient of 4.2 ± 0.4 meV/kbar.

The first reflectance spectra of Dingle et al[22] show peaks at 3.62 eV for the $E \perp c$ polarization and 3.72 eV for the $E \parallel c$ polarization, the latter being attributed to a transition from the spin-orbit and crystal field split valence band.

In a second study of purer material, Dingle et al[23] report the observation of three other peaks at 3.474, 3.480 and 3.495 eV. These peaks are attributed to exciton transitions reflecting structure in the valence band due to spin-orbit and crystal field splitting. A spin-orbit splitting of 11 meV and a crystal field splitting of 22.2 meV are deduced from this study. The discrepancies between these two studies have not been described in terms of material quality.

In our own study of the reflectance spectrum of GaN, no reproducible difference between $E \perp c$ and $E \parallel c$ could be detected. However, this may again be due to differences in crystal quality and to a relaxation of the polarization selection rules in the surface layer caused by the polishing of the surface.

Transmission measurements at 77°K on polished samples of 8 to 20 μm, thickness for $E \perp c$ and $E \parallel c$ gave a dichroism of the absorption edge of 20 to 25 meV, in good agreement with the second report of Dingle et al.[23]

3.2 Luminescence

Radiative recombination in GaN can produce a rich spectrum which we shall examine in more detail in the next section. In some materials, a broadband emission at about 3.5 eV is found which has been assigned to a band-to-band transition. Cunningham et al[15] have studied the shift of this peak with electron concentration in Ge-doped GaN. By attributing this shift to the concentration-dependent position of the Fermi level in the conduction band (Burstein-Moss shift), a density-of-state effective mass $m_e{}^* = 0.2\text{–}0.3$ m was deduced.

4. Transitions Within the Energy Bandgap

4.1 Absorption

Below the exponential edge corresponding to transitions between the perturbed band edges, the only notable structure in the absorption spectrum is observed in the range $1.7 < h\nu < 3.0$ eV. There, the optical density varies as $(h\nu - 1.75)^2$ as shown in Fig. 2. This dependence could be due to an indirect (momentum nonconserving) transition possibly involving a deep center at mid-gap. The intensity of this absorption is independent of the thickness of the crystal. Hence, this transition must be an effect occurring either at or near a surface.

At photon energies less than 1.5 eV, free carrier absorption is the dominant absorption process. Free carrier absorption varies as $(h\nu)^{-n}$ where n is in the range 2.5 to 3.9 depending on the doping.[15] By way of example, Fig. 3 shows that free carrier absorption obeys a 3.4 power law in one of our samples.

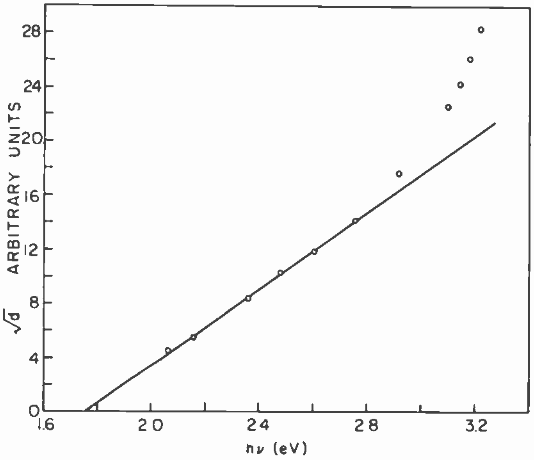

Fig. 2. Plot of square root of optical density at 6°K versus photon energy for undoped GaN.

4.2 Luminescence

Photoluminescence experiments have identified a great number of transitions: free excitons, excitons bound to donors, excitons bound to acceptors, donor-acceptor transitions, and phonon replicas of all these transitions. These transitions have been summarized in Table 2. The donors and acceptors have not been directly identified although it is generally believed that the donors are nitrogen vacancies.

When impurities are deliberately introduced, new emission peaks are observed. These are listed in Table 3. The position of the peaks due to known impurities are temperature independent. Hence, they have been attributed to transitions within a complex rather than a free-to-bound transition. However, if one takes into account à la Hayashi[30] the temperature-dependent change in electron distribution inside an exponential conduction bandtail, one may also expect a spectrally fixed free-to-bound peak. One evidence supporting the free-to-bound transition in Zn-doped GaN is the shift of the emission peak with excitation intensity, as shown in Fig. 4.[31]

Table 2—Near-Gap Luminescence Peaks (in eV) in GaN

	References					
Nature of Transition	(24) 1970	(25) 1971	(23) 1971	(26) 1972	(27) 1973	(28) 1974
Free Exciton	3.476		3.474			3.4751
Exciton bound to donor			3.467	3.471	3.465	3.470
Exciton bound to acceptor			3.455	3.455	3.455	
Exciton bound to Cd acceptor				3.4553		3.454
Exciton bound to Cd acceptor-LO						3.447
Exciton bound to Cd acceptor-14 meV				3.441		
Exciton bound to Cd acceptor-2 × 14 meV				3.427		
Unidentified	3.43		3.435			
Unidentified			3.420			
Exciton bound to donor-TO						3.400
Free exciton-LO			3.385			
Exciton bound to donor-LO			3.378			3.377
Unidentified			3.3716			
Exciton bound to Cd acceptor-LO				3.3638		
Exciton bound to acceptor-LO					3.362	
Exciton bound to Cd acceptor-2LO						3.355
Free exciton-2LO			3.293			3.287
Exciton bound to donor-2LO			3.286			
Donor-acceptor (DA)	3.27	3.2571			3.264	3.263
DA-LO	3.18	3.1672			3.174	3.174
DA-2LO	3.09	3.0768			3.084	3.084
DA-3LO	3.00				2.988	

Table 3—Luminescence Peaks Associated with Known Impurities

	References						
Impurity	(1) 1960	(26) 1972	(27) 1973	(9) 1973	(10) 1973	(28) 1974	(29) 1974
Mg			3.15–2.95	2.9			
Cd	2.44	2.85				2.937 2.898 2.863 2.846 2.807 2.772 2.755 2.716* 2.681	
Zn	2.87	2.85					2.87
Be			2.36–2.07		2.16		
Li	2.13				2.23		
Dy					3.15		

* Dominant

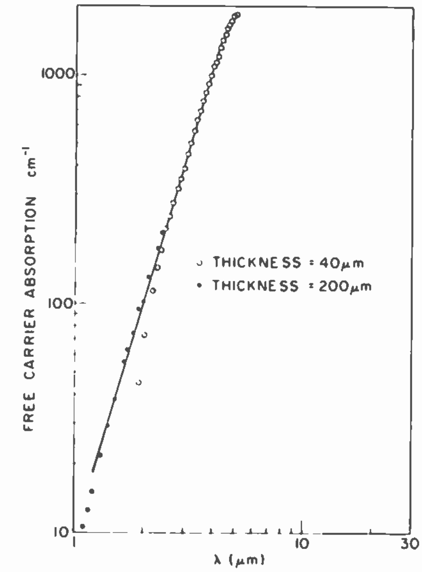

Fig. 3. Absorption spectrum of free carriers at 300°K for material with $N = 1.4 \times 10^{19}$ el/cm^3. The solid line has a slope of 3.4.

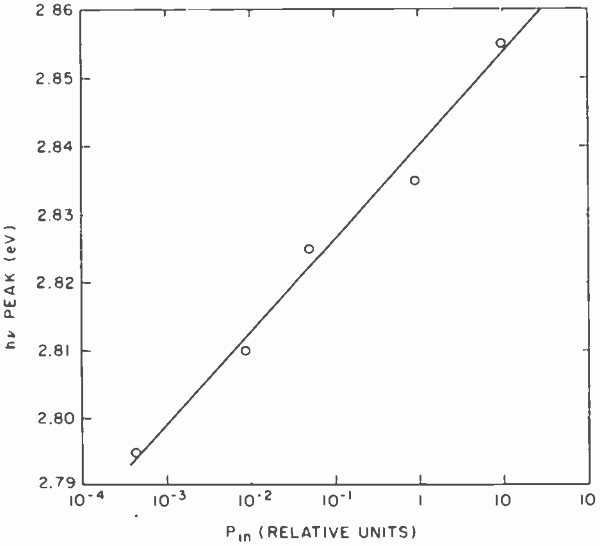

Fig. 4. Spectral shift of photoluminescence at 78°K as a function of excitation intensity at 3250 Å in Zn-doped GaN.

5. Transitions at $h\nu > E_g$ and Band Structure

The reflectance spectrum of polished GaN crystals was measured, the polished surface being normal to the c-axis. The results obtained on two samples, one measured at room temperature, the other at 4.2°K, are shown in Fig. 5. There is a general increase of the reflectivity

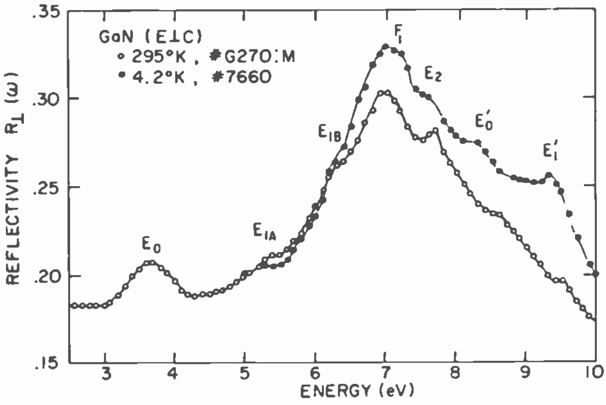

Fig. 5. Experimental reflectivity spectra of hexagonal GaN for $E \perp c$.

upon cooling, but there is also some variation in the fine structure from sample to sample or from surface to surface. This uncertainty in the peak position of 0.1 to 0.4 eV, notably for energies above 7 eV, must be caused by crystal imperfections. The number of peaks and the general shape, however, are reproducible in the entire energy range measured. Seven peaks are obtained over this range. Of these seven peaks only the 7 eV and 9.5 eV peaks had been reported previously by Kosicki et al[14] for polycrystalline films.

The band structure of GaN can be calculated by the empirical pseudopotential method.[32] Two of the peaks, the fundamental gap E_0 at $\Gamma_{6V} - \Gamma_{1V} = 3.6$ eV and the small shoulder at 5.3 eV identified here as E_{1A} at $\Gamma_{5V} - \Gamma_{3C}$, are used to select the form factors of the potential. The ZnO pseudopotential[33] is used as a first approximation for GaN. These two wurtzite compounds have almost equal lattice constants and the elements Zn, Ga and O, N are contiguous in the periodic table. Thus the approximation is valid mainly for the symmetric form factors V^s. It is less accurate for the antisymmetric form factors V^a; GaN is less ionic than ZnO and should have a smaller antisymmetric potential. For convenience the band structure of "cubic" GaN is first evaluated, using the ZnO form factors at the fewer cubic values of the reciprocal lattice vectors. The antisymmetric form factors alone are adjusted until the cubic band structure yields E_0 ($\Gamma_{15v} - \Gamma_{1c}$) and E_1($L_{3v} - L_{1c}$) closest to the aforementioned hexagonal values of 3.6 eV and 5.3 eV. Finally, these V^s and V^a form factors are interpolated to the reciprocal lattice vectors appropriate to the actual hexagonal structure and both V^s and V^a are readjusted to yield a final band structure with the 3.6 eV and 5.3 eV gaps.

The calculated band structure is shown in Fig. 6. We note the expected strong similarity with the band structure of ZnO.[33] The reflectivity for both perpendicular and parallel polarization is given in Fig. 7. There is seen to be good agreement with the experimental reflectivity in regard to energies and relative shapes of the peaks, although the absolute strength is stronger than observed.

Table 4 lists the calculated critical-point energies and reflectivity-peak energies for the major perpendicular–polarization transitions of hexagonal GaN, together with the experimental reflectivity peaks and their new assignments.[34] (The two empirically fitted peaks, E_0 and E_{1A}, are denoted by asterisks.) Also listed are the critical-point energies calculated for cubic GaN using the final values of the hexagonal GaN form factors. These cubic critical-point energies (calculated with an equivalent lattice constant of a(cub.) = 4.51 Å, based on equating nearest-neighbor distances in the cubic and hexagonal crys-

Table 4—Critical Point and Reflectivity Peak Energies (in eV) for Hexagonal GaN, and Critical Points for Cubic GaN Calculated Using Final Form Factors of Hexagonal GaN.

Hexagonal GaN					Cubic GaN		
Transition		Critical Point Energy (calc.)	Reflectivity $R_\perp$ (calc.)	(expt.)	Transition		Critical Point Energy (calc.)
E_0	$\Gamma_6 - \Gamma_1$	3.6	3.6*	3.6*	E_0	$\Gamma_{15} - \Gamma_1$	3.5
E_{1A}	$\Gamma_5 - \Gamma_3$	5.2	5.3*	5.3*			
					E_1	$\Lambda_3 - \Lambda_1$	5.6
E_{1B}	$U_4 - U_3$	6.2	6.0–6.3	6.2-6.3			
F_1	$M_2 - M_1$	7.2	7.3	7.0–7.1	E_2	$X_5 - X_1$	7.7
	$M_4 - M_3$	7.1			$E_2+\delta$	$X_5 - X_3$	7.8
E_2	$K_3 - K_2$	8.5	8.3	7.6–7.7			
E_0'	$\Gamma_6 - \Gamma_1$	8.2–8.6	8.7	8.3–8.7	E_0'	$\Gamma_{15} - \Gamma_{15}$	8.7
E_1'	$\Gamma_5 - \Gamma_6$	9.4	9.4	9.3–9.5	E_1'	$\Lambda_3 - \Lambda_3$	10.1

* Empirically fitted peaks.

tals) fit in well with the systematics for the other gallium III–V compounds, GaSb, GaAs and GaP.

The calculated[34] densities of states is shown in Fig. 8. The valence bandwidth is 7.8 eV, with maxima at −1.9 eV and −6.9 eV. The con-

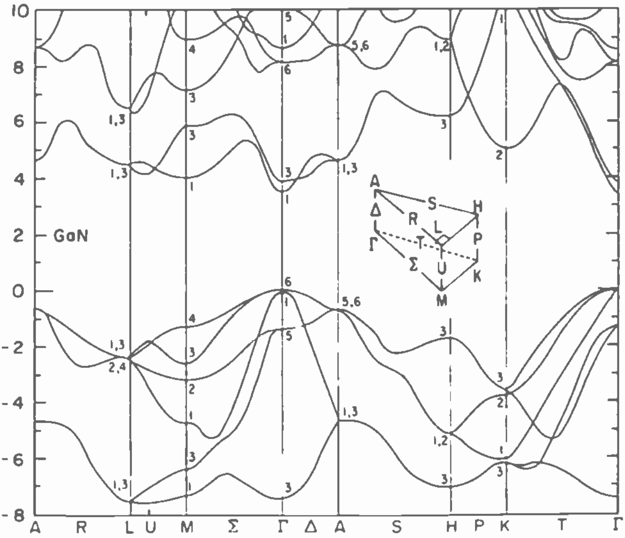

Fig. 6. Energy bands of hexagonal GaN.

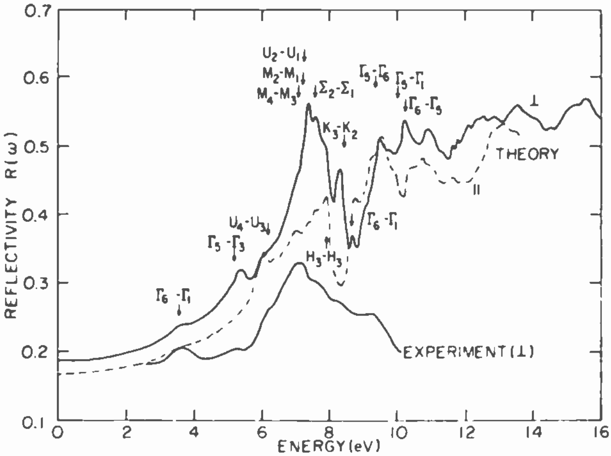

Fig. 7. Theoretical (⊥ and ∥ polarizations) and experimental (⊥ polarization) reflectivity spectra, versus photon energy. The arrows label the critical-point energies and transitions, all for perpendicular polarization with the exception of $H_3 - H_3$.

duction band shows maxima at 6.1 eV, 7.8 eV, and 8.9 eV. UV and x-ray photoemission spectroscopy measurements would be helpful in testing these values.

It is seen from Fig. 6 that the calculated Γ_6 band is very slightly higher than Γ_1, in agreement with the sign and smallness of the experimental[23] crystal field splitting (+0.022 eV). However, such an agreement could be fortuitous due to the high sensitivity of Γ_1 to changes in form factors. The measured bandgap value E_0 $(\Gamma_6 - \Gamma_1)$ of

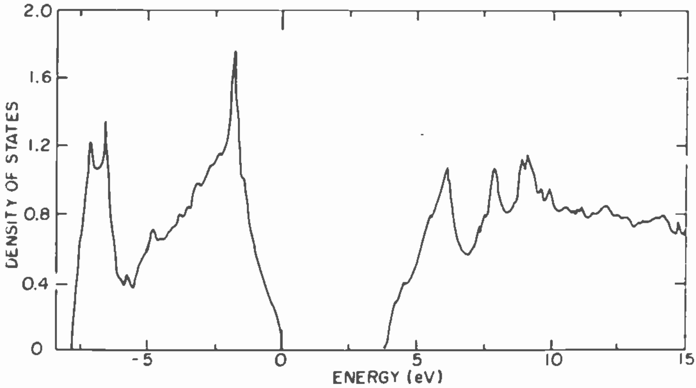

Fig. 8. Calculated density of states of GaN versus energy.

3.6 eV is taken from its broad reflectivity peak. This peak is certainly somewhat exciton enhanced.

The E_1 peak, due in cubic systems to transitions along Λ near L, is split in hexagonal systems into transitions near Γ and U, and labeled E_{1A}, E_{1B}. The measured structures at 5.3 eV and 6.2–6.3 eV, which have not previously been reported, are here attributed to such E_1 transitions. The 5.3 eV shoulder is empirically fitted to $\Gamma_5 - \Gamma_3$; the 6.2–6.3 eV shoulder then agrees quite well, both in shape and position, with that calculated near 6.0–6.3 eV due to $U_4 - U_3$.

Continuing to higher energies, the broad main peak measured at 7.0 eV is attributed here to transitions over a large region of the Brillouin zone centered at M, along U and Σ with $M_2 - M_1$ dominating. The transition $\Sigma_2 - \Sigma_1$ is possibly the cause of the slight enhancement measured on the high energy side of this dominant F_1 peak. The sharp rise in the computed reflectivity curve between the E_{1B} and F_1 structures is clearly duplicated in the experimental low-temperature curve. This F_1 peak is associated with the E_2 structure of cubic systems.

The next experimental structure, labeled E_2 in Fig. 5, is a shoulder at 7.6 eV in the low-temperature curve or, as a more pronounced peak, at 7.7 eV in the room temperature curve. This peak is assigned to transitions around $K_3 - K_2$, although the calculation places this transition at the too-high value of 8.3 eV. The $\Sigma_2 - \Sigma_1$ transition calculated at 7.6 eV, although closer in energy to the 7.6–7.7 peak, seems too weak to be the cause of this peak.

The reflectivity "notch" calculated near 8.5–9.0 eV represents the onset of transitions involving the second set of conduction band states. The long drop into this "notch" shows up best on the room-temperature curve of Fig. 5. The shoulder at 8.3 eV on the low-temperature curve and the small peak at 8.7 eV on the room temperature curve are labeled E_0' and assigned to $\Gamma_6 - \Gamma_1^{up}$ transitions. The calculated peak is at 8.7 eV. Neither this 8.3–8.7 eV structure nor the E_2 peak measured at 7.6–7.7 eV have been previously reported, although Jones and Lettington[35] mention unpublished experiments indicating weak structure at 7.6–7.9 eV.

Finally, the peak shown in Fig. 5 at 9.5 eV for room temperature and, more strongly, at 9.3 eV for low temperature was also observed by Kosicki et al[14] at 9.5 eV. This peak is labeled here E_1' and is assigned to the regions along T and Δ out from $\Gamma_5 - \Gamma_6^{up}$. The calculated E_1' peak is at 9.4 eV, in excellent agreement.

The peak observed by Kosicki et al[14] at 10.7 eV is beyond the range of the present measurements. The present calculation would indicate $\Gamma_5 - \Gamma_1^{up}$ or, more likely, $\Gamma_6 - \Gamma_5^{up}$ as possible assignments.

6. Conclusion

Although many features of the optical spectra of GaN are reasonably well understood, much work remains to be done.

The assignment of some reflectance peaks should be verified by an independent method such as the photoelectric emission. The calculated density of states suggests that the measurements should be extended to the 20-eV range.

There is a fair consistency between the various observations of emission peaks. Improvements in material technology will undoubtedly narrow the peaks and better define the peak positions. Further progress in unraveling the significance of the poorly understood emission peaks and certain features in the absorption spectra will require the availability of homogeneous strain-free crystals.

References:

[1] H. G. Grimmeiss, R. Groth and J. Maak, *Z. Naturforsch.*, **15a**, p. 799, (1960).

[2] J. I. Pankove, "Luminescence in GaN," *J. Luminescence*, 7, p. 114, (1973).

[3] R. Dingle, K. L. Shaklee, R. F. Leheny and R. B. Zetterstrom, "Stimulated Emission and Laser Action in Gallium Nitride," *Appl. Phys. Lett.*, **19**, p. 5, (1971).

[4] J. I. Pankove and H. Schade, "Photoemission from GaN," *Appl. Phys. Lett.*, **25**, p. 53, (1974).

[5] R. U. Martinelli and J. I. Pankove, "Secondary Electron Emission from GaN: Cs-O Surface," *Appl. Phys. Lett.*, **25**, p. 549, (1974).

[6] H. P. Maruska and J. J. Tietjen, "The Preparation and Properties of Vapor-Deposited Single-Crystalline GaN," *Appl. Phys. Lett.*, **15**, p. 327, (1969).

[7] M. Ilegems and H. C. Montgomery, "Electrical Properties of n-Type Vapor-Grown Gallium Nitride," *J. Phys. Chem. Solids*, **34**, p. 885, (1973).

[8] J. I. Pankove, D. Richman, E. A. Miller and J. E. Berkeyheiser, "Electroluminescence in GaN," *J. Luminescence*, **4**, p. 63, (1971).

[9] H. P. Maruska, W. C. Rhines and D. A. Stevenson, *Materials Res. Bull.*, **7**, p. 777, (1972); b. H. P. Maruska, D. A. Stevenson and J. I. Pankove, "Violet Luminescence of Mg-Doped GaN," *Appl. Phys. Lett.*, **22**, p. 303, (1973).

[10] J. I. Pankove, M. T. Duffy, E. A. Miller and J. E. Berkeyheiser, "Luminescence of Insulating Be-Doped and Li-Doped GaN," *J. Luminescence*, **8**, p. 89, (1973).

[11] M. Ilegems and R. Dingle, "Luminescence of Be- and Mg-Doped GaN," *J. Appl. Phys.*, **44**, p. 4234, (1973).

[12] R. Juza and H. Hahn, *Z. Anorg. Allg. Chem.*, **239**, p. 282, (1938); 244, p. 133, (1940).

[13] R. Groh, Gy. Gerey, L. Bartha and J. I. Pankove, *Physica Status Solidi (a)*, **26**, p. 353, (1974).

[14] B. B. Kosicki, R. J. Powell and J. C. Burgiel, "Optical Absorption and Vacuum—Ultraviolet Reflectance of GaN Thin Films," *Phys. Rev. Lett.*, **24**, p. 1421, (1970).

[15] R. D. Cunningham, R. W. Brander, N. D. Knee and D. K. Wickenden, "Variation of Photoluminescence with Carrier Concentration in GaN," *J. Luminescence*, **5**, p. 21, (1972).

[16] D. D. Manchon, A. S. Barker, Jr., P. J. Dean and R. B. Zetterstrom, "Optical Studies of the Phonons and Electrons in Gallium Nitride," *Solid State Commun.*, **8**, p. 1227, (1970).

[17] J. I. Pankove, H. P. Maruska and J. E. Berkeyheiser, "Optical Absorption of GaN," *Appl. Phys. Lett.*, **17**, p. 197, (1970).

[18] F. Urbach, *Phys. Rev.*, **92**, p. 1324, (1953).

[19] D. Redfield, "Effect of Defect Fields on the Optical Absorption Edge," *Phys. Rev.*, **130**, p. 916, (1963).

[20] E. Kauer and A. Rabenau, *Z. Naturforsch.*, **12a**, p. 942, (1959).

[21] D. Camphausen and G. A. N. Connell, "Pressure and Temperature Dependence of the Absorption Edge in GaN," *J. Appl. Phys.*, **42**, p. 4438, (1971).

[22] R. Dingle, D. D. Sell, S. E. Stokowski, P. J. Dean and R. B. Zetterstrom, "Absorption, Reflectance and Luminescence of GaN Single Crystals," *Phys. Rev.*, **B3**, p. 497, (1971).

[23] R. Dingle, D. D. Sell, S. E. Stokowski and M. Ilegems, "Absorption, Reflectance, and Luminescence of GaN Epitaxial Layers," *Phys. Rev.*, **B4**, p. 1211, (1971).

[24] H. G. Grimmeiss and B. Monemar, "Low-Temperature Luminescence in GaN," *J. Appl. Phys.*, **41**, p. 4054, (1970).

[25] R. Dingle and M. Ilegems, "Donor-Acceptor Pair Recombination in GaN," *Solid State Commun.*, **9**, p. 175, (1971).

[26] M. Illegems, R. Dingle and R. A. Logan, "Luminescence of Zn- and Cd-Doped GaN," *J. Appl. Phys.*, **43**, p. 3797, (1972).

[27] M. Ilegems and R. Dingle, "Luminescence of Be- and Mg-Doped GaN," *J. Appl. Phys.*, **44**, p. 4234, (1973).

[28] O. Lagerstedt and B. Monemar, "Luminescence in Epitaxial GaN:Cd," *J. Appl. Phys.*, **45**, p. 2266, (1974).

[29] J. I. Pankove and J. A. Hutchby, "Photoluminescence of Zn-Implanted GaN," *Appl. Phys. Lett.*, **24**, p. 281, (1974).

[30] I. Hayashi, "Effects of Band Shapes on Carrier Distribution at High Temperature," *IEEE J. Quant. Electronics*, **QE-4**, p. 113, (1968).

[31] J. I. Pankove, J. E. Berkeyheiser and E. A. Miller, "Properties of Zn-Doped GaN. I. Photoluminescence," *J. Appl. Phys.*, **45**, p. 1280, (1974).

[32] T. K. Bergstresser and M. L. Cohen, "Electronic Structure and Optical Properties of Hexagonal CdSe, CdS, and ZnS," *Phys. Rev.*, **164**, p. 1069, (1967).

[33] S. Bloom and I. B. Ortenburger, "Pseudopotential Band Structure of ZnO," *Phys. Stat. Solidi(b)*, **58**, p. 561, (1973).

[34] S. Bloom, G. Harbeke, E. Meier and I. B. Ortenburger, "Band Structure and Reflectivity of GaN," *Phys. Stat. Solidi(b)*, **66**, p. 161, (1974).

[35] D. Jones and A. H. Lettington, "The Electronic Band Structures of the Wide Band Gap Semiconductors GaN and AlN," *Solid State Commun.*, **11**, p. 701, (1972).

Electrochromism in WO_3 Amorphous Films

Brian W. Faughnan, Richard S. Crandall and Philip M. Heyman

RCA Laboratories, Princeton, N. J. 08540

Abstract—The electrical and optical properties of electrochromic WO_3 amorphous films are considered. The coloring current follows the Butler–Vollmer equation for applied voltages up to 0.5 volts. The coloring current at constant voltage decreases monotonically due to electrode processes. The bleaching current cuts off when the charge extracted equals the charge injected, at least at moderate coloration density. The experimental oscillator strength of the color center transition is 0.1. The position of the absorption peak increases from 1.3 to 1.4 eV as the absorption coefficient increases from 10^4 to 10^5 cm^{-1}, while the half-width of the absorption band increases by 40% over the same range. A model for the electrochromic effect is presented whereby the double injection of electrons and protons into the WO_3 film forms hydrogen tungsten bronze, H_xWO_3. The color center arises from the added electrons which are trapped by W ions. The optical transition arises from an intervalency transition absorption. This type of transition arises when an electron localized at one W ion is excited over a barrier and falls into another W ion-trapping site. All the experimental properties of the color center can be explained by this model, although other possible absorption mechanisms are considered.

1. Introduction

An electrochromic (EC) is a material in which an optical absorption band can be introduced, or an existing band altered, by the passage of current through the material or by the application of an electric field. These materials are currently of interest for display devices.[1,2] Perhaps the earliest known example, as well as the simplest, is the creation of F centers in an alkali halide crystal when a voltage is applied between two metal electrodes attached to two faces of the crystal which is heated to about 700°C.[3] Briefly, the effect occurs because electrons injected from the negative-pointed electrode are trapped at anion vacancies thereby forming F centers. Charge neutrality and current continuity is maintained by anion vacancy motion originating from the positive electrode. This implies a net mass transport of anions to the positive electrode where halogen gas is evolved. If the electrode potentials are reversed, V (hole) centers are produced accompanied by the release of alkali metal at the negative electrode.

This simple example illustrates most of the requirement for an electrochromic material. First of all, it must have a color center, or optical absorption, associated with it that is present or not, depending on certain conditions. A second feature is the presence of mixed conduction, i.e., electronic and ionic conduction. This is necessary for electrochromism, which depends on injected charge to produce the altered state, since charge neutrality must be preserved. These two requirements greatly restrict the range of available materials. In the example above, the crystal must be heated to 700°C to raise the ionic conductivity of the alkali halide sufficiently to produce a measurable current and, hence, optical density change. This renders it useless for most device applications.

A second example is the electro-coloration of transition metal doped $SrTiO_3$.[4] In a typical case the $SrTiO_3$ is doped with Fe and Mo which can exist in $SrTiO_3$ in a variety of oxydation states, some of which have optical absorption bands.[5] In this case, a color front moves into the crystal from each electrode as Fe is oxydized at the positive electrode and Mo is reduced at the negative electrode. Oxygen vacancies move toward the cathode to maintain charge neutrality. It appears that three types of carriers are involved in different parts of the crystal, electronic conduction in the Mo^{5+} rich region, hole conduction in the Fe^{4+} rich region, and ionic (vacancy) conduction in the central uncolored region. Again, the crystal must be heated to approximately 200°C to obtain a reasonable conductivity for the least conducting carrier, and practical devices have not been developed.

It is now clear that if good electrochromic (EC) performance is desired in a solid at room temperature, the activation energy for the slowest carrier must be quite low, say 0.4 eV or below. The slowest carrier is usually, but not always, the ionic carrier. This places the search for good EC materials within the class of fast-ion (or superionic) conductors.[6]

WO_3 films appear to satisfy both the requirement of fast-ion conduction at room temperature and a highly absorbing color center. Hence, it is under active study at a number of laboratories and is the subject of the present paper. Unfortunately, the phenomenon is considerably more complicated than the simple examples cited above for a number of reasons. Some of these are: events occurring within the WO_3 film, the amorphous nature of the films, and processes that occur at the electrodes and that can never be entirely separated from the bulk effect. Therefore, it appears that more research will have to be done before complete understanding is reached. Nevertheless, we believe the principal features of the EC phenomenon are now understood and will be presented in this paper. We will emphasize the simpler optical properties of EC-WO_3 rather than the complicated electrical properties that will be dealt with in later publications.

Section 2 of this paper consists of a description of the experimental properties of EC-WO_3 films, and Section 3 presents a model to explain the data. Some of the details of the model are still somewhat speculative, but we hope to demonstrate the close connection between electrochromism in WO_3 films and the relationship between single-crystal WO_3 and the tungsten bronzes, noteably hydrogen tungsten bronze (H_xWO_3). Finally, we mention that organic electrochromic materials also exist,[2] but these materials are outside the scope of the present paper.

2. Optical and Electrical Properties of WO_3 Films

The WO_3 films are made by vacuum evaporation on a heated substrate or by sputtering from a WO_3 target. X-ray analysis shows the films to be amorphous. Fig. 1 shows a typical device configuration suitable for coloring a WO_3 film. This arrangement provides an electron injecting contact on one side of the WO_3 film and a positive ion (proton) injecting contact on the other side. The effect of the electrolyte resistance and the voltage drop across the counter-electrode are relatively unimportant and they will not be considered here.

If a small voltage, e.g., 1–1.5 volts, is applied across this device, with the transparent conductive layer electrode negative, a blue color rapidly appears in that area of the WO_3 film in contact with the electrolyte. Reversing the polarity bleaches the film in a comparable time. A coloration and bleach current pulse and the accompanying change in optical reflection coefficient R, measured at 633 nm is shown in Fig. 2. The charge removed during the bleach pulse is just equal to the charge injected during the coloring pulse. At that point, the current turns off even though the voltage is still applied. This also corresponds to the time at which the film is completely bleached.

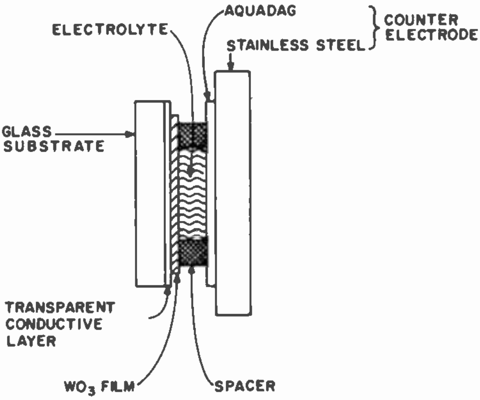

Fig. 1—Schematic diagram of an electrochromic cell. The electrolyte is a mixture of water, glycerol, H_2SO_4 and a finely divided white reflecting powder.

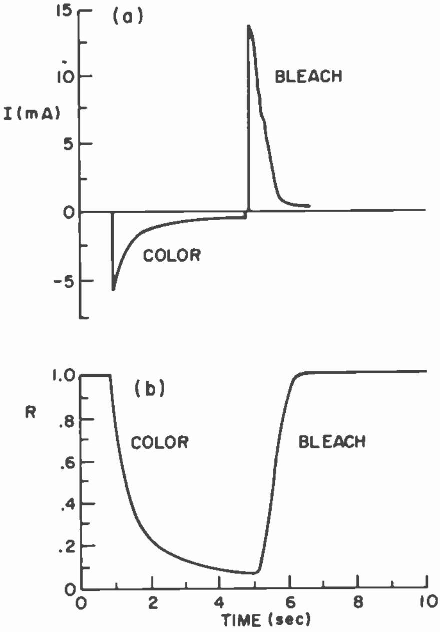

Fig. 2—Device characteristics of a WO_3 electrochromic cell. I is the current flowing through the cell with an active area of 0.33 cm^2. R is the diffuse reflectance of light passing through the WO_3 film from the glass substrate and reflected back by a white powder suspended in the liquid electrolyte.

A typical I_0-V curve for a WO_3 EC device is shown in Fig. 3. I_0 is the initial current after the capacitive spike has died down but before electrode polarization effects become important. The dashed line is obtained when a second counter-electrode is substituted for the WO_3 film. It represents a constant circuit resistance of approximately 100 ohms that is always in the circuit. The current voltage curve fits an equation of the form,

$$I_0 = I_0'\left[\exp\left\{(1-\beta)\frac{eV}{kT}\right\} - \exp\left\{-\beta\frac{eV}{kT}\right\}\right] \qquad [1]$$

up to approximately 0.5 volts with $I_0' = 1.1 \times 10^{-7}$ amp cm^{-2} and $\beta \approx 0.6$. This is the Butler–Vollmer equation[7] which describes electrode limited current flow at the WO_3-electrolyte interface. Above 0.5 volt, a V^2 region is usually found. Finally, at high voltages, the current approaches the circuit resistance limiting value. A thorough treatment of the I-V curve, the current versus time, and the coloration versus time, in the most general case, is very complicated and will be discussed in a future publication.

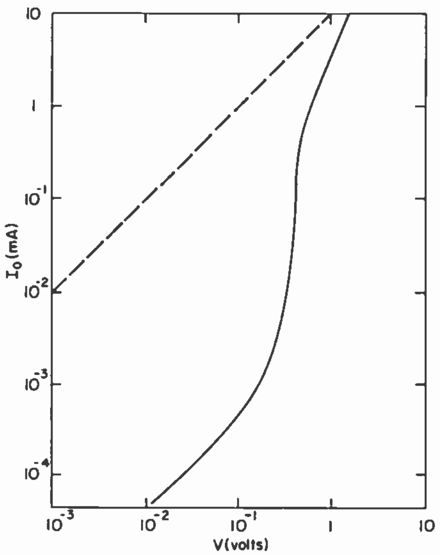

Fig. 3—Solid line shows current-voltage curve for an electrochromic cell and dotted line shows same cell with WO_3 film replaced by a second counter electrode.

It is of interest to ask whether all the charge injected into the device during the color pulse goes into forming color centers and whether it is extracted in the bleach pulse. This would be the case in an ideal system with reversible color centers but would not be the case if various electrochemical side reactions take place. For example, suppose some electrons traverse the WO_3 film and combine with protons at the WO_3 electrolyte interface forming H atoms and subsequently gas molecules. These molecules may then be too stable to be reversible or may even leave the system. Another example occurs if too high a voltage is used (>1.67 volts). Electrolysis of water takes place, leading to a steady current with no charge storage.

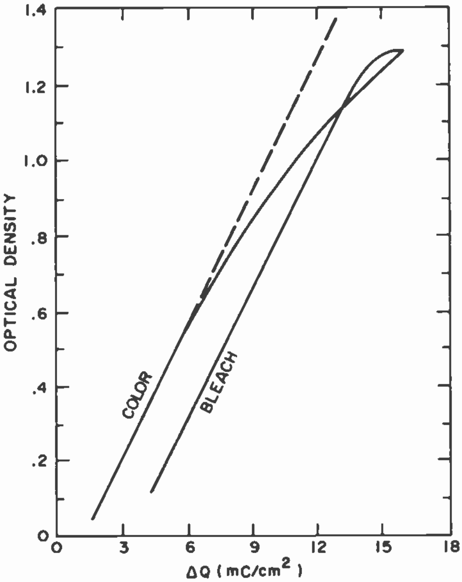

Fig. 4—Log of the diffuse contrast ratio CR of an electrochromic cell, at λ = 633 nm, versus the electronic charge injected and extracted during the color and bleach cycle respectively. CR = R/R_o, the ratio of the diffuse reflection of the colored and uncolored cell.

This question is examined experimentally in Fig. 4. The current into the device is passed through a charge integrator. The measured reflection coefficient, after detecting the chopped light (f = 2 kHz) by a phase sensitive detector, is passed through a logarithmic amplifier to give a signal proportional to optical density (OD), which in turn is proportional to the number of color centers formed. The experiment was done under approximately constant current conditions ($I \sim 0.3$ ma/cm^2). OD is proportional to δQ for relatively low contrast ratios, CR <3:1 (contrast ratio is defined as the ratio of the diffuse reflection coefficient before and after coloration). In this regime, the charge injected in the color pulse is retrieved in the bleach pulse. This suggests that each electron injected forms a color center. The electron is then removed when the color center is bleached. At high charge-injection levels the linear relationship breaks down. In this case, more charge is injected than goes into forming color centers. Furthermore, on the bleach pulse this excess charge is not recovered, only the color-center-forming charge is reversible. These results are not unreasonable. As the color-center density builds up, further coloration is more difficult and competing processes such as H_2 gas formation at the WO_3 electrolyte interface become relatively more important.

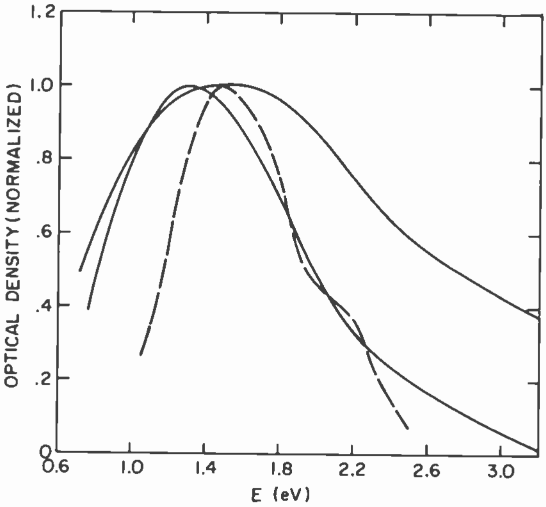

Fig. 5—Solid lines show optical absorption bands of lightly colored (narrow band) and heavily colored (wide band) electrochromic amorphous WO_3 film, measured in transmission. Lightly colored film is 1 μm thick and has a peak optical density of 0.45. Heavily colored film is 0.3 μm thick with a peak optical density of 1.8. Dotted line shows optical absorption in transmission of a powdered specimen of single crystal $Na_{0.6}WO_3$, discussed later in the text. (After Dickens et al., Ref [21]).

The optical absorption band is shown in Fig. 5. It is a broad, almost featureless, band peaking in the vicinity of 940–880 nm (1.3 to 1.4

eV). This agrees essentially with previously published absorption bands in electrochromic WO_3 films. From Figs. 4 and 5 and the use of Smakula's equation,[9] we can obtain an estimate of the oscillator strength f of the transition:

$$Nf = 0.87 \times 10^{7}\frac{n}{(n^2 + 2)^2}(k_{\max}L)W_{1/2} \qquad [2]$$

where a gaussian line width is assumed, and
N = number of color centers formed per cm^2
n = index of refraction of the material.
$k_{\max}$ = absorption coefficient (cm^{-1}) at the peak of the band.
L = thickness of colored region
$W_{1/2}$ = line width of half maximum in eV.

Using the values of $k_{\max}$, N, and $W_{1/2}$ obtained from the straight-line portion of Fig. 4, i.e., low coloration density, and an index of refraction equal to single crystal WO_3, $n = 2.5$, we obtain $f \sim 0.1$. The oscillator strength is defined so that the maximum value for a one-electron transition is unity. Its experimental magnitude can be used to help establish the nature of the transition. For example, the F center absorption in alkali halides has an oscillator strength of approximately $f \sim 0.6$, whereas excited state transitions within a transition-metal impurity in a solid normally have much smaller oscillator strengths ($10^{-4} \sim 10^{-2}$).

The absorption bands shown in Fig. 5 are asymmetrical, having more absorption on the high energy side of the absorption peak. Part of this extra absorption is due to an increase in the index of refraction with energy. This "correction" may be estimated from Eq [2] once the variation of the refractive index is known. The refractive index is obtained from the transmission interference fringes observed in uncolored WO_3 films, according to the equation

$$\frac{1}{\lambda} = \frac{1}{2ln}(m), \qquad [3]$$

where λ is the wavelength at interference minima, n is the optical index of refraction, l is the thickness of WO_3 film, and m is an integer, the order number of the interference minima. Eq. [3] is the approximate condition for transmission minima, which should be reasonably accurate for films with a high index of refraction. Fig. 6 shows the results of Eq. [3] for a 1-μm-thick WO_3 film. The inset is a plot of n versus λ. The long wavelength value obtained, namely 2.6, is higher than the single crystal value of 2.5. This could, however, be due to a 5% error in the nominal thickness of the film.

The index of refraction correction was applied to the absorption bands of a number of WO_3 films and the results are summarized in Fig. 7. There is a systematic increase in the energy of the absorption peak with increasing optical density per micron. In Fig. 7b, linewidth data are shown. For optical density per micron greater than 2.5, the index-of-refraction corrected line shape fits a gaussian curve whose half width increases with increased coloration density. For low coloration densities, however, the low energy side of the curve becomes narrower and the line shape becomes asymmetrical, although the low and high energy side can still be fit to a gaussian line shape.

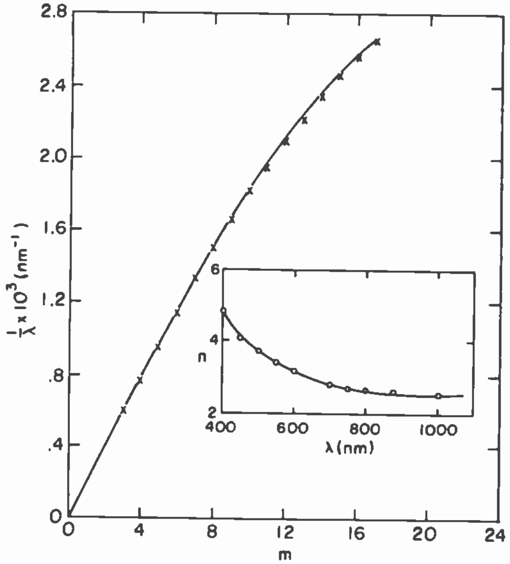

Fig. 6—Plot of 1/λ of the position of the interference fringe minima of an uncolored 1-μm-thick WO_3 film versus the integer *m*, labeling the minima. Inset shows wavelength variation of *n*, the index of refraction, obtained from the slope of the 1/λ versus *m* curve.

For uniformly colored films the optical density per micron is just proportional to the optical absorption coefficient. For example, an optical density per micron of 6 corresponds to $k = 1.4 \times 10^5$ cm^{-1}. The systematic variations observed in Fig. 7 suggest that for these films the coloration was uniform or, at least, has penetrated the entire thickness of the film. Otherwise the optical density per micron would be smaller for thick films that were not colored all the way through. The data was obtained for films with thicknesses varying from 0.3 to 1.0 μm, and no variation with film thickness was observed.

We conclude this section by remarking that it is quite common to find that the properties of amorphous films vary with deposition parameters.[10] WO_3 films are no exception to this rule. For example, Fig. 8 shows the band edge absorption for a variety of WO_3 films. Considerable variation is found between old films and fresh films, evaporated and sputtered films, etc. Nevertheless, the electrochromic properties do not change in any fundamental way.

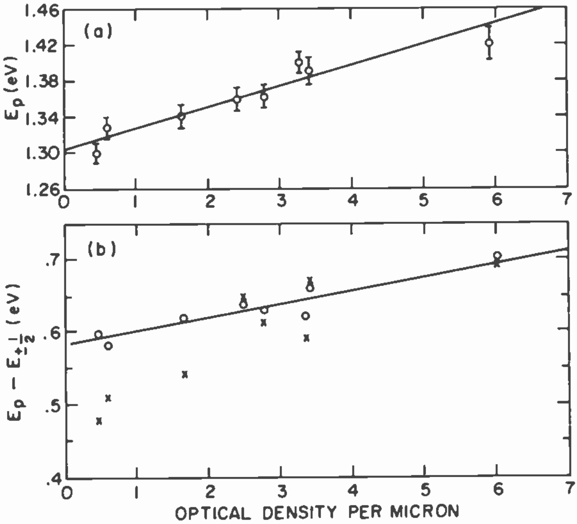

Fig. 7—(a) Position of the absorption peak versus the peak optical density per micron for a number of electrochromic WO_3 films. (b) One half the absorption band half-width at half maximum versus optical density per micron. (⊙) is high-energy side, $E_{+1/2} - E_p$, after correction for index of refraction variation; x is low energy side, $E_p - E_{-1/2}$. The full half width is $E_{+1/2} - E_{-1/2}$.

3. Model for Electrochromism in WO_3 and the Nature of the Color Center

In this section we propose a model for the electrochromic effect in WO_3 including electronic and ionic transport and the nature of the color center.

The magnitude of charge injected during coloration strongly supports the idea of double injection. The large charge densities injected must be neutralized. The negative carriers are clearly electrons. Indeed, the electronic conductivity can be easily measured by passing a current in the plane of a WO_3 film between two metallic contacts. But what of the positive carriers? Hole conduction, i.e., extraction of WO_3 valence band electrons from the positive contact, can also be ruled out because of the high density of carriers that the film can accommodate. A concentration of $10^{22}/cm^3$ color centers would mean that electron–hole pairs would be less than 10 Å apart, and tunneling would certainly occur between all electronic states. This leaves positive ions, and the obvious candidate is protons from the electrolyte.

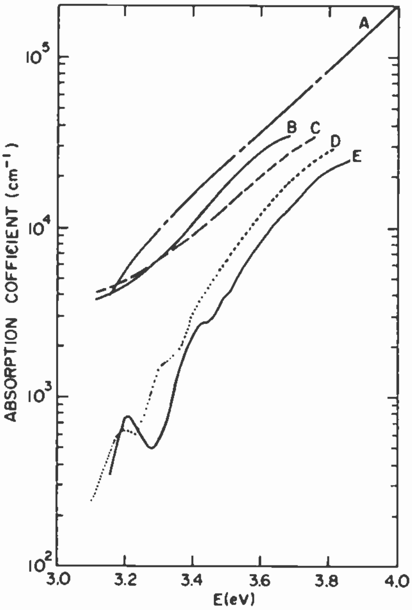

Fig. 8—Optical absorption coefficient near the band edge for a variety of amorphous WO_3 films. (a) After Deb (see Ref. [8]), (b) freshly evaporated film, (c) sputtered film, (d) freshly evaporated film, and (e) one-year-old evaporated film.

This explains why a liquid electrolyte works so well as the positive-ion injecting contact compared with a metallic contact which depends on the presence of moisture to obtain proton injection.[8] We are still left with the need to accommodate a very large density of protons and electrons, up to 50% of the number of tungsten ions. The answer lies in a study of the tungsten bronzes.

3.1 Single Crystal Tungsten Bronzes

The tungsten bronzes[11] are a class of materials, written M_xWO_3 where M = H, Li, Na, K, Rb, NH_4, etc. and $0 < x < 1$, and having an "extended defect" structure.[12] WO_3 has the ReO_3 structure, in which voids or vacancies exist in the space where the A cation would normally be in the ABO_3 perovskite. These voids can be filled more or less continuously up to $x = 1$ by the ions listed above as well as other ions. As x is varied from 0 to 1, for example in Na_xWO_3, a number of phase transitions occur for certain values of x. These transitions allow the structure to accommodate an ever increasing number of sodium ions. Generally, very low values of x are difficult to obtain in single-crystal form.

The bronzes are of much current interest for their unusual structural, optical, and electrical properties. They have been recently studied as possible fast ionic conductors.[13] To be a fast-ion solid conductor, a material should satisfy the following requirements.[14]

1. The solid should have an "open" crystal structure, preferably with "tunnels" in at least one direction that can accommodate the ion in question.
2. The ion that is to provide the conductivity should be part of the regular lattice, but should occupy significantly less than 100% of its available lattice sites.

The bronzes satisfy these requirements and attempts have been made to measure their ionic conductivities.[13] Direct measurement of ionic conductivities in solids is very difficult, and estimates of the related diffusion constants D are sometimes inferred from nuclear magnetic resonance studies. For the bronzes it is found that neither Na^+ nor Li^+ is mobile at room temperature whereas H^+ is. For sodium ions $D \sim 10^{-15}$ cm²/sec at 500°C. However, for the proton in H_xWO_3, a value of $D_p \sim 10^{-11}$–10^{-12} cm²/sec is inferred[15] at room temperature. Structural studies of H_xWO_3 have shown[16] that there is a distortion of the lattice. The hydrogen prefers to form an OH bond with one of its surrounding $0^=$ neighbors, so that the chemical formula should really be written $(OH)_xWO_{3-x}$. The diffusion constant has an activation energy of ~0.4 eV, and it is speculated that this is the energy required to break the OH bond in the crystal.[13]

3.2 Electrochromic Effect in Amorphous WO_3

In analogy with the properties of single-crystal tungsten bronzes, we now propose that during electrocoloration of WO_3 films H_xWO_3 is formed. Protons enter from the electrolyte and electrons from the electron injection contact. Where they combine, H_xWO_3 is formed, giving rise to a color center associated with electrons localized on the tungsten ions.

The nature of the coloration profile, i.e., the value of x versus distance into the film, as well as the speed of coloration and bleaching will depend on many details of the model. For example they will depend on the value of σ_e the electronic conductivity, and σ_p the proton conductivity as well as the corresponding diffusion coefficients, D_e, D_p. Also the question of whether there is a stabilizing energy associated with the formation of H_xWO_3 is important. The electrical properties of the overall EC cell are sufficiently complicated and dependent on interface effects that it is necessary to perform a wide variety of experiments to separate the effects of the transport coefficients mentioned above. For example, σ_e can be obtained directly as a function of x by resistivity measurements on colored films using two metallic electrodes. Under these conditions only electronic current flows. σ_e is found to vary over at least eight orders of magnitude, $\sigma_e \sim 10^{-6} \sim 10^2$ (ohm-cm)$^{-1}$, from insulating in the colorless state to metallic-like conductivity in the highly colored state. The electron diffusion coefficient has been measured by a novel technique in which color is observed to spread outward from an indium wire contacting the film through an acid electrolyte.[17] The value obtained is $D_e = 0.0025$ cm^2/sec, from which we infer $\mu_e = (e/kT)D_e = 0.1$ cm^2/volt-sec at room temperature. Measurement of proton transport properties are more difficult because of interface properties; that is, the flux of protons across the electrolyte-WO_3 interface frequently limits the coloration speed. Nevertheless we estimate from direct optical transmission versus coloration time experiments,[17] as well as bleaching current versus time measurements,[18] that $10^{-10} < D_p < 10^{-6}$ cm^2/sec. Because of the large discrepancy between electron and proton mobilities, the dynamics of electrocoloration will be limited by the proton transport properties. Furthermore in the colored region, which the protons are required to traverse, the electronic conductivity will be so high that it is unlikely that any electric field will exist there to drive the protons through. Therefore, the protons must diffuse through this region. This is no problem, since the diffusion constant is large enough to allow coloration by diffusion within the observed coloration times. For example, to color completely all the way through a 1-μm-thick film by diffusion would require a time $t_{\text{diff}} = l^2/D_p \sim 0.01$ to 100 sec for the range of D_p given above. Furthermore it is not necessary to color all the way through the film to produce a good coloration.

For partially colored films we might expect a standard-error-function diffusion profile or uniform coloration if the current is interface limited. Fig. 6 supports the latter interpretation, but the experimental evidence is still uncertain on this question. Free-energy considerations may favor the formation of H_xWO_3 with a high x value in some circumstances. This is an area requiring more research before the true situation can be determined.

The bleaching of the film will proceed by a completely different mechanism, i.e., space-charge-limited double extraction. The film will bleach from the electrolyte side inwards. In order for additional protons to leave the film they must pass through an ever growing region of charge-free film. The current flow will be space-charge limited, and most of the bleaching voltage will be across this region. The details will be described elsewhere,[18] but a $t^{-3/4}$ time dependence for the current predicted by the theory is found in the time regime where interface effects are not important.

3.3 The Color Center

In keeping with the hypothesis of H_xWO_3 formation, it is logical to ascribe the color center to an electron localized on a tungsten ion, i.e., W^{5+}. The proton remains ionized just as in the crystalline tungsten bronzes,[19,20] and the number of extra electrons, which fully account for the electrical and optical properties, is proportional to x.

Assuming that the electrons are located on W ions, we must still explain the nature of the optical absorption. There exists a theory that fits the experimental situation in a very natural way. This is the theory of intervalence transfer (I.T.) absorption as reviewed, for example, by Hush.[21] The possibility of I.T. absorption arises whenever transition metal ions of mixed valence state are present in a material. A classical example is the compound "Prussian Blue" [KFe(II) Fe(III) $(CN)_6 \cdot H_2O$], where the intervalence transition can be written, $Fe(A)^{2+} + Fe(B)^{3+} + h\nu \rightarrow Fe(A)^{3+} + Fe(B)^{2+}$ where A and B refer to the two different Fe sites. Energy is required to raise the electron from one transition metal (T.M.) site over a barrier, from whence it falls into another empty T.M. site via a radiationless transition (phonon emission). In the present case, the transition is $W^{5+}(A) + W^{6+}(B) + h\nu \rightarrow W^{6+}(A) + W^{5+}(B)$.

The presence of mixed valence states is not the only requirement for the observation of I.T. absorption. If the electron is sufficiently delocalized, a T.M. conduction band is formed and free-carrier absorption or plasma resonance reflection is observed. The latter is found in crystalline tungsten bronzes above some critical value of x. On the other hand, if the electrons are too localized on the T.M. sites, there will be a vanishing wave function overlap on adjacent T.M. sites, and the oscillator strength of the transition vanishes. In amorphous H_xWO_3 conditions for I.T. absorption appear to be satisfied.

3.4 Outline of Intervalence Transfer Absorption Theory

Only the briefest outline will be given here. For details, the reader is referred to the review by Hush.[21] Two nearly localized electronic states are assumed, centered on two nearby sites, A and B. The situation is shown schematically in a configuration coordinate diagram in Fig. 9. Let

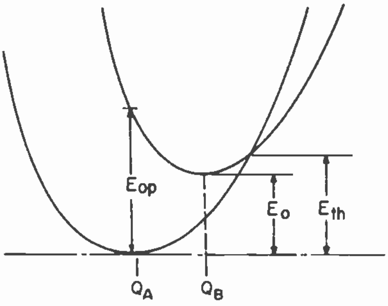

Fig. 9—Configuration coordinate diagram for an electron localized at a tungsten ion in amorphous H_xWO_3.

E_{op} = energy at the peak of the optical absorption band.

E_{th} = energy for thermal activation (hopping) of an electron from site A to site B.

E_0 = difference in ground state energy between site A and site B.

Q_A, Q_B = configuration coordinates for the electron on site A and site B, respectively.

It can be shown[21] that,

$$E_{th} = \frac{E_{op}^2}{4(E_{op} - E_0)}. \qquad [4]$$

In the special case of identical sites $E_{th} = (1/4)E_{op}$.

A detailed treatment based on the theory of moments of the absorption envelope predicts a relationship between the absorption peak and the absorption bandwidth. In the high-temperature limit, the absorption band tends towards a gaussian shape and the results simplify to

$$W_{1/2}^{2} = \frac{E_{op} - E_0}{16 \ln 2kT} = \frac{E_{op} - E_0}{3.6}, \qquad [5]$$

where $T = 300°C$, the units are electron volts, and $W_{1/2}$ is the width of the absorption band. This result assumes that the temperature is the only source of broadening. In disordered materials, the absorption band may be considerably broader.

The absorption maximum can also be written in terms of a vibrational energy term,

$$E_{op} = \chi + E_0, \qquad [6]$$

where χ can be expressed as a sum of a term arising from localized (metalligand) vibrational modes χ_{loc}, and a term arising from lattice vibrational modes, χ_{outer}. Thus,

$$\chi = \chi_{loc} + \chi_{outer}. \qquad [7]$$

χ_{loc} is found to be similar for metal ions in aqueous solution and in octahedral oxygen holes in a lattice.

A crude approximation for χ_{outer} is[21]

$$\chi_{outer} = \frac{e^2}{r}\left(\frac{1}{K_0} - \frac{1}{K}\right) \qquad [8]$$

where K_o and K are the optical and static dielectric constants, respectively, and r is the metal-metal separation.

A simple equation is obtained for the oscillator strength of the I.T. absorption based on the degree of overlap of an electron on site A on site B. For example, let us write the electron wave function approximately localized on site A as

$$\psi_A = \psi_a + \xi_{ab}\psi_b; \qquad [9a]$$

similarly,

$$\psi_B = \xi_{ba}\psi_a - \psi_b. \qquad [9b]$$

where ψ_a, ψ_b are the isolated one-electron orbitals, centered on sites A and B respectively. The degree of delocalization is then ξ^2. The oscillator strength is

$$f = 0.09(E_{op})D^2, \qquad [10]$$

where D is the dipole strength, defined by

$$D = \xi r \qquad [11]$$

and r is the distance between site A and site B.

3.5 Comparison with Experiment

We wish to examine the $W^{5+} \rightarrow W^{6+}$ transition in H_xWO_3 in light of the previous theory. The W-W separation in single crystal WO_3 is 5.4 Å, and we assume the same value for amorphous H_xWO_3. The single-crystal optical dielectric constant of WO_3 is $K_o = 6.25$ while estimates of the static dielectric constant vary between 50 ~ 1000.[22] Therefore $\chi_{outer} \sim 0.43$ eV. Experimentally, we find $E_{op} = 1.32$ eV. If $E_o \sim 0$, then $\chi_{loc} = 0.9$ eV, and $E_{th} = 0.33$ eV. Hush finds $\chi_{loc} = 0.8$ eV for Fe(II) in octahedral sites. Our measurements of electronic conductivity versus temperature on colored WO_3 films yields an activation energy of between 0.37 to 0.25 eV for optical densities between 0.15 to 0.7 for a 1-μm-thick film. The meaning of a single activation energy for an amorphous film is of doubtful significance; nevertheless, the results are consistent with an E_o close to zero.

Based on the experimental value of E_{op} and Eq. [5], the linewidth should be approximately 0.6 eV. The experimental linewidth is at least twice this magnitude, but the excess broadening could be due to the disordered nature of the amorphous material.

We have determined experimentally that the oscillator strength for the color center transition in electrochromic WO_3 is $f \sim 0.1$. This can be substituted into Eq. [10] to estimate the degree of localization. The dipole strength for a single transition is $D^1 = \xi r$. However each W^{5+} site may be surrounded by up to six W^{6+} sites, depending on the as yet undetermined structure of the amorphous films. Assuming this to be the case, the experimental dipole strength will be $D_{ex} = \sqrt{6}\, \xi r = 0.92$ from Eq. [10]. Since $r = 5.4$ Å, $\xi^2 = 0.005$. This represents the fraction of the time an electron on site A spends on each of the neighboring B sites. Therefore it is 97% localized on the A site. Thus, the experimental properties of the color center are consistent with a nearly localized electron. For comparison, the I.T. absorption of the Fe(II)-F(III) transition in Prussian Blue has the following properties: $E_{op} = 1.74$ eV, Fe(II) –Fe(III) site separation distance $r = 5.1$ Å, $\xi^2 = 1.6 \times 10^{-3}$, and the electron is 99% localized on the A site.

3.6 Optical Properties of Single Crystal Tungsten Bronzes

It is interesting to compare the optical properties of electrochromic amorphous films of WO_3 with the corresponding single crystal WO_3 and its related tungsten bronzes. Non-stoichiometric WO_3 (i.e., WO_{3-y}) and the tungsten bronze M_xWO_3 (M = H, Na, K, etc.) have very similar optical properties which are dominated by the phenomenon of plasma resonance. In these crystals the electrons are sufficiently delocalized that they form a conduction band (in the bronzes for $x > x_c$, where x_c is some critical value of x, for example). The crystals exhibit a high reflectivity with a characteristic plasma cut-off frequency ω_p given by

$$\omega_p = e\left[\frac{n}{m^*\epsilon_0 K_0}\right]^{1/2} \qquad [11]$$

where n is the concentration of free electrons, m^* the electron effective mass, ϵ_0 the permittivity of free space, and K_o is the dielectric constant of crystal in the absence of free-charge carriers.

The concentration of free electrons is proportional to x, and it is the sweeping of the plasma resonance through the visible region as x is varied that emparts the characteristic colors to the bronzes. Evidently the electrons are considerably more delocalized in the single-crystal material. This is in agreement with our finding that the electron mobility is 100 times smaller in amorphous WO_3 than in the single-crystal form.

Nevertheless if optical transmission data is taken on powdered samples diluted with non-absorbing powder to suppress the plasma reflection, an absorption band in the visible is also found.[20] The absorption spectrum for $Na_{0.6}WO_3$ is shown in Fig. 5. The absolute intensity of this absorption is not known, nor is the nature of the band identified. It was suggested[19] that it may arise from a $\pi^* \rightarrow \sigma^*$ transition which should exist in crystals with the ReO_3 band structure. It is also possible that intervalence absorption is responsible for this band.

4. Discussion and Conclusions

Amorphous films of WO_3 show interesting electrocoloration properties. Although understanding is still incomplete, we have attempted to relate the origin of this effect in WO_3 to its related bronze structures, specifically H_xWO_3. It is this fact that allows the high density of color centers to be injected and extracted electrically.

The color center properties of these films are unusual and contribute towards making these films of technological interest for display applications. The origin of this color center absorption undoubtedly falls under one of the following four categories.

(1) Intervalence transfer absorption ($W^{5+} \rightarrow W^{6+}$). This model was discussed in detail in the previous section. It requires largely "delocalized" electrons with some overlap between metal ions.

(2) Charge transfer absorption from the valence band to a "split-off" W^{5+} state. For example an electron on the W ion has its energy lowered because of the attractive Coulomb potential energy of the H^+ (or Na^+ etc.) ion as well as through self-trapping effects. A charge transfer transition from the oxygen valence band to the W^{5+} ion would be similar to the band gap absorption but occur at lower energy. Such charge transfer bands occur, for example, for Fe impurities in $SrTiO_3$.[25] The problem here is the low energy of the absorption peak compared to the band gap absorption. However, since we do not have detailed knowledge of the position of the W^{5+} state within the bandgap, this mechanism cannot be ruled out. Further experimental or theoretical work will be required to definitely choose between (1) and (2).

(3) Interband transitions from filled conduction band to higher excited state bands, e.g. $\pi^* \rightarrow \sigma^*$ absorption in ReO_3 compounds. It is possible that the absorption band observed[20] in $Na_{x=0.6}WO_3$ and also observed[23] in $(NH_4)_{0.25}WO_3$ and $K_{0.26}WO_3$ belongs to this category. However the adjusted band structure diagram[24] for ReO_3, which should apply[19] to WO_3, does not make this suggestion appear likely, since the density of states in the σ^* band is spread over a large energy range, which should lead to a very broad structureless low intensity absorption.

(4) F or F^+ centers in oxygen vacancies. This is the explanation favored by Deb.[8] There are several objections to this hypothesis. First, very little conclusive evidence exists for the observation of F^+ and F optical bands in oxides other than alkaline earth oxides.[26] Electrons "trapped" by oxygen vacancies are likely to reside on W orbitals with optical properties fitting into one of the previous categories. In single-crystal WO_3, any deviation from stoichiometry is accompanied by optical and electrical properties well accounted for in terms of the W^{5+} conduction electrons. It is difficult to see why amorphous WO_3 should be any different in this respect, yet the freshly deposited WO_3 films are usually colorless and have low conductivity. Finally, the high density of color centers possible in some films ($x = 0.5$) make it unlikely that they could arise from oxygen vacancies.

To summarize we propose that the color center absorption in amorphous WO_3 films is due to the intervalence transfer mechanism between an electron trapped at a W ion adjacent to a proton and a nearby W ion. The experimental evidence is consistent with this model and it appears to be the most natural explanation. It is also likely that the absorption band observed in the single-crystal bronzes at approximately the same energy has a similar origin. It is hoped that, as these systems are studied in more detail, more definitive conclusions will be reached about the validity of this model.

Acknowledgments

The authors gratefully acknowledge the contributions of Istvan Gorog, who was responsible for initiating this work, participated in the early experiments, and offered encouragement and advice throughout the course of this research. We also thank R. E. Nielsen, R. L. Quinn, and B. Tompkins for their able technical assistance in all phases of this work.

References

[1] S. K. Deb, "A Novel Electrophotographic System," *Appl. Optics*, Suppl. 3 on Electrophotography, p. 192 (1969); S. K. Deb, "Some Aspects of Electrochromic Display Systems," *Proc. 24th Elect. Comp. Conf.*, Statler Hilton, Wash., D. C., May 13-15, 1974, p. 11.

[2] C. J. Schoot, J. J. Ponjee', H. T. van Dam, R. A. van Doorn and P. T. Bolwijn, "A New Electrochromic Memory Display," *Appl. Phys. Lett.*, **23**, p. 64 (1973).

[3] J. H. Schulman and W. D. Compton, *Color Centers in Solids*, Pergamon Press (1963), p. 38.

[4] J. Blanc and D. L. Staebler, "Electrocoloration in $SrTiO_3$: Vacancy Drifts and Oxidation Reduction of Transition Metals," *Phys. Rev. B.*, **4**, p. 3548 (1971).

[5] B. W. Faughnan, "Photochromism in Transition Metal Doped $SrTiO_3$," *Phys. Rev. B-15*, **4**, p. 3623 (1971).

[6] "Fast Ion Transport in Solids," *Proc. of the NATO Sponsored Adv. Study Inst. on Fast Ion Transport in Solids*, Solid State Batteries and Devices, Belgirate, Italy, Sept. 5-15, 1972, W. Van Gool, Ed. North-Holland/American Elsevier (1973).

[7] J. O'M. Bockris and A. K. N. Reddy, "Modern Electrochemistry," *Plenum/Rosetta*, **2**, p. 883 (1973).

[8] S. K. Deb, "Optical and Photoelectric Properties and Color Centers in Thin Films of Tungsten Oxide," *Phil. Mag.*, **27**, p. 801 (1973).

[9] D. L. Dexter, *Solid State Physics*, **6**, p. 370 (1968).

[10] "Amorphous and Liquid Semiconductors," *Proc. of 5th Intl. Conf. in Amor. and Liq. Semicond.*, Garmish-DartenKirchen, FRG, Sept. 3-8, 1973 Ed. by T. Stake and W. Breng, Taylor and Francis Ltd. London (1974). See for example pp. 69-71.

[11] P. Hagenmuller, "Tungsten Bronzes, Vanadium Bronzes and Related Compounds" in *Comprehensive Inorganic Chemistry*, Pergamon Press, Vol. 4, p. 541 (1973).

[12] "The Chemistry of Extended Defects in Non-Metallic Solids," *Proc. of the Inst. for Adv. Study on the Chem. of Extended Defects in Non-Metallic Solids*, Casa Blanca Inn, Scottsdale, Arizona, April 16-26, 1969, Ed. by LeRoy Eyrung and Michael O'Keeffe, North Holland/American Elsevier, 1970.

[13] M. S. Whittingham and R. A. Huggins, "Transport Properties of Inorganic Bronzes," p. 645 in *Fast Ion Transport in Solids* (see Ref. [6]).

[14] W. Van Gool, "Fast Ion Conduction," *Ann. Review of Material Sci.*, **4**, p. 311 (1974).

[15] P. G. Dickens, D. J. Murphy and T. K. Holstead, "Pulsed NMR Study of Proton Mobility in a Hydrogen Tungsten Bronze," *J. Solid State Chem.*, **6**, p. 370 (1973).

[16] P. J. Wiseman and P. G. Dickens, "The Crystal Structure of Cubic Hydrogen Tungsten Bronze," *J. Solid State Chem.*, **6**, p. 374 (1973).

[17] Richard S. Crandall and Brian W. Faughnan, "Measurement of the Diffusion Coefficient of Electrons in WO_3 Films," *App. Phys. Lett.*, **26**, 120 (1975).

[18] Brian W. Faughnan, Richard S. Crandall and Murray Lampert, "Model for the Bleaching of Electrochromic Films by an Electric Field," to be published.

[19] John B. Goodenough, "Metallic Oxides," in *Prog. in Solid State Chemistry*, Ed. H. Reiss, Pergamon Press, Oxford, Vol. 5, p. 145 (1971).

[20] P. G. Dickens, R. M. P. Quillian and M. S. Whittingham, "The Reflectance Spectra of the Tungsten Bronzes," *Mat. Res. Bull.*, **3**, p. 941 (1968).

[21] N. S. Hush, "Intervalence Transfer Absorption. Part 2. Theoretical Considerations and Spectroscopic Data," in *Prog. in Inorganic Chemistry*, Ed. F. Albert Cotton, Interscience, Vol. 8, p. 391 (1967): see also, G. C. Allen and N. S. Hush, "Intervalence Transfer Absorption. Part I," p. 357 (same book).

[22] Z. I. Kirlashkina, F. M. Popov, D. L. Bilenko, and V. I. Kirlashkin, "An Investigation of the Dielectric Permittivity of Semiconductors," *Sov. Phys.-Tech. Phys.* (Eng. Transl.), **2**, p. 69 (1957); B. T. Matthias, "Ferro-electric Properties of WO_3," *Phys. Rev.*, **76**, p. 430 (1949).

[23] P. G. Dickens, A. C. Halliwell, D. J. Murphy, and M. S. Whittingham, "Preparation and Characterization of a Hexagonal Ammonium Tungsten Bronze Phase $(NH_4)_xWO_3$," *Trans. Faraday Soc.*, **67**, p. 794 (1971).

[24] L. F. Mattheiss, "Band Structure and Fermi Surface of ReO_3," *Phys. Rev.*, **181**, p. 987 (1969).

[25] K. W. Blazey, O. F. Schirmer, W. Berlinger, and K. A. Müller, "Identification of Fe^{4+} and Fe^{5+} Charge-Transfer Photochromic Absorption Bands in $SrTiO_3$," to be published.

[26] A. E. Hughes and B. Henderson, "Color Centers in Simple Oxides," in *Point Defects in Solids*, Eds. J. H. Crawford, Jr. and L. M. Slifkin, Plenum Press, New York (1972), Vol. 1, p. 435.

Recent Papers by RCA Authors

Listing is alphabetical by name of primary author. For copies of reprints, the reader should contact the publication directly.

B. Abeles and P. Sheng, "Electron Localization in Granular Metals," **Low. Temp. Physics–LT 13,** Vol. 3, p. 578.

M. S. Abrahams and C. J. Buiocchi, "Cross-Sectional Specimens for Transmission Electron Microscopy," **J. Appl. Phys.,** Vol. 45, No. 8, p. 3315, Aug. 1974.

K. Ametani, "Atomic Absorption Spectrophotometric Determination of Rare Earths (Y, Eu, Gd, Dy, Ho, and Er) in Single Crystals of Magnetic Garnets and Sulfides," **Bull. Chem. Soc. Japan,** Vol. 47, No. 9, p. 2238, Sept. 1974.

P. H. Bennett, "An Advanced Technology PABX Using Low-Power LSI Devices," **Telephone Engineering and Management Magazine,** p. 96, Oct. 7, 1974.

R. S. Braudy, "Characteristics of Organic Dyes Transferred by Laser Irradiation," **J. Appl. Phys.,** Vol. 45, No. 8, p. 3512, Aug. 1974.

D. E. Carlson, "Ion Depletion of Glass at a Blocking Anode: I. Theory and Experimental Results for Alkali Silicate Glasses," **J. Amer. Ceramic Soc.,** Vol. 57, No. 7, p. 291, July 1974.

D. E. Carlson, K. W. Hang, and G. F. Stockdale, "Ion Depletion of Glass at A Blocking Anode: II. Properties of Ion-Depleted Glasses," **J. Amer. Ceramic Soc.,** Vol. 57, No. 7, p. 295, July 1974.

D. J. Channin, "Liquid-Crystal Technique for Observing Integrated-Circuit Operation," **IEEE Trans. Electron Devices,** Vol. 21, No. 10, p. 650, Oct. 1974.

R. S. Crandall, "Lifetime of Surface-State Electrons of Liquid ^{4}He: II. Electron Lattice," **Phys. Rev. A,** Vol. 10, No. 4, p. 1370, Oct. 1974.

P. A. Crossley and W. E. Ham, "Use of Test Structures and Results of Electrical Tests for Silicon-on-Sapphire Integrated Circuit Processes," **J. Electronic Materials,** Vol. 2, No. 4, p. 466, 1973.

G. W. Cullen and J. F. Corboy, "A Comparison of the Semiconducting Properties of Thin Films of Silicon on Sapphire and Spinel," **J. Electrochem. Soc.,** Vol. 121, No. 10, p. 1345, Oct. 1974.

E. J. Denlinger, "Design of Partial Height Ferrite Waveguide Circulators," **IEEE Trans. Microwave Theory and Techniques,** p. 810, Aug. 1974.

E. C. Douglas and A. G. F. Dingwall, "Ion Implantation for Threshold Control in COSMOS Circuits," **IEEE Trans. Electron Devices,** Vol. 21, No. 6, p. 324, June 1974.

J. Dresner, "Mobility in Epitaxial GaAs Under 1-Mev Electron Irradiation," **J. Appl. Phys.,** Vol. 45, No. 9, p. 4118, Sept. 1974.

J. G. Endriz, "The Role of Plasmons in Photoemission from Metals," Proc. of the Conf. on Polaritons, P. 275.

R. S. Engelbrecht, "Electrostatic Recording on Insulators by Nonwetting Conducting Liquids," **J. Appl. Phys.,** Vol. 45, No. 8, p. 3421, Aug. 1974.

R. E. Enstrom, C. J. Nuese, J. R. Appert, and J. J. Gannon, "Influence of Gas-Phase Stoichiometry on the Defect Morphology, Impurity Doping, and Electroluminescence Efficiency of Vapor-Grown GaAs P-N Junctions," **J. Electrochem. Soc.,** Vol. 121, No. 11, p. 1516, Nov. 1974.

D. G. Fisher, "The Effect of Cs-O Activation Temperature of the Surface Escape Probability of NEA (In,Ga)As Photocathodes," **IEEE Trans. Electron Devices,** Vol. 21, No. 8, p. 541, Aug. 1974.

D. G. Fisher, R. E. Enstrom, J. S. Escher, H. F. Gossenberger, and J. R. Appert, "Photoemission Characteristics of Transmission-Mode Negative Electron Affinity GaAs and (In,Ga)As Vapor-Grown Structures," **IEEE Trans. Electron Devices,** Vol. 21, No. 10, p. 641, Oct. 1974.

P. V. Goedertier, I. Gorog, J. D. Knox, I. Ladany, and J. P. Wittke, "A Facsimile System Using Room-Temperature Injection-Laser Scanning," **RCA Review,** Vol. 35, No. 3, p. 335, Sept. 1974.

L. A. Goodman, "Liquid-Crystal Displays–Packaging and Surface Treatments," **RCA Review,** Vol. 35, No. 3, p. 447, Sept. 1974.

W. A. Harmening, "Static Mass Balancing with a Torsion Spring and Four Bar Linkage," **ASME Trans. J.,** Mechanism Case Studies, New York, Oct. 1974.

M. Hecht, "Signal to Noise Degradation Due to Amplitude and Bank Limiting in an MSK System," **Int'l. Conf. on Communications, Conf. Record,** Minneapolis, Minn., June 17, 1974.

G. B. Herzog, "The Impact of LSI Technology on Computer System," **Information Processing '74,** (Book) 1974.

H. Kawamoto, S. G. Liu, H. J. Prager, and E. L. Allen, "S-Band Trapatt Amplifiers with Four-Layer Diode Structures," **RCA Review,** Vol. 35, No. 3, p. 372, Sept. 1974.

S. A. Keneman, "Surface Relief Holograms in Evaporated Arsenic Trisulfide Films," **Thin Solid Films,** Vol 21, p. 281, 1974.

L. E. Kitchens, "AN/TPQ-39 Digital Instrumentation Radar–A Technology Payoff in Mobility, Performance, Flexibility, and Low Cost," **EASCON Conv. Record,** EASCON '74, Wash., D. C., Oct. 1974.

H. Kressel, P. Robinson, R. V. D'Aiello, and S. H. McFarlane, "Properties of High-Voltage Silicon Epitaxial Diodes," **J. Appl. Phys.,** Vol. 45, No. 9, p. 3930, Sept. 1974.

H. Kressel, "Gallium Arsenide and (AlGa)As Devices Prepared by Liquid-Phase Epitaxy," **J. Electronic Materials,** Vol. 3, No. 4, p. 747, 1974.

H. Kressel, H. F. Lockwood, I. Ladany, and M. Ettenberg, "Heterojunction Laser Diodes for Room Temperature Operation," **Optical Engineering,** Vol. 13, No. 5, p. 416, Sept/Oct. 1974.

A. W. Levine, M. Kaplan, and E. S. Poliniak, "The Interaction of 5-KeV Electrons with Polymers of Methyl Isopropenyl Ketone," Polymer Engineering & Science, Vol. 14, No. 7, p. 518, July 1974.

J. D. Levine, "Power Law Reverse Current-Voltage Characteristic in Schottky Barriers," **Solid State Electronics,** Vol. 17, p. 1083, 1974.

S. H. McFarlane and E. M. Ettenberg, "The Effect of Substrate Preparation on Surface Appearance of Liquid-Phase Epitaxial (Al,Ga)As on GaP," **J. Crystal Growth,** Vol 23, p. 233, 1974.

R. U. Martinelli and M. Ettenberg, "Electron Transport and Emission Characteristics of Negative Electron Affinity $Al_xGa_{1-x}As$ Alloys ($0 \leq x \leq 0.3$)," **J. Appl. Phys.,** Vol. 45, No. 9, p. 3896, Sept. 1974.

R. U. Martinelli and J. I. Pankove, "Secondary Electron Emission from the GaN; Cs-O Surface," **Appl. Phys. Lett.,** Vol. 25, No. 10, p. 549, Nov. 1974.

R. U. Martinelli and D. G. Fisher, "The Application of Semiconductors with Negative Electron Affinity Surfaces to Electron Emission Devices," **Proc. IEEE,** Vol. 62, No. 10, p. 1339, Oct. 1974.

H. R. Mathwich and J. F. Balcewicz, "The Effect of Tandem Band and Amplitude Limiting on the Performance of PSK," **Int'l. Conf. on Communications, Conf. Record,** Minneapolis, Minn., June 17–19, 1974.

W. J. Merz, "Introductory Lecture," **Ferroelectrics,** Vol. 7, p. 31, 1974.

D. Meyerhofer, "Electrohydrodynamic Instabilities in Nematic Liquid Crystals," **RCA Review,** Vol. 35, No. 3, p. 433, Sept. 1974.

C. J. Nuese, M. Ettenberg and G. H. Olsen, "Room-Temperature Heterojunction Laser Diodes from Vapor-Grown $In_{1-x}Ga_xP$/GaAs Structures," **Appl. Phys. Lett.,** Vol. 25, No. 10, p. 612, Nov. 1974.

G. H. Olsen and M. Ettenberg, "A Universal Stain/Etchant for Interfaces in III–V Compounds," **J. Appl. Phys.,** Vol. 45, No. 11, p. 5112, Nov. 1974.

G. H. Olsen, M. S. Abrahams, and T. J. Zamerowski, "Asymmetric Cracking in III–V Compounds," **J. Electrochem. Soc.,** Vol. 121, No. 12, p. 1650, Dec. 1974.

H. F. Olsen, "Comment on An Analysis of Design Conditions for a Phase-Inverter Speaker System with a Drone Cone," **Trans. Acoustics, Speech, & Signal Processes,** Vol. 22, No. 5, p. 389, Oct. 1974.

J. A. Olmstead, "Basic Solid State Physics," **Proc. SAE Automotive Engrg. Congress & Exposition,** March 1974.

J. I. Pankove and M. A. Lampert, "Model for Electroluminescence in GaN," **Phys. Rev. Lett.,** Vol. 33, No. 6, p. 361, Aug. 1974.

J. I. Pankove and J. E. Berkeyheiser, "Properties of Zn-Doped GaN: II Photoconductivity," **J. Appl. Phys.,** Vol. 45, No. 9, p. 3892, Sept. 1974.

R. J. Powell, J. R. Ligenza, and M. S. Schneider, "Selective Oxidation of Silicon in Low-Temperature High-Pressure Steam," **IEEE Trans. Electron Devices,** Vol. 21, No. 10, p. 636, Oct. 1974.

D. Redfield and W. J. Burke, "Optical Absorption Edge of $LiNbO_3$," **J. Appl. Phys.,** Vol. 45, No. 10, p. 4566, Oct. 1974.

D. Redfield, "Multiple-Pass Thin-Film Silicon Solar Cell," **Appl. Phys. Lett.,** Vol. 25, No. 11, p. 647, Dec. 1974.

W. R. Roach, "Resolution of Electro-Optic Light Valves," **IEEE Trans. Electron Devices,** Vol. 21, No. 8, p. 453, Aug. 1974.

D. P. Schnorr, "Printed Wiring Processing," **Electronic Packaging and Production,** Materials Techniques, Vol. 14, No. 7, p. 98, July 1974.

R. M. Scudder and W. H. Sheppard, "AN/SPY-1 Phase Array Antenna," **Microwave Jour.,** May 1974.

R. Shahbender, "Novel Magneto-Optic System," **IEEE Trans. Magnetics,** p. 575, Sept. 1974.

B. Shelpuk, "The Role of System Architecture in Cooling of Electronics Systems," **Electronics,** Vol. 47, No. 13, June 1974.

P. Sheng, "Introduction to the Elastic Continuum Theory of Liquid Crystals," **RCA Review,** Vol. 35, No. 3, p. 408, Sept. 1974.

E. F. Steigmeier, "Light Scattering Near Structural Phase Transitions," **Ferroelectrics,** Vol. 7, p. 65, 1974.

D. M. Stevenson and J. J. Hanak, "Low-Loss, Broadband Microwave Ultrasonic Delay Lines Using Ion-Beam-Milled Shear-Wave Transducers," **RCA Review,** Vol. 35, No. 3, p. 355, Sept. 1974.

R. A. Sunshine, "Infrared Observation of Current Distributions in Large Area Power Transistors," **IEEE Trans. Industrial Elect.,** Vol. 21, No. 3, p. 116, Aug. 1974.

R. A. Sunshine, "Multi-Dimensional Current Flow in Silicon Power Transistors Operating in the Saturation Mode," **Power Electronics Specialists Conf. Record,** p. 154, 1974.

T. Takahashi, K. Ametani, and O. Yamada, "Synthesis and Some Properties of RCr_3S_6 Crystals (R = Y, Gd, Dy, Ho and Er)," **J. Crystal Growth,** Vol. 24, No. 25, p. 151, 1974.

L. J. Vieland and A. W. Wicklund, "High T_c Nb_3Ga and Nb_3Ge by CVD," **Phys. Lett.,** Vol. 49, No. 5, p. 407, Oct. 1974.

J. L. Vossen, "A Sputtering Technique for Coating the Inside Walls of Through-Holes in Substrates," **J. Vacuum Science & Tech.,** Vol. 11, No. 5, p. 875, Sept/Oct. 1974.

C. C. Wang, I. Ladany, S. H. McFarlane, and F. C. Dougherty, "Two-Stage Epitaxial Growth of GaP on Spinel," **J. Crystal Growth,** Vol. 24, No. 25, p. 239, 1974.

P. K. Weimer, W. S. Pike, F. V. Shallcross, and M. G. Kovac, "Video Processing in Charge-Transfer Image Sensors by Recycling of Signals Through the Sensor," **RCA Review,** Vol. 35, No. 3, p. 341, Sept. 1974.

J. Weisbecker, "A Practical, Low-Cost Home/School Microprocessor System," **Computer Magazine,** Vol. 7, No. 8, p. 20, Aug. 1974.

A. E. Widmer and R. Fehlmann, "A Millivolt Source for Temperature Programming of Laboratory Furnaces," **J. Physics E: Scientific Instruments,** Vol. 7, p. 610, 1974.

R. Williams and A. M. Goodman, "Wetting of Thin Layers of SiO_2 by Water," **Appl. Phys. Lett.,** Vol. 25, No. 10, p. 531, Nov. 1974.

R. Williams, "Pressure Effects in Sealed Liquid-Crystal Cells," **RCA Review,** Vol. 35, p. 462, Sept. 1974.

P. J. Wojtowicz, "Introduction to the Molecular Theory of Smectic-A Liquid Crystals," **RCA Review,** Vol. 35, No. 3, p. 388, Sept. 1974.

Patents Issued to RCA Inventors Fourth Quarter, 1974

October

A. A. A. Ahmed Current Amplifier (3,843,933)
D. J. Channin Guided Light Structures Employing Liquid Crystal (3,838,908)
Y. Chiang Method of Making a Metal Silicide-Silicon Schottky Barrier (3,841,904)
J. K. Clemens Information Records and Recording/Playback Systems Therefor (3,842,194)
J. K. Clemens Record Fabrication of a Capacitive Type Storage Medium (3,842,217)
R. A. Craft Precision Digital Interpolator (3,840,174)
N. N. Feldstein and T. S. Lancsek Method for Electroless Deposition of Metal Using Improved Collodial Catalyzing Solution (3,841,881)
R. E. Fulton Label Writing Apparatus (3,839,644)
J. J. Gibson Telephone Image Transmission System (3,842,199)
J. I. Gittleman and J. J. Hanak Sputtered Granular Ferromagnetic Iron-Nickel-Silica Films (3,843,420)
E. J. Ham and R. R. Soden Method of Etching Silicon Oxide to Produce a Tapered Edge Thereon (3,839,111)
W. J. Hannan Color Motion Picture Film Playback System (3,843,836)
R. E. Hanson Apparatus for Engine Compression Testing (3,839,906)
R. E. Hanson and H. E. Fineman Engine Performance Analyzer Using Simulated Load (3,839,907)
L. F. Heckamn, Jr., Amplifier for Amplitude Modulated Waves with Means for Improving Sideband Response (3,845,403)
R. J. Hollingsworth Tri-State Logic Circuit (3,845,328)
R. S. Hopkins, Jr., and D. M. Miller Apparatus for Generating Sample Pulses in a Telephone Image Transmission System (3,843,837)
G. V. Jacoby and S. P. Woodsum Track Following Servo System (3,840,893)
M. Kaplan and D. L. Matthies Metallized Video Disc Having an Insulating Layer Thereon (3,843,399)
F. L. Katnack, M. F. Delise, and E. L. Jordan Overlay Transistor Employing Highly Conductive Semiconductor Grid and Method for Making (3,843,425)
A. J. Leidich Composite Transistor Device with Over Current Protection (3,845,405)
R. U. Martinelli and B. Goldstein Infrared Photocathode (3,845,496)
T. D. Michaelis Solar Torque Compensation for a Satellite (3,838,934)
M. E. Miller Demountable Capacitive Protective Coupling for Pickup Transducers (3,843,846)
J. T. O'Brien and P. Nyul Laser Diode Package Formed of Ceramic and Metal Materials Having High Electrical and Thermal Conductivity (3,840,889)
K. Solomon and J. R. Allen Time Division Multiple Access Synchronization Technique (3,843,843)
P. D. Southgate Contact Array and Method of Making the Same (3,842,189)
P. D. Southgate Thermal Radiation Detector (3,842,276)
S. A. Steckler Signal Combining Circuit (3,840,819)
M. Toda and S. Tosima Variable Delay Using Ferroelastic-Ferroelectric Materials (3,840,826)
B. F. Williams and W. F. Kosonocky Charge-Coupled Radiation Sensing Circuit with Charge Skim-Off and Reset (3,845,295)

November

A. A. A. Ahmed Current Attenuator (3,846,696)
L. H. Anderson Asynchronous Pulse Receiver (3,848,191)
S. Berkman Vapor Deposition Apparatus with Pyrolytic Graphite Heat Shield (3,845,738)
D. S. Bond Collision Prevention (3,849,782)
R. M. Carrell Optical Scanner Control System (3,848,087)
R. E. Debrecht and L. S. Napoli Microwave Transmission Line and Devices Using Multiple Coplanar Conductors (3,848,198)
M. Ettenberg and S. L. Gilbert Method of Applying an Anti-Reflective Coating on a Semiconductor Laser (3,846,165)
D. D. Freedman Gateless Logic for Producing Selectable Phase Clock Pulses (3,851,258)
D. D. Freedman High Speed Programmable Counter (3,849,635)
L. L. Gruber Method of Directly Spacing a Cathode-to-Grid Assembly for a Cathode-Ray Tube (3,848,301)
J. D. Hunt Bagger Station or Similar Article (D,233,496)
J. L. Ibaugh Electron Discharge Device Having Ellipsoid-Shaped Electrode Surfaces (3,849,644)
D. B. Kaiser Method of Aligning a Laser Tube within an Envelope (3,847,703)
L. A. Kaplan Oscillator Using Controllable Gain Differential Amplifier with Three Feedback Circuits (3,851,276)
H. Kawamoto, E. L. Allen, Jr., and S. Weisbrod Broadband Trapatt Diode Amplifier (3,848,196)
R. Kaysen Control Unit for an Antenna Rotator (D,233,668)
W. Kern Method of Densifying Silicate Glasses (3,850,687)
H. W. Lehmann and R. W. Widmer Piezoelectric Transducer Comprising Oriented Zinc Oxide Film and Method of Manufacture (3,846,649)
D. K. Livingston, B. F. Floden, H. G. Wright, and W. H. Tsien Cartridge for Elongated Record Medium (3,845,916)
H. Lodgemann, Jr., and D. F. Dion Bowling Pin Detector (3,847,394)
B. B. McCue Method for Separating Sulfide Phosphor Particles from Mixtures (3,846,328)
T. C. McNulty Overcurrent Protection Circuit Including a Heat Sensitive Element and Thyristor (3,846,674)
W. A. Parker and R. A. Kryder Automatic Brightness Control for Image Intensifier Tube (3,848,123)
R. Peter and H. P. Lambrich Vertical Convergence Circuits (3,849,696)
R. B. Platt Method for Rendering Cathode-Ray Tube More Resistant to Implosion and Product Thereof (3,845,530)
W. E. Rodda and D. P. Dorsey Storage Tube Control Apparatus for a Telephone Image Transmission System (3,848,084)
H. Sokolov Wrapped Wire Connection (3,851,298)
F. Sterzer Semiconductor Delay Lines Using Three Terminal Transferred Electron Devices (3,848,141)
J. A. Tourtellot and F. R. Stave AC Motor (3,848,146)
J. L. Vossen, Jr. Method of Coating the Interior Walls of Through-Holes (3,846,294)
H. R. Warren Method for Recording Two Separate Signals (3,846,829)
C. P. Wen and Y. Chiang Method of Making Semiconductor Devices Having Thin Active Regions of the Semiconductor Material (3,846,198)
C. P. Wen Method of Making a Quasi-Monolithic Integrated CircuitStructure 3,850,710)
C. F. Wheatley, Jr. Temperature Dependent Voltage Reference Circuit (3,851,241)

December

A. F. Arnold Method of Electroless Metal Deposition (3,857,733)
A. F. Arnold Method of Electrolessly Plating a Metal to a Body Which Includes Lead (3,856,565)
L. R. Avery Cascade Amplifier Using Complementary Transistors (3,857,105)
D. L. Balzer and R. J. Lake, Jr. Storage System for Two Phase Fluids (3,854,905)
B. F. Bogner Lens Fed Antenna Array System (3,852,761)
D. J. Carlson Transistor Oscillator with Diode in Feedback Circuit Providing Amplitude Stabilization (3,855,550)

W. A. Dischert Reel Mounting Apparatus (3,857,526)
D. P. Dorsey and W. E. Rodda Dual Bias Controlled Storage Tubes (3,855,497)
D. P. Dorsey, W. E. Rodda, and K. B. Bahrs Switchable Video Amplifier (3,854,006)
R. A. Gange, E. M. Nagle, and C. C. Steinmetz Holographic Thermoplastic Memory System (3,851,948)
J. I. Gittleman and L. M. Zappulla Tuneable Thin Film Inductor (3,858,138)
I. Gorog Color Encoded Hologram Playback Apparatus (3,858,239)
J. R. Hale Fabrication of Dark Heaters (3,852,105)
R. C. Heuner and R. P. Fillmore Circuit, such as CMOS Crystal Oscillator, with Reduced Power Consumption (3,855,549)
H. Huang Microwave Acoustic Delay Line (3,857,113)
L. R. Hulls Magnetic Reed Sensor Suitable for Use in Ignition Timing Systems (3,852,664)
W. L. Hurford PWM Multiplex System (3,855,419)
J. Kane Process for Depositing Electrically Conductive Indium Oxide Coatings on Substrate (3,854,992)
H. Kawamoto Carrier Injected Avalanche Device (3,855,605)
M. B. Knight Detector Employing a Current Mirror (3,857,047)
H. Kressel, H. F. Lockwood, and F. Z. Hawrylo Semiconductor Injection Laser with Reduced Divergence of Emitted Beam (3,855,607)
A. J. Leidich Push-Pull Transistor Amplifier with Drive Circuits Providing Over-Current Protection (3,855,540)
A. J. Ledich Current Proportioning Circuit (3,855,541)
J. A. Lunsford Square Root of Sum of Squares Approximator (3,858,036)
J. C. March Programming System for a Motor-Driven Television Receiver Tuning Apparatus (3,855,535)
L. S. Napoli and R. H. Dean Solid State Switch Using an Improved Junction Field Effect (3,855,613)
L. S. Napoli and J. J. Hughes Method for Making Beam Lead Device (3,856,591)
H. Weisberg Thyristor Devices (3,855,611)
P. L. Nestleroth Electrode Support Strap (3,857,058)
G. D. Pyles Tape Cartridge Play Mechanism (3,852,818)
H. Rhee Circuit Breaker with Ambient Temperature Compensation (3,855,562)
A. Rosen and J. F. Reynolds Amplifier Using a Negative Resistance Semiconductive Device Operative in the Anomalous Mode (3,852,680)
D. L. Ross and L. A. Barton Electron Beam Recording Process (3,852,771)
W. L. Ross Fixed Format Video Data Display Employing Crossed-Line Pattern Format Delineation (3,858,198)
K. Sadashige Color Amplitude Correction in Plural Transducer Signal Playback Systems (3,852,808)
O. H. Schade, Jr. Current Mirror Amplifiers (3,852,679)
J. F. Schanne Article Labeling and Identification System (RE28285)
H. Sorkin Fabrication of Liquid Crystal Devices (3,853,391)
P. K. Weimer Sensors Having Charge Transfer Recycling Means (3,856,989)

AUTHORS

R. Casanova Alig received the B.A. degree from Wabash College in 1963, and the M.S. and Ph.D. degrees in physics from Purdue University in 1965 and 1967. He did theoretical studies of acoustic transport phenomena in metals for his dissertation. In 1967 Dr. Alig joined RCA Laboratories as a member of the Physics and Chemistry of Solids Group in the Physical Electronics Laboratory. He has recently done theoretical studies of the optical spectra of impurities and color centers in crystals. During the academic year 1970–71 he was a visiting professor at the Instituto de Fisica e Quimica, Sao Carlos, S.P., Brasil; in addition, since 1967 he has given courses at Mercer County Community College, LaSalle College, and Princeton University. He is a member of Phi Beta Kappa, Sigma Xi, and the American Physical Society.

Kohei Ametani received his B.S. in Chemistry from Ibaraki University in Mito city in 1966. After graduation, he worked for one year in the laboratories of Kyowa Seito Co., a sugar refinery, on the analysis of glucose and fluctose by means of iodometry and colorimetry. He joined RCA Research Laboratories, Tokyo, as a Research Technician in 1967 and was promoted to Member of the Technical Staff in 1970. He is doing research in the latex chemistry and atomic absorption spectrophotometry of magnetic and magnetic-semiconductive materials. He is a member of the Chemical Society of Japan and the Japan Society for Analytical Chemistry.

Dionys Baerlswyl received his diploma in theoretical nuclear physics from the University of Basel in 1969 and his Ph.D degree in 1973 at the University of Geneva with a thesis on the elementary excitations in superfluid helium. In the same year he joined Laboratories RCA Ltd., Zurich. He is presently working on the theory of structural phase transitions and high-density exciton systems.

Stanley Bloom received his B.S. from Rutgers University in 1948 and Ph.D. in physics in 1952 from Yale University, after which he joined RCA Laboratories. He has worked on microwave-tube noise, quantum electronics, plasmas, parametric amplifiers, semiconductor band theory, cathodoluminescence, and television electron optics. He has received four RCA Laboratories Achievement Awards and in 1966 was awarded an RCA Fellowship for a year of study abroad, which was spent at Cambridge University. He is a member of the IEEE, the American Physical Society, Sigma Xi, and Phi Beta Kappa.

William Burke received his B.S. degree in Physics at Boston College in 1959. He obtained the graduate degrees M.S. in 1961 and the Ph.D in 1965 from Tufts University. His doctoral research was concerned with the low-temperature thermal conductivity of alkali-halides. For the next two years he was a National Science Foundation Post-Doctoral fellow at the University of Illinois working on the effects of applied fields on optical transitions. He joined RCA Laboratories in August 1967. At RCA he has worked on optical spectroscopy in photochromics and paraelectric materials and stress-induced phase transitions in paraelectric materials using light scattering and dielectric studies and has served on a committee of the National Academy of Sciences on dielectric and ferroelectric materials. For the past several years he has worked on materials and devices applicable to volume holographic storage systems and other optical recording systems.

Dr. Burke is a member of the American Physical Society, the IEEE, and Sigma Xi.

Richard S. Crandall received a B.S. degree in physics from Cornell University in 1960, an M.S. in physics in 1962, and a Ph.D. in physics from the University of Illinois. He joined the RCA Laboratories in 1964 and has worked in the fields of electron and phonon transport in insulators and semiconductors, electron surface states on liquids, and is now engaged in studies of electrochromism. Dr. Crandall received an RCA Achievement Award for work on the electron-proton interaction and spent the year from 1971 to 1972 at the Zurich Laboratories of RCA. He is a member of the American Physical Society and the IEEE.

Wolfgang Czaja, Laboratories RCA Ltd., Zurich, Switzerland, received the diploma in physics in 1950. When he received the Ph.D. in 1957 he had already worked for 3 years in the development laboratory of a small company. He then worked eight years at the Institute of Applied Physics, University of Basel, and two years at Bell Telephone Labs., Murray Hill. In 1966 he joined Laboratories RCA Ltd., Zurich. He has a teaching assignment for Solid State Physics at the University of Basel. He is a member of the Swiss, European, and American Physical Societies.

Brian W. Faughnan graduated from McGill University in 1955 with a B.E. in Engineering Physics. He attended the Massachusetts Institute of Technology from 1955 to 1959; he was awarded an M.S. degree in Electrical Engineering in 1957 and a Ph.D. in Physics in 1959. His thesis work was on spins and phonons in paramagnetic crystals. In September 1959 he joined RCA Laboratories in Princeton, New Jersey. Since that time he has carried out research in a variety of topics in solid-state physics. These include the study of negative mass cyclotron resonance effects in germanium, radiation damage to solar cells, and the study of radiation damage centers in silicon by electron spin resonance techniques. From 1963 to 1964, he spent a year at the RCA Laboratories, Tokyo, studying the propagation of Alfven waves in the semimetal bismuth. Upon returning to Princeton, he continued work on semimetals including device applications. From 1966 to 1969 he engaged in fundamental studies of various photochromic single crystals, especially $SrTiO_3$, using combined electron-spin resonance and optical techniques. From 1970 to 1972 he studied electron-beam coloration of materials (cathodochromism), especially sodalite, with the goal of understanding the physical mechanism and optimizing the materials for device applications. For the past several years he has been studying electrochromic materials, especially amorphous WO_3 films. He received RCA Achievement Awards in 1962, 1969, and 1972.

Dr. Faughnan is a member of Sigma Xi and the American Physical Society.

Hiizu Fujita received his B.S. in Geophysics in 1955, his M.S. in Physical Meteorology in 1957, his M.S. in Radiation Science in 1959, and his Ph.D. in Physics in 1963, all from the University of Tokyo. From 1962 to 1966 he was a Research Associate at the Institute for Solid State Physics of the University of Tokyo where he studied transport phenomenon in insulators. From 1966 to 1969 he studied the optical properties of alkali halides using synchrotron radiation at the University of Illinois, where he served as a Research Assistant Professor in the Department of Physics. Since joining RCA Research Laboratories, Tokyo, in 1969, his interests have been the optical properties of semiconductors. He is a member of the Physical Society of Japan.

Günther Harbeke received the Physics Diploma in 1955 and the Ph.D. in Physics in 1958 from the Technical University in Brunswick, Germany. In 1961 he joined the staff of Laboratories RCA Ltd., Zurich. Prior to that he has been with the Physikalisch-Technische Bundesanstalt in Brunswick. In 1963, he worked 9 months at the RCA Laboratories in Princeton. Dr. Harbeke has been working in research on the basic optical properties of semiconducting and insulating materials and on light scattering and phase transitions in solids. He received two RCA Laboratories Achievement Awards for team performance in 1962 and in 1969. Dr. Harbeke has a lecturing assignment at the University of Cologne and is a member of the Zurich, Swiss, German, and European Physical Societies.

Philip M. Heyman graduated cum laude from CCNY in January 1963. In February 1963 he joined the staff at RCA Laboratories where he worked in the field of crystal lasers. From 1963 to 1965 he was on an RCA-Princeton University Cooperative program leading to an M.S.E. degree in June 1965. During this time his work at the Laboratories included the study of dispersions of electric dipoles in liquids for use as electrically controllable light valves, the fabrication of thin film transistors on ferroelectric substrates for use as analog memory elements and the study of current transients in liquid crystals. For the 1965-66 academic year, he was granted an RCA Doctoral Study Award. At the end of that year he returned to the Laboratories to work on his doctoral thesis, *The Photoconductivity of Photochromic* CaF_2. In June 1967 he received an M.A. and in June 1970 a Ph.D., both from Princeton University. Concurrent with his work on photochromic CaF_2, he also studied the photoelectric properties of strontium titanate and the optical properties of cathodochromic powders. Recently, he has worked on the development of high contrast thermally erasable cathodochromic displays. He received an RCA Achievement Award for his contributions to a team effort in producing a superior cathodochromic tube. Currently, he is studying the fabrication and design of various electrochromic display devices.

Dr. Heyman is a member of Eta Kappa Nu, Tau Beta Pi, IEEE, and the Society for Information Display.

Michiko Inoue received her B.A. in Natural Science from the International Christian University in Tokyo in 1958, and her Ph.D. in Physics from Harvard University in 1964. From 1964 to 1969 she was a Research Associate at the Institute for Solid State Physics of the University of Tokyo. Miss Inoue joined RCA Research Laboratories, Tokyo, in 1969. She is a member of the Physical Society of Japan.

Victor Korsun received the B.S. and M.S. degrees in Electrical Engineering from the Moore School of Electrical Engineering at the University of Pennsylvania, Philadelphia, Pa., in 1966 and 1973, respectively. From 1966 to the end of 1967 he was a research assistant in the Solid State Electronics Laboratory of the Moore School at the University of Pennsylvania. He joined the RCA Laboratories, Princeton, N. J., in 1968 where he has been engaged in research on the fundamental optical properties of various semiconductors and insulators. He is currently involved in research on the electronic transport properties of disordered materials and on silicon-on-sapphire photovoltaic solar cells for terrestrial applications.

Jacques I. Pankove obtained his B.S. (1944) and M.S. (1948) degrees from the University of California. He received his doctorate from the University of Paris in 1960 for a study of infrared radiation and germanium. Since 1948, when he joined RCA Laboratories, he has made many contributions to the understanding, technology, and evolution of various semiconductor devices, including large-area photocells and transistors. He has worked in the field of superconductivity, studies of silicon carbide, and investigations of the optical properties of degenerate germanium and the electrical properties of tunnel diodes in germanium, as well as in superconductors and in thin oxide layers. Currently, he is concerned with the study of injection luminescence and laser action in gallium arsenic and other compounds.

David Redfield received the B.A. from UCLA in 1948, M.S. from the University of Maryland in 1953, and Ph.D. from the University of Pennsylvania in 1956, all in physics. He held the Mobil Oil Co. Fellowship at the Univ. of Pa. for 1953–54 and 1954–55. He worked as an Electronic Scientist at the Natl. Bureau of Standards from 1949–52, first in solid state device development and then in solid state physics research. From 1955 to 1964 he was a research physicist for the Union Carbide Corp. in Parma, O. and Tarrytown, N. Y. He was Associate Professor of Electrical Engineering at Columbia Univ. from 1964–67 and then came to RCA. His work has centered on the optical and electronic properties of solids—mostly semiconductors. He is responsible for the discovery of the magnitudes of natural electric fields in imperfect solids and their influence on a variety of phenomena including semiconductor luminescence and the intrinsic limitations on optical transmission by non-metals. His most recent work has been chiefly in the properties of disordered semiconductors and solar cells.

He is a Fellow of the American Physical Society, was elected to the Executive Committee of its Division of Solid State Physics for 1973–75 and Chairman of the Division Fellowship Committee. He is a Senior Member of the IEEE, member of the AAAS, Sigma Xi, Sigma Pi Sigma and the Federation of American Scientists. He was elected Chairman of the Princeton Chapter of FAS in 1971–72 and member of its Executive Committee in 1972–73 and 73–74.

John R. Sandercock graduated in physics from Oxford University with a B.A. in 1964 and D.Phil. in 1968 on hot electron effects in semiconductors. Since then has been working in Laboratories RCA Ltd., Zurich in the field of light scattering in solids and has brought about significant improvements in the instrumentation for high resolution interference spectroscopy. He holds one patent and is author of 12 publications.

Edgar F. Steigmeier received the Physics Diploma in 1955 and the Ph.D. in Physics in 1960 from the Swiss Federal Institute of Technology (ETH) in Zurich. From 1960 to 1962, he worked at ETH for Brown Boveri Corporation, Baden, Switzerland, engaged in studies of heat conductivity and thermoelectricity. In 1962 he joined the Materials Research Laboratory of RCA Laboratories, Princeton, where he was working on basic properties and applications of thermoelectric materials such as Ge-Si alloys and III-V alloys, which has lead to high efficiency materials for power generation. In 1964 he joined Laboratories RCA, Zurich where he worked on problems of phonon transport, on optical properties of magnetic semiconductors and on materials involving soft lattice vibrations and phase transitions. Currently he is concerned with studies of light scattering and critical opalescence in these materials. In 1969 he received an RCA Laboratories Achievement Award for his contributions to the study of materials by means of Raman effect. During the Academic year 1973/74, Dr. Steigmeier was teaching as a guest lecturer a post graduate course on Solid State Physics at the University of Fribourg, Switzerland. He has published 40 technical papers. He is a member of the Zurich, Swiss, European and American Physical Societies.

Erio Tosatti graduated in Physics at the University of Modena in 1967, and completed his doctoral studies in 1970 at the Scuola Normale Superiore in Pisa. He then moved to the University of Rome where he does research on the theory of solids, under the sponsorship of the Italian Research Council (CNR). His research has dealt mainly with optical properties and collective excitations of electrons in anisotropic semiconductors and graphite, and with the theory of excitons, dielectric screening, phonons and electron-phonon interaction in semiconductors. He has been visiting for the last two years the Cavendish Laboratory in Cambridge, England, and the Theoretical Physics Department at the University of Stuttgart, Germany, and has started there new interests in semiconductor surfaces and in high density exciton phenomena. Dr. Tosatti is a member of the Italian Physical Society.

Herbert A. Weakliem received his B.Sc. in Chemistry from Rutgers University in 1953 and his Ph.D. in Chemistry from Cornell University in 1958. His doctoral thesis was on the x-ray crystallographic structure determination of several complex metal chelate compounds. During 1953–1954 he was engaged in research in catalysis at the Central Research Laboratories, Allied Chemical Corporation. He joined RCA Laboratories, Princeton, N. J., in 1958. He was a visiting Professor of Chemistry during the Spring 1957 term at Cornell University and was a visiting Professor of Physics during 1972–1973 at the University of California, Los Angeles. He has done extensive research on spectroscopy of transition metal ions and rare-earth ions in crystals, and has made many contributions to ligand field theory. He has also done studies on magnetic circular dichroism, high pulsed magnetic field Zeeman effects, and shallow donor spectroscopy in the far infrared by the use of Fourier transform spectroscopy. He is a member of Sigma Xi, the American Physical Society, the American Chemical Society, and the Optical Society of America.

Roland K. Wehner received the Physics Diploma in 1961 and the Ph.D. degree in 1964 from the University of Freiburg, Germany. After two and a half years of postdoctoral research at the University of Frankfurt/M., he joined in 1967 the technical staff of Laboratories RCA, Zurich. Dr. Wehner has been working on topics of solid-state theory, such as infrared absorption and light scattering by phonons in dielectric crystals. He has carried out studies of phonon-phonon interaction in sound absorption and heat transport theory. In 1973, he spent 9 months at the RCA Laboratories in Princeton, where he was engaged in work on the dynamics of surfaces of elastic media and electrostatic surface forces. Dr. Wehner is currently concerned with studies of structural phase transitions. He is a member of the Zurich, Swiss, German, European, and American Physical Societies.

Peter J. Wojtowicz received his B.Sc. degree in chemistry (with highest honors) from Rutgers University in 1953. He received his M.S. in chemistry in 1954 and his Ph.D. in physical chemistry in 1956 from Yale University. He was a National Science Foundation Predoctoral fellow while at Yale, 1953–1956. His thesis was concerned with the statistical mechanics of the order-disorder phenomenon in solids and the theory of molten salts and fluid mixtures. Dr. Wojtowicz joined RCA Laboratories in 1956. He is a member of the Physics and Chemistry of Solids Group of the Physical Electronics Research Laboratory. During 1966–67 he was the acting head of the General Research Group. His research effort while at RCA has been directed chiefly toward the theory of magnetic materials including quantum and statistical mechanics of the thermal, structural, and magnetic properties of these substances. This work included the theory of the cooperative Jahn-Teller effect, the statistical mechanics of magnetic interactions and phase transitions, the theory of magnetic semiconductors, the theory of granular ferromagnetic metals, and the theory of the application of ferrites and garnets to various magnetic devices. He is currently engaged in the theory of liquid crystals and liquid-crystal phase transformations. Dr. Wojtowicz is the recipient of two RCA Laboratories Achievement Awards for the years 1962 and 1966. He is a fellow of the American Physical Society and a member of Sigma Xi and Phi Beta Kappa.

STATEMENT OF OWNERSHIP

Statement of Ownership, Management and Circulation (Act of October 23, 1962. Section 4369, Title 39, United States Code.)

1. Date of filing: September 25, 1974. 2. Title of publication: RCA REVIEW. Frequency of issue: Quarterly. 4. Location of known office of publication: RCA Laboratories, Princeton, New Jersey, 08540. 5. Location of headquarters or general business offices of the publishers: RCA Laboratories, Princeton, New Jersey, 08540. 6. Names and addresses of publisher and editor: Publisher, RCA Laboratories, Princeton, New Jersey, 08540. Editor, R. F. Ciafone, RCA Laboratories, Princeton, New Jersey, 08540. 7. Owner: RCA Corporation, 30 Rockefeller Plaza, New York, New York 10020; Cede & Company, Box 20, Bowling Green Stn., New York, New York 10004; Merrill, Lynch, Pierce, Fenner & Smith, Inc., 70 Pine Street, New York, New York 10005; Cudd & Company, c/o Chase Manhattan Bank, Box 1508, C.S.S., New York, New York 10008; Martin B. Seretean, c/o Coronet Industries, Box 1248, Dalton, Georgia 30720; Burl Jackson Bandy, c/o Coronet Industries, Box 1248, Dalton, Georgia 30720; TNOM & Company, Box 577, Central Station, St. Louis, Missouri 63188.

I certify that the statements made by me above are correct and complete.

Ralph F. Ciafone, Editor